Puppeteering of microtubule-kinetochore coupling proteins
On the molecular control of minimal spindles

Nick Maleki, A.

DOI
10.4233/uuid:be37ffcc-b22a-4dd8-8026-ff5b0edc6155

Publication date
2025

Document Version
Final published version

Citation (APA)
Nick Maleki, A. (2025). *Puppeteering of microtubule-kinetochore coupling proteins: On the molecular control of minimal spindles*. [Dissertation (TU Delft), Delft University of Technology].
https://doi.org/10.4233/uuid:be37ffcc-b22a-4dd8-8026-ff5b0edc6155

Puppeteering of Microtubule-Kinetochore Coupling Proteins

On The Molecular Control of Minimal Spindles

Ali Nick Maleki

PUPPETEERING OF MICROTUBULE-KINETOCHORE COUPLING PROTEINS

ON THE MOLECULAR CONTROL OF MINIMAL SPINDLES

PUPPETEERING OF MICROTUBULE-KINETOCHORE COUPLING PROTEINS

ON THE MOLECULAR CONTROL OF MINIMAL SPINDLES

Dissertation

for the purpose of obtaining the degree of doctor
at Delft University of Technology
by the authority of the Rector Magnificus, prof. dr. ir. T.H.J.J. van der Hagen,
chair of the Board for Doctorates
to be defended publicly on
Wednesday, 19/11/2025 at 12:30

by

Ali NICK MALEKI

This dissertation has been approved by the promotors.

Composition of the doctoral committee:

Rector Magnificus,	*chairperson*
Prof. dr. A. M. Dogterom,	Delft University of Technology, *promotor*
Prof. dr. G. H. Koenderink,	Delft University of Technology, *promotor*
Independent members:	
Prof. dr. S. Tans,	Delft University of Technology
Prof. dr. A. Musacchio,	Max Planck Institute of Molecular Physiology, Dortmund
Prof. dr. C. Joo,	Delft University of Technology
Prof. dr. L. Blanchoin,	Interdisciplinary Research Institute of Grenoble
Dr. L. Laan,	Delft University of Technology

Keywords: microtubule, spindle, Ndc80, kinetochore, DNA segregation

Printed by: Ridderprint

Cover by: Ali Nick Maleki. The background is generated by ChatGPT.

ISBN 978-94-6518-175-2

An electronic copy of this dissertation is available at
`https://repository.tudelft.nl/`.

NOTES

The following AI tools have been used for paraphrasing, improving language, polishing, scripting code, and other tasks to enhance the quality and clarity of this thesis:

ChatGPT, Claude, Grok, Gemini, Perplexity and Deepseek.

To my parents who raised me with love and to my sisters Parisa and Zohreh who have made my life much more beautiful and hopeful.

CONTENTS

SUMMARY

This thesis investigates the intricate mechanics of microtubule dynamics and kinetochore function during chromosome segregation, leveraging DNA origami nanosprings as a novel tool to measure forces and explore protein interactions. Microtubules and kinetochores play pivotal roles in cellular division, driving chromosome movement through polymerization and depolymerization forces. Multivalency of the force transmitting intermediary proteins has been shown to play a crucial role in this process. Traditional methods like optical trapping, while precise, demand specialized equipment, and lack precision in terms of controlling the number of interacting agents. This work introduces a DNA origami-based approach to overcoming these challenges, offering insights into mitotic processes with broader implications for cell biology and biophysics. The following sections summarize the progression of this research, from foundational context to innovative applications and future prospects.

First, the biological and mechanical context of chromosome segregation is introduced, with a focus on microtubules. Microtubules, dynamic cytoskeletal filaments, assemble into the mitotic spindle, a bipolar structure orchestrated by microtubule organizing centers (MTOCs). Kinetochores, complex protein assemblies on chromosomes, couple to microtubule ends, transmitting forces to segregate chromosomes. The Ndc80 complex, a key kinetochore component that links microtubules to chromosomes, was introduced and discussed how its multivalency is essential in executing its load-bearing function in the kinetochore, setting the stage for introducing DNA origami technology (a nanospring) as a platform for multimerization and a tool for force measurements.

Next, the development and validation of DNA origami nanosprings as force sensors for microtubule dynamics takes the center stage. These nanosprings, crafted by folding DNA into a spring-like structure, extend under force, observable via fluorescence microscopy. Their performance is benchmarked against optical trapping by measuring dynein motor stall forces, revealing comparable results. The nanosprings also capture sub-piconewton forces from growing microtubules, mediated by EB3 comets and cargo proteins, and track Ndc80-coupled forces during depolymerization. This dual capability—force measurement and protein visualization—establishes the nanospring as a versatile, accessible tool, broadening the scope of biomechanical studies.

The focus then shifts to enhancing nanosprings to accommodate varying copies of a truncated Ndc80 variant, termed jubaea, and examining its impact on force transmission and microtubule behavior. By engineering nanosprings with binding sites for 3 to 20 jubaea molecules, the relationship between oligomerization and function is probed. Higher jubaea numbers increase force capture, peaking at 10 copies, and significantly slow microtubule depolymerization . Constructs with 15–20 copies stabilize microtubule ends, inducing rescues in over 50% of interactions, mirroring physiological kinetochore conditions. The jubaea loop region enhances binding strength, underscoring its role in force coupling. These findings highlight how protein stoichiometry can tune mitotic stability.

Efforts to reconstitute mitotic spindle dynamics follow, tackling controlled microtubule nucleation, end-on kinetochore attachment, and DNA segregation triggering. Our experiments showed using hydrophilic surfaces is not ideal when working with DNA, since DNA has a tendency to non-specifically bind to these surfaces. Various strategies were explored to spatially regulate microtubule growth, including patterning nucleation sites on surfaces and beads in 2D and 3D. We found that the best option to achieve high specificity in microtubule growth regulation is the use of DNA origami platforms and microtubule seeds with complementary handles designed for these structures. End-on conversion, where kinetochores transition from lateral to stable microtubule attachments, is modeled with nanosprings bearing Ndc80 and kinesin, mimicking cellular processes. Using photocleavable DNA linkers was suggested as a method to enable DNA segregation. These reconstitutions reveal the complexity of spindle assembly and the potential of minimal systems to dissect mitotic mechanisms, advancing synthetic biology approaches to cellular function.

The thesis culminates in a synthesis of findings, reflecting on their significance and charting future directions. The nanospring emerges as a powerful tool, revealing that microtubule forces and kinetochore stability hinge on protein copy number and structural features like the Ndc80 loop. These insights suggest cellular regulation of mitotic fidelity through dynamic protein adjustments, with implications for understanding mitotic errors in disease. The reconstitution efforts lay groundwork for artificial spindles. Future work could refine nanospring stability for higher forces, expand reconstitution to include more spindle components, and bridge in vitro findings to in vivo contexts, enhancing both fundamental and applied research.

SAMENVATTING

Dit proefschrift beschrijft de complexe dynamiek van microtubuli en kinetochoren tijdens chromosoomsegregatie, waarbij DNA origami nanoveertjes gebruikt worden als nieuw hulpmiddel om krachten te meten en om eiwit-interacties te doseren. Microtubuli en kinetochoren spelen een cruciale rol bij de celdeling, waarbij ze chromosoombeweging in gang zetten middels polymerisatie- en depolymerisatiekrachten. De multivalentie van de tussenliggende krachtkoppelings eiwitten blijkt een essentiële rol te spelen in dit proces. Traditionele methoden zoals optische trapping zijn weliswaar nauwkeurig, maar vereisen gespecialiseerde apparatuur en missen precisie bij het controleren van het aantal interacterende componenten. Dit werk introduceert een DNA origami gebaseerde aanpak om deze uitdagingen te overwinnen, en biedt inzichten in mitotische processen met bredere implicaties voor celbiologie en biofysica. De volgende secties geven een overzicht van de deelprojecten van dit onderzoek, van de fundamentele context tot innovatieve toepassingen en toekomstige vooruitzichten.

Eerst wordt de biologische en mechanische context van chromosoomsegregatie geïntroduceerd, met de focus op microtubuli. Microtubuli, dynamische cytoskeletfilamenten, vormen de mitotische spoel, een bipolaire structuur die gecoördineerd wordt door microtubuli-organiserende centra (MTOCs). Kinetochoren, complexe eiwitassemblages op chromosomen, koppelen zich aan de uiteinden van microtubuli en dragen de krachten over die nodig zijn voor chromosoomsegregatie. Het Ndc80-complex, een sleutelfactor binnen de kinetochoor die microtubuli met chromosomen verbindt, wordt geïntroduceerd en besproken, waarbij de nadruk ligt op zijn multivalentie bij het uitvoeren van zijn koppelingsfunctie. Dit legt de basis voor de introductie van DNA-origami-technologie (een nanoveertje) als een platform voor multimerisatie en een instrument voor krachtmetingen.

Vervolgens staat de ontwikkeling en validatie van DNA-origami nanoveertjes als krachtsensoren voor de dynamiek van microtubuli centraal. Deze nanoveertjes, gevormd door DNA op te vouwen in een spiraalvormige structuur, rekken uit onder kracht en zijn zichtbaar via fluorescentiemicroscopie. Hun prestaties worden vergeleken met optische trapping door de vastloop-krachten van dyneïne-motoren te meten, waarbij vergelijkbare resultaten worden verkregen. De nanoveertjes detecteren ook sub-piconewtonkrachten van groeiende microtubuli, gemedieerd door zogenaamde "EB3-kometen" en cargo-eiwitten, en volgen de Ndc80-gekoppelde krachten tijdens depolymerisatie. Deze dubbele functionaliteit—krachtmeting en eiwitvisualisatie—illustreert de nanoveer als een veelzijdig en toegankelijk instrument dat het bereik van biomechanisch onderzoek vergroot.

De focus verschuift vervolgens naar het verbeteren van nanoveertjes om een variërend aantal kopieën van een verkorte Ndc80-variant, genaamd jubaea, te bevatten en de impact hiervan op krachtoverdracht en het gedrag van microtubuli te onderzoeken. Door nanoveertjes te ontwerpen met bindingsplaatsen voor 3 tot 20 jubaea-moleculen wordt de relatie tussen oligomerisatie en functie geanalyseerd. Hogere aantallen jubaea verhogen de krachtoverdracht, met een piek bij 10 kopieën, en vertragen microtubuli depolymerisatie aanzienlijk. Constructen met 15–20 kopieën stabiliseren microtubuli-uiteinden en induceren in meer dan 50% van de interacties een redding, wat overeenkomt met fysiologische kinetochorecondities. De Ndc80-lusregio versterkt de bindingssterkte en benadrukt zijn rol in krachtkoppeling. Deze bevindingen tonen aan hoe de stoichiometrie van koppelingseiwitten de mitotische stabiliteit kan beïnvloeden.

Daarna volgt een poging om mitotische spoeldynamiek in vitro te reconstitueren, waarbij gecontroleerde microtubuli-nucleatie, end-on kinetochore attachments en het initiëren van DNA-segregatie worden onderzocht. Onze experimenten toonden aan dat hydrofiele oppervlakken niet ideaal zijn voor het werken met DNA, aangezien DNA de neiging heeft zich aspecifiek aan deze oppervlakken te binden. Verschillende strategieën werden onderzocht om microtubuli-groei ruimtelijk te reguleren, waaronder het patroonmatig aanbrengen van nucleatiesites op oppervlakken en bolletjes in zowel 2D als 3D. We ontdekten dat het gebruik van DNA-origamiplatforms en microtubuli-zaden met complementaire handvatten de beste controle over microtubuli-groei biedt. End-on conversie, waarbij kinetochores van laterale naar stabiele microtubuli-attachments overgaan, werd gemodelleerd met nanoveertjes die Ndc80 en kinesine dragen, wat celprocessen nabootst. Het gebruik van fotosplitsbare DNA-linkers werd voorgesteld als een methode om DNA-segregatie mogelijk te maken. Deze reconstituties onthullen de complexiteit van spoel-assemblage en het potentieel van minimale systemen om mitotische mechanismen te ontrafelen, waarmee synthetische biologie wordt ingezet om cellulaire functies beter te begrijpen.

Dit proefschrift eindigt met een synthese van de bevindingen, waarbij de implicaties ervan worden besproken en toekomstige richtingen worden geschetst. De nanoveer komt naar voren als een krachtig hulpmiddel en onthult dat microtubulikrachten en kinetochoor-stabiliteit afhangen van het aantal eiwitkopieën en structurele elementen zoals de Ndc80-lus. Deze inzichten suggereren dat cellulaire regulatie van mitotische nauwkeurigheid plaatsvindt door dynamische eiwitinteracties, en hebben implicaties voor het begrijpen van mitotische fouten bij ziekten. De reconstitutie-inspanningen vormen een basis voor kunstmatige spoelen. Toekomstig werk zou de stabiliteit van nanoveertjes kunnen verfijnen voor hogere krachten, de reconstitutie kunnen uitbreiden met meer spoelcomponenten, en bruggen kunnen slaan tussen in vitro en in vivo bevindingen, ter bevordering van zowel fundamenteel als toegepast onderzoek.

PREFACE

We exist in a moment characterized by unprecedented acceleration. Technological advancements reshape our world at a dizzying pace, while the undercurrents of global instability create a sense of pervasive uncertainty. This era forces reflection not only on societal structures but on the very nature of complexity, information, and existence itself. Life, in its profound intricacy, can be understood as a remarkable phenomenon of localized ordering—a persistent eddy that temporarily concentrates energy and information, seemingly resisting the universe's inexorable drift towards diffusion and entropy. Yet, viewed through a longer lens, this creation of intricate biological order might itself be a mechanism that ultimately facilitates the universe's overall entropic progression in complex ways we are only beginning to grasp. The current, explosive rise of artificial intelligence, emerging directly from our own biological thought processes, adds another layer to this reflection. It prompts provocative questions about the long-term trajectory of information processing in the cosmos. Organic life, this carbon-based engine of consciousness and complexity, might merely be a transitional phase, a biological scaffold destined to give rise to a silicon-based successor potentially far more adept at manipulating information and, perhaps paradoxically, more efficient in accelerating the very cosmic unfolding that organic life seemed to momentarily contributed to.

Against this profound backdrop, where the definition, purpose, and future of 'life' itself seem open to radical re-evaluation, the scientific endeavor feels both vastly expanded in its implications and fundamentally essential in its practice. The drive to innovate pushes boundaries outward at breakneck speed, yet concurrently, there remains a deep-seated, perhaps increasingly urgent, need to look inward – to understand the fundamental principles governing the complex, information-processing systems that currently constitute life on Earth. This work finds its place within that quieter, more deliberate pursuit of foundational knowledge. But before diving into the technical aspects I would like to share my general experiences learnt in this journey.

If I had to condense my entire PhD into a single word, it would be optimization—the continuous attempt to establish order within uncertainty. Optimization is the invisible ocean we live in without noticing it. It mirrors the forces of evolution: a step-by-step journey where we leap from one stable point to another, exploring the unknown, and staying only when stability is found. Looking back, this journey forms a trajectory—a record of all the states we once occupied.

Our capacity to explore is limited not only by our abilities but also by our judgments, biases, and the inertia we carry. Life, in many ways, is an art of stacking delicate pieces while maintaining enough balance so nothing collapses. My PhD honed this mindset: life itself becomes a system to optimize. First, map the landscape in low resolution. This preliminary, blurry image becomes the frame within which details can be refined. That low-resolution frame is what we often call the "invisible ceiling", a boundary we are not even aware of, yet it constrains us.

PhD reshaped my understanding of learning. I realized that most skills can be learned quickly, often within the first month. After that, little new content is added, yet performance still improves over time. This improvement is not from acquiring new knowledge, but from continuously pushing the boundaries of what we already know. Experience expands the visible landscape. It is like asking two people to walk across a vast, flat plateau. One has seen it clearly and knows there is space to run and jump freely. The other has never seen it and must proceed cautiously, consuming energy to map each inch. Experience is therefore not just technical, it is psychological. It reduces anxiety, increases confidence, and grants freedom of motion.

We underestimate how crippling anxiety can be because it rarely announces itself. It disguises itself as practicality, as “what if” thinking. In modern life, most of these “what ifs” are maladaptive, a residue from a past landscape of danger. They should be discarded by default. A simple question can neutralize them: Will this matter in a year? When we expand our temporal horizon, immediate emotions lose their grip. Just as a cat eventually realizes a new house is safe and begins to play, we too must allow ourselves that acclimation through perspective.

From my physics background, several concepts have deeply influenced my worldview: fundamental uncertainty and dualities and the principle of least action. The fundamental aspect of the irreconcilability of some observables in physics helped me understand other analogies in the world such as speed vs. accuracy, completeness vs. consistency, and short-term vs. long-term thinking. These are not binary choices, they exist on a spectrum. Choosing one side always comes at the expense of the other, and that sacrifice is unavoidable. This realization introduced me to the concept of context-dependent trade-offs and niche selection. The contrast between completeness and consistency humbled me by revealing how non-algorithmic and complex the world truly is. It was profound enough to convince me to tilt a bit more towards Plato from my initial absolute Aristotelian stance. Short-term versus long-term thinking became a powerful lens through which I could understand philosophical and religious teachings about life. Costs are inherent in every decision, including the decision not to act. Once we accept this, costs stop being sources of pain and instead become sources of pride, because they are chosen voluntarily.

Cultural traditions have long recognized the importance of long-term thinking, often culminating in beliefs about the afterlife. In that context, the afterlife functions as a stabilizing axiom that prioritizes long-term consequences. Similar approach can be taken, if you recognize goals that we are very sure they would be beneficial in the long run (such as physical exercises) and have faith in them. Without that faith, motivation evaporates. Discipline is simply the natural byproduct of long-term faith.

In essence, ideas begin to cluster into two groups: short-term thinking aligns with flexibility, creativity, and fun; long-term thinking aligns with discipline, structure, consistency and satisfaction. Both are necessary, but knowing when to favor one over the other is the hallmark of optimization.

And finally I found it useful to expand the non-binary vision to daily activities and realize nothing we do is in vain, and everything we do is recorded in our life resume. It is useful to think in spectrum about getting a job done. Arrhenius equation and the least action principle teach us not to force things to happen, but to lower the barriers. Set the stage, then just sit back and watch the events orchestrated by nature.

This text is getting long. I stop by leaving some insights I learned during my PhD for those who decide to do a PhD here.

- Tilt your baseline toward exploration. Our default setting is over-cautious. Reduce it intentionally.
- Start by generating "bullshit", then refine. The force of criticism within you is already strong. Don't strengthen it further. Remember that perfection is the enemy of good. Tune down criticizing other as well and instead propose better alternatives.
- Quantify everything in the PhD. Even trivial observations increase your ability to see patterns and expand your mental landscape.
- There is no perfect moment. The perfect moment is now. Live the life you want immediately. The conditional view on happiness or sadness is futile. More often than not, mental states come first and then the mind looks for stories to justify it. These stories are not necessarily correct. There is a lot of room in deciding which sets of observation to pick and interpret. The likelihood of false narratives are incredibly high.
- In the Netherlands, overworking yields minimal returns. The landscape is flat. Embrace the 8-hour work culture and use the rest of your time to live meaningfully. Brute force Sundays to be completely free and do what you've wanted to do if you had the choice to do voluntarily.
- Move in a band, not a line. Be flexible, but have boundaries. Always maintain a long-term project to give structure to your life.
- Let your creative instinct shine. by creative I mean carving out of noise, setting limitations and boundaries to the possibilities. Building physical things builds psychological stability. Order creation is necessary for mental clarity.
- Practice mental hygiene. Prioritize simplicity and clarity. In personal life, choose speed over accuracy and accept occasional errors along with it.
- Frame is everything. Wether we live in a good time or bad time, good location or bad location all depends on the frame. There is no objective singular true frame. Choosing a useful one doesn't mean you are deceiving yourself.
- Reject victimhood. Blame is disempowering. What is emerged from free exchanges is true and just. Ally yourself with truth, it should not be imposed but discovered. Let freedom and voluntary action guide you. Influence through invitation.
- Optimizing your daily life is more powerful than consuming more information. Reading more books is not as useful as designing better routines. Take into account not just you at the moment but your future selves and surroundings.

- Recognize dualities. Personal life and PhD life follow different optimization logics. Sometimes at the expense of each other. If you chose to prioritize PhD do opposite of what I said. Embrace accuracy, complexity, being detail oriented, be critical and overwork.

Ali Nick Maleki
Delft, October 2025

1

INTRODUCTION

For in and out, above, about, below,
'Tis nothing but a Magic Shadow-show,
Played in a Box whose Candle is the Sun,
Round which we Phantom Figures come and go

Omar Khayyam

What we observe is not nature itself, but nature exposed to our method of questioning.

Werner Heisenberg

A critical step in eukaryotic cell division is the faithful segregation of chromosomes. The cell employs the mitotic spindle machinery to achieve this goal. The microtubules originating from these poles grow and form a connection to the kinetochores of the chromosomes. The challenge is the overwhelming complexity of this process as the number of involved proteins exceeds hundreds. In this chapter, the main role players in the process are introduced and basic information about mechanisms such as dynamic instability of microtubules, microtubule nucleation and force generation is provided.

1.1. CELL DIVISION

CELL division, a fundamental feature of life, is a process of a parent cell dividing into two new daughter cells. Most cells undergo four phases to complete this process: cell growth, DNA replication, DNA distribution and finally division. Although cell growth and DNA replication occur throughout most of the cell cycle of bacterial cells, in eukaryotic cells these phases are discrete [1]. Failures in this process can lead to mis-segregation of genetic material and cell death and thereby it needs to be highly regulated to take place with high fidelity.

Eukaryotic cells employ active forces generated by cytoskeletal filaments and motor proteins to ensure genetic material is equally distributed in the daughter cells. This is done via the 'mitotic spindle'. The mitotic spindle is an apparatus in the cell with two poles and is made of microtubules (MT) and many other associated proteins [2]. The mitotic spindle consists of three types of microtubules that mostly originate from spindle poles: kinetochore MTs, astral MTs and non-kinetochore MTs [3]. Astral MTs emanate from spindle poles and play a crucial role in the position of the spindle as their interaction with the cell cortex can generate the forces that are necessary for creating a balanced position [4]. Non-kinetochore MTs are involved in spindle stabilization and generating opposing forces by sliding to separate poles [5]. Finally, kinetochore MTs stabilize into a bundle, called K-fiber, that plays a pivotal role in chromosome displacement [6]. Thus, controlled dynamics of MTs is required for both function and spindle formation [2] . In the following sections, we will dive deeper into each element of the spindle machine, especially MTs.

1.2. HISTORY OF MICROTUBULE RESEARCH

Microtubules are cytoskeletal filaments that play various roles, such as giving mechanical shape to the cell, intracellular transport, motility (e.g. in cilia and flagella) and cell division (mitotic spindle). In the late nineteenth century, "Fibrillae" were observed in the flagella and mitotic spindles ([7] but their relationship with each other and their existence was disputed [8]. Later, polarizing microscopy enabled higher quality of MT images as they differentially refract polarized light due to their highly ordered structures, which leads to the formation of a birefringence pattern [9]
.

In 1939, W.J.Schmidt provided clear images of MTs in marine eggs using polarizing microscopy, referring to as fibers [10]. It was first proposed by Inoué and co-workers that labile subunits in the spindle must be responsible for formation of the observed birefringence and exposure to cold temperature can disrupt the polymers [11–13]. In the following years, more direct evidence came from EM images of MTs and initially they were described as "long tubular elements of the endoplasmic reticulum, about 180 Å wide and remarkably straight" [14]. The name "microtubule" was later coined by Slautterback, Ledbetter and Porter for these filaments ([15, 16]) and one year after the publication of these articles, Gary Borisy managed to purify the main component of MTs [8].

Inoué and co-workers provided evidence that these polymers are in dynamic equilibrium with soluble subunits present in the cytoplasm of the cell [17, 18]. In

1968, the term ’tubulin’ was given to the MT subunits, while other terms such as ’tektin’, ’flactin’ and ’spactin’ were among the candidates [19]. Later, it was discovered that tubulin binds to GTP [20] which acts as a fuel for its polymerization [21] and this leads to the formation of a layer of GTP-bound tubulin cap at the end of MTs [22].

Subsequent studies found that tubulin can hydrolyze GTP and this process can make MTs unstable and lead to their depolymerization [23]. This observation, together with evidence from EM showing that MT number reduction can coexist with its mean length growth, helped Mitchison and Kirschner to conclude that MTs can switch from a growing to a shrinking phase if they lose their GTP cap, a phenomenon they called ’dynamic instability’ [24].

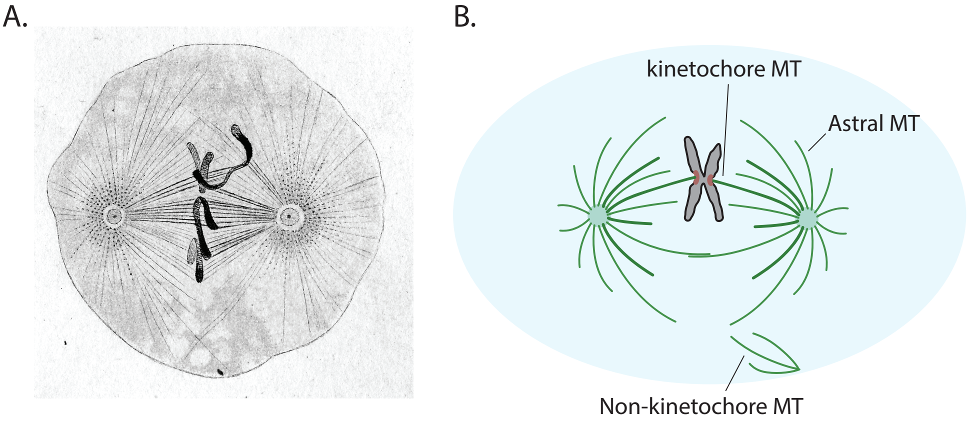

Figure 1.1: *Cell at metaphase. (A) Drawings of Ascaris cell division made by German zoologist, comparative anatomist, Theodore Boveri. The ‘fibrils’, which later named microtubules, are connected to the chromosomes from two poles. Image from (Boveri, 1888) [7]*

(B) Schematic representation of different types of microtubule according to Dumont et al. Kinetochore microtubules attach chromosomes to spindle poles, polymerize at the kinetochore and depolymerize at the pole, continuously slide poleward, form thick bundles, and have long lifetimes. Non-kinetochore microtubules – Nucleated throughout the spindle, slide toward the poles, have dynamic plus-ends, and minus-ends that are not directly anchored or probed. Astral microtubules radiate from centrosomes toward the cell cortex, do not slide, have dynamic plus-ends and fixed minus-ends, and can overlap with other microtubules [3].

1.3. DYNAMIC INSTABILITY

Microtubules (MTs) are biopolymers made of small subunit proteins called tubulin. Tubulin itself is a heterodimer comprised of α-tubulin and β-tubulin (in addition to α and β there are 5 more so far identified members of the tubulin superfamily: γ-, δ-, ϵ-, ζ- and η-tubulin) [25–27].

These heterodimers form lateral and longitudinal bonds with each other and can form a hollow tube (i.e. MT) with 25 nm diameter [28]. The longitudinal binding between tubulin dimers is estimated to be stronger than the lateral connections, with the former having a free energy of dissociation of 14.9 ± 1.5 kcal/mol and the latter 6.9 ± 0.4 kcal/mol [12]. As a result, it is typical to observe a chain of longitudinally connected tubulin oligomers in the EM images of MTs, which are called protofilaments (Fig 1.2C).

The number of protofilaments in each MT can vary, with 13 being the most typical number in eukaryotic cells [29]. In the in-vitro assay, this number can be between 8-16 depending on the conditions of polymerization [30–33]. Among different organisms with tubulin-like proteins, even lower and higher protofilament numbers are found: PhuZ filaments from bacteriophage $201\phi2-1$ have only 3 protofilaments [34] protofilaments and mantifly sperm have 40-protofilament microtubules [35]

The ability of tubulins to form a MT depends on their nucleotide state [24]. Both α-tubulin and β-tubulin have GTP/GDP binding sites. The GTP binding pocket of the α subunit (non exchangeable site or in short N-site) is buried at its intradimer interface with the β subunit and is always in a GTP state. The nucleotide binding site of the β subunit (exchangable site, E-site) on the other hand, is accessible for free floating GTP/GDP in the solution for exchange [36]. The binding of GTP to the β subunit causes a conformational change that increases its affinity for stronger lateral and longitudinal connections with other tubulin dimers and this makes MT grow from both of its ends [37]. However, whether it does it primarily by increasing lateral bonds or longitudinal or by changing the flexibility of intra and interdimer connections is still under debate. Once the tubulin is polymerized and positioned in the lattice of a MT, the β-tubulin GTP hydrolysis rate increases from 0.054 min-1 in the isolated dimer to 12-20 min-1 in the polymerized dimer, which corresponds to an energetic barrier of 3.9 ± 0.1 kcal/mol [38–40].

Hydrolysis of GTP in the lattice destabilizes the MT thereby a competition is formed between the stabilizing effect of the newly incorporated GTP-tubulin and the GTP hydrolysis that turns the GTP lattice to GDP lattice [41]. This observation led to the development of the ‘GTP-cap’ model in which a microtubule continues to grow as long as there are a sufficient number of GTP-tubulin subunits at the tip of the microtubules. On the one hand, GTP-tubulin keeps being added to the tip and, on the other hand, GTP is being hydrolyzed once tubulin incorporates into the lattices. This GTP cap can be stochastically lost as a result of hydrolysis of terminal subunits or dissociation of GTP-tubulin and, as a result, the microtubule starts to depolymerize [42]. This transition, from a growing phase to shrinking, is called a catastrophe event. However, the GTP-cap loss model for explaining catastrophe events has been recentrly challenged. Kok et al. showed the relevant parameter in determining wether a MT undergoes a catastrophe is not GTP-cap loss per se but local GDP-rich patches at the tip (at least 15 subunits) determine catastrophe initiation [43].

It is also possible for MTs to change their state from shrinking to growing, a process called MT rescue. Although not fully understood, islands of GTP-tubulin within the lattice away from the tip due to incomplete hydrolysis might be responsible for causing rescues.

The evidence in favor of the GTP cap model is abundant. This includes [44]:

1. GTP or its analogues are required for MT polymerization [45].
2. Ablating MTs that leaves the cleaved part uncapped leads to its depolymerization [46, 47]
3. A single layer of slowly-hydrolysable form of GTP called GMPCPP can change the state of depolymerizing MTs into a growing state [48].
4. In the absence of tubulin in the solution, the fast depolymerization does not start immediately, but it happens after a slow depolymerization phase [49, 50].
5. The observation that end-binding proteins (EBs) and nucleotide-sensitive antibodies recognize the tip of MTs that is interpreted at the GTP-bound lattice [51, 52]. The affinity of EBs to the tip of MTs is an order of magnitude higher than to the region of MT away from the tip [53].
6. Mutated tubulin without GTP hydrolyzing capability form long and stable MTs with EB decorating their entire length [40].

The hydrolysis of GTP in the β-tubulin takes place in two steps once the tubulin is polymerized: first a transitional stage where cleavage of one phosphate group from GTP while remaining in the GTP binding pocket (GDP-Pi state) and second release of the Pi while GDP remained bounded [22, 54].

There are some GTP/GDP analogs that are used to mimic each of the states mentioned above. GMPCP is used as GDP analog [55]. GMPCPP is commonly used to make MT lattices resembling GTP-bound tubulin part of the MT [45]. GMPPNP and GMPPCP are non-hydrolyzable analogues of GTP used to mimic GTP lattice [56]. GTPγS (the phosphate groups of the GTP are denoted as α, β and γ from interior to the exterior) is another non-hydrolyzable or slowly hydrolyzable analog that is suggested to mimic the GDP-Pi state of tubulin [56]. In another category of analogs, the γ phosphate of the GTP is replaced by molecules that mimic the chemical structure of phosphate such as AlFx and BeFx where the former is used to mimic GDP-Pi state and the latter to mimic GTP state [57].

Whether the destabilizing effect of GTP hydrolysis is caused by direct conformational changes in the tubulin structure is debated [36]. The early studies proposed a simple model in which the GTP-tubulin has a more straight conformation than GDP-tubulin and the straighter conformation is more favorable for MT growth. Upon the hydrolysis of GTP tubulin adopts a more bent conformation that favors depolymerization [58–61].

Therefore, the expectation would be that the tips of growing MTs must have more straight protofilaments, while the protofilament of the depolymerizing MTs should be more curved (‘ram-horns’) or tapered [39]. Although the early EM images provided evidence for this view [59], later cryo-EM studies challenged this report and showed both GTP-tubulin and GDP-tubulin are curved [62–64] and that both out curling and tapered tips are observed with MTs at their growing states [65].

These findings suggested that GTP hydrolysis does not directly induce large-scale structural changes but instead modulates microtubule stability through other mechanisms. Computational studies, including atomistic molecular dynamics (MD) simulations [66–68], further indicated that nucleotide state affects protofilament mechanics and lateral interactions but did not fully explain how hydrolysis drives dynamic instability.

Paydar et al assumed curved GTP-tubulin binds to the end of protofilaments and due to its higher affinity for forming longitudinal and lateral connections, the protofilaments are straightened and forced to fit into the straight conformation in the lattice [39]. Cryo-EM studies revealed that MT at GDP state has a more compact lattice [37, 69], this fact together with findings showing the α-tubulin completes the β-tubulin GTP hydrolysis site lead to the hypothesis that lattice compaction is needed for GTP hydrolysis, especially if we consider the findings from lattice spacing measurements done with phosphate mimicking analogs showing the expanded lattice observed in the GMPCPP MTs is an artifact of GMPCPP implying lattice compaction may not be the result of GTP hydrolysis but could be a precondition for it [57].

A study using TTMetaD (transition-tempered metadynamics) enhanced free-energy sampling in combination with quantum mechanics/molecular mechanics (QM/MM) simulation supported this claim by showing the activation barrier of GTP hydrolysis is highest in the expanded lattice (even higher than free dimers), mentioning the disruption of a interunit salt bridge that makes α:E254 unreachable as a potential reason [70]. This idea was supported further by an in vitro study showing the conformational change precedes the GTP hydrolysis in tubulin [39].

A more recent study from 2025 attempted to explain dynamic instability by using coarse-grained modeling (validated by atomistic simulations and cryoelectron tomography) to show how the switch between microtubule growth and shortening is determined by the way bent protofilaments at the ends of microtubules cluster together. This process is directly influenced by the nucleotide state of tubulin. GTP-bound protofilaments form short, flexible clusters that last longer and easily straighten into the microtubule lattice. This promotes elongation by allowing new dimers to fit in. In contrast, GDP-bound protofilaments are longer and stiffer. They create uneven clusters with higher internal tension, which destabilizes the end and encourages depolymerization. Thus, protofilament clustering serves as the structural and mechanical link between GTP hydrolysis in individual tubulins and the overall polymerization state of the microtubule [71].

Dynamical behavior of MTs has characteristics that are often used to make or test simulated models of MT dynamicity. For example, the rate of tubulin polymerization and depolymerization differs at each of its ends. The β-tubulin exposed end, known as plus end, exhibits higher rates of polymerization [72]. On the other hand, the α -tubulin exposed end, known as minus end, shows a higher depolymerization rate. Although the polymerization rate at both ends shows a linear dependence to the tubulin concentration, there is not a specific relationship between depolymerization rate and the tubulin concentration [72]. The catastrophe rate at both ends slightly diminshes with increasing tubulin concentration, whereas the rescue rate increases [72]. The catastrophe rate is reported to increase as MTs get longer and older, a phenomenon that is referred to as ’MT aging’ [73, 74]. In general, the rescue rate at the minus end is higher than the plus end, while in the case of the rate of catastrophe events the opposite is true [72, 75].

The age dependency of the catastrophe rate cannot be explained by the GTP cap model alone [44]. Accumulation of defects or destabilizing agents or gradual tapering of the MT tip has been proposed as potential reasons [73, 76–78]. To resolve these conflicts, a third model was developed recently that argues GTP-tubulin forms bent protofilaments at the end of the MT and these protofilaments frequently change their curvature due to thermal fluctuations and form and break lateral bonds with adjacent protofilaments [79]. This model can reproduce the MT tip structures observed in Cryo-EM studies and in combination with lattice mechanism of GTP hydrolysis can explain a wide range of in-vitro observations including the age-dependent catastrophe events [44].

1.4. TUBULIN STRUCTURE

Both of α and β tubulin subunits are made of ~450 amino acid residues and have a molecular weight of 50-55 KDa. The proper folding of tubulin subunits needs the assistance of chaperons. The newly translated tubulin chain binds to prefoldin, a protein that keep it in a highly unstructured state and then delivers it into the open TRiC chaperon [80]. TRiC folds the N-domain, C-domain, core domain (containing GTP binding domain) and M domain sequentially to make the native state (Gestaut et al., 2022).

The N-termini of both α- and β-tubulin are buried and not easily accessible on the exterior of intact MTs. The interaction between tubulin dimers along protofilaments involves the N-terminal domain of the β-subunit binding to the C-terminal domain of the α-subunit [81]. On the other hand, the C-termini of α- and β-tubulin are exposed with the last ~20 residues forming an unstructured tail that is rich in glutamate [82]. The C-terminal tail (CTT) has an influence on MT functions such as its polymerization [83], interaction with microtubule associated proteins (MAPs)[84, 85], kinetochore dynamics [86] and MT severing [87]. The CTT is also a site for a variety of post-translational modifications (PTMs) such as polyglycylation, polyglutamylation, detyrosination/tyrosination, phosphorylation [88].

These PTMs are essential for regulating microtubule dynamics, stability, and interactions with microtubule-associated proteins (MAPs). For example, polyglutamylation is observed to be associated with stable microtubules in cilia, centrioles, mitotic spindles, and axons [89]. The combination and extent of these modifications contribute to the functional diversity of microtubules in different cellular contexts [90].

It’s worth noting that the pattern and extent of these modifications can vary between different tubulin isotypes and cellular locations. For instance, in Drosophila ovaries, the general α-tubulins (αTub84B/D) exhibited glutamylation in their C-terminal tails, while the ovarian-specific αTub67C did not [88].

Each α and β tubulin come in different isotypes, which can provide tissue-specific functions [91]. Humans have 12 genes encoding α-tubulin (9 genes, 2 pseudogenes,

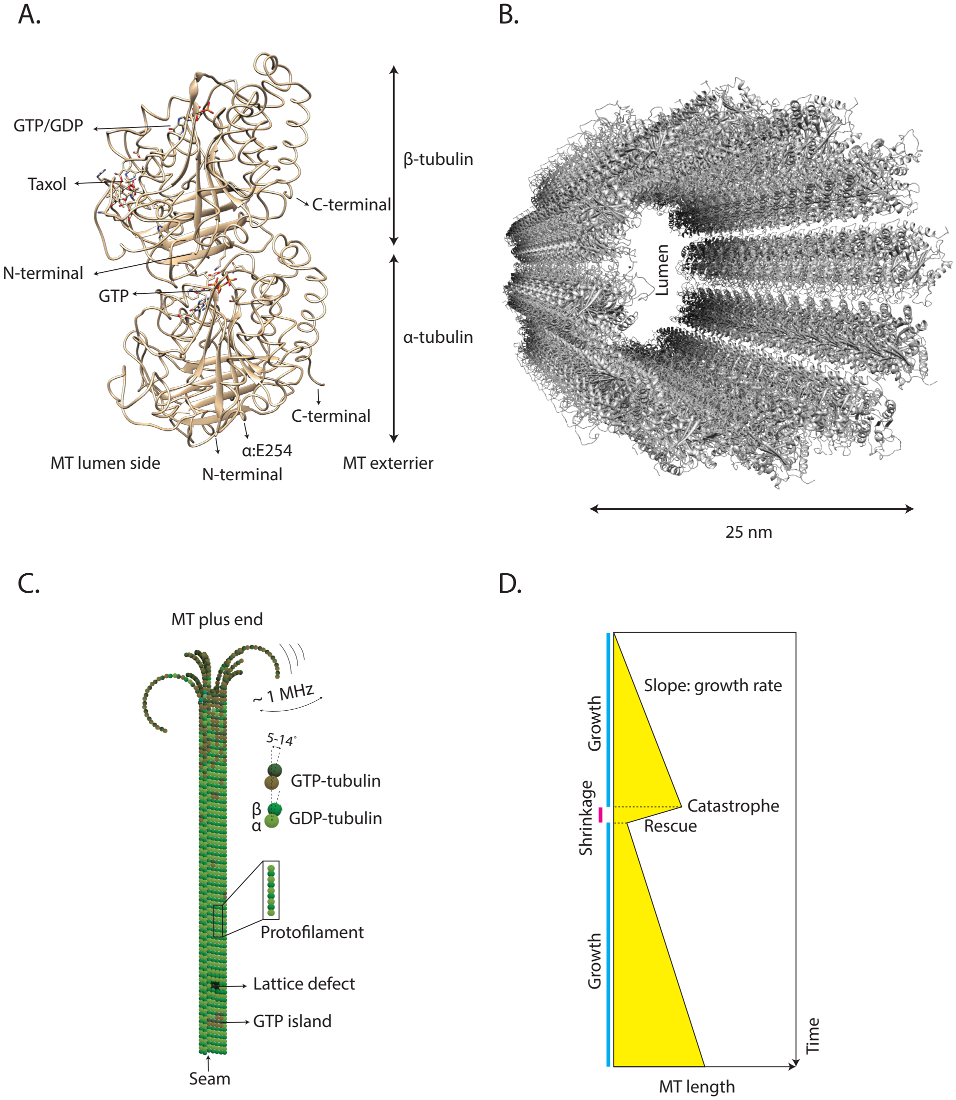

Figure 1.2: *Tubulin structure and self-assembly dynamics. (A) Crystal structure of α and β tubulin from thr protein data bank (PDB). The N-terminals of both subunits are buried in the structure, but the C-terminals are accessible on the MT exterior side. The E-site of β-tubulin and N site of α-tubulin as well as taxol binding site are highlighted. (B) GTP-tubulin self assembles to form a hollow cylinder (here with 12 protofilaments) of a diameter of 25 nm (C) Schematic representation of a dynamic MT. The protofilaments move due to thermal fluctuations and sometimes can form lateral bonds with neighboring protofilament resulting in MT growth. The GTP hydrolyses faster once the tubulin incorporates into the MT lattice, which leads to MT destabilization. The loss of the GTP cap can eventually lead to MT shrinkage. (D) A kymograph is often used to illustrate the dynamic behavior of MTs. The vertical axis is time and the horizontal axis shows the length of MT. The key events such as rescue and catastrophe are marked on the kymograph.*

1 putative gene) and 10 genes that encode β-tubulin (9 genes and 1 pseudogene) [92] which provide programmable modules for expression of tubulin for different cell types and developmental stages [93, 94]. For example, the brain and nervous system specifically make α-I, β-II, and β-III isotypes, while testis and ovary produce α-II, β-II, and β-IV isotypes[92].

The GTP hydrolysis pocket of β tubulin is located at its N-terminal. Apart from GTP, the tubulin dimer has multiple binding sites and at least 27 of them have been identified so far, such as tubulin-tubulin lateral and longitudinal, MT-stabilizing drug binding sites (taxane binding site, laulimalide binding site), MT-destabilizing drug binding sites, protein interaction binding sites (dynein, kinesin, tau, etc.) [95].

1.5. MICROTUBULE NUCLEATION

Microtubule nucleation is a key step in how the cytoskeleton self-assembles. It determines how microtubule networks are organized in terms of space and time within cells. Even though it plays an important role in cell division, transporting materials inside the cell, and maintaining structure, nucleation is one of the hardest phases of microtubule dynamics to observe directly. This difficulty arises because nucleation is not only thermodynamically unfavorable but also slow, involving rare and short-lived intermediates that are tough to spot in real time. As a result, researchers have created specialized in vitro tests to track the earliest stages of polymerization. These tests allow them to explore the molecular mechanisms and regulatory factors that oversee this essential process.

For elongated, rod-like particles with a diameter significantly smaller than the incident light's wavelength, turbidity demonstrates an inverse cubic relationship with wavelength (l^{-3}) and MTs serve as an effective model for the long rod limit when analyzing turbidity using light in the 320–600 nm wavelength range [96]. Gaskin et al. showed the turbidity is directly related to the amount of tubulin mass polymerized [97], as polymerized microtubules scatter more light. The turbidity assays of MT polymerization (absorbance at 350 nm vs. time) produce an S like plot where there is a slow phase of growth and then a linear region and finally slowing down and reaching a plateau as the tubulin gets depleted [98].

The initial lag phase in the microtubule polymerization is interpreted as the nucleation phase [99] and it was concluded that nucleation is the rate-limiting factor in the whole process of MT formation and growth. Thereby, microtubule sustained growth (~1 μM) is observed at much lower (~20 μM) than critical concentrations required for MT nucleation [100, 101]. The formation of an initial template to support further growth of MT involves a process of thermodynamically unfavorable assembly of tubulin oligomers [102]. The first stable oligomer whose polymerization is thermodynamically more favorable than its disintegration is referred to as critical nucleus, and the aforementioned lag phase is attributed to the formation of this unit [100].

The data from bulk assays (i.e. turbidity assay) of MT polymerization can be used to estimate the size of the critical nucleus, which is suggested to be 5-20 tubulin dimers [100, 103]. The size of the critical nucleus is independent of tubulin concentration but depends on other factors such as GTP hydrolysis rate [45], crowding agents) [104], viscogens [105], MT stabilizing/destabilizing drugs [106] and certain MAPs [107–109]. EM image analysis of oligomers during the early stages of nucleation and growth provides valuable insight into this process. According to a recent EM study, the mechanism of microtubule nucleation involves the formation of straight oligomers of tubulin, marking them as being essential for the nucleation process [110]. GTP binding to tubulin induces a conformational change that shifts the curvature distribution of oligomers, favoring the formation of straight oligomers. As the straight oligomers reach a critical size, they are able to overcome the energy barrier for nucleation. This allows them to serve as a foundation for the growth of microtubules [62]. To test this idea, researchers mutated the β-tubulin to promote straighter conformations (Y222F in the β-tubulin subunit) and found the straighter oligomers lowered the nucleation barrier [110].

1.6. KINETOCHORE

The kinetochore is a disc-shaped proteinaceous structure that plays a pivotal role in cell division. It forms on the centromere of duplicated chromatids in eukaryotic cells and serves as the attachment point for spindle MTs . Its primary function is to form sturdy connections between chromosomes and microtubules, enabling the accurate partitioning of genetic material into the emerging daughter cells. [111].

The two main parts of the kinetochore are the outer kinetochore (a 50–60-nm-thick region) which interacts with microtubules and is only assembled during cell division, and the inner kinetochore, which is firmly linked to centromere DNA and endures throughout the cell cycle [112]. A fibrous structure, known as fibrous corona, protrudes from the outer plate and contains proteins such as CENP-E and CENP-F that help capturing dynamic MTs and stabilizing them, a model which is referred to as ‘search and capture’ [113–115]. CENP-E is a plus-end-directed motor protein that laterally binds to the MT lattice and participates in the process of chromosome segregation [116]. Tubulin detyrosination, a PTM that is shown to be more concentrated in the microtubules oriented towards the mid-plane of the mitotic spindle and is depleted in the cortex-connected microtubules [117, 118], guides the direction of the movement of chromosomes by CENP-E. After this initial lateral attachment, the kinetochore must establish an end-on attachment in order to be able to utilize the depolymerization forces of MTs for chromosome segregation [119]. Ndc80 is one of the proteins in the outer kinetochore that plays a crucial part in the development of stable microtubule attachments, but its function in microtubule tip tracking is still obscure. Unless the complex is (artificially) oligomerized [120–122], Ndc80 complexes cannot track depolymerizing microtubules in vitro [123].

Additionally, there is proof that the kinetochore can either nucleate, as a result of the Ran pathway, or at least trap and promote the growth of small MTs that are formed in their vicinity [124, 125]. MTs can remain attached to the kinetochore at the same time as new tubulin is being added to its plus end, while dimers are disassembled from its minus end, a treadmilling behavior known as ‘microtubule flux’ [126]. This means kinetochores have the capability of forming a stable connection to the MT ends at both growing and shrinking phases.

1.7. MICROTUBULE TIP TRACKING

Although the lateral motor proteins play a role in chromosome displacement, they are largely dispensable [127, 128], indicating that the forces originated from end-on dynamics are mainly responsible for chromosome movements [129, 130].

Several models have been put forward to explain the movement of chromosomes due to depolymerizing MTs. In 1981, it was proposed that the kinetochore might form a processive sliding collar around microtubules to maintain its attachment [131]. When GTP cap is removed the protofilament releases the stored mechanical strain when they adopt the bent conformation [132] and the tugging of the peeling protofilament can slide the ring [133]. This is an example of 'forced walk' model in which the tracking is a direct result of the conformational wave produced by peeling protofilaments (Joglekar et al., 2010). Movement by binding of fibrils at the top of the protofilaments is another example of forced walk model [134].

Another model proposed for the mechanism of MAP tip tracking on both growing and shrinking MTs is affinity-driven tracking. This model assumes the higher affinity of a MAP to the end of the MT helps to have a sustained attachment to the growing/shrinking end, especially if the MAP is present in multiple numbers [135]. The tip tracking activity of human kinetochore proteins CENP-F and Ska1 can be explained by this model [123, 136], but not exclusively.

Another model proposed for explaining the tip tracking of shrinking MTs is called biased diffusion. A MAP with binding sites for MT can attach to it and diffuse on the lattice as a result of thermal fluctuations. Although the diffusion resulting from thermal fluctuations is not directional, it can be biased by factors such as higher affinity for the tip or merely encountering a shrinking end that reflects the diffuser [137, 138]. While in the affinity-based model the molecule can only transiently bind to the lattice and then dissociate, in the biased diffusion model a key property of the diffusive molecule is its processivity in binding which enables it to hop from one binding site to another without completely dissociating from MT [135]. This processivity cannot be infinitely long because of the possibility of hopping not to the next binding site but to the void. Nevertheless, it can be greatly enhanced if the diffusers are bundled together in multiple copies [135].

There is another requirement needed for a diffusive molecule to be a tip tracker, and this is the magnitude of the diffusion coefficient compared to the speed of depolymerization. As mentioned, when tip tracking is involved, the depolymerizing end causes the diffusers to bounce back when they encounter the end, but if the diffusion is fast the particle can move away before the shrinking end of the MT can catch up. If the diffusion is too slow, then the diffuser may simply block the depolymerization of the MT until the tubulin dimer at the end or the diffuser itself dissociates [139].

1.8. MECHANISM OF MICROTUBULE LOAD BEARING

The processive motion of an object under a force with a direction that is opposite of the direction of movement is called load bearing [135]. The energy sources used for load bearing in case of a shrinking MT tip tracker can either be from thermal motion combined with lattice affinity or the stored mechanical energy in protofilaments [140]. Thermal fluctuations are the main driver of biased diffusion behavior, but the thermal energy cannot be larger than the binding energy of the diffuser to the MT, otherwise the diffuser will be detached. Therefore, the load bearing force must be smaller than the thermal force to prevent the diffuser from falling off the MT end, indicating even a small load of < 1pN can stop tip tracking of the diffuser [139].

The maximum load bearing is expected to increase if multiple diffusing molecules are employed [121]. For example, a molecular-mechanical model using 13 binders with a diffusion coefficient of Ndc80 showed the stall force in this case could be 6-7 pN [139]. For larger amounts of forces, the mechanical energy of the protofilaments need to be harnessed. In a model, independent binders were assumed to bind firmly to the base of the curls of the protofilament and as shrinking continues, part of the force is transferred via the coupler and the binder is 'recycled' to bind again to the base of the curling protofilaments as its affinity for fully bent protofilaments is significantly reduced [122]. The stall forces predicted by this model could be as large as 70 pN [122].

In a more recent modeling of MT dynamics where it was straightening of protofilaments as a result of thermal fluctuations and formation of lateral bonds was proposed, the forces applied by curling protofilaments on a hypothetical ring were calculated, which could reach to up to 9 pN per protofilament depending on the protofilament stiffness and showed the shrining rate of depolymerizing MTs can be significantly reduced if the lateral bond between protofilaments is week [79]. The model's output also matched the experimental data about the relationship between exerting opposing forces and the polymerization rate.

Another model explained the load bearing of shrinking/growing MTs as a result of capillary forces [141]. The model suggests a network of microtubule plus end-binding proteins (+TIP bodies) form protein condensate at MT tip and that there is an optimal angle at which protein droplet contacts the microtubule shaft. This angle is determined by two competing forces: cohesion (which is caused by multiple binding sites within the droplet) and adhesion (which comes from the affinity of proteins to MTs). These two forces work together to create a specific preferred angle of contact. The resulting capillary velocity was measured to be faster than MT shrinking rate, which means the timescale of tubulin removal is longer than the timescale of +TIP body relaxation. Therefore, as the MT end shrinks, the peeling protofilaments push the protein condensate along the lattice and deform it and the condensate can move in the same direction by its tendency for relaxation [141]. It was proposed "an elastic modulus of the +TIP body can transmit this force to the cortex" [141]. It might seem this model is essentially the same as the biased diffusion model described at different representation levels, but in fact it also adds another important component to the equation and that is the multivalent interactions between the diffusers themselves.

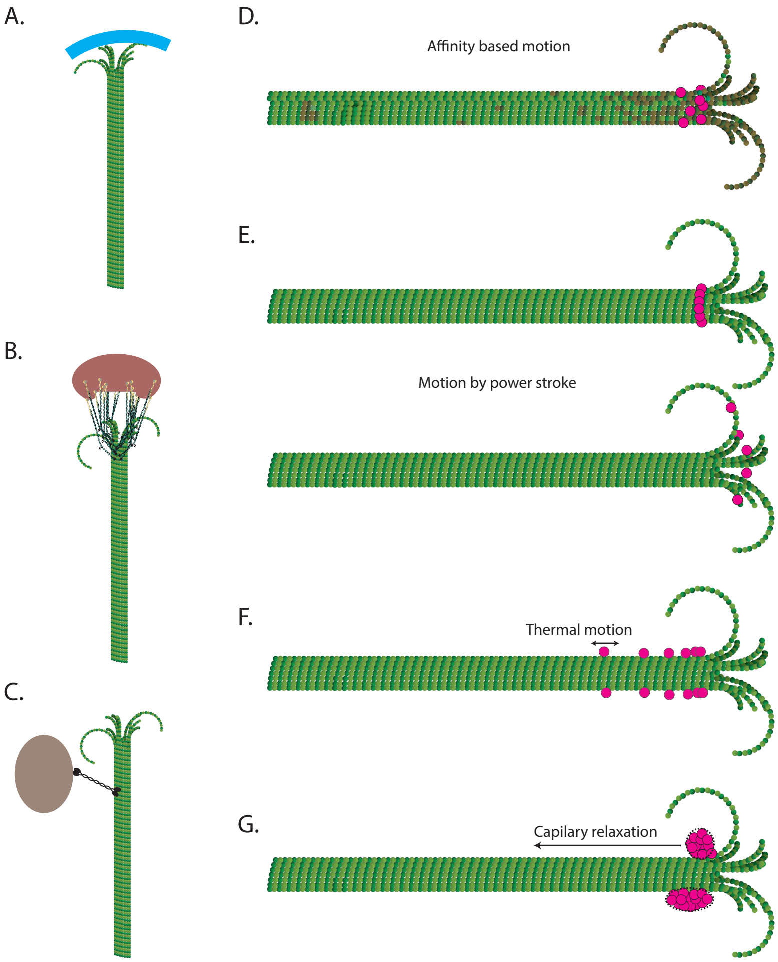

Figure 1.3: *MT involved force generation. (A) Growing MTs can generate pushing forces. This is especially important in spindle positioning where the growing MTs faced with the cell cortex generate pushing forces. (B) Depolymerizing MT generate forces that can be harnessed for chromosome movement. (C) Motor proteins use ATP as fuel and generate forces that can be employed for chromosome congression. (D) Affinity based model of tip tracking. In this model the MAP is assumed to have higher affinity to the MT tip and thereby follows the growing/shrinking end. (E) Forced walk model: In this model it is assumed the tip tracking protein binds firmly the MT and it is displaced as a result of mechanical movement of the peeling protofilaments, it could be in form of a ring or individual proteins that bind to the curled protofilaments. (F) Biased diffusion model: The tip tracking protein weakly binds to the MT lattice and diffuses on it as a result of thermal motions. The depolymerizing end of MT shrinks at a faster rate and catches up these diffusing entities, with the assumption that the diffusers will bounce back once they encounter the end. (G) Capillary force model: it is assumed the diffusers have an affinity among themselves and form a molecular condensate with a certain contact angle at equilibrium. The shrinking end of MT disrupts this equilibrium and changes the contact angle of the droplet. The droplet relaxes to its minimal free energy state by expanding away from the end.*

1.9. DNA ORIGAMI

DNA origami is the art of folding DNA into a desired shape. The folding is based on pair-bonding of DNA bases and thereby it is possible to engineer accurate and programmable structures using DNA code. The use of DNA origami could be highly advantages in in-vitro studies, especially when multiprotein complexes are involved, because of its programmability and it could be used as a platform to precisely control type and stichometry of interacting proteins of interest. As reviewed earlier, the multivalency is a key property in the tip tracking activity of MAPs. Traditionally the multimerization of tip trackers was obtained by immobilizing them on the surface of beads. This method is straightforward and provides valuable information about the collective vs. singular behavior of MT tip trackers, however it comes with potentially undesired consequences such as inevitability of always carrying a huge cargo and its potential geometric and mechanical influence, dissociation of non-specifically bound proteins from the bead and a lack of precise control over the number and spacing of interacting agents. A platform made of DNA origami can mitigate such issues. Verma et al used a sheet-like DNA origami structure and engineered it to have 3 or 6 hexagonally arranged binding sites for Ndc80 (Sequoia version) however the focus of this study was increasing the hybridization efficiency of DNA-labeled Ndc80 to the DNA origami scaffold rather than its interaction with MTs [142]. It was shown in this study that dimerization of hybridizing protein can be an effective strategy to increase the efficiency of protein-scaffold binding.

In another study [143] a ring-shaped DNA origami structure was made and tethered to the surface with its exposed side having 24 handles to bind proteins like Ndc80 or CLASP2 (a modified version of CLASP protein that is proposed to bind to curled protofilaments at the end of MTs and possibly help MT polymerization). It was demonstrated that CLASP, multimerized by DNA origami, is able to form load-bearing attachment to MT ends in the absence of GTP.

1.10. RECONSTITUTING MINIMAL MITOTIC SPINDLES

In this section we briefly review the history of the development of minimal mitotic spindle reconstitution studies and mention milestones in a chronological order. The foundation for in vitro studies of mitotic spindles was established in the mid-20th century with the pioneering experiments of trying to purify and characterize spindle constituents. Mazia first isolated the mitotic apparatus of dividing cells, providing the initial biochemical characterization of spindle components which subsequent researchers would emulate [144]. The work continued in the following decade, refining direct isolation techniques to further guarantee the investigation of the spindle's structure in detail [145]. The importance of maintaining proper chemical conditions was understood by the work of Kane [146], who studied physical and chemical determinants of mitotic apparatus stability in vitro and in particular the roles played by pH and dielectric constants. These early isolation methods were then refined by Forer and Sakai [147, 148].

A turning point was achieved in the late 1980s when researchers began demonstrating functional reconstitution of spindle processes. Rebhun and Palazzo succeeded in reconstructing anaphase B spindle elongation in isolated sea urchin egg spindles, the first to show the potential of isolated spindle components to recapitulate dynamic cellular behavior [149]. This was succeeded by the accomplishments of Lohka and Maller, where formation of the spindle was attained in cell-free Xenopus egg extracts, a landmark step towards investigating the dynamics of the spindle in fully defined in vitro systems [150]. The strength of this method revealed itself as Sawin and Mitchison recognized two different avenues of spindle assembly in Xenopus egg extracts, demonstrating the intricate dynamics of chromatin and microtubule interactions responsible for spindle formation [151].

In the 1990s, Dogterom et al. made microtubule asters in vitro by combining Xenopus laevis egg extracts with purified centrosomes, employing salmon sperm nuclei to concentrate clumps of chromatin in meiotic extracts or λ-phage DNA-based synthetic chromatin stripes on gold-patterned coverslips in mitotic extracts, supplemented with rhodamine-labeled tubulin for fluorescence microscopy [152]. These experiments allowed to study the local effect of M-phase chromatin on MT dynamics, a process believed to contribute to the formation of mitotic spindles.

In one of the earliest aster-in-confinement reconstitution studies, Holy et al. utilized microfabricated chambers to mimic cellular confinement, enabling the in vitro assembly and positioning of microtubule asters using purified tubulin, centrosomes, demonstrating that microtubule polymerization alone can center asters without molecular motors [153].

Over the following years the spindle formation mechanisms were further elucidated. Khodjakov demonstrated that chromatin alone can drive spindle formation without centrosomes [154], the RanGTP gradient was established as a spatial organizing system that locally releases spindle assembly factors around chromosomes [155–157], and multiple studies revealed how kinetochore-microtubule interactions, motor proteins, and structural matrices work together to create bipolar spindle organization through spatially controlled molecular activities [158–162].

Additional clarification of how crucial spindle assembly factors are regulated was provided by Kelly et al., which illustrated that Aurora B phosphorylates and activates TPX2 to facilitate spindle assembly through positive feedback [163]. The importance of specific protein interactions was further illustrated by Bird et al., who showed that the interaction between TPX2 and Aurora A is needed to form spindles of the appropriate length in human cells [164].

In 2010, Bieling et al. reconstituted a minimal midzone protein module with PRC1 with high precision for control of antiparallel microtubule overlap formation and length in vitro, closely reproducing the structure and function of the spindle midzone [165].

2 years later, Laan et al. recreated cortical dynein-microtubule interactions in vitro by utilizing microfabricated chambers with functionalized barriers to mimic the cellular cortex [166]. They attached dynein motors to these barriers and introduced dynamic microtubules nucleated from centrosomes to form asters.

In 2013 Portran et al published a reliable method to create MT nucleation centers with a controlled distance from each other, a step towards making microtubule bi-asters. they used UV micropatterning to create adhesive patterns on PEG-passivated glass surfaces, preventing non-specific protein adsorption. Biotinylated microtubule (MT) microseeds, stabilized with taxol and GMPCPP, were attached to these patterns via neutravidin, making it possible to make asters facing each other within a defined distance [167].

Subsequently, Vleugel et al. developed a method to reconstitute simplified mitotic spindles inside tiny water-in-oil droplets, which mimic the confined space of a cell. They started with just centrosomes and tubulininside these droplets. As microtubules grew, they pushed against the droplet boundary, causing the centrosomes to move apart—similar to how spindle poles separate in cells. They then added key proteins to study their effects: dynein pulled microtubules inward, counteracting the pushing forces, while kinesin-5 and Ase1 helped shape the spindle. This paper established the basic system to study spindle mechanics by adding components one at a time [168].

Building on this work, this team explored how the balance of forces between microtubules and proteins determines spindle structure. They measured how microtubule length and density affect aster positioning and combined experiments with computer simulations to show that asters naturally repel each other due to steric clashes. They then tested how different proteins compete: Ase1 pulled asters closer by bundling microtubules, while kinesin-5 pushed them apart. Even without chromosomes, the system could switch between "metaphase-like" (asters held at mid-distance) and "anaphase-like" (asters fully separated) states, revealing how spindles achieve flexibility. This work provided a quantitative framework for how spindle architecture emerges from simple physical rules and molecular interactions [169].

Reconstitution of kinetochore-microtubule attachments has also been a main focus of study over the past few years. Cheeseman et al.defined the KMN complex of KNL-1, the Mis12 complex, and the Ndc80 complex as the innermost microtubule-binding site of the kinetochore with enhanced microtubule-binding activity in purified systems [170].

In addition, the reconstitution of branching microtubule nucleation has illuminated mechanisms of spindle amplification. Travis et al. reconstituted branching microtubule nucleation in vitro from purified Drosophila embryo Augmin and γ-TuRC, demonstrating cell cycle-dependent microtubule amplification necessary for assembly of spindles in large cells [171]. The study revealed molecular mechanisms by which cells amplify microtubule density during mitosis to enable vigorous spindle formation.

The cumulative results of these reconstitution experiments have provided us with fundamental understanding of the self-assembly mechanisms of the mitotic spindle and how motor proteins, microtubules, and cross-linking factors act together to generate effective structures that can segregate chromosomes. The experiments showed that highly complex organizational behavior can often be reconstructed from simple molecular building blocks if they are placed in the correct geometric and biochemical contexts. Looking to the future, reconstitution studies will strive to incorporate increasingly sophisticated biologically-relevant elements in minimal spindles, in order to achieve spindle reconstitution experiments simulating all relevant aspects of cellular mitosis. For example, the addition of minimal (bi-oriented) chromosome mimics will be an important step forward that will help understand the basic principles of chromosome positioning and dynamics in spindles. This thesis is motivated by achieving this goal.

1.11. THESIS MOTIVATION AND OUTLINE

Studying spindle-mediated chromosome segregation is challenging due to its high complexity and tight regulation, involving hundreds of proteins. Traditionally, researchers employ either top-down or bottom-up approaches to reduce complexity and identify a minimal set of components capable of performing biologically relevant functions. Building on the long history of in vitro studies in our lab, the goal of this work was to reconstitute mitotic spindle–mediated DNA segregation in a modular manner (Figure 1.4).

In this modular approach, the process was broken down into four functional units: Module 1: Establishing a stable, processive, and load-bearing connection between a shrinking microtubule (MT) plus end and the load (mimicking the kinetochore–MT interface).

Module 2: Reconstituting microtubule asters and controlling their positioning (analogous to astral MTs in cells).

Module 3: Mimicking DNA congression by using plus-end–directed motors to transport the load toward MT plus ends.

Module 4: Reproducing chromosome bi-orientation by symmetrically linking load-bearing cargos (homodimers) to MTs from opposite sides by using photocleable linkers, allowing for controlled external cleavage of the connection.

These modules map directly onto the core biological features of spindle-mediated segregation: Modules 1 and 4 address the MT–DNA connection (plus-end interactions and bi-orientation), while Modules 2 relate to MT organization and positioning (minus-end nucleation control). Module 3 attempts to reconstitute end-on conversion phenomenon. By integrating all four, a minimal, fully reconstituted spindle segregation machinery can be achieved.

The content of the thesis is structured as follows:

Chapter 1:Elucidating the context and explaining the components used in this reconstitution study, starting from a general view (cell cycle and division) and gradually zooming in into detailed explanation of some of the main players in the process (e.g. tubulin, Ndc80).

Chapter 2: Introduction of the nanospring tool for precise control over the number of load-bearing Ndc80 complexes during MT interactions (Module 1). Its force measurement validity was confirmed, and it was applied to study how Ndc80 oligomers capture force in the presence of the SKA complex.

Chapter 3: Systematic variation of Ndc80 complex number using DNA origami, approaching physiological copy numbers (20), and assessment of the resulting effects on force transmission and MT dynamics (Module 1). This chapter is an exploration to find the condition for a stable and procesive connenction between microtubule and the load.

Chapter 4: Application of microfabrication and DNA origami methods to pattern MT seeds and control nucleation sites, culminating in the reconstitution of a 3D artificial MT aster (Module 2).

Chapter 5: Development of a load-bearing homodimer capable of interacting with microtubules (MTs) from both directions was achieved. A 2D mitotic spindle with crosslinked antiparallel MTs was reconstituted to provide the structural framework for this system. Such an arrangement is essential for establishing a bioriented connection, in which two opposing MTs attach to the same DNA cargo from opposite sides. The two load-bearing motile units are linked via a photocleavable linker, rendering the system photoresponsive. Once a stable bioriented connection is formed, DNA segregation can be triggered by light-induced cleavage of this linker, thereby mimicking the separation process observed in cells. (Modules 2–4)

Chapter 6: Discussion of reconstituted systems focusing on MT nucleation and MT–DNA connections, with perspectives for future developments toward fully integrating all four modules into a minimal, functional spindle-mediated segregation system.

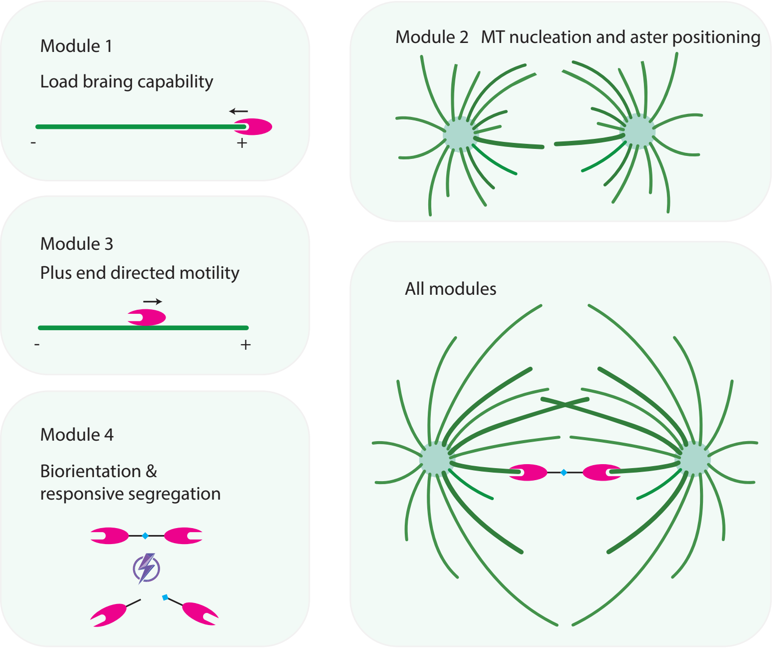

Figure 1.4: *Modules involved in spindle-mediated DNA segregation. Module 1: Reconstitution of a stable connection between the load and a shrinking microtubule. Ideally, this connection should be processive and capable of bearing the load. Module 2: Comprising two parts—(a) reconstitution of microtubule asters and (b) their precise positioning. Module 3: Mimicking DNA congression in cells by using plus-end–directed motors to transport the load toward the microtubule plus end. Module 4: Mimicking chromosome bi-orientation, where the plus-end–moving, load-bearing cargo is symmetrically connected (homodimer) and can interact with microtubules from both sides. This homodimer can be cleaved by an external trigger (in this study by 405 nm laser light). A fully reconstituted minimal spindle-mediated DNA segregation machinery is obtained by integrating all four modules.*

REFERENCES

[1] G. M. Cooper. “The Eukaryotic Cell Cycle”. In: *The Cell: A Molecular Approach. 2nd edition.* Sinauer Associates, 2000. URL: `https://www.ncbi.nlm.nih.gov/books/NBK9876/` (visited on 02/12/2025).

[2] J. R. McIntosh. “Mitosis”. In: *Cold Spring Harbor Perspectives in Biology* 8.9 (Sept. 2016), a023218. ISSN: 1943-0264. DOI: `10.1101/cshperspect.a023218`. URL: `http://cshperspectives.cshlp.org/lookup/doi/10.1101/cshperspect.a023218` (visited on 02/12/2025).

[3] S. Dumont and T. J. Mitchison. “Force and length in the mitotic spindle”. In: *Current biology: CB* 19.17 (Sept. 15, 2009), R749–761. ISSN: 1879-0445. DOI: `10.1016/j.cub.2009.07.028`.

[4] F. J. McNally. “Mechanisms of spindle positioning”. In: *The Journal of Cell Biology* 200.2 (Jan. 21, 2013), pp. 131–140. ISSN: 1540-8140. DOI: `10.1083/jcb.201210007`.

[5] S. L. Prosser and L. Pelletier. “Mitotic spindle assembly in animal cells: a fine balancing act”. In: *Nature Reviews Molecular Cell Biology* 18.3 (Mar. 2017). Publisher: Nature Publishing Group, pp. 187–201. ISSN: 1471-0080. DOI: `10.1038/nrm.2016.162`. URL: `https://www.nature.com/articles/nrm.2016.162` (visited on 02/12/2025).

[6] M. A. Begley, A. L. Solon, E. M. Davis, M. G. Sherrill, R. Ohi, and M. W. Elting. “K-fiber bundles in the mitotic spindle are mechanically reinforced by Kif15”. In: *Molecular Biology of the Cell* 32.22 (Dec. 1, 2021), br11. ISSN: 1059-1524. DOI: `10.1091/mbc.E20-06-0426`. URL: `https://www.ncbi.nlm.nih.gov/pmc/articles/PMC8694074/` (visited on 02/12/2025).

[7] T. Boveri. “Die Befruchtung und Teilung des Eies von Ascaris megalocephala”. In: (1888). URL: `https://www.biodiversitylibrary.org/page/6303876#page/7/mode/1up`.

[8] W. A. Wells. “The discovery of tubulin”. In: *Journal of Cell Biology* 169.4 (May 23, 2005), p. 552. ISSN: 0021-9525. DOI: `10.1083/jcb1694fta1`. URL: `https://doi.org/10.1083/jcb1694fta1` (visited on 01/30/2025).

[9] W. J. Schmidt. “Zur Doppelbrechung der Chromosomen in den Speicheldrüsenkernen der Chironomuslarven”. In: *Naturwissenschaften* 25.31 (July 1, 1937), pp. 506–507. ISSN: 1432-1904. DOI: `10.1007/BF01498058`. URL: `https://doi.org/10.1007/BF01498058` (visited on 01/30/2025).

[10] W. J. Schmidt. “Doppelbrechung der Kernspindel und Zugfasertheorie der Chromosomenbewegung”. In: *Zeitschrift für Zellforschung und Mikroskopische Anatomie Abt. B Chromosoma* 1.1 (Dec. 1, 1939), pp. 253–264. ISSN: 1432-0886. DOI: 10.1007/BF01271634. URL: https://doi.org/10.1007/BF01271634 (visited on 01/30/2025).

[11] L. Bonetta. “Microtubules shape the cell”. In: *Journal of Cell Biology* 169.4 (May 23, 2005), p. 553. ISSN: 0021-9525. DOI: 10.1083/jcb1694fta2. URL: https://doi.org/10.1083/jcb1694fta2 (visited on 01/30/2025).

[12] W. (R.) Brinkley. “Microtubules: A Brief Historical Perspective”. In: *Journal of Structural Biology* 118.2 (Mar. 1, 1997), pp. 84–86. ISSN: 1047-8477. DOI: 10.1006/jsbi.1997.3854. URL: https://www.sciencedirect.com/science/article/pii/S1047847797938545 (visited on 01/30/2025).

[13] S. Inoue´ and K. Dan. “Birefringence in edosperm mitosis”. In: *J. Morphol.* 89 (1951), pp. 48–63.

[14] S. L. PALAY. “Synapses in the central nervous system”. In: *The Journal of biophysical and biochemical cytology* 2.4 (July 1, 1956), pp. 193–202. ISSN: 0095-9901. DOI: 10.1083/jcb.2.4.193. URL: https://europepmc.org/articles/PMC2229686 (visited on 01/30/2025).

[15] M. C. Ledbetter and K. R. Porter. “A "MICROTUBULE" IN PLANT CELL FINE STRUCTURE”. In: *The Journal of Cell Biology* 19.1 (Oct. 1, 1963), pp. 239–250. ISSN: 0021-9525. URL: https://www.ncbi.nlm.nih.gov/pmc/articles/PMC2106853/ (visited on 01/30/2025).

[16] D. B. Slautterback. “CYTOPLASMIC MICROTUBULES. I. HYDRA”. In: *The Journal of Cell Biology* 18.2 (Aug. 1963), pp. 367–388. ISSN: 0021-9525. DOI: 10.1083/jcb.18.2.367.

[17] S. Inoué and H. Sato. “Cell motility by labile association of molecules. The nature of mitotic spindle fibers and their role in chromosome movement”. In: *The Journal of General Physiology* 50.6 (July 1967), Suppl:259–292. ISSN: 0022-1295.

[18] S. Inoué, J. Fuseler, E. D. Salmon, and G. W. Ellis. “Functional organization of mitotic microtubules. Physical chemistry of the in vivo equilibrium system”. In: *Biophysical Journal* 15.7 (July 1975), pp. 725–744. ISSN: 0006-3495. DOI: 10.1016/S0006-3495(75)85850-4.

[19] H. Mohri. “Amino-acid composition of "Tubulin" constituting microtubules of sperm flagella”. In: *Nature* 217.5133 (Mar. 16, 1968), pp. 1053–1054. ISSN: 0028-0836. DOI: 10.1038/2171053a0.

[20] R. C. Weisenberg, G. G. Broisy, and E. W. Taylor. “Colchicine-binding protein of mammalian brain and its relation to microtubules”. In: *Biochemistry* 7.12 (Dec. 1, 1968). Publisher: American Chemical Society, pp. 4466–4479. ISSN: 0006-2960. DOI: 10.1021/bi00852a043. URL: https://doi.org/10.1021/bi00852a043 (visited on 01/30/2025).

[21] R. C. Weisenberg. “Microtubule Formation in vitro in Solutions Containing Low Calcium Concentrations”. In: *Science* 177.4054 (Sept. 22, 1972). Publisher: American Association for the Advancement of Science, pp. 1104–1105. DOI: `10.1126/science.177.4054.1104`. URL: `https://www.science.org/doi/10.1126/science.177.4054.1104` (visited on 01/30/2025).

[22] M. F. Carlier and D. Pantaloni. “Kinetic analysis of guanosine 5’-triphosphate hydrolysis associated with tubulin polymerization”. In: *Biochemistry* 20.7 (Mar. 31, 1981). Publisher: American Chemical Society, pp. 1918–1924. ISSN: 0006-2960. DOI: `10.1021/bi00510a030`. URL: `https://doi.org/10.1021/bi00510a030` (visited on 01/27/2025).

[23] M. F. Carlier, T. L. Hill, and Y. Chen. “Interference of GTP hydrolysis in the mechanism of microtubule assembly: an experimental study.” In: *Proceedings of the National Academy of Sciences* 81.3 (Feb. 1984). Publisher: Proceedings of the National Academy of Sciences, pp. 771–775. DOI: `10.1073/pnas.81.3.771`. URL: `https://www.pnas.org/doi/abs/10.1073/pnas.81.3.771` (visited on 01/30/2025).

[24] T. Mitchison and M. Kirschner. “Dynamic instability of microtubule growth”. In: *Nature* 312.5991 (Nov. 1984). Publisher: Nature Publishing Group, pp. 237–242. ISSN: 1476-4687. DOI: `10.1038/312237a0`. URL: `https://www.nature.com/articles/312237a0` (visited on 01/30/2025).

[25] M. A. Kristensson. “The Game of Tubulins”. In: *Cells* 10.4 (Mar. 28, 2021), p. 745. ISSN: 2073-4409. DOI: `10.3390/cells10040745`. URL: `https://www.ncbi.nlm.nih.gov/pmc/articles/PMC8065753/` (visited on 01/31/2025).

[26] F. Ruiz, P. Dupuis-Williams, C. Klotz, F. Forquignon, M. Bergdoll, J. Beisson, and F. Koll. “Genetic Evidence for Interaction between η- and β-Tubulins”. In: *Eukaryotic Cell* 3.1 (Feb. 2004), pp. 212–220. ISSN: 1535-9778. DOI: `10.1128/EC.3.1.212-220.2004`. URL: `https://www.ncbi.nlm.nih.gov/pmc/articles/PMC329518/` (visited on 01/31/2025).

[27] E. Turk, A. A. Wills, T. Kwon, J. Sedzinski, J. B. Wallingford, and T. Stearns. “Zeta-Tubulin Is a Member of a Conserved Tubulin Module and Is a Component of the Centriolar Basal Foot in Multiciliated Cells”. In: *Current biology: CB* 25.16 (Aug. 17, 2015), pp. 2177–2183. ISSN: 1879-0445. DOI: `10.1016/j.cub.2015.06.063`.

[28] E. Nogales. “Structural insights into microtubule function”. In: *Annual review of biophysics and biomolecular structure* 30.1 (2001), pp. 397–420.

[29] L. G. Tilney, J. Bryan, D. J. Bush, K. Fujiwara, M. S. Mooseker, D. B. Murphy, and D. H. Snyder. “MICROTUBULES: EVIDENCE FOR 13 PROTOFILAMENTS”. In: *Journal of Cell Biology* 59.2 (Nov. 1, 1973), pp. 267–275. ISSN: 0021-9525. DOI: `10.1083/jcb.59.2.267`. URL: `https://doi.org/10.1083/jcb.59.2.267` (visited on 01/27/2025).

[30] K. J. Böhm, W. Vater, H. Fenske, and E. Unger. “Effect of microtubule-associated proteins on the protofilament number of microtubules assembled in vitro”. In: *Biochimica Et Biophysica Acta* 800.2 (July 30, 1984), pp. 119–126. ISSN: 0006-3002. DOI: 10.1016/0304-4165(84)90049-7.

[31] D. Chrétien, F. Metoz, F. Verde, E. Karsenti, and R. Wade. “Lattice defects in microtubules: protofilament numbers vary within individual microtubules”. In: *Journal of Cell Biology* 117.5 (June 1, 1992), pp. 1031–1040. ISSN: 0021-9525. DOI: 10.1083/jcb.117.5.1031. URL: https://doi.org/10.1083/jcb.117.5.1031 (visited on 01/27/2025).

[32] J. F. Díaz, J. M. Valpuesta, P. Chacón, G. Diakun, and J. M. Andreu. “Changes in Microtubule Protofilament Number Induced by Taxol Binding to an Easily Accessible Site: INTERNAL MICROTUBULE DYNAMICS*”. In: *Journal of Biological Chemistry* 273.50 (Dec. 11, 1998), pp. 33803–33810. ISSN: 0021-9258. DOI: 10.1074/jbc.273.50.33803. URL: https://www.sciencedirect.com/science/article/pii/S0021925819886027 (visited on 01/27/2025).

[33] L. Evans, T. Mitchison, and M. Kirschner. “Influence of the centrosome on the structure of nucleated microtubules.” In: *Journal of Cell Biology* 100.4 (Apr. 1, 1985), pp. 1185–1191. ISSN: 0021-9525. DOI: 10.1083/jcb.100.4.1185. URL: https://doi.org/10.1083/jcb.100.4.1185 (visited on 01/27/2025).

[34] J. A. Kraemer, M. L. Erb, C. A. Waddling, E. A. Montabana, E. A. Zehr, H. Wang, K. Nguyen, D. S. L. Pham, D. A. Agard, and J. Pogliano. “A phage tubulin assembles dynamic filaments by a novel mechanism to center viral DNA within the host cell”. In: *Cell* 149.7 (June 22, 2012), pp. 1488–1499. ISSN: 0092-8674. DOI: 10.1016/j.cell.2012.04.034. URL: https://www.ncbi.nlm.nih.gov/pmc/articles/PMC3401054/ (visited on 01/27/2025).

[35] S. Chaaban and G. J. Brouhard. “A microtubule bestiary: structural diversity in tubulin polymers”. In: *Molecular Biology of the Cell* 28.22 (Nov. 2017). Ed. by W. Bement, pp. 2924–2931. ISSN: 1059-1524, 1939-4586. DOI: 10.1091/mbc.e16-05-0271. URL: https://www.molbiolcell.org/doi/10.1091/mbc.e16-05-0271 (visited on 01/27/2025).

[36] J. Zhou, A. Wang, Y. Song, N. Liu, J. Wang, Y. Li, X. Liang, G. Li, H. Chu, and H.-W. Wang. “Structural insights into the mechanism of GTP initiation of microtubule assembly”. In: *Nature Communications* 14.1 (Sept. 25, 2023). Publisher: Nature Publishing Group, p. 5980. ISSN: 2041-1723. DOI: 10.1038/s41467-023-41615-w. URL: https://www.nature.com/articles/s41467-023-41615-w (visited on 01/27/2025).

[37] G. M. Alushin, G. C. Lander, E. H. Kellogg, R. Zhang, D. Baker, and E. Nogales. “High-Resolution Microtubule Structures Reveal the Structural Transitions in $\alpha\beta$-Tubulin upon GTP Hydrolysis”. In: *Cell* 157.5 (May 22, 2014), pp. 1117–1129. ISSN: 0092-8674. DOI: 10.1016/j.cell.2014.03.053. URL: https:

//www.sciencedirect.com/science/article/pii/S0092867414004838 (visited on 01/28/2025).

[38] R. Melki, S. Fievez, and M. F. Carlier. "Continuous monitoring of Pi release following nucleotide hydrolysis in actin or tubulin assembly using 2-amino-6-mercapto-7-methylpurine ribonucleoside and purine-nucleoside phosphorylase as an enzyme-linked assay". In: *Biochemistry* 35.37 (Sept. 17, 1996), pp. 12038–12045. ISSN: 0006-2960. DOI: 10.1021/bi961325o.

[39] M. Paydar and B. H. Kwok. *Evidence for conformational change-induced hydrolysis of β-tubulin-GTP*. Pages: 2020.09.08.288019 Section: New Results. Sept. 10, 2020. DOI: 10.1101/2020.09.08.288019. URL: https://www.biorxiv.org/content/10.1101/2020.09.08.288019v1 (visited on 01/27/2025).

[40] J. Roostalu, C. Thomas, N. I. Cade, S. Kunzelmann, I. A. Taylor, and T. Surrey. "The speed of GTP hydrolysis determines GTP cap size and controls microtubule stability". In: *eLife* 9 (Feb. 13, 2020), e51992. ISSN: 2050-084X. DOI: 10.7554/eLife.51992.

[41] J. Howard and A. A. Hyman. "Dynamics and mechanics of the microtubule plus end". In: *Nature* 422.6933 (2003), pp. 753–758.

[42] P. N. Zakharov, V. K. Arzhanik, E. V. Ulyanov, N. B. Gudimchuk, and F. I. Ataullakhanov. "Microtubules: dynamically unstable stochastic phase-switching polymers". In: *Physics-Uspekhi* 59.8 (Aug. 1, 2016). Publisher: IOP Publishing, p. 773. ISSN: 1063-7869. DOI: 10.3367/UFNe.2016.04.037779. URL: https://iopscience.iop.org/article/10.3367/UFNe.2016.04.037779/meta (visited on 01/27/2025).

[43] M. Kok, F. Huber, S.-M. Kalisch, and M. Dogterom. "EB3-informed dynamics of the microtubule stabilizing cap during stalled growth". In: *Biophysical Journal* 124.2 (Jan. 2025), pp. 227–244. ISSN: 00063495. DOI: 10.1016/j.bpj.2024.11.3314. URL: https://linkinghub.elsevier.com/retrieve/pii/S0006349524040530 (visited on 08/14/2025).

[44] N. B. Gudimchuk and J. R. McIntosh. "Regulation of microtubule dynamics, mechanics and function through the growing tip". In: *Nature Reviews Molecular Cell Biology* 22.12 (Dec. 2021). Publisher: Nature Publishing Group, pp. 777–795. ISSN: 1471-0080. DOI: 10.1038/s41580-021-00399-x. URL: https://www.nature.com/articles/s41580-021-00399-x (visited on 01/27/2025).

[45] A. A. Hyman, S. Salser, D. N. Drechsel, N. Unwin, and T. J. Mitchison. "Role of GTP hydrolysis in microtubule dynamics: information from a slowly hydrolyzable analogue, GMPCPP." In: *Molecular Biology of the Cell* 3.10 (Oct. 1992), pp. 1155–1167. ISSN: 1059-1524. URL: https://www.ncbi.nlm.nih.gov/pmc/articles/PMC275679/ (visited on 01/27/2025).

[46] P. T. Tran, R. A. Walker, and E. D. Salmon. “A metastable intermediate state of microtubule dynamic instability that differs significantly between plus and minus ends”. In: *The Journal of Cell Biology* 138.1 (July 14, 1997), pp. 105–117. ISSN: 0021-9525. DOI: 10.1083/jcb.138.1.105.

[47] R. A. Walker, S. Inoué, and E. D. Salmon. “Asymmetric behavior of severed microtubule ends after ultraviolet-microbeam irradiation of individual microtubules in vitro”. In: *The Journal of Cell Biology* 108.3 (Mar. 1989), pp. 931–937. ISSN: 0021-9525. DOI: 10.1083/jcb.108.3.931.

[48] M. Caplow and J. Shanks. “Evidence that a single monolayer tubulin-GTP cap is both necessary and sufficient to stabilize microtubules”. In: *Molecular Biology of the Cell* 7.4 (Apr. 1996), pp. 663–675. ISSN: 1059-1524. DOI: 10.1091/mbc.7.4.663.

[49] C. Duellberg, N. I. Cade, D. Holmes, and T. Surrey. “The size of the EB cap determines instantaneous microtubule stability”. In: *eLife* 5 (Apr. 6, 2016), e13470. ISSN: 2050-084X. DOI: 10.7554/eLife.13470.

[50] R. A. Walker, N. K. Pryer, and E. D. Salmon. “Dilution of individual microtubules observed in real time in vitro: evidence that cap size is small and independent of elongation rate”. In: *The Journal of Cell Biology* 114.1 (July 1991), pp. 73–81. ISSN: 0021-9525. DOI: 10.1083/jcb.114.1.73.

[51] A. Dimitrov, M. Quesnoit, S. Moutel, I. Cantaloube, C. Poüs, and F. Perez. “Detection of GTP-tubulin conformation in vivo reveals a role for GTP remnants in microtubule rescues”. In: *Science (New York, N.Y.)* 322.5906 (Nov. 28, 2008), pp. 1353–1356. ISSN: 1095-9203. DOI: 10.1126/science.1165401.

[52] S. P. Maurer, P. Bieling, J. Cope, A. Hoenger, and T. Surrey. “GTPgammaS microtubules mimic the growing microtubule end structure recognized by end-binding proteins (EBs)”. In: *Proceedings of the National Academy of Sciences of the United States of America* 108.10 (Mar. 8, 2011), pp. 3988–3993. ISSN: 1091-6490. DOI: 10.1073/pnas.1014758108.

[53] D. Seetapun, B. T. Castle, A. J. McIntyre, P. T. Tran, and D. J. Odde. “Estimating the Microtubule GTP Cap Size In Vivo”. In: *Current Biology* 22.18 (Sept. 25, 2012), pp. 1681–1687. ISSN: 0960-9822. DOI: 10.1016/j.cub.2012.06.068. URL: https://www.sciencedirect.com/science/article/pii/S0960982212007440 (visited on 01/27/2025).

[54] R. C. Weisenberg, W. J. Deery, and P. J. Dickinson. “Tubulin-nucleotide interactions during the polymerization and depolymerization of microtubules”. In: *Biochemistry* 15.19 (Sept. 21, 1976). Publisher: American Chemical Society, pp. 4248–4254. ISSN: 0006-2960. DOI: 10.1021/bi00664a018. URL: https://doi.org/10.1021/bi00664a018 (visited on 01/27/2025).

[55] B. Vulevic and J. J. Correia. “Thermodynamic and structural analysis of microtubule assembly: the role of GTP hydrolysis”. In: *Biophysical Journal* 72.3 (Mar. 1, 1997), pp. 1357–1375. ISSN: 0006-3495. DOI: 10.1016/S0006-3495(97)78782-4. URL: https://www.sciencedirect.com/science/article/pii/S0006349597787824 (visited on 01/28/2025).

[56] M. R. Mejillano, J. S. Barton, and R. H. Himes. “Stabilization of microtubules by GTP analogues”. In: *Biochemical and Biophysical Research Communications* 166.2 (Jan. 30, 1990), pp. 653–660. ISSN: 0006-291X. DOI: 10.1016/0006-291X(90)90859-L. URL: https://www.sciencedirect.com/science/article/pii/0006291X9090859L (visited on 01/27/2025).

[57] J. Estévez-Gallego, F. Josa-Prado, S. Ku, R. M. Buey, F. A. Balaguer, A. E. Prota, D. Lucena-Agell, C. Kamma-Lorger, T. Yagi, H. Iwamoto, L. Duchesne, I. Barasoain, M. O. Steinmetz, D. Chrétien, S. Kamimura, J. F. Díaz, and M. A. Oliva. “Structural model for differential cap maturation at growing microtubule ends”. In: *eLife* 9 (Mar. 10, 2020), e50155. ISSN: 2050-084X. DOI: 10.7554/eLife.50155. URL: https://elifesciences.org/articles/50155 (visited on 01/28/2025).

[58] J. R. Simon and E. D. Salmon. “The structure of microtubule ends during the elongation and shortening phases of dynamic instability examined by negative-stain electron microscopy”. In: *Journal of Cell Science* 96.4 (Aug. 1, 1990), pp. 571–582. ISSN: 0021-9533, 1477-9137. DOI: 10.1242/jcs.96.4.571. URL: https://journals.biologists.com/jcs/article/96/4/571/60898/The-structure-of-microtubule-ends-during-the (visited on 08/18/2025).

[59] E. Mandelkow, E. Mandelkow, and R. Milligan. “Microtubule dynamics and microtubule caps: a time-resolved cryo-electron microscopy study”. In: *Trends in Cell Biology* 1.6 (Dec. 1991), p. 153. ISSN: 09628924. DOI: 10.1016/0962-8924(91)90015-2. URL: https://linkinghub.elsevier.com/retrieve/pii/0962892491900152 (visited on 01/27/2025).

[60] D. Chrétien, S. D. Fuller, and E. Karsenti. “Structure of growing microtubule ends: two-dimensional sheets close into tubes at variable rates.” In: *Journal of Cell Biology* 129.5 (June 1, 1995), pp. 1311–1328. ISSN: 0021-9525. DOI: 10.1083/jcb.129.5.1311. URL: https://doi.org/10.1083/jcb.129.5.1311 (visited on 01/27/2025).

[61] T. Müller-Reichert, D. Chrétien, F. Severin, and A. A. Hyman. “Structural changes at microtubule ends accompanying GTP hydrolysis: Information from a slowly hydrolyzable analogue of GTP, guanylyl (α,β)methylenediphosphonate”. In: *Proceedings of the National Academy of Sciences* 95.7 (Mar. 31, 1998), pp. 3661–3666. ISSN: 0027-8424, 1091-6490. DOI: 10.1073/pnas.95.7.3661. URL: https://pnas.org/doi/full/10.1073/pnas.95.7.3661 (visited on 08/18/2025).

[62] R. M. Buey, J. F. Díaz, and J. M. Andreu. “The Nucleotide Switch of Tubulin and Microtubule Assembly: A Polymerization-Driven Structural Change”. In: *Biochemistry* 45.19 (May 1, 2006). Publisher: American Chemical Society, pp. 5933–5938. ISSN: 0006-2960. DOI: 10.1021/bi060334m. URL: https://doi.org/10.1021/bi060334m (visited on 01/27/2025).

[63] A. Nawrotek, M. Knossow, and B. Gigant. “The determinants that govern microtubule assembly from the atomic structure of GTP-tubulin”. In: *Journal of Molecular Biology* 412.1 (Sept. 9, 2011), pp. 35–42. ISSN: 1089-8638. DOI: 10.1016/j.jmb.2011.07.029.

[64] L. M. Rice, E. A. Montabana, and D. A. Agard. “The lattice as allosteric effector: Structural studies of $\alpha\beta$- and γ-tubulin clarify the role of GTP in microtubule assembly”. In: *Proceedings of the National Academy of Sciences* 105.14 (Apr. 8, 2008). Publisher: Proceedings of the National Academy of Sciences, pp. 5378–5383. DOI: 10.1073/pnas.0801155105. URL: https://www.pnas.org/doi/abs/10.1073/pnas.0801155105 (visited on 01/27/2025).

[65] J. R. McIntosh, E. O’Toole, G. Morgan, J. Austin, E. Ulyanov, F. Ataullakhanov, and N. Gudimchuk. “Microtubules grow by the addition of bent guanosine triphosphate tubulin to the tips of curved protofilaments”. In: *Journal of Cell Biology* 217.8 (May 23, 2018), pp. 2691–2708. ISSN: 0021-9525. DOI: 10.1083/jcb.201802138. URL: https://doi.org/10.1083/jcb.201802138 (visited on 01/27/2025).

[66] M. Igaev and H. Grubmüller. “Bending-torsional elasticity and energetics of the plus-end microtubule tip”. In: *Proceedings of the National Academy of Sciences* 119.12 (Mar. 22, 2022), e2115516119. ISSN: 0027-8424, 1091-6490. DOI: 10.1073/pnas.2115516119. URL: https://pnas.org/doi/full/10.1073/pnas.2115516119 (visited on 08/18/2025).

[67] D. Tong and G. A. Voth. “Microtubule Simulations Provide Insight into the Molecular Mechanism Underlying Dynamic Instability”. In: *Biophysical Journal* 118.12 (June 2020), pp. 2938–2951. ISSN: 00063495. DOI: 10.1016/j.bpj.2020.04.028. URL: https://linkinghub.elsevier.com/retrieve/pii/S0006349520303726 (visited on 08/18/2025).

[68] J. Wu, S. Dasetty, D. Beckett, Y. Wang, W. Xue, T. Skóra, T. C. Bidone, A. L. Ferguson, and G. A. Voth. “Data-driven equation-free dynamics applied to many-protein complexes: The microtubule tip relaxation”. In: *Biophysical Journal* (Jan. 2025), S0006349525000220. ISSN: 00063495. DOI: 10.1016/j.bpj.2025.01.009. URL: https://linkinghub.elsevier.com/retrieve/pii/S0006349525000220 (visited on 08/18/2025).

[69] R. Zhang, B. LaFrance, and E. Nogales. “Separating the effects of nucleotide and EB binding on microtubule structure”. In: *Proceedings of the National Academy of Sciences* 115.27 (July 3, 2018). Publisher: Proceedings of the National Academy of Sciences, E6191–E6200. DOI: 10.1073/pnas.1802637115.

URL: https://www.pnas.org/doi/10.1073/pnas.1802637115 (visited on 01/28/2025).

[70] D. Beckett and G. A. Voth. “Unveiling the catalytic mechanism of GTP hydrolysis in microtubules”. In: *Proceedings of the National Academy of Sciences* 120.27 (July 4, 2023). Publisher: Proceedings of the National Academy of Sciences, e2305899120. DOI: 10.1073/pnas.2305899120. URL: https://www.pnas.org/doi/full/10.1073/pnas.2305899120 (visited on 01/28/2025).

[71] M. Kalutskii, H. Grubmüller, V. A. Volkov, and M. Igaev. “Microtubule dynamics are defined by conformations and stability of clustered protofilaments”. In: *Proceedings of the National Academy of Sciences* 122.22 (June 3, 2025), e2424263122. ISSN: 0027-8424, 1091-6490. DOI: 10.1073/pnas.2424263122. URL: https://pnas.org/doi/10.1073/pnas.2424263122 (visited on 08/14/2025).

[72] R. A. Walker, E. T. O’Brien, N. K. Pryer, M. F. Soboeiro, W. A. Voter, H. P. Erickson, and E. D. Salmon. “Dynamic instability of individual microtubules analyzed by video light microscopy: rate constants and transition frequencies.” In: *The Journal of cell biology* 107.4 (Oct. 1, 1988), pp. 1437–1448. ISSN: 0021-9525, 1540-8140. DOI: 10.1083/jcb.107.4.1437. URL: https://rupress.org/jcb/article/107/4/1437/58973/Dynamic-instability-of-individual-microtubules (visited on 01/28/2025).

[73] M. K. Gardner, M. Zanic, C. Gell, V. Bormuth, and J. Howard. “Depolymerizing Kinesins Kip3 and MCAK Shape Cellular Microtubule Architecture by Differential Control of Catastrophe”. In: *Cell* 147.5 (Nov. 23, 2011), pp. 1092–1103. ISSN: 0092-8674. DOI: 10.1016/j.cell.2011.10.037. URL: https://www.sciencedirect.com/science/article/pii/S0092867411012876 (visited on 01/28/2025).

[74] D. J. Odde, L. Cassimeris, and H. M. Buettner. “Kinetics of microtubule catastrophe assessed by probabilistic analysis”. In: *Biophysical Journal* 69.3 (Sept. 1, 1995), pp. 796–802. ISSN: 0006-3495. DOI: 10.1016/S0006-3495(95)79953-2. URL: https://www.sciencedirect.com/science/article/pii/S0006349595799532 (visited on 01/28/2025).

[75] A.-M. C. Yvon and P. Wadsworth. “Non-centrosomal microtubule formation and measurement of minus end microtubule dynamics in A498 cells”. In: *Journal of Cell Science* 110.19 (Oct. 1, 1997), pp. 2391–2401. ISSN: 0021-9533, 1477-9137. DOI: 10.1242/jcs.110.19.2391. URL: https://journals.biologists.com/jcs/article/110/19/2391/25136/Non-centrosomal-microtubule-formation-and (visited on 01/28/2025).

[76] H. Bowne-Anderson, M. Zanic, M. Kauer, and J. Howard. “Microtubule dynamic instability: A new model with coupled GTP hydrolysis and multistep catastrophe”. In: *BioEssays* 35.5 (May 2013), pp. 452–461. ISSN: 0265-9247, 1521-1878. DOI: 10.1002/bies.201200131. URL: https:

//onlinelibrary.wiley.com/doi/10.1002/bies.201200131 (visited on 01/28/2025).

[77] C. E. Coombes, A. Yamamoto, M. R. Kenzie, D. J. Odde, and M. K. Gardner. “Evolving Tip Structures Can Explain Age-Dependent Microtubule Catastrophe”. In: *Current Biology* 23.14 (July 2013), pp. 1342–1348. ISSN: 09609822. DOI: 10.1016/j.cub.2013.05.059. URL: https://linkinghub.elsevier.com/retrieve/pii/S0960982213006842 (visited on 01/28/2025).

[78] P. Zakharov, N. Gudimchuk, V. Voevodin, A. Tikhonravov, F. I. Ataullakhanov, and E. L. Grishchuk. “Molecular and Mechanical Causes of Microtubule Catastrophe and Aging”. In: *Biophysical Journal* 109.12 (Dec. 2015), pp. 2574–2591. ISSN: 00063495. DOI: 10.1016/j.bpj.2015.10.048. URL: https://linkinghub.elsevier.com/retrieve/pii/S000634951501156X (visited on 01/28/2025).

[79] N. B. Gudimchuk, E. V. Ulyanov, E. O’Toole, C. L. Page, D. S. Vinogradov, G. Morgan, G. Li, J. K. Moore, E. Szczesna, A. Roll-Mecak, F. I. Ataullakhanov, and J. Richard McIntosh. “Mechanisms of microtubule dynamics and force generation examined with computational modeling and electron cryotomography”. In: *Nature Communications* 11.1 (July 28, 2020), p. 3765. ISSN: 2041-1723. DOI: 10.1038/s41467-020-17553-2.

[80] Y. Gu, Z. Deng, A. R. Paredez, S. DeBolt, Z.-Y. Wang, and C. Somerville. “Prefoldin 6 is required for normal microtubule dynamics and organization in Arabidopsis”. In: *Proceedings of the National Academy of Sciences* 105.46 (Nov. 18, 2008). Publisher: Proceedings of the National Academy of Sciences, pp. 18064–18069. DOI: 10.1073/pnas.0808652105. URL: https://www.pnas.org/doi/10.1073/pnas.0808652105 (visited on 01/31/2025).

[81] P. Dráber, E. Dráberová, I. Linhartová, and V. Viklický. “Differences in the exposure of c- and n-terminal tubulin domains in cytoplasmic microtubules detected with domain-specific monoclonal antibodies”. In: *Journal of Cell Science* 92.3 (Mar. 1, 1989), pp. 519–528. ISSN: 0021-9533. DOI: 10.1242/jcs.92.3.519. URL: https://doi.org/10.1242/jcs.92.3.519 (visited on 01/31/2025).

[82] E. Nogales, S. G. Wolf, and K. H. Downing. “Structure of the $\alpha\beta$ tubulin dimer by electron crystallography”. In: *Nature* 391.6663 (Jan. 1998). Publisher: Nature Publishing Group, pp. 199–203. ISSN: 1476-4687. DOI: 10.1038/34465. URL: https://www.nature.com/articles/34465 (visited on 01/31/2025).

[83] L. Serrano, J. de la Torre, R. B. Maccioni, and J. Avila. “Involvement of the carboxyl-terminal domain of tubulin in the regulation of its assembly.” In: *Proceedings of the National Academy of Sciences* 81.19 (Oct. 1984). Publisher: Proceedings of the National Academy of Sciences, pp. 5989–5993. DOI: 10.1073/pnas.81.19.5989. URL: https://www.pnas.org/doi/abs/10.1073/pnas.81.19.5989 (visited on 01/31/2025).

[84] M. H. Hinrichs, A. Jalal, B. Brenner, E. Mandelkow, S. Kumar, and T. Scholz. “Tau Protein Diffuses along the Microtubule Lattice*”. In: *Journal of Biological Chemistry* 287.46 (Nov. 9, 2012), pp. 38559–38568. ISSN: 0021-9258. DOI: 10.1074/jbc.M112.369785. URL: https://www.sciencedirect.com/science/article/pii/S0021925820623225 (visited on 01/31/2025).

[85] U. Z. Littauer, D. Giveon, M. Thierauf, I. Ginzburg, and H. Ponstingl. “Common and distinct tubulin binding sites for microtubule-associated proteins.” In: *Proceedings of the National Academy of Sciences* 83.19 (Oct. 1986). Publisher: Proceedings of the National Academy of Sciences, pp. 7162–7166. DOI: 10.1073/pnas.83.19.7162. URL: https://www.pnas.org/doi/abs/10.1073/pnas.83.19.7162 (visited on 01/31/2025).

[86] S. A. Miller, M. L. Johnson, and P. T. Stukenberg. “Kinetochore Attachments Require an Interaction between Unstructured Tails on Microtubules and Ndc80Hec1”. In: *Current Biology* 18.22 (Nov. 25, 2008), pp. 1785–1791. ISSN: 0960-9822. DOI: 10.1016/j.cub.2008.11.007. URL: https://www.sciencedirect.com/science/article/pii/S096098220801484X (visited on 01/31/2025).

[87] A. Roll-Mecak and R. D. Vale. “Structural basis of microtubule severing by the hereditary spastic paraplegia protein spastin”. In: *Nature* 451.7176 (Jan. 2008). Publisher: Nature Publishing Group, pp. 363–367. ISSN: 1476-4687. DOI: 10.1038/nature06482. URL: https://www.nature.com/articles/nature06482 (visited on 01/31/2025).

[88] M. Bao, R. E. Dörig, P. M. Vazquez-Pianzola, D. Beuchle, and B. Suter. “Differential modification of the C-terminal tails of different α-tubulins and their importance for microtubule function in vivo”. In: *eLife* 12 (June 22, 2023). Ed. by K. M. Ori-McKenney and A. Akhmanova. Publisher: eLife Sciences Publications, Ltd, e87125. ISSN: 2050-084X. DOI: 10.7554/eLife.87125. URL: https://doi.org/10.7554/eLife.87125 (visited on 01/31/2025).

[89] Y.-M. Lu, S. Yan, S.-C. Ti, and C. Zheng. “Editing of endogenous tubulins reveals varying effects of tubulin posttranslational modifications on axonal growth and regeneration”. In: *eLife* 13 (June 18, 2024). Publisher: eLife Sciences Publications Limited. DOI: 10.7554/eLife.94583.2. URL: https://elifesciences.org/reviewed-preprints/94583 (visited on 01/31/2025).

[90] V. Redeker. “Mass spectrometry analysis of C-terminal posttranslational modifications of tubulins”. In: *Methods in Cell Biology* 95 (2010), pp. 77–103. ISSN: 0091-679X. DOI: 10.1016/S0091-679X(10)95006-1.

[91] A. Latremoliere, L. Cheng, M. DeLisle, C. Wu, S. Chew, E. B. Hutchinson, A. Sheridan, C. Alexandre, F. Latremoliere, S.-H. Sheu, S. Golidy, T. Omura, E. A. Huebner, Y. Fan, M. C. Whitman, E. Nguyen, C. Hermawan, C. Pierpaoli, M. A. Tischfield, C. J. Woolf, and E. C. Engle. “Neuronal-Specific TUBB3 Is Not Required for Normal Neuronal Function but Is Essential for Timely Axon Regeneration”. In: *Cell Reports* 24.7 (Aug. 14, 2018), 1865–1879.e9.

ISSN: 2211-1247. DOI: 10.1016/j.celrep.2018.07.029. URL: https://www.sciencedirect.com/science/article/pii/S2211124718311197 (visited on 01/31/2025).

[92] F. Amargant, M. Barragan, R. Vassena, and I. Vernos. “Insights of the tubulin code in gametes and embryos: from basic research to potential clinical applications in humans†”. In: *Biology of Reproduction* 100.3 (Mar. 1, 2019), pp. 575–589. ISSN: 1529-7268. DOI: 10.1093/biolre/ioy203.

[93] P. Findeisen, S. Mühlhausen, S. Dempewolf, J. Hertzog, A. Zietlow, T. Carlomagno, and M. Kollmar. “Six Subgroups and Extensive Recent Duplications Characterize the Evolution of the Eukaryotic Tubulin Protein Family”. In: *Genome Biology and Evolution* 6.9 (Sept. 1, 2014), pp. 2274–2288. ISSN: 1759-6653. DOI: 10.1093/gbe/evu187. URL: https://doi.org/10.1093/gbe/evu187 (visited on 01/31/2025).

[94] K. Park, K. J. Hoff, L. Wethekam, N. Stence, M. Saenz, and J. K. Moore. “Kinetically Stabilizing Mutations in Beta Tubulins Create Isotype-Specific Brain Malformations”. In: *Frontiers in Cell and Developmental Biology* 9 (Nov. 18, 2021). Publisher: Frontiers. ISSN: 2296-634X. DOI: 10.3389/fcell.2021.765992. URL: https://www.frontiersin.org/journals/cell-and-developmental-biology/articles/10.3389/fcell.2021.765992/full (visited on 01/31/2025).

[95] T. Mühlethaler, D. Gioia, A. E. Prota, M. E. Sharpe, A. Cavalli, and M. O. Steinmetz. “Comprehensive Analysis of Binding Sites in Tubulin”. In: *Angewandte Chemie International Edition* 60.24 (2021). _eprint: https://onlinelibrary.wiley.com/doi/pdf/10.1002/anie.202100273, pp. 13331–13342. ISSN: 1521-3773. DOI: 10.1002/anie.202100273. URL: https://onlinelibrary.wiley.com/doi/abs/10.1002/anie.202100273 (visited on 01/30/2025).

[96] B. J. Berne. “Interpretation of the light scattering from long rods”. In: *Journal of Molecular Biology* 89.4 (Nov. 15, 1974), pp. 755–758. ISSN: 0022-2836. DOI: 10.1016/0022-2836(74)90049-7. URL: https://www.sciencedirect.com/science/article/pii/0022283674900497 (visited on 02/05/2025).

[97] F. Gaskin, C. R. Cantor, and M. L. Shelanski. “Turbidimetric studies of the *in vitro* assembly and disassembly of porcine neurotubules”. In: *Journal of Molecular Biology* 89.4 (Nov. 15, 1974), pp. 737–755. ISSN: 0022-2836. DOI: 10.1016/0022-2836(74)90048-5. URL: https://www.sciencedirect.com/science/article/pii/0022283674900485 (visited on 02/05/2025).

[98] F. Gaskin. “Analysis of Microtubule Assembly Kinetics Using Turbidimetry”. In: *Microtubule Dynamics: Methods and Protocols*. Ed. by A. Straube. Totowa, NJ: Humana Press, 2011, pp. 99–105. ISBN: 978-1-61779-252-6. DOI: 10.1007/978-1-61779-252-6_7. URL: https://doi.org/10.1007/978-1-61779-252-6_7 (visited on 02/05/2025).

[99] K. A. Johnson and G. G. Borisy. “Kinetic analysis of microtubule self-assembly *in vitro*”. In: *Journal of Molecular Biology* 117.1 (Nov. 25, 1977), pp. 1–31. ISSN: 0022-2836. DOI: `10.1016/0022-2836(77)90020-1`. URL: `https://www.sciencedirect.com/science/article/pii/0022283677900201` (visited on 02/05/2025).

[100] W. A. Voter and H. P. Erickson. “The kinetics of microtubule assembly. Evidence for a two-stage nucleation mechanism”. In: *The Journal of Biological Chemistry* 259.16 (Aug. 25, 1984), pp. 10430–10438. ISSN: 0021-9258.

[101] M. Wieczorek, S. Bechstedt, S. Chaaban, and G. J. Brouhard. “Microtubule-associated proteins control the kinetics of microtubule nucleation”. In: *Nature Cell Biology* 17.7 (July 2015), pp. 907–916. ISSN: 1476-4679. DOI: `10.1038/ncb3188`.

[102] D. Kuchnir Fygenson, H. Flyvbjerg, K. Sneppen, A. Libchaber, and S. Leibler. “Spontaneous nucleation of microtubules”. In: *Physical Review E* 51.5 (May 1, 1995). Publisher: American Physical Society, pp. 5058–5063. DOI: `10.1103/PhysRevE.51.5058`. URL: `https://link.aps.org/doi/10.1103/PhysRevE.51.5058` (visited on 01/22/2025).

[103] H. Flyvbjerg and E. Jobs. “Microtubule dynamics. II. Kinetics of self-assembly”. In: *Physical Review E* 56.6 (Dec. 1, 1997). Publisher: American Physical Society, pp. 7083–7099. DOI: `10.1103/PhysRevE.56.7083`. URL: `https://link.aps.org/doi/10.1103/PhysRevE.56.7083` (visited on 02/06/2025).

[104] J. Basu, A. Soni, and C. A. Athale. “Microtubule polymerization tuned by macromolecular crowdant size and density”. In: (Feb. 7, 2024). Repository: Biophysics. DOI: `10.1101/2024.02.02.578534`. URL: `http://biorxiv.org/lookup/doi/10.1101/2024.02.02.578534` (visited on 02/06/2025).

[105] A. T. Molines, C. H. Edrington, S. C. Tetlalmatzi, F. Chang, and G. J. Brouhard. *Microtubule dynamic instability is sensitive to specific biological viscogens in vitro*. Pages: 2024.05.27.596091 Section: New Results. May 27, 2024. DOI: `10.1101/2024.05.27.596091`. URL: `https://www.biorxiv.org/content/10.1101/2024.05.27.596091v1` (visited on 02/06/2025).

[106] E. Hamel, A. A. del Campo, M. C. Lowe, and C. M. Lin. “Interactions of taxol, microtubule-associated proteins, and guanine nucleotides in tubulin polymerization”. In: *The Journal of Biological Chemistry* 256.22 (Nov. 25, 1981), pp. 11887–11894. ISSN: 0021-9258.

[107] X. Liang. “Microtubule nucleation and dynamic instability in interphase fission yeast”. In: *Journal of Molecular Cell Biology* 11.11 (Dec. 23, 2019), pp. 941–943. ISSN: 1759-4685. DOI: `10.1093/jmcb/mjz044`. URL: `https://doi.org/10.1093/jmcb/mjz044` (visited on 02/06/2025).

[108] A. V. Popov, F. Severin, and E. Karsenti. “XMAP215 is required for the microtubule-nucleating activity of centrosomes”. In: *Current biology: CB* 12.15 (Aug. 6, 2002), pp. 1326–1330. ISSN: 0960-9822. DOI: `10.1016/s0960-9822(02)01033-3`.

[109] J. Roostalu, N. I. Cade, and T. Surrey. “Complementary activities of TPX2 and chTOG constitute an efficient importin-regulated microtubule nucleation module”. In: *Nature Cell Biology* 17.11 (Nov. 2015), pp. 1422–1434. ISSN: 1476-4679. DOI: `10.1038/ncb3241`.

[110] R. Ayukawa, S. Iwata, H. Imai, S. Kamimura, M. Hayashi, K. X. Ngo, I. Minoura, S. Uchimura, T. Makino, M. Shirouzu, H. Shigematsu, K. Sekimoto, B. Gigant, and E. Muto. “GTP-dependent formation of straight tubulin oligomers leads to microtubule nucleation”. In: *Journal of Cell Biology* 220.4 (Apr. 5, 2021), e202007033. ISSN: 0021-9525, 1540-8140. DOI: `10.1083/jcb.202007033`. URL: `https://rupress.org/jcb/article/220/4/e202007033/211760/GTP-dependent-formation-of-straight-tubulin` (visited on 02/06/2025).

[111] S. Santaguida and A. Musacchio. “The life and miracles of kinetochores”. In: *The EMBO Journal* 28.17 (Sept. 2, 2009). Num Pages: 2531 Publisher: John Wiley & Sons, Ltd, pp. 2511–2531. ISSN: 0261-4189. DOI: `10.1038/emboj.2009.173`. URL: `https://www.embopress.org/doi/full/10.1038/emboj.2009.173` (visited on 01/31/2025).

[112] I. M. Cheeseman and A. Desai. “Molecular architecture of the kinetochore–microtubule interface”. In: *Nature Reviews Molecular Cell Biology* 9.1 (Jan. 2008). Publisher: Nature Publishing Group, pp. 33–46. ISSN: 1471-0080. DOI: `10.1038/nrm2310`. URL: `https://www.nature.com/articles/nrm2310` (visited on 01/31/2025).

[113] M. K. Johnson and D. A. Wise. “The Kinetochore Moves Ahead: Contributions of Molecular and Genetic Techniques to Our Understanding of Mitosis”. In: *BioScience* 59.11 (Dec. 1, 2009), pp. 933–943. ISSN: 0006-3568. DOI: `10.1525/bio.2009.59.11.5`. URL: `https://doi.org/10.1525/bio.2009.59.11.5` (visited on 01/31/2025).

[114] M. Kirschner and T. Mitchison. “Beyond self-assembly: From microtubules to morphogenesis”. In: *Cell* 45.3 (May 9, 1986), pp. 329–342. ISSN: 0092-8674. DOI: `10.1016/0092-8674(86)90318-1`. URL: `https://www.sciencedirect.com/science/article/pii/0092867486903181` (visited on 02/04/2025).

[115] J. K. Monda and I. M. Cheeseman. “The kinetochore–microtubule interface at a glance”. In: *Journal of Cell Science* 131.16 (Aug. 16, 2018), jcs214577. ISSN: 0021-9533. DOI: `10.1242/jcs.214577`. URL: `https://doi.org/10.1242/jcs.214577` (visited on 01/31/2025).

[116] B. F. McEwen, G. K. Chan, B. Zubrowski, M. S. Savoian, M. T. Sauer, and T. J. Yen. “CENP-E Is Essential for Reliable Bioriented Spindle Attachment, but Chromosome Alignment Can Be Achieved via Redundant Mechanisms in Mammalian Cells”. In: *Molecular Biology of the Cell* 12.9 (Sept. 2001). Publisher: American Society for Cell Biology (mboc),

pp. 2776–2789. ISSN: 1059-1524. DOI: 10.1091/mbc.12.9.2776. URL: https://www.molbiolcell.org/doi/10.1091/mbc.12.9.2776 (visited on 01/31/2025).

[117] G. G. Gundersen and J. C. Bulinski. "Distribution of tyrosinated and nontyrosinated alpha-tubulin during mitosis." In: *Journal of Cell Biology* 102.3 (Mar. 1, 1986), pp. 1118–1126. ISSN: 0021-9525. DOI: 10.1083/jcb.102.3.1118. URL: https://doi.org/10.1083/jcb.102.3.1118 (visited on 01/31/2025).

[118] M. Barisic, R. Silva e Sousa, S. K. Tripathy, M. M. Magiera, A. V. Zaytsev, A. L. Pereira, C. Janke, E. L. Grishchuk, and H. Maiato. "Microtubule detyrosination guides chromosomes during mitosis". In: *Science* 348.6236 (May 15, 2015). Publisher: American Association for the Advancement of Science, pp. 799–803. DOI: 10.1126/science.aaa5175. URL: https://www.science.org/doi/10.1126/science.aaa5175 (visited on 01/31/2025).

[119] P. Aravamudhan, A. A. Goldfarb, and A. P. Joglekar. "The kinetochore encodes a mechanical switch to disrupt spindle assembly checkpoint signalling". In: *Nature Cell Biology* 17.7 (July 2015). Publisher: Nature Publishing Group, pp. 868–879. ISSN: 1476-4679. DOI: 10.1038/ncb3179. URL: https://www.nature.com/articles/ncb3179 (visited on 01/31/2025).

[120] V. A. Volkov, P. J. Huis in 't Veld, M. Dogterom, and A. Musacchio. "Multivalency of NDC80 in the outer kinetochore is essential to track shortening microtubules and generate forces". In: *eLife* 7 (Apr. 9, 2018). Ed. by J. K. Tyler. Publisher: eLife Sciences Publications, Ltd, e36764. ISSN: 2050-084X. DOI: 10.7554/eLife.36764. URL: https://doi.org/10.7554/eLife.36764 (visited on 10/10/2024).

[121] A. F. Powers, A. D. Franck, D. R. Gestaut, J. Cooper, B. Gracyzk, R. R. Wei, L. Wordeman, T. N. Davis, and C. L. Asbury. "The Ndc80 Kinetochore Complex Forms Load-Bearing Attachments to Dynamic Microtubule Tips via Biased Diffusion". In: *Cell* 136.5 (Mar. 6, 2009), pp. 865–875. ISSN: 0092-8674. DOI: 10.1016/j.cell.2008.12.045. URL: https://www.sciencedirect.com/science/article/pii/S0092867409000233 (visited on 01/15/2025).

[122] J. R. McIntosh, E. L. Grishchuk, M. K. Morphew, A. K. Efremov, K. Zhudenkov, V. A. Volkov, I. M. Cheeseman, A. Desai, D. N. Mastronarde, and F. I. Ataullakhanov. "Fibrils Connect Microtubule Tips with Kinetochores: A Mechanism to Couple Tubulin Dynamics to Chromosome Motion". In: *Cell* 135.2 (Oct. 17, 2008), pp. 322–333. ISSN: 0092-8674. DOI: 10.1016/j.cell.2008.08.038. URL: https://www.sciencedirect.com/science/article/pii/S0092867408011197 (visited on 01/15/2025).

[123] J. C. Schmidt, H. Arthanari, A. Boeszoermenyi, N. M. Dashkevich, E. M. Wilson-Kubalek, N. Monnier, M. Markus, M. Oberer, R. A. Milligan, M. Bathe, G. Wagner, E. L. Grishchuk, and I. M. Cheeseman. “The Kinetochore-Bound Ska1 Complex Tracks Depolymerizing Microtubules and Binds to Curved Protofilaments”. In: *Developmental Cell* 23.5 (Nov. 13, 2012), pp. 968–980. ISSN: 1534-5807. DOI: `10.1016/j.devcel.2012.09.012`. URL: `https://www.sciencedirect.com/science/article/pii/S1534580712004236` (visited on 01/15/2025).

[124] C. B. O’Connell and A. L. Khodjakov. “Cooperative mechanisms of mitotic spindle formation”. In: *Journal of Cell Science* 120.10 (May 15, 2007), pp. 1717–1722. ISSN: 0021-9533. DOI: `10.1242/jcs.03442`. URL: `https://doi.org/10.1242/jcs.03442` (visited on 02/04/2025).

[125] U. S. Tulu, C. Fagerstrom, N. P. Ferenz, and P. Wadsworth. “Molecular Requirements for Kinetochore-Associated Microtubule Formation in Mammalian Cells”. In: *Current Biology* 16.5 (Mar. 7, 2006). Publisher: Elsevier, pp. 536–541. ISSN: 0960-9822. DOI: `10.1016/j.cub.2006.01.060`. URL: `https://www.cell.com/current-biology/abstract/S0960-9822(06)01127-4` (visited on 02/04/2025).

[126] T. J. Mitchison and E. D. Salmon. “Poleward kinetochore fiber movement occurs during both metaphase and anaphase-A in newt lung cell mitosis.” In: *Journal of Cell Biology* 119.3 (Nov. 1, 1992), pp. 569–582. ISSN: 0021-9525. DOI: `10.1083/jcb.119.3.569`. URL: `https://doi.org/10.1083/jcb.119.3.569` (visited on 02/04/2025).

[127] E. L. Grishchuk and J. R. McIntosh. “Microtubule depolymerization can drive poleward chromosome motion in fission yeast”. In: *The EMBO Journal* 25.20 (Oct. 18, 2006). Num Pages: 4896 Publisher: John Wiley & Sons, Ltd, pp. 4888–4896. ISSN: 0261-4189. DOI: `10.1038/sj.emboj.7601353`. URL: `https://www.embopress.org/doi/full/10.1038/sj.emboj.7601353` (visited on 02/04/2025).

[128] K. Tanaka, E. Kitamura, Y. Kitamura, and T. U. Tanaka. “Molecular mechanisms of microtubule-dependent kinetochore transport toward spindle poles”. In: *Journal of Cell Biology* 178.2 (July 9, 2007), pp. 269–281. ISSN: 0021-9525. DOI: `10.1083/jcb.200702141`. URL: `https://doi.org/10.1083/jcb.200702141` (visited on 02/04/2025).

[129] S. Inoué and E. D. Salmon. “Force Generation by Microtubule Assembly/Disassembly in Mitosis and Related Movements”. In: *Molecular Biology of the Cell* 6.12 (Dec. 1995). Publisher: American Society for Cell Biology (mboc), pp. 1619–1640. ISSN: 1059-1524. DOI: `10.1091/mbc.6.12.1619`. URL: `https://www.molbiolcell.org/doi/abs/10.1091/mbc.6.12.1619` (visited on 02/04/2025).

[130] J. R. McIntosh, V. Volkov, F. I. Ataullakhanov, and E. L. Grishchuk. “Tubulin depolymerization may be an ancient biological motor”. In: *Journal of Cell Science* 123.20 (Oct. 15, 2010), pp. 3425–3434. ISSN: 0021-9533. DOI: 10.1242/jcs.067611. URL: https://doi.org/10.1242/jcs.067611 (visited on 02/04/2025).

[131] R. L. Margolis and L. Wilson. “Microtubule treadmills—possible molecular machinery”. In: *Nature* 293.5835 (Oct. 1981). Publisher: Nature Publishing Group, pp. 705–711. ISSN: 1476-4687. DOI: 10.1038/293705a0. URL: https://www.nature.com/articles/293705a0 (visited on 02/04/2025).

[132] D. E. Koshland, T. J. Mitchison, and M. W. Kirschner. “Polewards chromosome movement driven by microtubule depolymerization in vitro”. In: *Nature* 331.6156 (Feb. 1988). Publisher: Nature Publishing Group, pp. 499–504. ISSN: 1476-4687. DOI: 10.1038/331499a0. URL: https://www.nature.com/articles/331499a0 (visited on 02/04/2025).

[133] E. L. Grishchuk, M. I. Molodtsov, F. I. Ataullakhanov, and J. R. McIntosh. “Force production by disassembling microtubules”. In: *Nature* 438.7066 (Nov. 2005). Publisher: Nature Publishing Group, pp. 384–388. ISSN: 1476-4687. DOI: 10.1038/nature04132. URL: https://www.nature.com/articles/nature04132 (visited on 02/04/2025).

[134] A. P. Joglekar, K. S. Bloom, and E. Salmon. “Mechanisms of force generation by end-on kinetochore-microtubule attachments”. In: *Current Opinion in Cell Biology* 22.1 (Feb. 2010), pp. 57–67. ISSN: 09550674. DOI: 10.1016/j.ceb.2009.12.010. URL: https://linkinghub.elsevier.com/retrieve/pii/S0955067409002397 (visited on 02/04/2025).

[135] E. L. Grishchuk. “Biophysics of Microtubule End Coupling at the Kinetochore”. In: *Centromeres and Kinetochores: Discovering the Molecular Mechanisms Underlying Chromosome Inheritance*. Ed. by B. E. Black. Cham: Springer International Publishing, 2017, pp. 397–428. ISBN: 978-3-319-58592-5. DOI: 10.1007/978-3-319-58592-5_17. URL: https://doi.org/10.1007/978-3-319-58592-5_17 (visited on 02/04/2025).

[136] V. A. Volkov, P. M. Grissom, V. K. Arzhanik, A. V. Zaytsev, K. Renganathan, T. McClure-Begley, W. M. Old, N. Ahn, and J. R. McIntosh. “Centromere protein F includes two sites that couple efficiently to depolymerizing microtubules”. In: *Journal of Cell Biology* 209.6 (June 22, 2015), pp. 813–828. ISSN: 0021-9525. DOI: 10.1083/jcb.201408083. URL: https://doi.org/10.1083/jcb.201408083 (visited on 02/04/2025).

[137] J. Mai, I. M. Sokolov, and A. Blumen. “Directed particle diffusion under “burnt bridges” conditions”. In: *Physical Review E* 64.1 (June 11, 2001). Publisher: American Physical Society, p. 011102. DOI: 10.1103/PhysRevE.64.011102. URL: https://link.aps.org/doi/10.1103/PhysRevE.64.011102 (visited on 02/04/2025).

[138] A. Efremov, E. L. Grishchuk, J. R. McIntosh, and F. I. Ataullakhanov. "In search of an optimal ring to couple microtubule depolymerization to processive chromosome motions". In: *Proceedings of the National Academy of Sciences* 104.48 (Nov. 27, 2007). Publisher: Proceedings of the National Academy of Sciences, pp. 19017–19022. DOI: 10.1073/pnas.0709524104. URL: https://www.pnas.org/doi/full/10.1073/pnas.0709524104 (visited on 02/04/2025).

[139] E. L. Grishchuk, J. R. McIntosh, M. I. Molodtsov, and F. I. Ataullakhanov. "4.7 Force Generation by Dynamic Microtubule Polymers". In: *Comprehensive Biophysics*. Ed. by E. H. Egelman. Amsterdam: Elsevier, Jan. 1, 2012, pp. 93–117. ISBN: 978-0-08-095718-0. DOI: 10.1016/B978-0-12-374920-8.00409-4. URL: https://www.sciencedirect.com/science/article/pii/B9780123749208004094 (visited on 02/04/2025).

[140] J. W. Driver, E. A. Geyer, M. E. Bailey, L. M. Rice, and C. L. Asbury. "Direct measurement of conformational strain energy in protofilaments curling outward from disassembling microtubule tips". In: *eLife* 6 (June 19, 2017). Ed. by A. Akhmanova. Publisher: eLife Sciences Publications, Ltd, e28433. ISSN: 2050-084X. DOI: 10.7554/eLife.28433. URL: https://doi.org/10.7554/eLife.28433 (visited on 02/04/2025).

[141] K. Morelli, S. M. Meier, A. Zhao, M. Choudhury, M. Willis, Y. Barral, and J. Vogel. *A fluid droplet harvests the force generated by shrinking microtubules in living cells*. Pages: 2024.09.09.612121 Section: New Results. Sept. 10, 2024. DOI: 10.1101/2024.09.09.612121. URL: https://www.biorxiv.org/content/10.1101/2024.09.09.612121v1 (visited on 02/05/2025).

[142] V. Verma, L. Mallik, R. F. Hariadi, S. Sivaramakrishnan, G. Skiniotis, and A. P. Joglekar. "Using Protein Dimers to Maximize the Protein Hybridization Efficiency with Multisite DNA Origami Scaffolds". In: *PLoS ONE* 10.9 (Sept. 8, 2015), e0137125. ISSN: 1932-6203. DOI: 10.1371/journal.pone.0137125. URL: https://www.ncbi.nlm.nih.gov/pmc/articles/PMC4562706/ (visited on 02/06/2025).

[143] W. Luo, V. Demidov, Q. Shen, H. Girão, M. Chakraborty, A. Maiorov, F. I. Ataullakhanov, C. Lin, H. Maiato, and E. L. Grishchuk. "CLASP2 recognizes tubulins exposed at the microtubule plus-end in a nucleotide state–sensitive manner". In: *Science Advances* 9.1 (Jan. 4, 2023). Publisher: American Association for the Advancement of Science, eabq5404. DOI: 10.1126/sciadv.abq5404. URL: https://www.science.org/doi/full/10.1126/sciadv.abq5404 (visited on 02/06/2025).

[144] D. Mazia and K. Dan. "The Isolation and Biochemical Characterization of the Mitotic Apparatus of Dividing Cells". In: *Proceedings of the National Academy of Sciences* 38.9 (Sept. 1952), pp. 826–838. ISSN: 0027-8424, 1091-6490. DOI: 10.1073/pnas.38.9.826. URL: https://pnas.org/doi/full/10.1073/pnas.38.9.826 (visited on 07/31/2025).

[145] D. Mazia, J. M. Mitchison, H. Medina, and P. Harris. “THE DIRECT ISOLATION OF THE MITOTIC APPARATUS”. In: *The Journal of Cell Biology* 10.4 (Aug. 1, 1961), pp. 467–474. ISSN: 1540-8140, 0021-9525. DOI: 10.1083/jcb.10.4.467. URL: https://rupress.org/jcb/article/10/4/467/13344/THE-DIRECT-ISOLATION-OF-THE-MITOTIC-APPARATUS (visited on 07/31/2025).

[146] R. E. Kane. “THE MITOTIC APPARATUS”. In: *The Journal of Cell Biology* 25.1 (Apr. 1, 1965), pp. 137–144. ISSN: 1540-8140, 0021-9525. DOI: 10.1083/jcb.25.1.137. URL: https://rupress.org/jcb/article/25/1/137/1394/THE-MITOTIC-APPARATUS-Physical-Chemical-Factors (visited on 07/31/2025).

[147] A. Forer and A. M. Zimmerman. “Characteristics of sea-urchin mitotic apparatus isolated using a dimethyl sulphoxide/glycerol medium”. In: *Journal of Cell Science* 16.3 (Dec. 1, 1974), pp. 481–497. ISSN: 0021-9533, 1477-9137. DOI: 10.1242/jcs.16.3.481. URL: https://journals.biologists.com/jcs/article/16/3/481/57627/Characteristics-of-sea-urchin-mitotic-apparatus (visited on 07/31/2025).

[148] H. Sakai, S. Shimoda, and Y. Hiramoto. “Mass isolation of mitotic apparatus using a glycerol/Mg2+/Triton X-100 medium”. In: *Experimental Cell Research* 104.2 (Feb. 1977), pp. 457–461. ISSN: 00144827. DOI: 10.1016/0014-4827(77)90117-3. URL: https://linkinghub.elsevier.com/retrieve/pii/0014482777901173 (visited on 07/31/2025).

[149] L. I. Rebhun and R. E. Palazzo. “In vitro reactivation of anaphase B in isolated spindles of the sea urchin egg”. In: *Cell Motility* 10.1 (Jan. 1988), pp. 197–209. ISSN: 0886-1544. DOI: 10.1002/cm.970100124. URL: https://onlinelibrary.wiley.com/doi/10.1002/cm.970100124 (visited on 07/31/2025).

[150] M. J. Lohka and J. L. Maller. “Induction of nuclear envelope breakdown, chromosome condensation, and spindle formation in cell-free extracts.” In: *The Journal of cell biology* 101.2 (Aug. 1, 1985), pp. 518–523. ISSN: 0021-9525, 1540-8140. DOI: 10.1083/jcb.101.2.518. URL: https://rupress.org/jcb/article/101/2/518/28120/Induction-of-nuclear-envelope-breakdown-chromosome (visited on 07/31/2025).

[151] K. E. Sawin and T. J. Mitchison. “Mitotic spindle assembly by two different pathways in vitro.” In: *The Journal of cell biology* 112.5 (Mar. 1, 1991), pp. 925–940. ISSN: 0021-9525, 1540-8140. DOI: 10.1083/jcb.112.5.925. URL: https://rupress.org/jcb/article/112/5/925/14036/Mitotic-spindle-assembly-by-two-different-pathways (visited on 07/31/2025).

[152] M. Dogterom, M. A. Félix, C. C. Guet, and S. Leibler. “Influence of M-phase chromatin on the anisotropy of microtubule asters.” In: *The Journal of cell biology* 133.1 (Apr. 1, 1996), pp. 125–140. ISSN: 0021-9525, 1540-8140. DOI: 10.1083/jcb.133.1.125. URL: https://rupress.org/jcb/article/133/1/125/59099/Influence-of-M-phase-chromatin-on-the-anisotropy (visited on 08/01/2025).

[153] T. E. Holy, M. Dogterom, B. Yurke, and S. Leibler. “Assembly and positioning of microtubule asters in microfabricated chambers”. In: *Proceedings of the National Academy of Sciences* 94.12 (June 10, 1997). Publisher: Proceedings of the National Academy of Sciences, pp. 6228–6231. DOI: 10.1073/pnas.94.12.6228. URL: https://www-pnas-org.tudelft.idm.oclc.org/doi/10.1073/pnas.94.12.6228 (visited on 12/20/2024).

[154] A. Khodjakov, R. W. Cole, B. R. Oakley, and C. L. Rieder. “Centrosome-independent mitotic spindle formation in vertebrates”. In: *Current Biology* 10.2 (Jan. 2000), pp. 59–67. ISSN: 09609822. DOI: 10.1016/S0960-9822(99)00276-6. URL: https://linkinghub.elsevier.com/retrieve/pii/S0960982299002766 (visited on 07/31/2025).

[155] A. Wilde, S. B. Lizarraga, L. Zhang, C. Wiese, N. R. Gliksman, C. E. Walczak, and Y. Zheng. “Ran stimulates spindle assembly by altering microtubule dynamics and the balance of motor activities”. In: *Nature Cell Biology* 3.3 (Mar. 2001), pp. 221–227. ISSN: 1465-7392, 1476-4679. DOI: 10.1038/35060000. URL: https://www.nature.com/articles/ncb0301_221 (visited on 07/31/2025).

[156] P. Kalab, K. Weis, and R. Heald. “Visualization of a Ran-GTP Gradient in Interphase and Mitotic *Xenopus* Egg Extracts”. In: *Science* 295.5564 (Mar. 29, 2002), pp. 2452–2456. ISSN: 0036-8075, 1095-9203. DOI: 10.1126/science.1068798. URL: https://www.science.org/doi/10.1126/science.1068798 (visited on 07/31/2025).

[157] O. J. Gruss, R. E. Carazo-Salas, C. A. Schatz, G. Guarguaglini, J. Kast, M. Wilm, N. Le Bot, I. Vernos, E. Karsenti, and I. W. Mattaj. “Ran Induces Spindle Assembly by Reversing the Inhibitory Effect of Importin α on TPX2 Activity”. In: *Cell* 104.1 (Jan. 2001), pp. 83–93. ISSN: 00928674. DOI: 10.1016/S0092-8674(01)00193-3. URL: https://linkinghub.elsevier.com/retrieve/pii/S0092867401001933 (visited on 07/31/2025).

[158] A. Khodjakov, L. Copenagle, M. B. Gordon, D. A. Compton, and T. M. Kapoor. “Minus-end capture of preformed kinetochore fibers contributes to spindle morphogenesis”. In: *The Journal of Cell Biology* 160.5 (Mar. 3, 2003), pp. 671–683. ISSN: 1540-8140, 0021-9525. DOI: 10.1083/jcb.200208143. URL: https://rupress.org/jcb/article/160/5/671/33220/Minus-end-capture-of-preformed-kinetochore-fibers (visited on 07/31/2025).

[159] P. D. Andrews, Y. Ovechkina, N. Morrice, M. Wagenbach, K. Duncan, L. Wordeman, and J. R. Swedlow. “Aurora B Regulates MCAK at the Mitotic Centromere”. In: *Developmental Cell* 6.2 (Feb. 2004), pp. 253–268. ISSN: 15345807. DOI: 10.1016/S1534-5807(04)00025-5. URL: https://linkinghub.elsevier.com/retrieve/pii/S1534580704000255 (visited on 07/31/2025).

[160] R. Ohi, T. Sapra, J. Howard, and T. J. Mitchison. “Differentiation of Cytoplasmic and Meiotic Spindle Assembly MCAK Functions by Aurora B-dependent Phosphorylation”. In: *Molecular Biology of the Cell* 15.6 (June 2004), pp. 2895–2906. ISSN: 1059-1524, 1939-4586. DOI: 10.1091/mbc.e04-02-0082. URL: https://www.molbiolcell.org/doi/10.1091/mbc.e04-02-0082 (visited on 07/31/2025).

[161] G. Goshima, F. Nédélec, and R. D. Vale. “Mechanisms for focusing mitotic spindle poles by minus end–directed motor proteins”. In: *The Journal of Cell Biology* 171.2 (Oct. 24, 2005), pp. 229–240. ISSN: 1540-8140, 0021-9525. DOI: 10.1083/jcb.200505107. URL: https://rupress.org/jcb/article/171/2/229/52011/Mechanisms-for-focusing-mitotic-spindle-poles-by (visited on 07/31/2025).

[162] M.-Y. Tsai, S. Wang, J. M. Heidinger, D. K. Shumaker, S. A. Adam, R. D. Goldman, and Y. Zheng. “A Mitotic Lamin B Matrix Induced by RanGTP Required for Spindle Assembly”. In: *Science* 311.5769 (Mar. 31, 2006), pp. 1887–1893. ISSN: 0036-8075, 1095-9203. DOI: 10.1126/science.1122771. URL: https://www.science.org/doi/10.1126/science.1122771 (visited on 07/31/2025).

[163] A. E. Kelly, S. C. Sampath, T. A. Maniar, E. M. Woo, B. T. Chait, and H. Funabiki. “Chromosomal Enrichment and Activation of the Aurora B Pathway Are Coupled to Spatially Regulate Spindle Assembly”. In: *Developmental Cell* 12.1 (Jan. 2007), pp. 31–43. ISSN: 15345807. DOI: 10.1016/j.devcel.2006.11.001. URL: https://linkinghub.elsevier.com/retrieve/pii/S1534580706005065 (visited on 08/01/2025).

[164] A. W. Bird and A. A. Hyman. “Building a spindle of the correct length in human cells requires the interaction between TPX2 and Aurora A”. In: *The Journal of Cell Biology* 182.2 (July 28, 2008), pp. 289–300. ISSN: 1540-8140, 0021-9525. DOI: 10.1083/jcb.200802005. URL: https://rupress.org/jcb/article/182/2/289/34985/Building-a-spindle-of-the-correct-length-in-human (visited on 08/01/2025).

[165] P. Bieling, I. A. Telley, and T. Surrey. “A Minimal Midzone Protein Module Controls Formation and Length of Antiparallel Microtubule Overlaps”. In: *Cell* 142.3 (Aug. 2010), pp. 420–432. ISSN: 00928674. DOI: 10.1016/j.cell.2010.06.033. URL: https://linkinghub.elsevier.com/retrieve/pii/S0092867410007233 (visited on 08/01/2025).

[166] L. Laan, N. Pavin, J. Husson, G. Romet-Lemonne, M. van Duijn, M. P. López, R. D. Vale, F. Jülicher, S. L. Reck-Peterson, and M. Dogterom. “Cortical Dynein Controls Microtubule Dynamics to Generate Pulling Forces that Position Microtubule Asters”. In: *Cell* 148.3 (Feb. 2012), pp. 502–514. ISSN: 00928674. DOI: 10.1016/j.cell.2012.01.007. URL: https://linkinghub.elsevier.com/retrieve/pii/S009286741200013X (visited on 08/01/2025).

[167] D. Portran, J. Gaillard, M. Vantard, and M. Thery. “Quantification of MAP and molecular motor activities on geometrically controlled microtubule networks”. In: *Cytoskeleton* 70.1 (2013). _eprint: https://onlinelibrary.wiley.com/doi/pdf/10.1002/cm.21081, pp. 12–23. ISSN: 1949-3592. DOI: 10.1002/cm.21081. URL: https://onlinelibrary.wiley.com/doi/abs/10.1002/cm.21081 (visited on 12/23/2024).

[168] M. Vleugel, S. Roth, C. F. Groenendijk, and M. Dogterom. “Reconstitution of Basic Mitotic Spindles in Spherical Emulsion Droplets”. In: *Journal of Visualized Experiments* 114 (Aug. 13, 2016), p. 54278. ISSN: 1940-087X. DOI: 10.3791/54278. URL: https://app.jove.com/t/54278 (visited on 07/31/2025).

[169] S. Roth, I. C. Gârlea, M. Vleugel, B. M. Mulder, and M. Dogterom. *Reconstitution of basic mitotic spindles in cell-like confinement.* Sept. 16, 2019. DOI: 10.1101/770602. URL: http://biorxiv.org/lookup/doi/10.1101/770602 (visited on 07/31/2025).

[170] I. M. Cheeseman, J. S. Chappie, E. M. Wilson-Kubalek, and A. Desai. “The Conserved KMN Network Constitutes the Core Microtubule-Binding Site of the Kinetochore”. In: *Cell* 127.5 (Dec. 2006), pp. 983–997. ISSN: 00928674. DOI: 10.1016/j.cell.2006.09.039. URL: https://linkinghub.elsevier.com/retrieve/pii/S0092867406013456 (visited on 08/01/2025).

[171] S. M. Travis, B. P. Mahon, and S. Petry. “How Microtubules Build the Spindle Branch by Branch”. In: *Annual Review of Cell and Developmental Biology* 38.1 (Oct. 6, 2022), pp. 1–23. ISSN: 1081-0706, 1530-8995. DOI: 10.1146/annurev-cellbio-120420-114559. URL: https://www.annualreviews.org/doi/10.1146/annurev-cellbio-120420-114559 (visited on 08/01/2025).

2

ESTIMATION OF MICROTUBULE-GENERATED FORCES USING A DNA ORIGAMI NANOSPRING

Ali NICK MALEKI, Pim J. HUIS IN 'T VELD, Anna AKHMANOVA, Marileen DOGTEROM, Vladimir A. VOLKOV

To see what is right in front of one's nose needs a constant struggle

George Orwell

Nature uses only the longest threads to weave her patterns, so that each small piece of her fabric reveals the organization of the entire tapestry

Richard Feynman

Microtubules are dynamic cytoskeletal filaments that can generate forces when polymerizing and depolymerizing. Proteins that follow growing or shortening

---

This chapter has been published in J Cell Sci (2023) 136 (5): jcs260154.

microtubule ends and couple forces to cargo movement are important for a wide range of cellular processes. Quantifying these forces and the composition of protein complexes at dynamic microtubule ends is challenging and requires sophisticated instrumentation. Here, we present an experimental approach to estimate microtubule-generated forces through the extension of a fluorescent spring-shaped DNA origami molecule. Optical readout of the spring extension enables recording of force production simultaneously with single-molecule fluorescence of proteins getting recruited to the site of force generation. DNA nanosprings enable multiplexing of force measurements and only require a fluorescence microscope and basic laboratory equipment. We validate the performance of DNA nanosprings against results obtained using optical trapping. Finally, we demonstrate the use of the nanospring to study proteins that couple microtubule growth and shortening to force generation.

2.1. INTRODUCTION

Microtubules are dynamic polymers that can exert pushing and pulling forces when they grow and shorten. Microtubule-generated forces are important at various stages of the cell cycle in a variety of cell types and contexts (reviewed in [1]). One of the most well-studied processes relying on microtubule-generated forces is mitotic cell division, when the ends of microtubules pull on the centromeric regions of chromosomes through protein structures called kinetochores [2]. The microtubule–kinetochore interface is force sensitive – tension at the centromere is thought to be converted into a biochemical signal that silences the mitotic checkpoint. However, the nature of the force sensor that responds to the microtubule-generated tension in the kinetochore is still unclear (reviewed in [3]).

Precise measurements of microtubule-generated forces and responses to these forces are challenging in vivo, because of crowded cellular environments, a multitude of differently directed forces that are exerted by different cellular components, and difficulties in incorporating force-measuring equipment into the cell. The method of choice for precision force measurements has been in vitro reconstitution and optical trapping. An optical trap holds a plastic or glass sphere (bead) in the center of a tightly focused infrared laser beam. Bead displacement from the beam can be monitored with nanometre precision using sophisticated optical equipment [4, 5]. Forces measured using beads coated with microtubule-binding proteins or purified kinetochore particles have provided important insights into the action of a microtubule as a motor [6] , the force-dependent stabilization of the kinetochore–microtubule interface [7] [8], and molecular determinants of kinetochore-mediated stabilization of microtubule ends [9, 10].

Although having outstanding force and time resolution, the optical trapping approaches present several challenges. First, building an optical trap requires optical and engineering expertise, and commercial systems are expensive. Second, the trap acts on the centre of a bead, while force-generating biomolecules act on the surface of the bead, which can create asymmetry of the applied force in the bead–microtubule system [11, 12]. Finally, to study effects of force on dynamics of microtubule-binding or kinetochore proteins, one has to record these dynamics simultaneously with force. Addition of single-molecule fluorescence imaging to an optical trap is technically demanding [13–15] and not widely accessible.

Here, we present a method to simultaneously measure microtubule-generated forces and single-molecule fluorescence intensities in vitro without an optical trap. The method is based on a previously described DNA origami spring-shaped structure, designed to determine forces directly from its extension [16]. The nanospring is assembled by folding a long single-stranded DNA with short DNA oligonucleotides (staples), resulting in a spring-shaped bundle of four DNA strands (Fig. 2.1A; [16]). We provide detailed instructions to modify the original spring design, purify the DNA nanosprings, and use them as sensors for forces produced by growing and shortening microtubules.

We provide typical results in three different in vitro systems. First, we validate the nanospring-based estimation of force against optical trapping by measuring the stall force of dynein motors walking along the stabilized microtubules. We then demonstrate the use of the nanosprings to measure the forces generated by dynamic microtubules. Focusing on forces produced by microtubule growth, we reconstitute the forces exerted through an EB3 (encoded by MAPRE3) comet following the growing microtubule ends and pulling on nanospring-bound cargo containing an EB-binding SxIP motif.

Finally, we focus on forces produced by shortening microtubule ends in the context of kinetochore–microtubule interactions. We attach human kinetochore complex Ndc80 to the nanospring, and monitor spring extension simultaneously with the binding and unbinding of the spindle and kinetochore-associated (Ska) complex, another microtubule-binding kinetochore component. Using the DNA origami nanospring, we demonstrate that the presence of additional copies of Ndc80, but not Ska, increases the amount of force that shortening microtubule ends transmit to their cargo.

2.2. DESIGN AND CALIBRATION OF THE NANOSPRINGS

To make the DNA nanospring, we adapted the reported DNA origami design [16] to other single-stranded DNA scaffolds (see Materials and Methods for a detailed protocol). The spring was assembled into a four-stranded DNA bundle with a three nucleotide-long hairpin inserted at every 14 bp, creating an offset to twist the spring (Fig. 2.1A). Digoxigenin (DIG)- and biotin-labelled DNA staples were introduced at the termini of the spring for attachment to the molecules of interest. Further, nine Atto488-labelled staple oligonucleotides were evenly distributed along the length of the spring, and another five Atto488-labelled oligonucleotides added next to the biotin-labelled end (Fig. 2.1A). Spring design can be easily modified using caDNAno software (Fig. 2.1B; https://cadnano.org/) [17]. Folded springs need to be separated from the short staple oligonucleotides and partially folded products (Fig. 2.1C). We validated the purity and folding of our DNA nanosprings using negative stain electron microscopy (EM) (Fig. 2.1D).

To calibrate the force–extension profile of the springs, we attached the springs to the hydrophobic silanized glass surface of a flow chamber using anti-DIG IgG (Fig. 2.2A). Following a passivation step using Pluronic F-127, we obtained a uniform coating of single fluorescently labelled springs on the coverslip (Fig. 2.2B). We then used 1 μm streptavidin-coated beads bound to the springs via biotin–streptavidin linkage (Fig. 2.2C). Upon trapping a bead that was bound to the coverslip via the nanospring, displacement of the bead from the trap was measured as the flow chamber was moved using a piezo-driven stage in 100 nm steps, following a 2D matrix (Fig. 2.2D). After radial averaging of the force–extension data for six beads and accounting for the bead radius, the resulting force–extension curve was identical to that previously published [16]. Fitting the data to an exponential growth equation produced the following relationship, which we used further to convert nanospring extension into force (Fig. 2.2E):

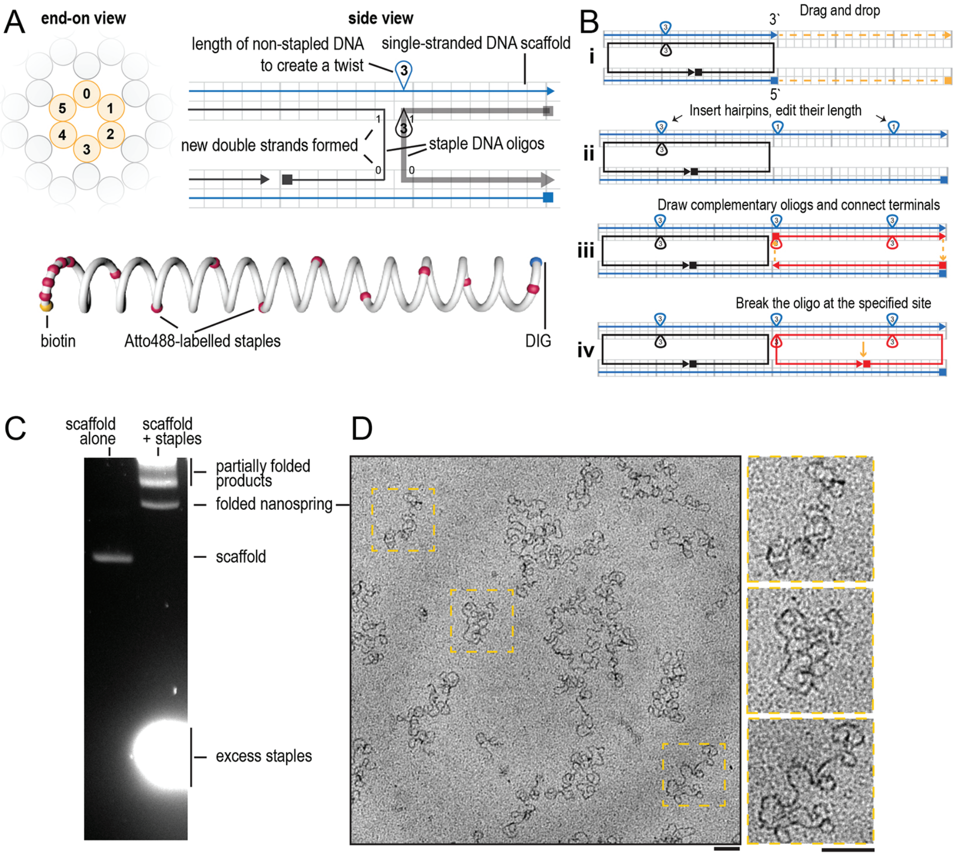

Figure 2.1: *Nanospring representation in caDNAno and quality control of folded nanospring by agarose gel electrophoresis and electron microscopy. (A) An example of a slice panel (left) and a path panel (right) of the DNA origami design in caDNAno. Below: a schematic illustration of the nanospring with colour-coded staples (yellow, biotin; red, fluorescently labelled staples; blue, DIG). (B) Step by step visual guide to extend an existing nanospring design using caDNAno. (C) Purification of nanosprings by agarose gel electrophoresis. The left lane shows migration of unfolded scaffold in absence of staples, the right lane is loaded with staple-scaffold mixture after temperature cycling and contains the products of folding. (D) Transmission electron microscopy of nanosprings negatively stained by 2% uranyl acetate. Enlarged images of the indicated regions are shown on the right. Scale bars: 100 nm. Images in C and D are representative of 11 experiments.*

$$F = 0.182e^{3.3x} \tag{2.1}$$

where F is force in piconewtons and x is nanospring extension in micrometres. We used fitted residuals to estimate the uncertainty of force measurement from spring extension (Fig. 2.2F). Owing to the non-linear force–extension curve, uncertainty in force estimation increased with the nanospring extension from ±0.1 pN at forces below 0.3 pN to about ±1 pN for maximal nanospring extensions corresponding to forces above 5 pN (Fig. 2.2G).

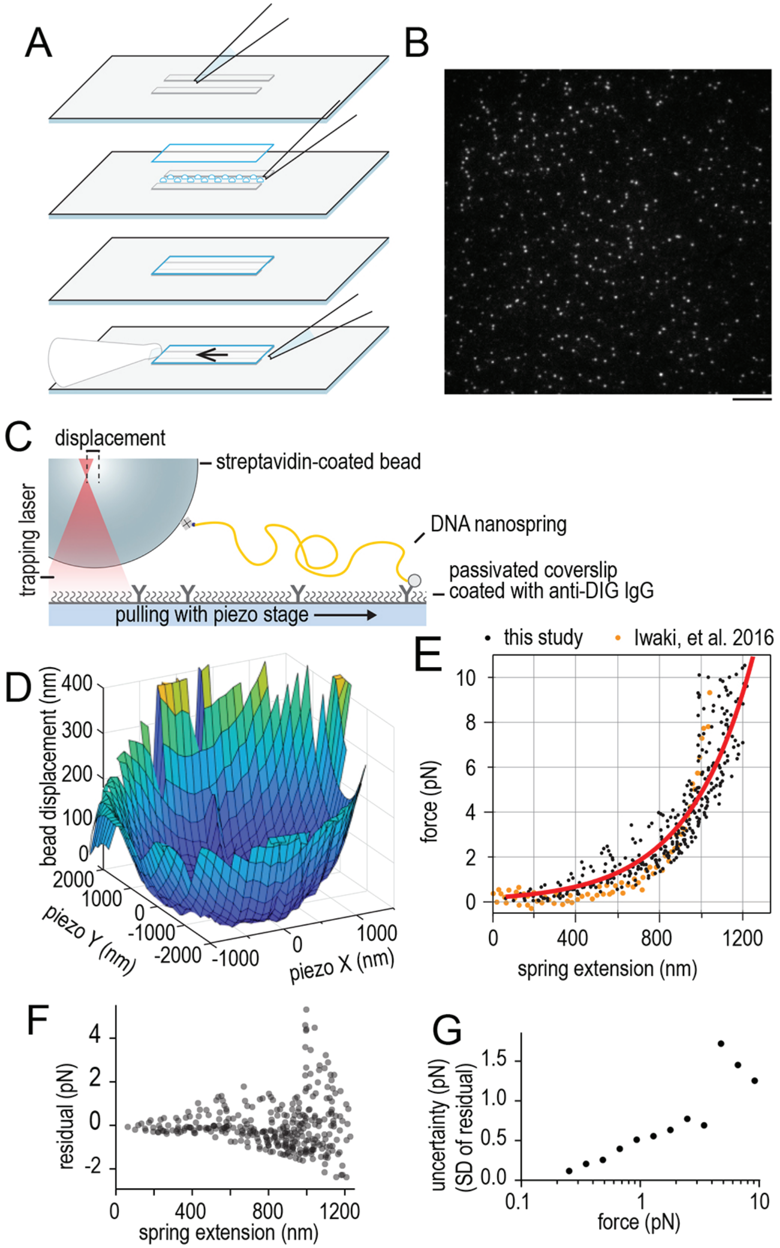

Figure 2.2: *Surface attachment and calibration of nanospring force–extension. (A) Schematic diagram showing assembly of a flow chamber using silanized slides and coverslips. (Continued ...)*

(Figure 2.2 continued) (B) Typical microscopic field of view with 10× Atto-labelled nanosprings attached to glass surface using DIG and anti-DIG IgG. Scale bar: 10 µm. (C) Schematic diagram of an experiment with surface-bound nanospring being stretched using a bead in an optical trap. (D) A typical result (from six repeats) showing nanospring extension (vertical axis) as a function of the 2D coordinates of the microscopic stage (horizontal axes x and y). The bell-like shape of the curve signifies a single attachment point for the nanospring. (E) Force–extension curve resulting from measurements using six nanospring-attached beads (black), overlayed on top of the results presented in the original publication (orange; Iwaki et al., 2016 [16]). Solid red line shows results of exponential fitting. (F) Residuals of exponential fitting presented in E. (G) Standard deviation of residuals binned by force (as calculated from spring extension).

2.3. VALIDATION OF NANOSPRING-BASED FORCE MEASUREMENTS

To benchmark the performance of the nanospring in measuring single-molecule forces, we used biotinylated dynein motor domains from S. cerevisiae [5, 18]. In this experiment, the nanospring was attached to anti-DIG IgG on the coverslip via DIG, and a streptavidin-coated Qdot bound both biotinylated dynein and a biotinylated DNA staple at the end of the nanospring (Fig. 2.3A). We used total internal reflection fluorescence (TIRF) microscopy to record images of microtubules, Atto488-labelled nanosprings and Qdot565-bound dynein at the end of the nanospring. Owing to dimensions of the nanospring spanning several hundreds of nanometres, the best contrast was achieved using an imaging mode with deeper penetration than TIRF, such as HiLo [19], or intermediate settings between TIRF and epifluorescence. Using these settings, we could readily observe spring-bound Qdots walking along the microtubule, extending the springs, and stalling upon reaching the stall force of dynein (Fig. 2.3B).

To determine spring extensions from kymographs such as the one presented in Fig. 3B, we used two methods. First, to determine the length of the spring, in each line of a kymograph containing the Atto488 signal, we measured the centre position of pixels that were brighter than the background fluorescence level. Second, to determine the position of the end of the spring, we fitted a gaussian to each of the lines of a kymograph containing the Qdot-565 signal. Both of these measurements yielded estimates of spring extension (Fig. 2.3C). However, subpixel localization of the Qdot position provided less noisy data (Fig. 2.3D, compare magenta and yellow traces) and was therefore used in further analysis to determine the position of the spring end. Nanospring length was then converted into stalling force using Eqn 2.1.

As a control, we used optical trapping to measure the stall forces of bead-bound dynein (Fig. 3E). Optical trapping provided high temporal and spatial resolution (Fig. 2.3F); however, the stall force values extracted from both force measurement methods were similar (Fig. 2.3G). These results are consistent with other reports of S. cerevisiae dynein stall force [20, 21].

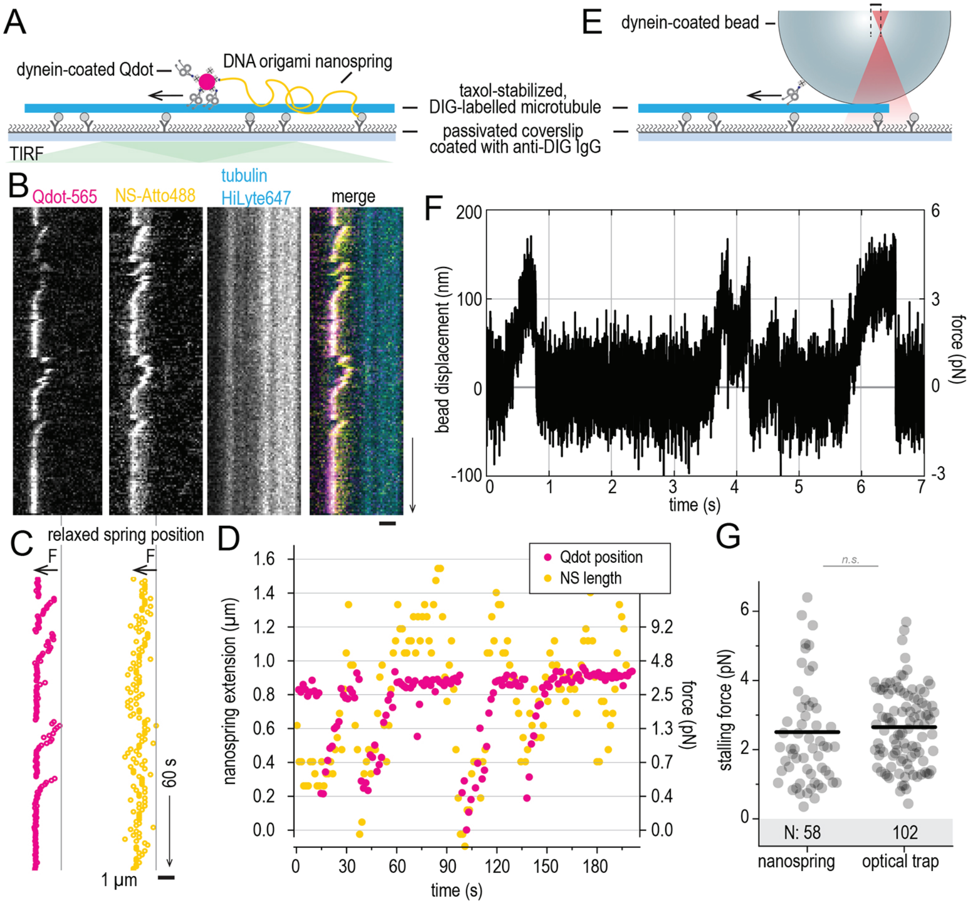

Figure 2.3: *Analysis of spring extension and validation of force measurements. Experiment schematics (A) and a typical kymograph from three repeats (58 force traces in total) (B) showing a coverslip-bound taxol-stabilized microtubule (cyan), Atto488-labelled nanospring (yellow) and dynein-conjugated Qdot-565 (magenta). Note that the spring spends most of the observation time in the stretched state. As the spring design we used featured 5× Atto488 at the biotinylated spring end, and 10× Atto488 along the spring length (see Fig. 1A), the fully stretched spring has one end brightly labelled, as can be seen in the Atto488 channel of the kymograph. (C) Coordinates on the nanospring end (Qdot, left), and nanospring middle (right) obtained by analysing the kymographs in B using the Julia script (see Materials and Methods for details). Vertical line shows the coordinates of the relaxed spring, arrows labelled F show direction of dynein-generated force. (D) Nanospring extension (left y-axis) and force (right y-axis) measured using these two methods and plotted as a function of time. (E) Experimental setup to estimate dynein stall force using an optical trap. (F) Typical time trace from three repeats (102 force traces in total) of a dynein walking against the applied force, recorded in an optical trap. (G) Dynein stalling forces measured using nanospring (left) and optical trapping (right). Circles, individual stall events; line: median, number of measurements is shown in the shaded area. P-value (two-tailed Mann–Whitney test): 0.06 (n.s., not significant). Scale bars: horizontal (1 µm), vertical (60 s) (B,C).*

2.4. ESTIMATION OF FORCES GENERATED BY GROWING MICROTUBULES

Growing microtubule ends recruit end-binding (EB) proteins in the shape of a comet; these comets in turn recruit a number of secondary proteins that carry EB-binding SxIP motifs [22]. The affinity of an EB comet to SxIP-containing proteins was reported to generate sub-piconewton forces that could extend membranes, transport actin filaments along with microtubule growth and reverse the direction of a kinesin-14 motor [23–25]. Although prior measurements have been performed using optical trapping, measuring sub-piconewton forces using this method is challenging, because it is easy to lose a bead from a soft trap. We therefore thought that the DNA nanospring, with its high precision in a low-force regime could provide an advantage (Fig. 2.2G).

To couple nanospring extension to microtubule growth, we used a nanospring-bound Qdot705 coated with an mCherry-tagged and biotinylated C-terminal fragment of human MACF2 (also known as DST, hereafter just referred to as MACF) [23] in the presence of dynamic microtubules and mCherry–EB3 (Fig. 2.4A). In these conditions, we observed nanosprings getting extended in the direction of microtubule growth when interacting with the mCherry–EB3 comets through mCherry–MACF (Fig. 2.4B). Quantification of nanospring extension using our Julia scripts, and subsequent conversion of spring extension into force yielded sub-piconewton force generation events that lasted for multiple seconds (Fig. 2.4C).

This experiment highlights how protein complexes at the interface of the nanospring and the microtubule end can be directly visualized using fluorescence microscopy. Our results are consistent with observations using optical trapping, where a MACF-coated bead was interacting with a growing microtubule end (Fig. 2.4D). In both conditions, we observed forces in sub-piconewton range lasting for many seconds (Fig. 2.4C,D). On average, nanospring-measured forces were smaller than optical trap-measured ones (Fig. 2.4F). This difference could be related to different amount of MACF molecules interacting with a comet in each case – no more than 20 in case of Qdot-nanospring, and several thousand in case of MACF-coated beads [23].

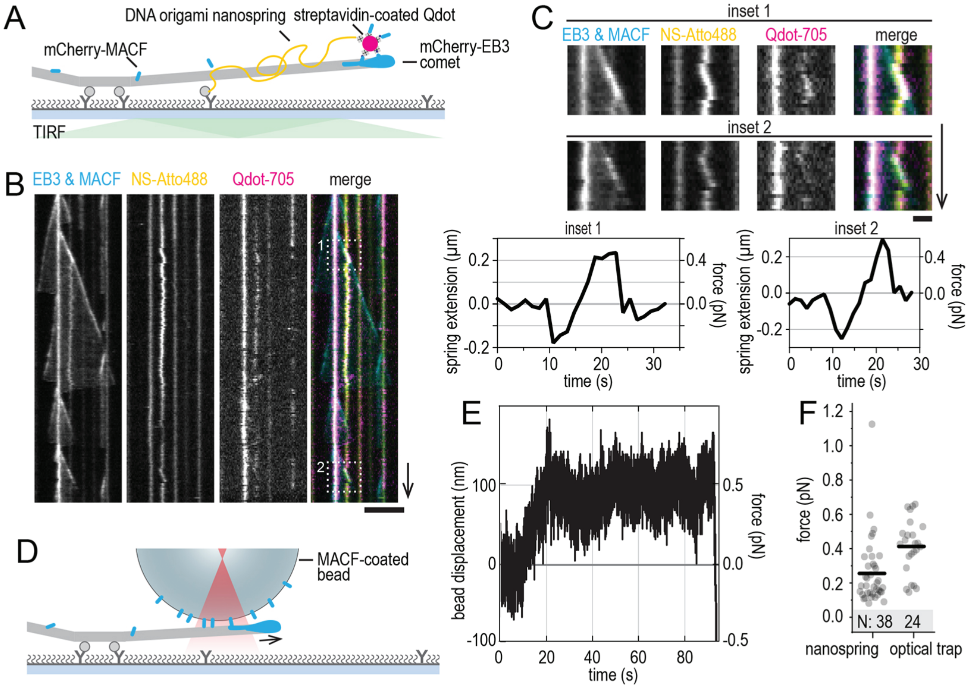

Figure 2.4: *Estimation of microtubule growth force using the DNA origami nanospring. Experimental setup (A) and typical kymographs from four repeats (38 force signals in total) (B); microtubules are grown from coverslip-attached GMPCPP-stabilized seeds (grey). Yellow shows the nanospring. Streptavidin-coated Qdot-705 (magenta) binds to the nanospring and is further saturated using mCherry-tagged MACF C-terminus (cyan). MACF is concentrated at the growing microtubule end thanks to the presence of mCherry-EB3 comets (cyan). Given that tubulin is unlabelled in this experiment, microtubule dynamics can be observed in MACF and EB3 channel. Boxes show events of a nanospring being stretched by growing microtubule ends. (C) Events of growing microtubule ends pulling on the nanosprings via MACF magnified from boxed regions in B. Graphs show quantification of nanospring extension and force over time for these events. (D) Experimental setup to estimate the MACF-transmitted force using the optical trap. (E) Typical time trace from three repeats (24 force signals in total) of a glass bead following microtubule growth against the applied force. (F) Forces measured in the direction of microtubule growth using MACF-conjugated nanosprings or MACF-coated beads in an optical trap. Horizontal lines show median. Scale bars: horizontal 5 µm (B) or 1 µm (C), vertical (60 s).*

2.5. ESTIMATION OF FORCES GENERATED BY MICROTUBULE SHORTENING

We have previously shown that multimerization of the human kinetochore complex Ndc80 enables it to follow microtubule shortening against an applied force [9]. Multiple copies of Ndc80 oligomers can stall microtubule shortening, and the duration of these stalls is increased in the presence of another multi-protein kinetochore complex known as the Ska complex, which cross-links Ndc80 and microtubules [10]. However, these observations were performed using bead-bound Ndc80 in an optical trap, in conditions preventing us from having precise information about the number of Ndc80 and Ska copies interacting with the force-generating microtubule ends.

To study the Ndc80–Ska–microtubule force-coupling system in single-molecule conditions, we used streptavidin-oligomerized Ndc80 bound to biotinylated nanosprings in the presence of dynamic microtubules and Ska (Fig. 2.5A). Using TIRF microscopy, we could simultaneously record microtubule dynamics, position of the spring-bound Ndc80, and dynamics of Ska binding to both microtubules and Ndc80 (Fig. 2.5B). Note that the run length of the nanospring-bound Ndc80 was limited by the extension of the nanospring (±1 μm), restricting the previously observed distances that an Ndc80 trimer can cover with the shortening microtubule end [9].

Forces measured using a nanospring carrying a single Ndc80 trimer in the absence of Ska were similar to previously reported forces measured using beads sparsely coated with the Ndc80 trimers in an optical trap (Fig. 2.5C) [9]. We then compared these forces to nanospring-measured forces recorded when Ska signals colocalized with the spring-bound Ndc80 (Fig. 2.5B, top), and to forces recorded in the same sample, but without Ska colocalization (Fig. 2.5B, bottom). As reported previously, at low Ska concentrations, the Cdk1 phosphorylation of the SKA3 C-terminus enhanced Ska–Ndc80 interactions [10], which is evident from the higher frequency of Ska-positive force events (Fig. 2.5C). At 100 nM Ska, Cdk1 phosphorylation was no longer necessary for Ska–Ndc80 binding; however, we did not observe a difference in nanospring-measured force resulting from the presence or absence of Ska during force development (Fig. 2.5C).

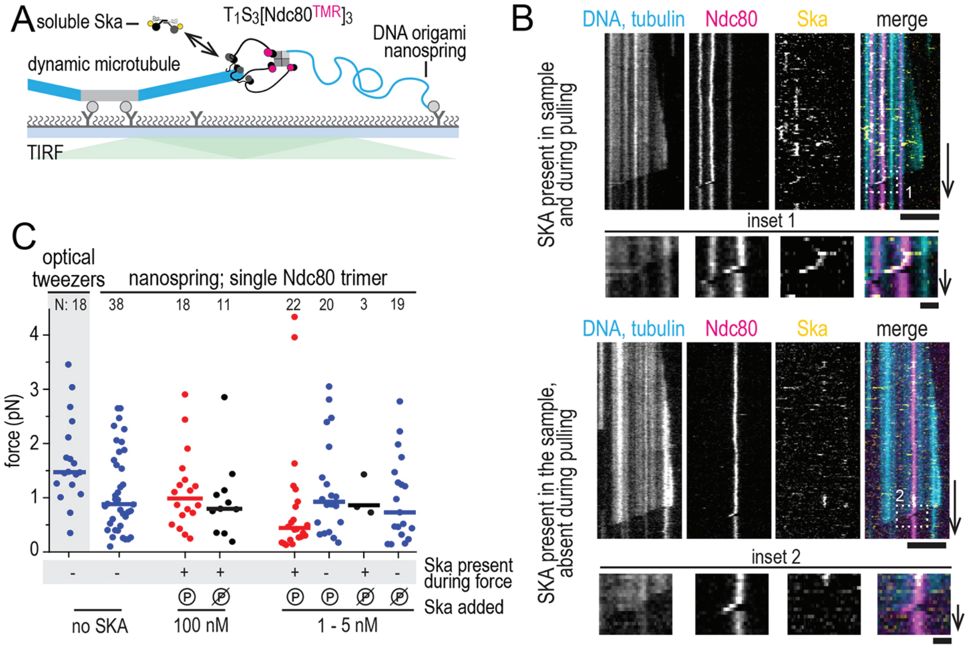

Figure 2.5: *Estimation of microtubule shortening force using DNA origami nanospring. (A) Experimental setup. GMPCPP-stabilized microtubule seeds (grey) are attached to the coverslip and nucleate dynamic fluorescently labelled microtubules (cyan). An Atto488-labelled nanospring (cyan) is conjugated to Ndc80–TMR trimers (magenta) oligomerized using streptavidin. Ska complex labelled with HiLyte-647 (yellow) is present in solution and can bind both to Ndc80 and to microtubules. (B) Typical results from five repeats showing shortening microtubule ends pulling on nanospring-conjugated Ndc80 trimers (boxes). Top example, Ska is bound to the Ndc80 trimer during force development. Bottom example, Ska is present in the sample, but not bound to the Ndc80 trimer during force development. Boxed regions are magnified below the full kymographs. (C) Forces measured using a single Ndc80 trimer following microtubule shortening against the force exerted by the stretched nanospring. Shaded area, stalling forces measured using beads sparsely coated with Ndc80 trimers in an optical trap [9] Circles, individual measurements; lines, median. Cdk1 phosphorylation of SKA3 leads to increased recruitment of Ska to Ndc80 trimers during force development [10], but has no effect on the measured force within the Ska concentrations in the range between 1 and 100 nM. Scale bars: horizontal 5 μm (B), 1 μm (insets), vertical 60 s (B), 10 s (magnified views).*

2.6. PRESENCE OF MULTIPLE MICROTUBULE BINDERS AT THE NANOSPRING ENHANCES FORCE COUPLING

The failure of Ska to increase the Ndc80-transmitted force was consistent with our earlier estimates using optical trapping, where the presence of Ska mainly affected the duration of stalls, and to a lesser extent the stalling force [10]. We wondered, however, whether there were conditions in which we could capture higher microtubule-generated forces using nanospring-bound Ndc80. One way to increase the amount of transmitted force is to engage more copies of a force-coupling molecule [9, 26]. To test this hypothesis, we sought to increase the multimerization of Ndc80 at the end of the spring.

We took advantage of the SpyCatcher–SpyTag interactions forming a covalent bond, and a previously described protocol to biochemically separate streptavidin tetramers refolded from mixtures of SpyCatcher–avidin, SpyTag–avidin and Traptavidin [27, 28]. We first expressed, refolded and purified streptavidin tetramers containing three SpyTag–avidin subunits and one Traptavidin subunit (T1ST3) and then mixed these with an excess of SpyCatcher avidin tetramers (S4) (Fig. 2.6A; Fig. 2S.1A,B). The resulting T1ST3S12 scaffolds were mixed with an excess of Ndc80SpyTag to generate objects containing up to nine Ndc80 copies. Ndc80 was labelled with TMR using sortase and a fluorescently labelled peptide in the same reaction and the final product, T1ST3S12[Ndc80]x, was purified using a glycerol gradient (Fig. 2.6A; Fig. 2S.1B,C). Examining the resulting Ndc80 multimers by electron microscopy, we found Ndc80 multimers with varying stoichiometries. Typical Ndc80 multimers contained four to seven Ndc80 arms (Fig. 2.6C).

Attaching these multivalent objects to the biotinylated nanosprings, we could measure the force they transmitted from the microtubule shortening, and their brightness (Fig. 2.6D). Consistent with our observations by EM, the distribution of Ndc80 copy number was quite wide, peaking at six Ndc80 copies per object (Fig. 2.6E). Consistent with increased Ndc80 copy numbers, Ndc80 multimers transmitted up to 10 pN of microtubule-generated force, compared to a maximum of 3 pN transmitted by a single Ndc80 trimer (Fig. 2.6F). Contrary to the experiments with bead-bound Ndc80 trimers, we did not observe force-dependent microtubule rescue with Ndc80 multimers bound to nanosprings despite forces in the 5–10 pN range.

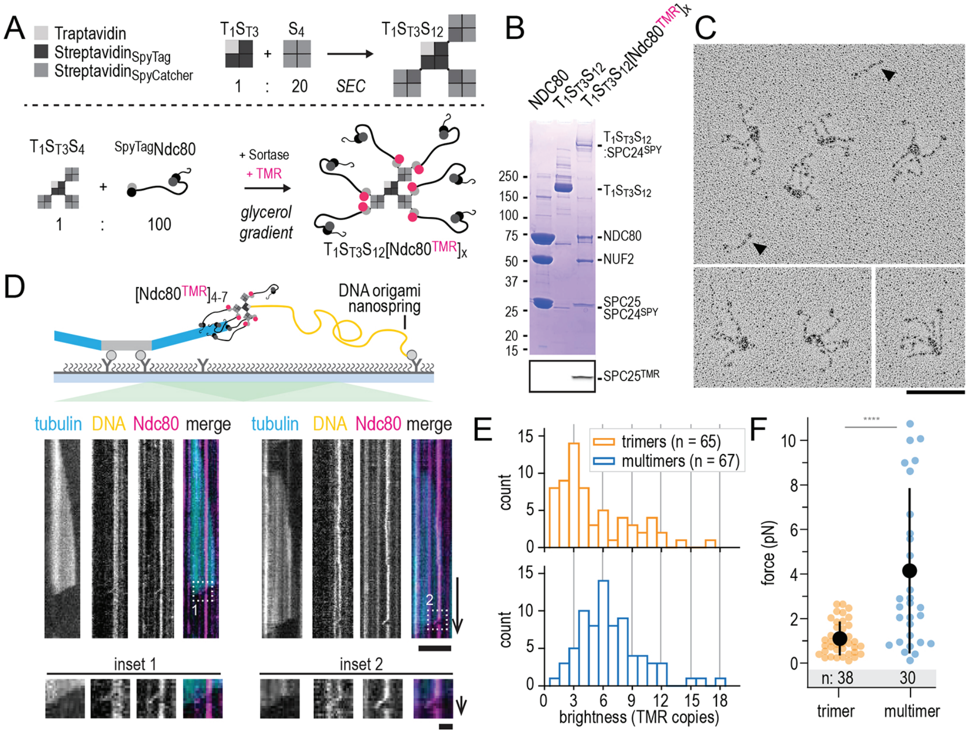

Figure 2.6: *Presence of multiple microtubule-binders at the nanospring enhances force-coupling. (A) T1ST3SC12 assemblies were generated from T1ST3 and SC12 tetramers, purified using size-exclusion chromatography, and incubated with Ndc80. See Fig. S1 for more information. (B) The final product, T1ST3SC12[Ndc80TMR]x containing up to nine Ndc80 copies, is also shown side-by-side with monomeric Ndc80 and the spy-avidin scaffold. The top gel image is taken after Coomassie staining and the bottom is the image of the same gel taken at 561 nm fluorescence channel. Streptavidin remains tetrameric during SDS-PAGE given that samples were not heated before analysis. The four subunits of the Ndc80 complex (NDC80, NUF2, SPC24 and SPC25), however, run separately, as their interactions are broken in the presence of SDS. (C) Multimeric Ndc80 assemblies were purified on a density gradient and inspected by electron microscopy after low-angle platinum shadowing. Monomeric Ndc80 complexes (arrowheads) are shown next to multimeric Ndc80 modules. The sample shown in B and C was used for experiments presented in D–F. (D) Experimental setup and typical kymographs from five repeats showing DNA nanosprings (yellow) extended by Ndc80 multimers (magenta) following the shortening ends of dynamic microtubules (cyan). Enlarged images of the indicated regions shown are magnified below the full kymographs. (E) Brightness of Ndc80 trimers (orange) and multimers (blue) expressed as a copy number of Ndc80-TMR. (F) Forces calculated from nanospring extension for a single Ndc80 trimer (orange) and a single Ndc80 multimer (blue). Black circles show mean, error bars show s.d. P-value (two-tailed Mann–Whitney test): 2.2×10-5 (****, <10-4). Scale bars: horizontal 100 nm (C), 5 µm (D), 1 µm (magnified views in D), vertical 60 s (D), 10 s (insets in D).*

2.7. DISCUSSION

Classically, force production by the mitotic spindle and force sensitivity of the mitotic checkpoint were studied using microneedles inserted into a dividing cell [29, 30]. Recent developments of this approach yielded important insights into the organization of mitotic spindle [31, 32], but precise quantification of forces in vivo remains challenging. Alternatively, tension at the centromeric region of the chromosomes can be estimated indirectly, based on assumptions about stiffness of stretchable elements in the cells [33, 34].

The third method of estimating microtubule-generated tension in vivo is based on Förster resonance energy transfer (FRET) sensors. With a FRET sensor, the efficiency of energy transfer between donor and acceptor fluorophores depends on the distance between these fluorophores, allowing reading out tension using fluorescence intensity of the acceptor fluorophore [35, 36]. Although the FRET approach provides important evidence regarding the role of tension in regulating the kinetochore–microtubule attachments in vivo, multiple copies of microtubule binders interacting with multiple microtubule ends result in ensemble readouts that are challenging to interpret at the single-molecule level [37–41].

The DNA nanospring is a force sensor that outputs a force signal directly through measurement of its extension. Potential advantages of nanosprings include multiplexed force measurements in a single microscopic field of view, simultaneous visualization of additional factors being recruited during force production (Fig. 2.5), and implementation in laboratories without access to an optical trap. Compared to an optical trap, nanosprings have a lower time resolution, limited to 1–100 Hz by the frame rate of the timelapse image acquisition as opposed to the kilohertz range in an optical trap. At the same time, the use of the nanospring alleviates concerns related to the 'lever arm' effects arising from the geometry of microtubule–bead connection [11, 12].

Because of a non-linear force–extension curve [16], the nanospring provides a particularly clear readout in the sub-piconewton force range. This enabled us to measure forces generated by a protein complex tracking growing microtubule ends (Fig. 2.4). Although the same phenomenon could also be observed using optical trapping [23–25], measurement of such small forces is usually technically challenging. It should be noted that at higher extensions (and higher forces), nanosprings are less precise than optical tweezers in force estimation (uncertainty up to ±1 pN at above 5 pN, Fig. 2.2G, compared to ~ 0.1 pN or lower for optical tweezers).

Forces generated by shortening microtubules can sometimes exceed 10 pN [7, 11], the upper limit of the force–extension curve for the nanospring (Fig. 2.2E). At higher forces, the DNA origami structure might unfold [42] or detach from its surface anchor [43]. A possible improvement of the attachment strength could be obtained by using DIG10.3 instead of anti-DIG IgG [44, 45]. In addition, multiple DIG- and biotin-labelled staples could be introduced to share the load evenly. In our experience, the DNA origami nanosprings were stable in microtubule force experiments for up to 30–60 min. To further improve the lifetime of the nanospring under force, ligation [46] or chemical crosslinking of strands [47, 48] after purification could be beneficial.

In this study, nanosprings provided similar force amplitude values to those in published optical trapping experiments in different experimental settings. MACF-mediated force transmission resulted in consistently lower forces produced by microtubule growth and measured using the nanospring. We hypothesise that the nanospring could be particularly sensitive in the sub-piconewton regime, where extension of the spring within the 200–300 nm range leads to estimation of the force with ~ 0.1 pN accuracy (Fig. 2.2F,G).

Ndc80 oligomers attached to nanosprings did not rescue microtubule depolymerization under force (Figs. 2.5 2.6), in contrast to our previous experiments where beads densely coated with Ndc80 rescued microtubule shortening under force [9]. In experiments with beads, the exact copy number of microtubule-coupled Ndc80 is unknown. The direct quantification of Ndc80 copy number at the interface between the nanospring and the dynamic microtubule end allows us to conclude that the presence of additional copies of Ndc80, but not Ska, correlates with an increase in the force transmitted by a shortening microtubule. Increased force captured by the nanospring, however, did not result in an increased rescue frequency, consistent with our systematic analysis of microtubule rescue mechanisms, which revealed the stall duration, rather than stall force, was the most reliable predictor of rescue [10]. It is possible that the DNA springs were too unstable at high forces to sustain a stall long enough to produce a microtubule rescue, or that more than nine copies of Ndc80 are necessary to reliably prevent re-initiation of shortening after a short stall. Mechanistic insight into these questions requires further experiments.

In summary, we demonstrate the use of the DNA origami nanospring in measuring the force of microtubule motors walking along a stable microtubule lattice, as well as the forces exerted by dynamic microtubule ends via proteins following their growth or shortening. In addition, we extend the use of this method to recording single-molecule dynamics of proteins binding and unbinding at the site of force generation. We conclude that the DNA origami nanospring is a powerful tool to study transmission and sensing of microtubule-generated forces in vitro.

2.8. MATERIALS AND METHODS

2.8.1. DESIGN AND PURIFICATION OF THE DNA NANOSPRING

The originally described DNA nanospring design is based on the M13mp18 single-stranded DNA scaffold [16], but it could also be adapted to other commercially available scaffolds such as p7560 using caDNAno software [17]and the json file describing the original design.

Step-by-step protocol for modification of the spring design using a different single-stranded DNA scaffold, or to re-staple using a different set of DNA oligonucleotides is:

- Open the .json file in caDNAno; on the left, in the slice panel, you will see six cells are highlighted. This is the cross-section view of potential helices. The right panel (path panel) shows the side view of the DNA construct with cells representing DNA bases. In this design, there are only two DNA double strands being formed, 0 and 1 (Fig 2.1A).

- Zoom in the cells 0 and 1 in the path panel to see DNA strands. The blue line shows the single-strand DNA scaffold that will be folded on itself over cells 0 and 1 via staple DNA oligonucleotides, which are shown in dark grey.
- Go to the right terminal of scaffold (hold control/command and drag) where you can see the 3′ end (represented as an arrow in caDNAno) and the 5′ end (a square).
- Choose the 'select' tool in the control bar in the right and click on the 3′ arrow. Once it is selected, the arrow turns red. Now you can drag the arrow to extend the scaffold (Fig 2.1B). If there is not enough space to extend the strand, go to the rightmost part of the grid and click on the double head arrow. Then you can add more bases to the grid (should be a multiple of 21).
- Repeat the previous step for the 5′ square. Keep in mind that the total length of the blue line should not exceed the length of the actual single-stranded (ss)DNA scaffold.

  Tip: hold the ALT key and click on 3′ or 5′ ends to push them to the extremes of the grid.
- In this design, a hairpin of three bases is introduced at every 14 bases in one of the scaffold strands (strand 1). Extend this pattern in the newly added bases by clicking on 'Insert' in the left bar and then clicking on every 14 squares in the grid (Fig 2.1Bi).
- Click on hairpins and type the number of bases that you want to have in the hairpin (3). Press Enter to apply. Varying the length of the hairpins will affect the twisting of the resulting spring (Fig 2.1Bii).
- At this point it is possible to use the 'Auto Staple' tool on the top bar to generate folding staples and distribute them over the scaffold, but this also resets the present design of staples. Alternatively, you can add staples manually using the 'Pencil' tool. Following the existing pattern, insert a complementary oligonucleotide next to strands 0 and 1. Connect the oligos by dragging the 3′ of one of them and releasing it over 5′ of the opposite oligonucleotide on the other strand of scaffold. This creates a circular oligonucleotide that connects two scaffold strands (Fig 2.1Biii).
- Since linear oligonucleotides will be used to fold the scaffold, they need to be broken at a certain site. In the current design the breaking site is 11 bases away from the nearest left crossover. Select the 'Break' tool and click on this site to generate the break (Fig 2.1Biv). The 'Auto break' tool can be used for the same purpose, but the break sites will be decided by the program and propagated to the whole design, overriding manual settings.

- If you want to use the same staples as for the shorter nanospring, you should count how many bases have been added to the 5′ path of scaffold in caDNAno design. Cut the same number of the bases from the 3′ end of the scaffold sequence and paste it before the 5′ terminal of the sequence.

Depending on the scaffold used (i.e. M13mp18, p7308, p7560, p7704, p8064, p8100 or p8634) and on the starting position in the scaffold, the same design produces different staple sequences. We provide a json file describing the nanospring design at https://github.com/volkovdelft/kymo.jl. The scaffold and staple DNA oligonucleotides were obtained from Tilibit Nanosystems. The nanospring was folded by mixing 20 nM scaffold and 200 nM staples in the folding buffer (40 mM Tris-HCl pH 8.0 with 1 mM EDTA and 12 mM $MgCl_2$) followed by an incubation in a thermocycler (80°C for 10 min, gradient from 80°C to 60°C over 2 h, gradient from 60°C to 20°C over 2 h). Folded DNA nanosprings were separated from excess staples and partially folded products on a 1% agarose gel in Tris-Borate-EDTA buffer supplemented with 12 mM $MgCl_2$. Nanospring-containing bands were excised and extracted from the gel using Freeze 'N Squeeze™ DNA gel extraction spin columns (Bio-Rad).

2.8.2. NEGATIVE STAIN ELECTRON MICROSCOPY

A solution of purified nanosprings (3 μl) was placed on a recently glow-discharged grid with a continuous layer of carbon, blotted and immediately washed three times, followed by the application of 3 μl of the 2% uranyl acetate solution for 3 min. The grids were then blotted once more with a blotting paper and dried for 20 min. Images were acquired on a JEOL JEM1200 microscope equipped with a TVIPS F416 camera at a nominal magnification of 41,000×, resulting in a pixel size of 0.38 nm.

2.8.3. PROTEIN EXPRESSION AND PURIFICATION

The dynein motor domain was purified and biotinylated as described previously [5, 18]. EB3 and the MACF2 C-terminus was expressed and purified as described previously [23]. Ndc80 and Ska were expressed and purified, and Ndc80 was assembled into trimers as described previously [9, 10].

2.8.4. ASSEMBLY OF MULTIMERIC NDC80 MODULES

Subunits of spyavidin scaffolds were expressed using Traptavidin, Dead-Streptavidin-SpyCatcher, Dead-Streptavidin-SpyTag and Traptavidin-E6 plasmids. These plasmids were generated by the Howarth laboratory [27, 28], we obtained them through Addgene (26054, 59547, 59548 and 59549).

T1SC3, T1ST3 tetramers and SC4 modules were prepared as described previously [28]. To generate multimeric T1ST3SC12 Spyavidin scaffolds, T1ST3 and SC4 tetramers were mixed and purified by size-exclusion chromatography (Superose 6 10/300) as detailed in Fig. 2S.1A,B.

Ndc80 with SPC24SpyTag and SPC25SortaseHis was incubated at 30 μM with T1ST3SC12 assemblies at 0.3 μM in a 16 h reaction at 10°C in Ndc80 buffer containing 20 mM Tris-HCl pH 8, 200 mM NaCl, 2% glycerol (v/v) and 2 mM TCEP. Protease inhibitor (HP PLUS, Serva 39107) was present at 2.5-fold the recommended concentration. 5 M Sortase [49], Ca_{2+} and GGGGK-TMR peptide (Genscript) were added at concentrations of 10 μM, 10 mM and 150 μM, respectively, to fluorescently label Ndc80. The reaction volume was 1 ml and reaction progress was monitored as detailed in Fig. 2S.1C.

T1ST3SC12(Ndc80)x modules were separated from monomeric Ndc80 on a 15–50% glycerol gradient of ~ 12 ml in a SW40 rotor (Beckman) at 40,000 rpm for 16 h at 4°C. Manually collected fractions were analysed as detailed in Fig. S1C and selected fractions were pooled, frozen in liquid nitrogen, and stored at -80°C until further use. Shadowing electron microscopy was performed as described previously [50].

2.8.5. Coverslip and slide passivation

Glass slides and coverslips were treated with oxygen plasma for 3 min in a PSI Plasma Prep III plasma cleaner at 60 mTorr, 20–50W. Immediately after plasma treatment, the coverslips were immersed into a repel-silane solution (2% dichlorodiethylsilane in trichloroethylene or octamethylcyclooctasilane) for 5 min [51, 52]. After the incubation, silanized coverslips were transferred to 96% ethanol solution and sonicated in a water bath sonicator for 20 min, following by 5–10 rinses with purified water. Silanization was considered successful if the glass was almost dry when emerging from water. Slides and coverslips were dried and stored for up to 2 months.

2.8.6. Assembly of flow chambers and attachment of nanosprings to the coverslip surface

Silanizing both slides and coverslips provides superior control of non-specific adsorption of proteins to glass but presents a challenge when introducing water solutions into a pre-assembled hydrophobic flow chamber. To overcome this, we used the following sequence. Anti-DIG IgG (Roche 11333089001) diluted in MRB80 (80 mM K-PIPES pH 6.9, 1 mM EGTA, 4 mM $MgCl_2$) to a final concentration of 0.2 μM was placed in 0.5–1 μl drops between the strips of double-sided tape (10–15 μl in total) and covered with a piece of silanized coverslip, followed by a 15 min incubation. The chamber was washed with 100 μl MRB80, then with 50 μl 1% Pluronic F-127 in MRB80 and incubated further for 20–60 min (Fig. 2.2A). Finally, 10 μl of nanospring diluted in MRB80 was added. Fig. 2B shows a microscopic field of view after addition of Atto-488 labelled nanosprings diluted 1:10 from a 5 nM stock solution. Alternatively, surface passivation after silanization can be achieved by replacing 1% Pluronic F-127 with 1% Tween-20. Tween-20 passivation was shown to be particularly effective against non-specific adsorption of streptavidin [53].

2.8.7. Experiments with dynein

Taxol-stabilized microtubules were prepared by polymerization of 50 μM tubulin (with 5–10% fluorescent- and DIG-labelled tubulin) in MRB80 supplemented with 1 mM GTP and 25% glycerol for 20 min at 37°C, followed by addition of 25 μM taxol and another 10–20 min incubation. Microtubules were sedimented in a Beckman Airfuge at 14 psi for 3 min and resuspended in MRB80 with 40 μM taxol.

To conjugate nanospring with Qdot and dynein, 4.5 μl nanospring was mixed with 0.5 μl streptavidin-Qdot (final concentration 100 nM) on ice for several hours or overnight. Biotinylated dynein (final concentration 1–20 nM) was mixed with 50 μl MRB80 with 1 mM ATP, 1 mM DTT and 0.5 mg/ml κ-casein (Sigma-Aldrich), spun in a Beckman Airfuge (30 psi, 5 min), and 5 μl of the supernatant was mixed with 5 μl Qdot-nanospring reaction from the previous step.

A flow-chamber prepared with silanized slides and coverslips and passivated with 1% Tween-20 as described above was filled with nanospring-Qdot-dynein reaction supplemented with 0.5 mg/ml κ-casein. After washing with MRB80 with 0.5 mg/ml κ-casein, taxol-stabilized microtubules were added and incubated for 3 min, followed by another wash with MRB80 with 0.5 mg/ml κ-casein. Finally, the chamber was filled with imaging buffer (MRB80 with 1 mg/ml κ-casein, 50 mM KCl, 1 mM ATP, 40 μM taxol, 20 mM glucose, 4 mM DTT, 0.2 mg/ml catalase, 0.4 mg/ml glucose oxidase).

2.8.8. EXPERIMENTS WITH MACF2

GMPCPP seeds were polymerized by incubating 25 μM tubulin (40% DIG-labelled, total volume 8 μl) and 1 mM GMPCPP (Jena Biosciences) for 30 min at 37°C. Polymerized microtubules were sedimented in a Beckman Airfuge (30 psi, 5 min), and the pellet was resuspended on ice in 6 μl MRB80 with addition of 1 mM GMPCPP, followed by a 30 min incubation on ice. The reaction was then transferred to 37°C, and microtubules polymerized for 30 min and sedimented as above. The pellet was resuspended in 50 μl MRB80 with 10% glycerol, and aliquots snap-frozen in liquid nitrogen and stored at -80°C for up to 3 months.

Nanosprings were first attached to Qdots as described above. After an incubation on ice, biotinylated MACF2 C-terminus was added at 1 μM to saturate remaining biotin-binding sites on the Qdots. Flow chambers were assembled from silanized slides and coverslips and passivated with 1% Tween-20 as described above. The nanospring-Qdot-MACF reaction was then supplemented with 0.5 mg/ml κ-casein and added to the chamber, the chamber was transferred to 37°C. Tubulin polymerization mix containing 15 μM tubulin, 1 mg/ml κ-casein, 0.01% methylcellulose, 1 mM GTP, 20 mM glucose, 4 mM DTT, 0.2 mg/ml catalase, 0.4 mg/ml glucose oxidase, 50 mM KCl, 100 nM EB3 and 15 nM MACF was cleared by centrifugation in a Beckman Airfuge (30 psi, 5 min). Cleared tubulin mix was added to GMPCPP-stabilized seeds and incubated for 10 min at 37°C. Finally, polymerized microtubules were added to the pre-warmed chamber, the chamber was sealed and immediately imaged.

2.8.9. EXPERIMENTS WITH NDC80 AND SKA

Nanospring–Ndc80 trimer conjugation was set up by mixing 10 μl Ndc80 buffer NB (50 mM NaHepes pH 7.5 with 250 mM NaCl and 5% glycerol) with 1 μl nanospring, 0.5 mg/ml κ-casein, 1 mM DTT and 100-200 nM Ndc80 trimers, followed by an incubation for 1–3 h on ice. The flow chamber was assembled using silanized slides and coverslips, and passivated with 1% Tween-20 as described above. Tubulin polymerization mix was prepared by mixing 1 mg/ml κ-casein, 0.01% methylcellulose, 1 mM GTP, 20 mM glucose, 4 mM DTT, 0.2 mg/ml catalase, 0.4 mg/ml glucose oxidase and 8–10 μM tubulin (5–10% fluorescently labelled) and clearing it in a Beckman Airfuge (30 psi, 5 min). GMPCPP seeds were then added to this mix and incubated at 37°C to start microtubule polymerization (optionally, with addition of 1-100 nM Ska).

The passivated flow-chamber was washed with 100 μl buffer NB, then with 50 μl buffer NB with 0.5 mg/ml κ-casein and 1 mM DTT. The nanospring–Ndc80 reaction was diluted by adding 3 μl to 7 μl NB with 0.5 mg/ml κ-casein and 1 mM DTT (dilution tuned based on desired nanospring density), and added to the chamber for 3–5 min, followed by a wash with 100 μl MRB80 with 0.5 mg/ml κ-casein and 1 mM DTT. The chamber was then pre-warmed at 37°C, followed by addition of pre-polymerized microtubules and seeds, immediately sealed and imaged at the microscope.

2.8.10. IMAGING AND IMAGE ANALYSIS

Images were acquired using Nikon Ti-E microscope (Nikon, Japan) with the perfect focus system (Nikon) equipped with a Plan Apo 100×1.45 NA TIRF oil-immersion objective (Nikon), iLas2 ring TIRF module (Roper Scientific) and an Evolve 512 EMCCD camera (Roper Scientific). The sample was illuminated with 488 nm (150 mW), 561 nm (100 mW) and 642 nm (110 mW) lasers through a quad-band filter set containing a ZT405/488/561/640rpc dichroic mirror and a ZET405/488/561/640 m emission filter (Chroma). Images were acquired sequentially with MetaMorph 7.8 software (Molecular Devices, San Jose, CA). The final resolution was 0.107 μm/pixel, using an additional 1.5× lens. The objective was heated to 34°C by a custom-made collar coupled with a thermostat, resulting in the flow chamber being heated to 30°C. TIRF penetration depth was fine-tuned separately for each fluorescent channel.

Further analysis was undertaken in Fiji software [54] and using Julia using custom scripts available at https://github.com/volkovdelft/kymo.jl. Kymographs were made through a reslice operation using the kymograph_3channel.ijm macro. Position of the nanospring end was determined by running kymoNS.ipynb in a jupyter notebook and following in-line comments. In brief, the script opens the kymograph and waits for the user to (1) select a portion of the kymograph with only one particle to trace, and (2) select a 'background' region and the initial position of the particle. Then each line of the kymograph is fitted to a gaussian to determine localization of a particle and its brightness.

2.8.11. PREPARATION OF BEADS AND OPTICAL TRAPPING

Glass 1 μm beads were covalently bound to poly-L-lysine grafted with biotinylated poly-ethyleneglycole (PLL-PEG) as described previously [9]. Biotin molecules on the bead surface were then saturated with neutravidin. Optical trapping was performed using a custom instrument described before [5]. To calibrate the nanospring force–extension curve, neutravidin-coated beads were introduced into a flow-chamber with a DIG–nanospring–biotin bound to the surface through anti-DIG-IgG (see above). After a bead was trapped, the piezo stage was moved manually in 100-nm steps to scan the bead displacements around the nanospring attachment point. Successful attachment of a bead to exactly one spring produced a bell-shaped displacement profile, like the one shown in Fig. 2.2D. Beads producing other types of profiles (interpreted as attachment to the coverslip, or to more than one spring) were discarded from further analysis.

For experiments with dynein, biotinylated dynein motor domains were bound to streptavidin-coated PLL-PEG beads. We tuned surface density of dynein such that 30% or fewer beads interacted with a microtubule, ensuring predominantly single-motor events. Experiments were performed in a buffer that contained MRB80 with 1 mg/ml κ-casein, 50 mM KCl, 1 mM ATP, 40 μM taxol, 20 mM glucose, 4 mM DTT, 0.2 mg/ml catalase and 0.4 mg/ml glucose oxidase. The position of the bead was recorded with a quadrant photo detector at 10 kHz, and simultaneously using differential interference microscopy to monitor bead-microtubule interaction. Experiments with MACF-coated beads were performed as described previously [23].

2.9. ACKNOWLEDGEMENTS

We are grateful to Jean-Philippe Sobczak (Tilibit Nanosystems) for discussions and assistance with design of the modified nanosprings, to Ruben Kazner and Isabelle Stender (MPI Dortmund) for assistance preparing Ndc80 multimers, and to Nemo Andrea (TU Delft) for help with negative stain EM. We also thank Marian Baclayon and Esengül Yildirim (TU Delft) for dynein purification, and Andrea Musacchio and members of the Dogterom lab for discussions.

2.10. FOOTNOTES

2.10.1. AUTHOR CONTRIBUTIONS

Conceptualization: V.A.V., A.N.M., P.J.H.; Methodology: V.A.V., P.J.H. ; Software: V.A.V.; Validation: A.N.M., V.A.V.; Formal analysis: V.A.V.; Investigation: A.N.M., P.J.H., V.A.V.; Resources: A.N.M., P.J.H., A.A., M.D., V.A.V.; Data curation: A.N.M., P.J.H., V.A.V.; Writing – original draft: A.N.M., V.A.V.; Writing – editing & review: A.N.M., P.J.H., A.A., M.D., V.A.V.; Visualization: A.N.M., P.J.H., V.A.V.; Supervision: V.A.V.; Project administration: V.A.V.; Funding acquisition: A.A., M.D.

2.10.2. FUNDING

This work was supported by a European Molecular Biology Organization (EMBO) short-term fellowship (grant 7203) to P.J.H., a European Research Council Synergy Grant MODELCELL (grant 609822) to M.D. and A.A., and by a Queen Mary University of London (QMUL) startup grant SBC8VOL2 to V.A.V.

2.10.3. DATA AVAILABILITY

Image analysis code is available from GitHub: https://github.com/volkovdelft/kymo.jl. Imaging data are available from Zenodo: https://doi.org/10.5281/zenodo.6977065.

SUPPLEMENTARY FIGURES

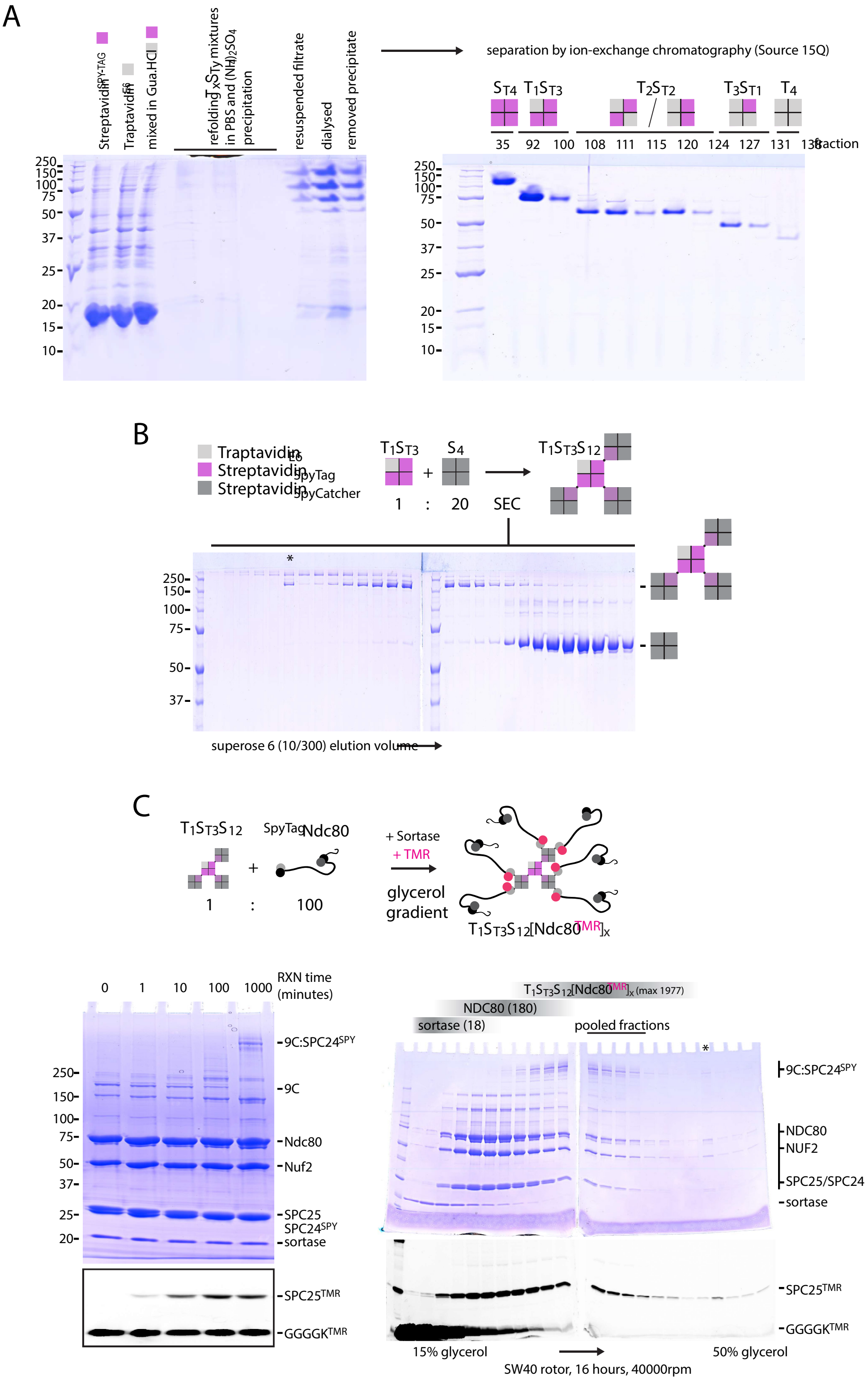

Figure 2S.1: *(A) Monomeric Traptavidin and Streptavidin-SpyTag were mixed, refolded into tetramers in PBS, and separated using ion-exchange chromatography as described (Fairhead et al., 2014). Streptavidin remains a tetramer during SDS-PAGE since samples were not heated before analysis. (B) T1ST3SC12 scaffolds were generated from T1ST3 and SC4 tetramers and purified by size-exclusion chromatography (Superose 6 10/300). Fractions containing T1ST3SC12 were pooled and stored for further use. SC subunits are shown in grey when the SpyCatcher module is free to react and in light purple when covalently bound to ST subunits. The asterisk indicates material from a later eluting fraction that was loaded by mistake. (C) A large molar excess of Ndc80 was incubated with the T1ST3SC12 scaffolds for assembly, and simultaneously fluorescently labeled. Streptavidin and Streptavidin-SPC24 assemblies remain multimeric during SDS-PAGE since samples were not heated before analysis. SDS-PAGE analysis of the reaction mixture separated on a glycerol density gradient. Peptide, sortase, monomeric Ndc80, and multimeric Ndc80 are separated into different zones of the gradient. Selected fractions containing T1ST3SC12-(Ndc80)x modules are indicated. Streptavidin and Streptavidin-SPC24 assemblies remain multimeric during SDS-PAGE since samples were not heated before analysis. In-gel fluorescence analysis and Coomassie staining of the same gels.*

REFERENCES

[1] N. B. Gudimchuk and J. R. McIntosh. "Regulation of microtubule dynamics, mechanics and function through the growing tip". In: *Nature Reviews Molecular Cell Biology* 22.12 (Dec. 2021). Publisher: Nature Publishing Group, pp. 777–795. ISSN: 1471-0080. DOI: `10.1038/s41580-021-00399-x`. URL: `https://www.nature.com/articles/s41580-021-00399-x` (visited on 01/27/2025).

[2] A. Musacchio and A. Desai. "A Molecular View of Kinetochore Assembly and Function". In: *Biology* 6.1 (Mar. 2017). Number: 1 Publisher: Multidisciplinary Digital Publishing Institute, p. 5. ISSN: 2079-7737. DOI: `10.3390/biology6010005`. URL: `https://www.mdpi.com/2079-7737/6/1/5` (visited on 01/31/2025).

[3] M. R. Audett and T. J. Maresca. "The whole is greater than the sum of its parts: at the intersection of order, disorder, and kinetochore function". In: *Essays in Biochemistry* 64.2 (Aug. 5, 2020), pp. 349–358. ISSN: 0071-1365. DOI: `10.1042/EBC20190069`. URL: `https://doi.org/10.1042/EBC20190069` (visited on 02/17/2025).

[4] M. P. Nicholas, L. Rao, and A. Gennerich. "An Improved Optical Tweezers Assay for Measuring the Force Generation of Single Kinesin Molecules". In: *Mitosis: Methods and Protocols*. Ed. by D. J. Sharp. New York, NY: Springer, 2014, pp. 171–246. ISBN: 978-1-4939-0329-0. DOI: `10.1007/978-1-4939-0329-0_10`. URL: `https://doi.org/10.1007/978-1-4939-0329-0_10` (visited on 02/17/2025).

[5] M. Baclayon, S.-M. Kalisch, E. Hendel, L. Laan, J. Husson, E. L. Munteanu, and M. Dogterom. "Optical Tweezers-Based Measurements of Forces and Dynamics at Microtubule Ends". In: *Optical Tweezers: Methods and Protocols*. Ed. by A. Gennerich. New York, NY: Springer, 2017, pp. 411–435. ISBN: 978-1-4939-6421-5. DOI: `10.1007/978-1-4939-6421-5_16`. URL: `https://doi.org/10.1007/978-1-4939-6421-5_16` (visited on 02/17/2025).

[6] E. L. Grishchuk, M. I. Molodtsov, F. I. Ataullakhanov, and J. R. McIntosh. "Force production by disassembling microtubules". In: *Nature* 438.7066 (Nov. 2005). Publisher: Nature Publishing Group, pp. 384–388. ISSN: 1476-4687. DOI: `10.1038/nature04132`. URL: `https://www.nature.com/articles/nature04132` (visited on 02/04/2025).

[7] B. Akiyoshi, K. K. Sarangapani, A. F. Powers, C. R. Nelson, S. L. Reichow, H. Arellano-Santoyo, T. Gonen, J. A. Ranish, C. L. Asbury, and S. Biggins. "Tension directly stabilizes reconstituted kinetochore-microtubule attachments". In: *Nature* 468.7323 (Nov. 2010). Publisher: Nature Publishing Group, pp. 576–579. ISSN: 1476-4687. DOI: `10.1038/nature09594`. URL: `https://www.nature.com/articles/nature09594` (visited on 02/17/2025).

[8] M. P. Miller, C. L. Asbury, and S. Biggins. "A TOG Protein Confers Tension Sensitivity to Kinetochore-Microtubule Attachments". In: *Cell* 165.6 (June 2, 2016), pp. 1428–1439. ISSN: 0092-8674. DOI: `10.1016/j.cell.2016.04.030`. URL: `https://www.sciencedirect.com/science/article/pii/S009286741630424X` (visited on 02/17/2025).

[9] V. A. Volkov, P. J. Huis in 't Veld, M. Dogterom, and A. Musacchio. "Multivalency of NDC80 in the outer kinetochore is essential to track shortening microtubules and generate forces". In: *eLife* 7 (Apr. 9, 2018). Ed. by J. K. Tyler. Publisher: eLife Sciences Publications, Ltd, e36764. ISSN: 2050-084X. DOI: `10.7554/eLife.36764`. URL: `https://doi.org/10.7554/eLife.36764` (visited on 10/10/2024).

[10] P. J. Huis in 't Veld, V. A. Volkov, I. D. Stender, A. Musacchio, and M. Dogterom. "Molecular determinants of the Ska-Ndc80 interaction and their influence on microtubule tracking and force-coupling". In: *eLife* 8 (Dec. 5, 2019). Ed. by A. D. McAinsh and V. Malhotra. Publisher: eLife Sciences Publications, Ltd, e49539. ISSN: 2050-084X. DOI: `10.7554/eLife.49539`. URL: `https://doi.org/10.7554/eLife.49539` (visited on 10/09/2024).

[11] V. A. Volkov, A. V. Zaytsev, N. Gudimchuk, P. M. Grissom, A. L. Gintsburg, F. I. Ataullakhanov, J. R. McIntosh, and E. L. Grishchuk. "Long tethers provide high-force coupling of the Dam1 ring to shortening microtubules". In: *Proceedings of the National Academy of Sciences* 110.19 (May 7, 2013). Publisher: Proceedings of the National Academy of Sciences, pp. 7708–7713. DOI: `10.1073/pnas.1305821110`. URL: `https://www.pnas.org/doi/full/10.1073/pnas.1305821110` (visited on 02/17/2025).

[12] S. Pyrpassopoulos, H. Shuman, and E. M. Ostap. "Modulation of Kinesin's Load-Bearing Capacity by Force Geometry and the Microtubule Track". In: *Biophysical Journal* 118.1 (Jan. 7, 2020), pp. 243–253. ISSN: 0006-3495. DOI: `10.1016/j.bpj.2019.10.045`. URL: `https://www.sciencedirect.com/science/article/pii/S0006349519343553` (visited on 02/17/2025).

[13] M. J. Lang, P. M. Fordyce, A. M. Engh, K. C. Neuman, and S. M. Block. "Simultaneous, coincident optical trapping and single-molecule fluorescence". In: *Nature Methods* 1.2 (Nov. 2004). Publisher: Nature Publishing Group, pp. 133–139. ISSN: 1548-7105. DOI: `10.1038/nmeth714`. URL: `https://www.nature.com/articles/nmeth714` (visited on 02/17/2025).

[14] W. M. Lee, P. J. Reece, R. F. Marchington, N. K. Metzger, and K. Dholakia. “Construction and calibration of an optical trap on a fluorescence optical microscope”. In: *Nature Protocols* 2.12 (Dec. 2007). Publisher: Nature Publishing Group, pp. 3226–3238. ISSN: 1750-2799. DOI: 10.1038/nprot.2007.446. URL: https://www.nature.com/articles/nprot.2007.446 (visited on 02/17/2025).

[15] Y. Deng and C. L. Asbury. “Simultaneous Manipulation and Super-Resolution Fluorescence Imaging of Individual Kinetochores Coupled to Microtubule Tips”. In: *Optical Tweezers: Methods and Protocols*. Ed. by A. Gennerich. New York, NY: Springer, 2017, pp. 437–467. ISBN: 978-1-4939-6421-5. DOI: 10.1007/978-1-4939-6421-5_17. URL: https://doi.org/10.1007/978-1-4939-6421-5_17 (visited on 02/17/2025).

[16] M. Iwaki, S. F. Wickham, K. Ikezaki, T. Yanagida, and W. M. Shih. “A programmable DNA origami nanospring that reveals force-induced adjacent binding of myosin VI heads”. In: *Nature Communications* 7.1 (Dec. 12, 2016). Publisher: Nature Publishing Group, p. 13715. ISSN: 2041-1723. DOI: 10.1038/ncomms13715. URL: https://www.nature.com/articles/ncomms13715 (visited on 10/09/2024).

[17] S. M. Douglas, A. H. Marblestone, S. Teerapittayanon, A. Vazquez, G. M. Church, and W. M. Shih. “Rapid prototyping of 3D DNA-origami shapes with caDNAno”. In: *Nucleic Acids Research* 37.15 (Aug. 1, 2009), pp. 5001–5006. ISSN: 0305-1048. DOI: 10.1093/nar/gkp436. URL: https://doi.org/10.1093/nar/gkp436 (visited on 02/17/2025).

[18] S. L. Reck-Peterson, A. Yildiz, A. P. Carter, A. Gennerich, N. Zhang, and R. D. Vale. “Single-Molecule Analysis of Dynein Processivity and Stepping Behavior”. In: *Cell* 126.2 (July 28, 2006), pp. 335–348. ISSN: 0092-8674. DOI: 10.1016/j.cell.2006.05.046. URL: https://www.sciencedirect.com/science/article/pii/S0092867406008622 (visited on 02/17/2025).

[19] M. Tokunaga, N. Imamoto, and K. Sakata-Sogawa. “Highly inclined thin illumination enables clear single-molecule imaging in cells”. In: *Nature Methods* 5.2 (Feb. 2008). Publisher: Nature Publishing Group, pp. 159–161. ISSN: 1548-7105. DOI: 10.1038/nmeth1171. URL: https://www.nature.com/articles/nmeth1171 (visited on 02/17/2025).

[20] A. Gennerich, A. P. Carter, S. L. Reck-Peterson, and R. D. Vale. “Force-Induced Bidirectional Stepping of Cytoplasmic Dynein”. In: *Cell* 131.5 (Nov. 30, 2007), pp. 952–965. ISSN: 0092-8674. DOI: 10.1016/j.cell.2007.10.016. URL: https://www.sciencedirect.com/science/article/pii/S0092867407012871 (visited on 02/17/2025).

[21] L. Laan, N. Pavin, J. Husson, G. Romet-Lemonne, M. van Duijn, M. P. López, R. D. Vale, F. Jülicher, S. L. Reck-Peterson, and M. Dogterom. “Cortical Dynein Controls Microtubule Dynamics to Generate Pulling Forces that Position Microtubule Asters”. In: *Cell* 148.3 (Feb. 2012), pp. 502–514. ISSN: 00928674. DOI: 10.1016/j.cell.2012.01.007. URL:

https://linkinghub.elsevier.com/retrieve/pii/S009286741200013X (visited on 08/01/2025).

[22] S. Honnappa, S. M. Gouveia, A. Weisbrich, F. F. Damberger, N. S. Bhavesh, H. Jawhari, I. Grigoriev, F. J. A. van Rijssel, R. M. Buey, A. Lawera, I. Jelesarov, F. K. Winkler, K. Wüthrich, A. Akhmanova, and M. O. Steinmetz. “An EB1-Binding Motif Acts as a Microtubule Tip Localization Signal”. In: *Cell* 138.2 (July 23, 2009), pp. 366–376. ISSN: 0092-8674. DOI: 10.1016/j.cell.2009.04.065. URL: https://www.sciencedirect.com/science/article/pii/S0092867409006382 (visited on 02/17/2025).

[23] R. Rodríguez-García, V. A. Volkov, C.-Y. Chen, E. A. Katrukha, N. Olieric, A. Aher, I. Grigoriev, M. P. López, M. O. Steinmetz, L. C. Kapitein, G. Koenderink, M. Dogterom, and A. Akhmanova. “Mechanisms of Motor-Independent Membrane Remodeling Driven by Dynamic Microtubules”. In: *Current Biology* 30.6 (Mar. 23, 2020), 972–987.e12. ISSN: 0960-9822. DOI: 10.1016/j.cub.2020.01.036. URL: https://www.sciencedirect.com/science/article/pii/S0960982220300361 (visited on 02/17/2025).

[24] C. Alkemade, H. Wierenga, V. A. Volkov, M. Preciado López, A. Akhmanova, P. R. ten Wolde, M. Dogterom, and G. H. Koenderink. “Cross-linkers at growing microtubule ends generate forces that drive actin transport”. In: *Proceedings of the National Academy of Sciences* 119.11 (Mar. 15, 2022). Publisher: Proceedings of the National Academy of Sciences, e2112799119. DOI: 10.1073/pnas.2112799119. URL: https://www.pnas.org/doi/full/10.1073/pnas.2112799119 (visited on 02/17/2025).

[25] M. I. Molodtsov, C. Mieck, J. Dobbelaere, A. Dammermann, S. Westermann, and A. Vaziri. “A Force-Induced Directional Switch of a Molecular Motor Enables Parallel Microtubule Bundle Formation”. In: *Cell* 167.2 (Oct. 6, 2016), 539–552.e14. ISSN: 0092-8674. DOI: 10.1016/j.cell.2016.09.029. URL: https://www.sciencedirect.com/science/article/pii/S0092867416313113 (visited on 02/17/2025).

[26] V. A. Volkov. “Microtubules pull the strings: disordered sequences as efficient couplers of microtubule-generated force”. In: *Essays in Biochemistry* 64.2 (June 5, 2020), pp. 371–382. ISSN: 0071-1365. DOI: 10.1042/EBC20190078. URL: https://doi.org/10.1042/EBC20190078 (visited on 02/17/2025).

[27] C. E. Chivers, E. Crozat, C. Chu, V. T. Moy, D. J. Sherratt, and M. Howarth. “A streptavidin variant with slower biotin dissociation and increased mechanostability”. In: *Nature Methods* 7.5 (May 2010). Publisher: Nature Publishing Group, pp. 391–393. ISSN: 1548-7105. DOI: 10.1038/nmeth.1450. URL: https://www.nature.com/articles/nmeth.1450 (visited on 02/17/2025).

[28] M. Fairhead, G. Veggiani, M. Lever, J. Yan, D. Mesner, C. V. Robinson, O. Dushek, P. A. van der Merwe, and M. Howarth. “SpyAvidin Hubs Enable Precise and Ultrastable Orthogonal Nanoassembly”. In: *Journal of the American Chemical Society* 136.35 (Sept. 3, 2014). Publisher: American Chemical Society, pp. 12355–12363. ISSN: 0002-7863. DOI: `10.1021/ja505584f`. URL: `https://doi.org/10.1021/ja505584f` (visited on 10/21/2024).

[29] X. Li and R. B. Nicklas. “Mitotic forces control a cell-cycle checkpoint”. In: *Nature* 373.6515 (Feb. 1995). Publisher: Nature Publishing Group, pp. 630–632. ISSN: 1476-4687. DOI: `10.1038/373630a0`. URL: `https://www.nature.com/articles/373630a0` (visited on 02/17/2025).

[30] R. B. Nicklas. “Measurements of the force produced by the mitotic spindle in anaphase.” In: *Journal of Cell Biology* 97.2 (Aug. 1, 1983), pp. 542–548. ISSN: 0021-9525. DOI: `10.1083/jcb.97.2.542`. URL: `https://doi.org/10.1083/jcb.97.2.542` (visited on 02/17/2025).

[31] A. F. Long, P. Suresh, and S. Dumont. “Individual kinetochore-fibers locally dissipate force to maintain robust mammalian spindle structure”. In: *Journal of Cell Biology* 219.8 (May 20, 2020), e201911090. ISSN: 0021-9525. DOI: `10.1083/jcb.201911090`. URL: `https://doi.org/10.1083/jcb.201911090` (visited on 02/17/2025).

[32] P. Suresh, A. F. Long, and S. Dumont. “Microneedle manipulation of the mammalian spindle reveals specialized, short-lived reinforcement near chromosomes”. In: *eLife* 9 (Mar. 19, 2020). Ed. by A. Akhmanova, T. Surrey, S. Redemann, and Y. Shimamoto. Publisher: eLife Sciences Publications, Ltd, e53807. ISSN: 2050-084X. DOI: `10.7554/eLife.53807`. URL: `https://doi.org/10.7554/eLife.53807` (visited on 02/17/2025).

[33] L. A. Harasymiw, D. Tank, M. McClellan, N. Panigrahy, and M. K. Gardner. “Centromere mechanical maturation during mammalian cell mitosis”. In: *Nature Communications* 10.1 (Apr. 15, 2019). Publisher: Nature Publishing Group, p. 1761. ISSN: 2041-1723. DOI: `10.1038/s41467-019-09578-z`. URL: `https://www.nature.com/articles/s41467-019-09578-z` (visited on 02/17/2025).

[34] S. Mukherjee, B. J. Sandri, D. Tank, M. McClellan, L. A. Harasymiw, Q. Yang, L. L. Parker, and M. K. Gardner. “A Gradient in Metaphase Tension Leads to a Scaled Cellular Response in Mitosis”. In: *Developmental Cell* 49.1 (Apr. 8, 2019), 63–76.e10. ISSN: 1534-5807. DOI: `10.1016/j.devcel.2019.01.018`. URL: `https://www.sciencedirect.com/science/article/pii/S1534580719300462` (visited on 02/17/2025).

[35] A.-L. Cost, P. Ringer, A. Chrostek-Grashoff, and C. Grashoff. “How to Measure Molecular Forces in Cells: A Guide to Evaluating Genetically-Encoded FRET-Based Tension Sensors”. In: *Cellular and Molecular Bioengineering* 8.1 (Mar. 1, 2015), pp. 96–105. ISSN: 1865-5033. DOI: `10.1007/s12195-014-0368-1`. URL: `https://doi.org/10.1007/s12195-014-0368-1` (visited on 02/17/2025).

[36] C. Grashoff, B. D. Hoffman, M. D. Brenner, R. Zhou, M. Parsons, M. T. Yang, M. A. McLean, S. G. Sligar, C. S. Chen, T. Ha, and M. A. Schwartz. “Measuring mechanical tension across vinculin reveals regulation of focal adhesion dynamics”. In: *Nature* 466.7303 (July 2010). Publisher: Nature Publishing Group, pp. 263–266. ISSN: 1476-4687. DOI: `10.1038/nature09198`. URL: `https://www.nature.com/articles/nature09198` (visited on 02/17/2025).

[37] J. Kuhn and S. Dumont. “Mammalian kinetochores count attached microtubules in a sensitive and switch-like manner”. In: *Journal of Cell Biology* 218.11 (Sept. 6, 2019), pp. 3583–3596. ISSN: 0021-9525. DOI: `10.1083/jcb.201902105`. URL: `https://doi.org/10.1083/jcb.201902105` (visited on 02/17/2025).

[38] D. Liu, G. Vader, M. J. M. Vromans, M. A. Lampson, and S. M. A. Lens. “Sensing Chromosome Bi-Orientation by Spatial Separation of Aurora B Kinase from Kinetochore Substrates”. In: *Science* 323.5919 (Mar. 6, 2009). Publisher: American Association for the Advancement of Science, pp. 1350–1353. DOI: `10.1126/science.1167000`. URL: `https://www.science.org/doi/10.1126/science.1167000` (visited on 02/17/2025).

[39] A. Suzuki, B. L. Badger, J. Haase, T. Ohashi, H. P. Erickson, E. D. Salmon, and K. Bloom. “How the kinetochore couples microtubule force and centromere stretch to move chromosomes”. In: *Nature Cell Biology* 18.4 (Apr. 2016). Publisher: Nature Publishing Group, pp. 382–392. ISSN: 1476-4679. DOI: `10.1038/ncb3323`. URL: `https://www.nature.com/articles/ncb3323` (visited on 01/22/2025).

[40] A. A. Ye, S. Cane, and T. J. Maresca. “Chromosome biorientation produces hundreds of piconewtons at a metazoan kinetochore”. In: *Nature Communications* 7.1 (Oct. 20, 2016). Publisher: Nature Publishing Group, p. 13221. ISSN: 2041-1723. DOI: `10.1038/ncomms13221`. URL: `https://www.nature.com/articles/ncomms13221` (visited on 02/17/2025).

[41] T. Y. Yoo, J.-M. Choi, W. Conway, C.-H. Yu, R. V. Pappu, and D. J. Needleman. “Measuring NDC80 binding reveals the molecular basis of tension-dependent kinetochore-microtubule attachments”. In: *eLife* 7 (July 25, 2018). Ed. by T. N. Davis and A. Akhmanova. Publisher: eLife Sciences Publications, Ltd, e36392. ISSN: 2050-084X. DOI: `10.7554/eLife.36392`. URL: `https://doi.org/10.7554/eLife.36392` (visited on 02/17/2025).

[42] M. C. Engel, D. M. Smith, M. A. Jobst, M. Sajfutdinow, T. Liedl, F. Romano, L. Rovigatti, A. A. Louis, and J. P. K. Doye. “Force-Induced Unravelling of DNA Origami”. In: *ACS Nano* 12.7 (July 24, 2018). Publisher: American Chemical Society, pp. 6734–6747. ISSN: 1936-0851. DOI: `10.1021/acsnano.8b01844`. URL: `https://doi.org/10.1021/acsnano.8b01844` (visited on 02/17/2025).

[43] G. Neuert, C. Albrecht, E. Pamir, and H. Gaub. “Dynamic force spectroscopy of the digoxigenin–antibody complex”. In: *FEBS Letters* 580.2 (2006). _eprint: https://onlinelibrary.wiley.com/doi/pdf/10.1016/j.febslet.2005.12.052, pp. 505–509. ISSN: 1873-3468. DOI: `10.1016/j.febslet.2005.12.052`. URL: `https:`

//onlinelibrary.wiley.com/doi/abs/10.1016/j.febslet.2005.12.052 (visited on 02/17/2025).

[44] C. E. Tinberg, S. D. Khare, J. Dou, L. Doyle, J. W. Nelson, A. Schena, W. Jankowski, C. G. Kalodimos, K. Johnsson, B. L. Stoddard, and D. Baker. “Computational design of ligand-binding proteins with high affinity and selectivity”. In: *Nature* 501.7466 (Sept. 2013). Publisher: Nature Publishing Group, pp. 212–216. ISSN: 1476-4687. DOI: 10.1038/nature12443. URL: https://www.nature.com/articles/nature12443 (visited on 02/17/2025).

[45] W. J. Van Patten, R. Walder, A. Adhikari, S. R. Okoniewski, R. Ravichandran, C. E. Tinberg, D. Baker, and T. T. Perkins. “Improved Free-Energy Landscape Quantification Illustrated with a Computationally Designed Protein–Ligand Interaction”. In: *ChemPhysChem* 19.1 (2018). _eprint: https://onlinelibrary.wiley.com/doi/pdf/10.1002/cphc.201701147, pp. 19–23. ISSN: 1439-7641. DOI: 10.1002/cphc.201701147. URL: https://onlinelibrary.wiley.com/doi/abs/10.1002/cphc.201701147 (visited on 02/17/2025).

[46] S. Ramakrishnan, L. Schärfen, K. Hunold, S. Fricke, G. Grundmeier, M. Schlierf, A. Keller, and G. Krainer. “Enhancing the stability of DNA origami nanostructures: staple strand redesign versus enzymatic ligation”. In: *Nanoscale* 11.35 (Sept. 12, 2019). Publisher: The Royal Society of Chemistry, pp. 16270–16276. ISSN: 2040-3372. DOI: 10.1039/C9NR04460D. URL: https://pubs.rsc.org/en/content/articlelanding/2019/nr/c9nr04460d (visited on 02/17/2025).

[47] A. Rajendran, M. Endo, Y. Katsuda, K. Hidaka, and H. Sugiyama. “Photo-Cross-Linking-Assisted Thermal Stability of DNA Origami Structures and Its Application for Higher-Temperature Self-Assembly”. In: *Journal of the American Chemical Society* 133.37 (Sept. 21, 2011). Publisher: American Chemical Society, pp. 14488–14491. ISSN: 0002-7863. DOI: 10.1021/ja204546h. URL: https://doi.org/10.1021/ja204546h (visited on 02/17/2025).

[48] G. Thomas, K. Massimo, K. Benjamin, and D. Hendrik. “Sequence-programmable covalent bonding of designed DNA assemblies”. In: *Sci. Adv* 4 (2022), eaau1157.

[49] H. Hirakawa, S. Ishikawa, and T. Nagamune. “Ca2+-independent sortase-A exhibits high selective protein ligation activity in the cytoplasm of Escherichia coli”. In: *Biotechnology Journal* 10.9 (2015). _eprint: https://onlinelibrary.wiley.com/doi/pdf/10.1002/biot.201500012, pp. 1487–1492. ISSN: 1860-7314. DOI: 10.1002/biot.201500012. URL: https://onlinelibrary.wiley.com/doi/abs/10.1002/biot.201500012 (visited on 02/17/2025).

[50] P. J. Huis in ’t Veld, S. Jeganathan, A. Petrovic, P. Singh, J. John, V. Krenn, F. Weissmann, T. Bange, and A. Musacchio. “Molecular basis of outer kinetochore assembly on CENP-T”. In: *eLife* 5 (Dec. 24, 2016). Ed. by J. Pines. Publisher: eLife Sciences Publications, Ltd, e21007. ISSN: 2050-084X. DOI:

10.7554/eLife.21007. URL: https://doi.org/10.7554/eLife.21007 (visited on 02/17/2025).

[51] C. Gell, V. Bormuth, G. J. Brouhard, D. N. Cohen, S. Diez, C. T. Friel, J. Helenius, B. Nitzsche, H. Petzold, J. Ribbe, E. Schäffer, J. H. Stear, A. Trushko, V. Varga, P. O. Widlund, M. Zanic, and J. Howard. "Microtubule Dynamics Reconstituted *In Vitro* and Imaged by Single-Molecule Fluorescence Microscopy". In: *Methods in Cell Biology*. Ed. by L. Wilson and J. J. Correia. Vol. 95. Microtubules, in vitro. Academic Press, Jan. 1, 2010, pp. 221–245. DOI: 10.1016/S0091-679X(10)95013-9. URL: https://www.sciencedirect.com/science/article/pii/S0091679X10950139 (visited on 02/17/2025).

[52] V. A. Volkov, A. V. Zaytsev, and E. L. Grishchuk. "Preparation of Segmented Microtubules to Study Motions Driven by the Disassembling Microtubule Ends". In: *Journal of Visualized Experiments : JoVE* 85 (Mar. 15, 2014), p. 51150. ISSN: 1940-087X. DOI: 10.3791/51150. URL: https://www.ncbi.nlm.nih.gov/pmc/articles/PMC4100436/ (visited on 02/17/2025).

[53] B. Hua, K. Y. Han, R. Zhou, H. Kim, X. Shi, S. C. Abeysirigunawardena, A. Jain, D. Singh, V. Aggarwal, S. A. Woodson, and T. Ha. "An improved surface passivation method for single-molecule studies". In: *Nature Methods* 11.12 (Dec. 2014). Publisher: Nature Publishing Group, pp. 1233–1236. ISSN: 1548-7105. DOI: 10.1038/nmeth.3143. URL: https://www.nature.com/articles/nmeth.3143 (visited on 02/17/2025).

[54] J. Schindelin, I. Arganda-Carreras, E. Frise, V. Kaynig, M. Longair, T. Pietzsch, S. Preibisch, C. Rueden, S. Saalfeld, B. Schmid, J.-Y. Tinevez, D. J. White, V. Hartenstein, K. Eliceiri, P. Tomancak, and A. Cardona. "Fiji: an open-source platform for biological-image analysis". In: *Nature Methods* 9.7 (July 2012). Publisher: Nature Publishing Group, pp. 676–682. ISSN: 1548-7105. DOI: 10.1038/nmeth.2019. URL: https://www.nature.com/articles/nmeth.2019 (visited on 02/17/2025).

3

REGULATION OF STABILITY AND FORCE COUPLING AT THE MICROTUBULE-KINETOCHORE INTERFACE VIA NDC80 COPY NUMBER

Ali NICK MALEKI, Eli VAN DER SLUIS, Marileen DOGTEROM

If you torture the data long enough, it will confess to anything.

Ronald Coase

The behavior of the aggregate is complex, but the rules for the individual agents can be simple

John Holland

Accurate chromosome segregation in eukaryotes relies on stable kinetochore-microtubule (KT-MT) attachments mediated by the Ndc80 complex, which couples microtubule dynamics to chromosome movement. While single Ndc80 complexes lack persistent end-tracking ability, oligomerization enables robust force coupling and microtubule tip tracking, with physiological kinetochores hosting 15–25 Ndc80 complexes per microtubule. Here, we investigate the role of Ndc80 copy number in regulating microtubule dynamics and force transmission using a truncated, bacterially expressible variant, Ndc80jubaea (jubaea), integrated into DNA origami *nanospring (NS) constructs with precisely controlled valency (3–20 copies). We demonstrate that jubaea oligomers recapitulate key functional properties of native Ndc80, including microtubule end-tracking and force-coupling. Increasing jubaea copy number enhances microtubule interaction frequency, promotes rescue and stall events, and progressively suppresses microtubule depolymerization rates, with NS20-jubaea (containing up to 20 copies) reducing shrinkage by up to 70%. Force measurements reveal that jubaea oligomers capture forces with averages up to 2 pN and maximum forces up to 10 pN, with NS10-jubaea exhibiting the largest forces, suggesting an optimal stoichiometry for mechanical efficiency. Furthermore, freely diffusing jubaea-NS complexes show reduced mobility with higher copy numbers. The presence of soluble jubaea enables capaturing higher forces, implicating presence of jubaea-jubaea interactions in complex stabilization. Together, our findings reveal that jubaea copy number affects both the mechanical output and regulatory influence of KT-MT attachments, supporting that cells may need to tune Ndc80 occupancy to balance attachment stability and force transmission during mitosis.*

3.1. INTRODUCTION

Accurate chromosome segregation in eukaryotes necessitates the establishment of amphitelic attachment, wherein sister chromatids form stable connections to microtubules emanating from opposing spindle poles, a configuration termed biorientation [1, 2] . This process is regulated by the spindle assembly checkpoint (SAC), a sophisticated surveillance mechanism that delays anaphase onset until proper kinetochore-microtubule attachment is established [3, 4]. Upon establishment of stable kinetochore-microtubule interfaces, chromosome segregation proceeds through force generation coupled to microtubule depolymerization dynamics [5].

The Ndc80 complex represents a critical constituent of the outer kinetochore in humans, demonstrating both microtubule-binding capacity and force-coupling functionality during chromosome segregation [6, 7] (Fig. 3.1). This heterotetrameric complex comprises four distinct subunits: Hec1 (NDC80), Nuf2, Spc24, and Spc25, with the latter pair mediating kinetochore integration while the former pair exhibits microtubule-binding domains (Fig. 3.1B) [8, 9]. Notably, the Hec1 subunit possesses an additional 80-residue unstructured N-terminal tail that enhances the Ndc80-microtubule interface in vitro [9] and plays an essential role for end-tracking of microtubules [10]. It is proposed that when Ndc80 is bound to MT, the phosphorylation-competent regions within this tail undergo ordering at its interface regions with tubulin and adjacent Ndc80 complex Hec1 subunits [11]. Furthermore, a discrete sequence within the Hec1 subunit (residues 396-470), designated as the Ndc80 loop, facilitates inter-complex interactions in the microtubule-bound state, with even single-residue substitutions in this region compromising kinetochore-microtubule attachment stability [12].

Single-molecule analyzes have demonstrated that individual Ndc80 complexes lack the capacity for persistent microtubule end-tracking [13, 14]. However, oligomeric assemblies acquire both end-tracking capability and force-coupling ability during microtubule depolymerization [15]. This observation aligns with physiological stoichiometry, wherein approximately 15-25 Ndc80 complexes engage each microtubule at the kinetochore (Fig. 3.1A) [16, 17]. In vitro reconstitution studies utilizing streptavidin-mediated oligomerization revealed that minimal assemblies containing two Ndc80 complexes already exhibit limited end-tracking behavior, with tracking efficiency positively correlating with increasing Ndc80 complex number. Notably, tetrameric assemblies demonstrated robust end-tracking capability, with approximately 90% of oligomers maintaining persistent microtubule tip association [18].

Quantitative force measurements utilizing optical trapping methodology demonstrated that these end-tracking oligomeric assemblies can cause force-dependent microtubule stall and rescue events when brought together at sufficiently high numbers on micron-sized beads., In these experiments average stall forces up to about 4 pN were measured for densely coated beads, whereas average forces of about 1 pN were measured for sparsely coated beads [18].

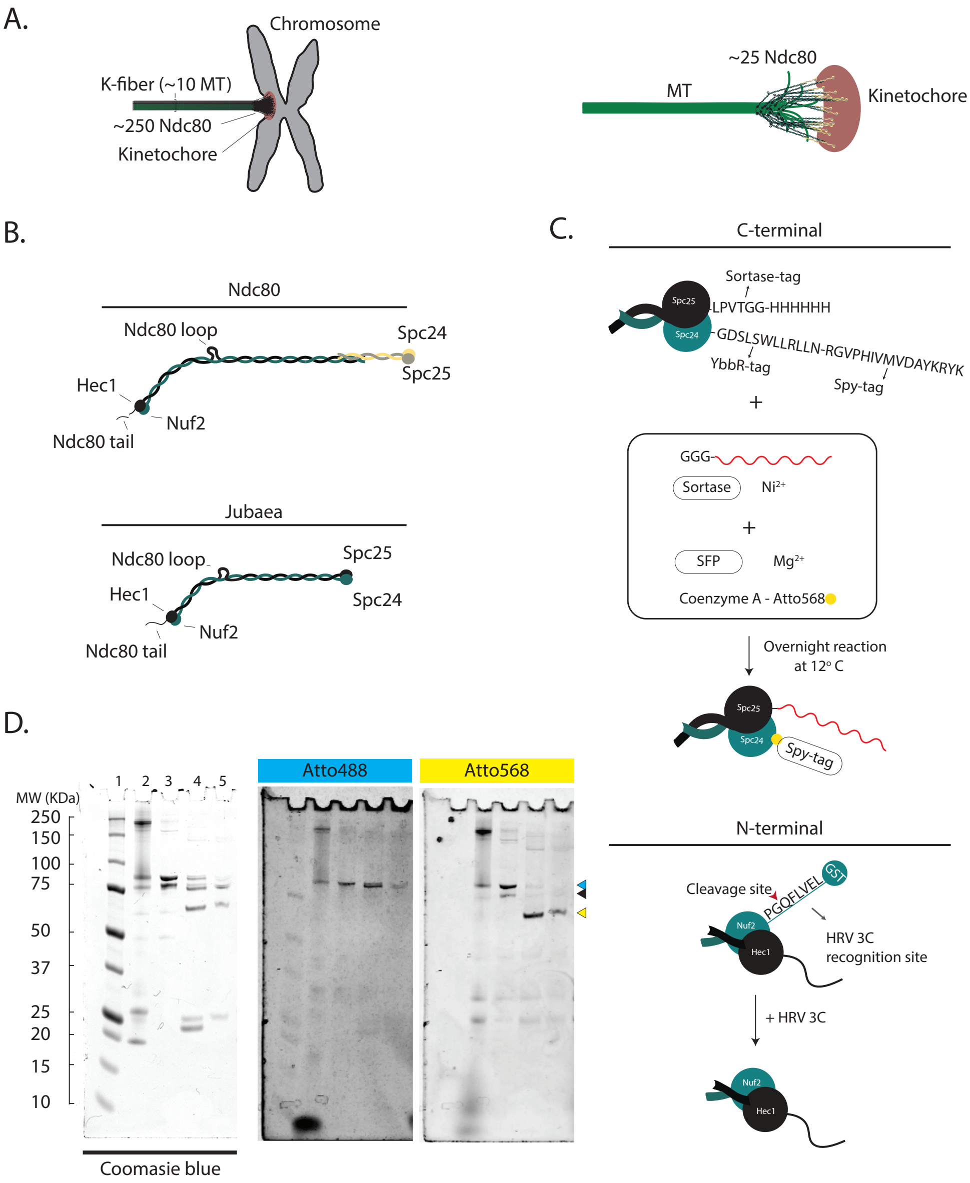

Figure 3.1: *Multiple Ndc80s form a load-bearing attachment with microtubules. (A) Schematics showing a K-fiber connected to a chromosome via kinetochore. On the right is the zoomed-in image illustrating how an individual microtubule can be attached to the kinetochore via Ndc80 complexes. (B) Ndc80 is made of 4 subunits: Hec1, Nuf2, Spc24 and Spc25. Spc24 and Spc25 domains dock Ndc80 into the kinetochore and CH domain on Nuf2 together with CH domain on Hec1 and its 80-residue tail binds to microtubules. Jubaea is the truncated version of Ndc80 from which 34% of the coiled coil region is removed. Also, Nuf2 and Spc24 are fused into one subunit and Hec1 and Spec25 are fused with each other. These two subunits form jubaea heterodimer. (Continued ...)*

(Figure 3.1 continued) (C) A GST-tag on the N-terminal of Nuf2-Spc24 subunit was used for the purification of jubaea which was later cleaved using HRV 3C protease. A Sortase-tag on the C-terminal of Hec1-Spc25 subunit and a YBBR-tag on the C-terminal of the Nuf2-Spc24 subunit was used for DNA and fluorescent labeling, respectively. Sortase recognizes the LPVTGG site, cleaves the last residue and conjugates the triglycinated oligonucleotide to it. Fluorescently labeled coenzyme A will be conjugated to jubaea as a result of SFP activity. (D) Coomasie blue stained polyacrylamide gel ; lanes 1 and 10: molecular-weight size marker, lane 2: the reaction mix containing jubaea, sortase, Ni^{2+}, triglycinated oligonucleotide (jubaea handle), lane 3: dually labeled jubaea after being purified by size exclusion chromatography, lane 4: dually labeled jubaea after treatment with HRV 3C protease, lane 5: flowthrough of the previous step after being applied to a Ni-NTA column. Images taken in the 488 nm and 561 nm fluorescent channels of the same gel are shown on the right. The appearance of a strong fluorescent band at the position corresponding to 88 KDa MW (lanes 4) confirms successful fluorescent labeling of the Nuf2-Spc24 subunit. This band completely disappears after treatment with HRV 3C protease and shifts to the 66 KDa MW position (indicated by yellow triangle) as a result of GST-tag removal. The 488 nm fluorescent channel was used to visualize the SYBR™ Gold stained DNA. The appearance of a fluorescent band at the position corresponding to the molecular weight of 88 KDa indicates jubaea is labeled by DNA (cyan triangle). this is also evident from the up-shift of the band corresponding to HEC1-Spc25 from 78 KDa (black triangle) to 88 KDa position (cyan triangle) in the Coomasie Blue stained gel, as a result of being labeled by DNA strand

In this context, stall force was defined as the applied force at which microtubule depolymerization ceased while maintaining attachment to a Ndc80-functionalized bead. In these experiments, a positive correlation was observed between stall force magnitude and the frequency of microtubule rescue events following the MT stall [18],], although in a later paper it was shown that rather the duration of the stall (and not the magnitude of the force) affects the rescue probability [10].

These observations prompted questions about the exact quantitative relationship between Ndc80 complex stoichiometry, stall force and rescue probability, as precise stoichiometric control could not be achieved in bead-based assays. A follow-up study was performed using a DNA origami force sensor, a nanospring (NS), with the ability to measure forces up to 10 pN [19]. (see Chapter 2). This approach enabled precise control of Ndc80 complex stoichiometry through the implementation of modified streptavidin molecules containing one biotin-binding site and three Ndc80-binding sites, which were tethered to a biotinylated NS. Force generation was quantified through measurement of NS extension during microtubule end-tracking by Ndc80 trimers. In addition, constructs were designed that could accommodate up to 9 Ndc80s complexes and it was shown these can, on average, capture 4 times higher forces (~4 pN) compared to trimers. However, no force-dependent microtubule rescue was observed with this method, in contrast to the observations made with beads in an optical trap. Building on this study, we therefore set out to further increase Ndc80 copy number in a controlled manner. Instead of the full-length complex, we investigated a truncated Ndc80 variant, Ndc80^{jubaea} (hereinafter referred to as jubaea). Jubaea is an engineered recombinant construct of the Ndc80 complex, designed as an extended analogue of the shorter Ndc80^{bonsai} variant to facilitate bacterial expression and biochemical studies of kinetochore-microtubule interactions. Unlike Ndc80bonsai, which retains only 17% of the predicted coiled-coil regions across the Ndc80 subunits, jubaea encompasses 66% of these coiled-coils, specifically covering residues 286-504 of NDC80 and 169-351 of NUF2, while lacking the tetramerization domain [10]. We chose this variant because it is amenable to bacterial expression in E. coli [10] and contains the loop region of NDC80, which has been shown to be crucial for force-resistant attachments [12]. We demonstrate that jubaea trimers retain both microtubule end-tracking capability and force-coupling ability in oligomeric assemblies. Building upon previous methodologies [19], we engineered modified nanospring constructs accommodating increased jubaea copy numbers approximating physiological stoichiometry, enabling systematic investigation of force transmission and microtubule dynamics as a function of jubaea copy number. A series of NS variants were designed with binding capacities of 3, 4, 6, 10, 15, and 20 jubaea molecules. Force measurements using these NS suggest an optimal jubaea copy number (10 copies) for maximal force transmission. At high copy numbers complex diffusion on the MT lattice is severely reduced which possibly hampers the ability to track a depolymerizing MT under force. By contrast, rescues only started to manifest themselves for NS constructs with 15 and 20 jubaea binding sites.

3.2. RESULTS

3.2.1. APPROACHES FOR MULTIMERIZATION OF JUBAEA

The main body of the NS used in this study was the same (same scaffold with the same starting 1-151 staples, Fig. 3.2A and S1A) across all NS constructs and was synthesized according to our previously published protocol [19].] (see Chapter 2). While one terminal of the NS was used for immobilization, the other terminal was used flexibly to include a desired number of linkers for accommodating jubaea in different numbers and geometry of connections. This includes: 1. NS with a biotinylated oligo at its end that can bind to the trimerized jubaea using streptavidin (NS-T1S3) [19], 2. NS with a holiday junction connection (NS-HJ); 3. NS with a 500-b ssDNA megamer with 4 jubaea linkers (NS4); 4. NS with 6 jubaea linkers added directly to the unfolded scaffold of the NS (NS6); 5. NS with 10 jubaea linkers added to the scaffold (NS10); 6. NS with 15 jubaea linkers added to the scaffold (NS15); 7. NS with 20 jubaea linkers added to the scaffold (NS20).

NS-HJ and NS-T1S3 are both designed to bind up to three jubaea but at slightly different distances from each other. The holiday junction on the NS-HJ has three DNA overhangs that are complementary to the DNA handle attached to jubaea (hereafter referred to as the jubaea handle). To confirm the availability of these binding sites, an oligonucleotide with the same sequence as the jubaea handles and a fluorophore (DY647) attached at the 5′ end was added to the NS-HJ DNA origami mixture and purified using agarose gel electrophoresis. A photobleaching experiment was conducted on these nanosprings and the fluorescent signal at the 642 nm channel was monitored over time and a step detector algorithm [20] was used to determine the number of bleaching steps, the histogram of which peaked at 3 (Fig. 3.2B).

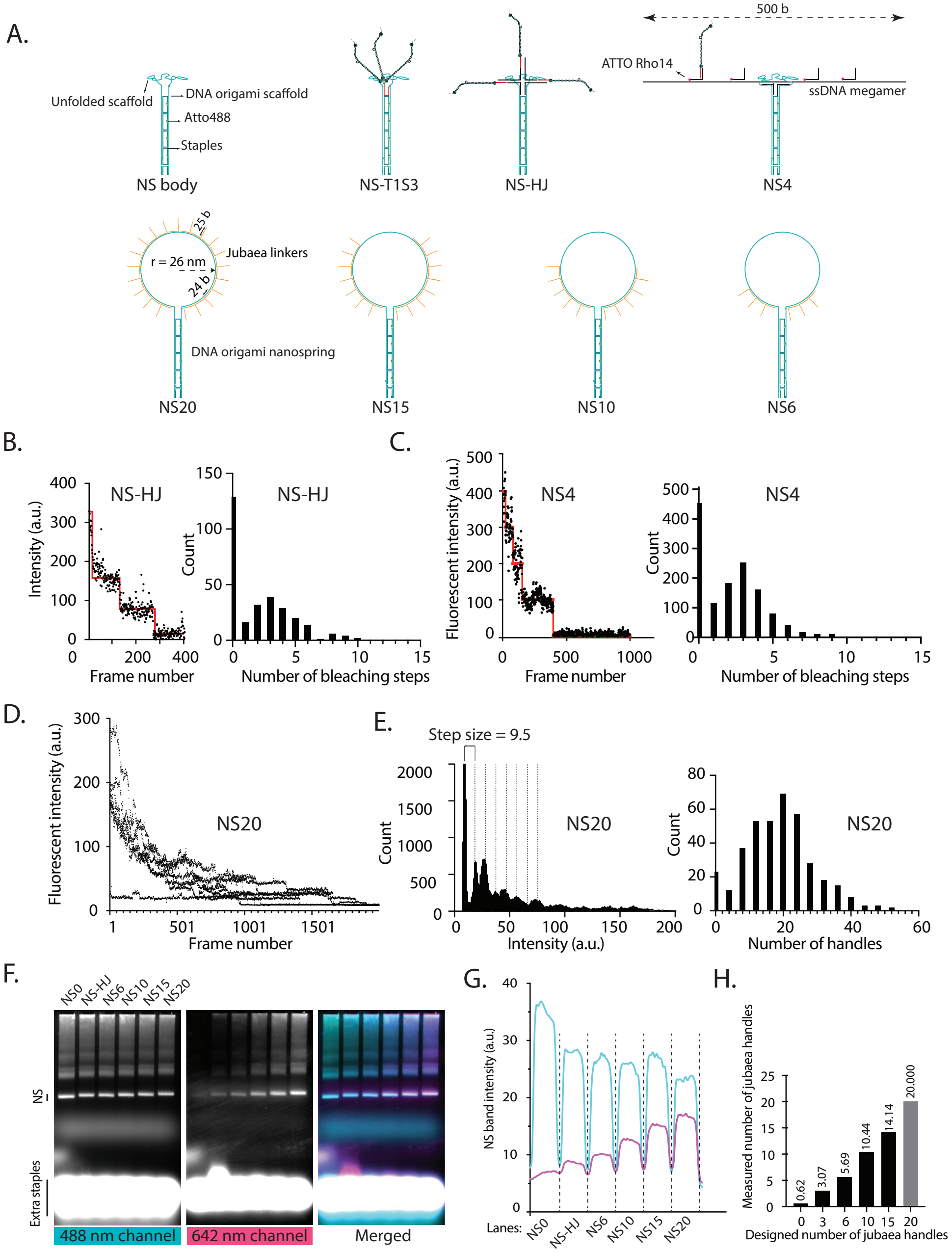

Figure 3.2: *DNA origami nanospring as a force sensor and a platform for multimerization of jubaea. (A) From left to right respectively, upper row: schematics of a NS with no jubaea binding linker, jubaea trimer made by modified streptavidin (T1S3 construct) attached to nanospring, jubaea trimer formed using a holiday junction at the terminus of NS, a 500 b ssDNA connected to NS to accommodate 4 jubaea copies. (Continued to the next page ...)*

(Figure 3.2 continued) Lower row: oligonucleotide handles connected to the NS scaffold that can allow binding of up to 6, 10, 15 and 20 jubaea copies. (B) Photobleaching analysis of individual NS-HJ molecules hybridized with fluorophore-conjugated complementary DNA strands. Representative single-molecule fluorescence intensity trace demonstrating discrete photobleaching steps (left). The distribution of observed photobleaching steps was quantified via an automated step-detection algorithm (right). (C) An example of stepwise bleaching of a NS4 molecule. The fluorescent intensity of individual spots was monitored overtime, and a step-finder algorithm was applied to determine the number of bleaching steps. A histogram of the number of bleaching steps is provided on the right. (D) Multiple bleaching trajectories of NS20 molecules. (E) The datapoints shown in panel D were binned based on the fluorescent intensity and a histogram was made. The average bleaching step intensity was calculated from this histogram (left). The right graph shows the histogram of NS20 initial intensity divided by the bleaching step intensity. (F) Agarose gel electrophoresis of NS with 0, 3, 6, 10, 15 and 20 jubaea handles. A fluorescently labeled (DY647) oligonucleotide complementary to the jubaea linkers on the NS was added to the DNA origami synthesis mixture. The gel was imaged at 642 nm and 488 nm fluorescent channels to visualize the incorporated DY647 oligos (magenta) and the base of the NS (cyan). (G) The bands corresponding to the different NS versions in panel F were quantified and plotted on the graph. The band intensity of NS emanating from the base of the NS (Atto488, the 488 nm channel in the gel image) is plotted in cyan. The band intensity emanating from the fluorescent oligo bound to the jubaea binding linkers is plotted in magenta. (H) The graph shows the number of jubaea handles on each NS construct calculated from NS band intensities obtained from 488 nm and 642 nm fluorescent channels (panel G). It was assumed the signal from the NS20 construct corresponds to having 20 jubaea handles (the gray bar) and the number of jubaea handles of other constructs were calculated (exact values written on top of each bar) based on the relative band intensities.

The jubaea linker oligos in the NS4 construct also had Atto-Rho14 fluorophore in their 5′ end. The fluorescent signal observed in both the 488 nm (NS body) and 642 nm (jubaea binding linker) channels suggests that the construct was successfully assembled (Fig. S3.1C).). Examining the same sample via TIRF microscopy revealed a colocalization of 70%. Further analysis was made by photobleaching experiments where the intensity of individual spots in the TIRF image was monitored over time in the 642 nm channel. The histogram of the number of bleaching steps for this construct peaked at 3 (Fig. 3.2C).

In an attempt to increase the assembly efficiency between the NS base and higher numbers of the jubaea binding oligos, we added 6, 10, 15 and 20 jubaea linkers (for NS6, NS10, NS15 and NS20 respectively) directly to the unfolded scaffold of the NS (Fig. 3.2A, lower row). A photobleaching experiment was conducted on the NS20 construct to confirm the number of jubaea binding sites on the NS construct. In these experiments, NS20 was purified under conditions where a fluorescently labeled (DY647) oligo, complementary to the Jubaea binding handles, was added to the DNA origami mixture. Therefore, upon purification, it is expected that the fluorescently labeled oligos are hybridized to its Jubaea binding sites. However, the step detection algorithm was now more prone to error due to a higher number of bleaching steps and reduction in the sharpness of steps. We aggregated the bleaching trajectory of multiple spots (Fig. 3.2D) and made a histogram by binning the intensity (Fig. 3.2E, left panel) according to [21]. The average distance of the peaks in the histogram showed an intensity step size of 950. The histogram of the handle number for NS20 peaked at 20 (Fig. 3.2E) obtained by dividing the initial intensity of the spots by the step size after subtracting the background intensity.

To further confirm the availability of binding sites for the high copy number constructs, we also used a gel-based method. Using this construct (NS20) as a reference, we purified other NS variants (NS0, NS6, NS10, NS15), to which fluorescently (DY647) labeled oligos complementary to the jubaea linkers were added. As a result, each NS version contains Atto488 dyes embedded in the NS body, which is a shared feature across all versions. Depending on the number of jubaea linkers present in each NS version, they can have different numbers of DY647 dyes. The fluorescent signals from NS0, NS6, NS10, NS15, and NS20 constructs run on an agarose gel were used to estimate the number of jubaea binding handles on each construct (Fig. 3.2F). The signal in the 488 nm channel was used as a measure of the number of NS constructs in each band and used for calibration (see materials and methods), while the signal in the 647 nm channel was used as a measure of the number of DY647-labeled oligos bound to the jubaea linkers (Fig. 3.2G). The band intensity of NS20 was taken as a reference, corresponding to 20 handles, and the handle numbers for the other constructs were calculated by comparing their relative band intensities. Our analysis confirmed that the measured number of jubaea handles closely matched the intended design values (Fig. 3.2H).

3.2.2. NS-JUBAEA BINDING AND IMPACT OF JUBAEA COPY NUMBER ON DIFFUSION

Before performing any force measurements, we characterized the diffusive behavior of our constructs on MT lattices. Jubaea shares the same microtubule binding domain (MTBD) as Ndc80. Jubaea shares the same microtubule binding domain (MTBD) as Ndc80. Previous research on Ndc80 [12] has demonstrated that an increase in the copy number within oligomers can reduce its diffusion coefficient along microtubules. Given this precedent, we hypothesized that a similar trend would hold for jubaea when incorporated into nanospring (NS) constructs with varying numbers of binding sites. To test this, we systematically investigated how the oligomerization of jubaea affects its diffusive behavior on microtubules.

First, an agarose gel electrophoresis shift assay was used to confirm the binding of jubaea molecules to NS constructs with varying numbers of jubaealinkers (NS0, NS6, NS10, NS15, and NS20) (Fig. 3.3A). The gel image in Fig. 3.2F), which contained NS constructs without DNA-labeled jubaea molecules, displayed only minor mobility reductions due to the handles alone. In Fig. 3.3A the notable increase in NS6, NS10, NS15, and NS20 bands, compared to the NS0 band (without jubaea linkers), confirms the successful incorporation of increasing numbers of jubaea molecules. To further validate these complexes, we conducted a TIRF assay. NS constructs were immobilized on a surface via digoxigenin (DIG), the DNA-labeled jubaea was introduced, and then unbound jubaea was washed away. Imaging revealed strong colocalization of NS and jubaea signals in the majority of spots (Fig. 3.3B), corroborating the gel-based evidence of stable binding.

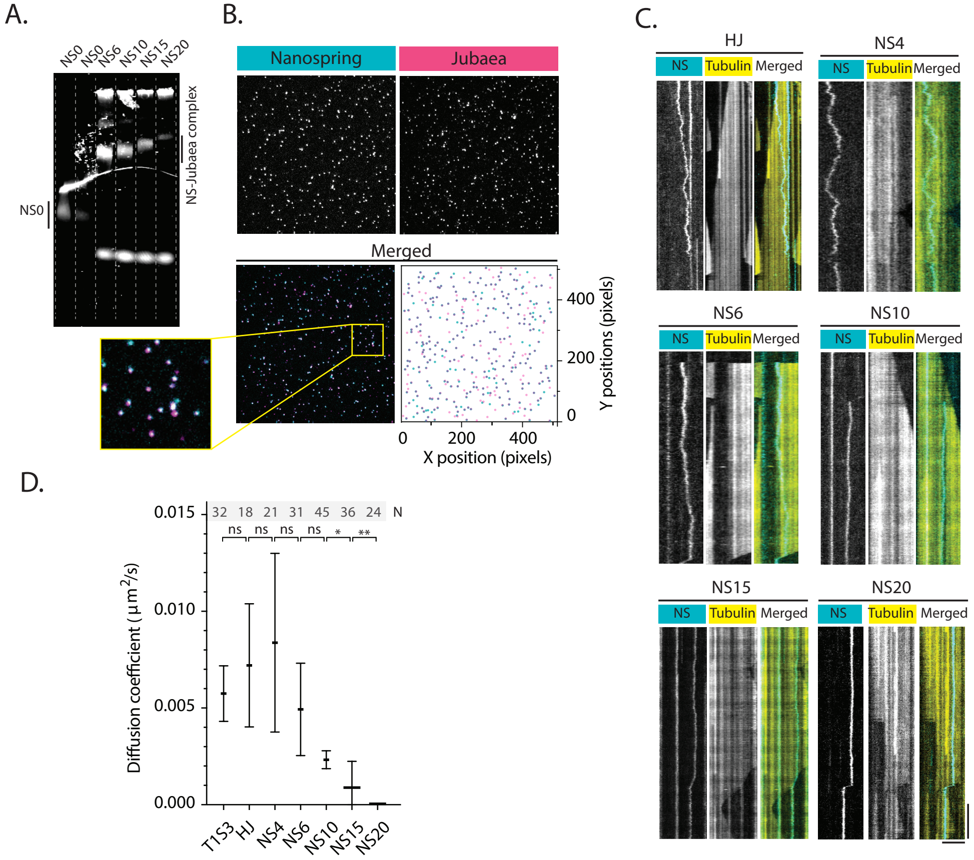

Figure 3.3: *The effect of the number of jubaea molecules on nanospring diffusion on microtubules. (A) Electrophoretic mobility shift assay of NS0, NS6, NS10, NS15 and NS20 mixed with DNA-labeled jubaea in denaturing conditions (0.8% agarose in TAE + 12 mM $MgCl_2$ + 0.5% LDS). The first lane from the left only contains NS0, without jubaea molecules. As the number of jubaea linkers increases on the NS constructs, the bands corresponding to NS-jubaea complexes shift upward. (B) The fluorescent signal from NS20 (cyan) and from fluorescently labeled jubaea (magenta) in TIRF. In the lower row the combined image made from merging these two signals is shown. For a clearer visualization, a scatter plot of the position of detected jubaea clusters (magenta) and NS (cyan) is added next to the merged image. The inset shows a zoomed-in image of the selected square. (C) Example kymographs of NS-jubaea complex diffusion on MT lattices. The NS20-jubaea complexes were immobile on the MT lattice but could occasionally be seen moving when encountering a shrinking MT. The example provided here illustrates this fact. (D) Diffusion coefficients of diffusive NS-jubaea complexes on the MT lattice. The NS15-jubaea and NS20-jubaea complex were almost stationary and thereby had a very small diffusion coefficient of ($8\times10^{-4}\mu m^2/s$ and $4\times10^{-5}\mu m^2/s$). Horizontal lines show mean values, error bars are SEM and statistical significance was determined using an unpaired two-tailed t test (P-values; NS-HJ vs. NS-T1S3: 0.6352, NS4 vs NS-HJ: 0.8410, NS4 vs. NS6: 0.4738, NS6 vs. NS10: 0.2083, NS10 vs. NS20: 0.0006, NS10 vs. NS15: 0.0113, NS15 vs. NS20: 0.004)*

We then utilized the same assay that was used to study interactions between dynamic MTs and surface-attached NSs (see Figs 3.5A and 3.6A) to study the diffusive properties of jubaea oligomers. This dynamic microtubule assay involves NS-jubaea complexes immobilized on coverslips using anti-DIG IgG antibodies. The surface attachment, despite being capable of withstanding forces up to ten piconewton [18], occasionally detached under experimental conditions. When this occurs, a NS bound to jubaea oligomers goes into the solution, sometimes binding to a microtubule followed by diffusion along its lattice (Fig. 3.3C). We tracked the one-dimensional (1D) diffusion of various jubaea-containing NS constructs—NS-HJ, NS-T1S3, NS4, and NS10 in short time intervals (averaging 0.9 s). Notably, NS15 and NS20 constructs with jubaea exhibited no diffusive behavior, remaining completely immobile on the microtubule lattice.

To quantify this, we calculated the mean square displacement (MSD) of diffusing spots and plotted it against time and used the slope of the plot to calculate the diffusio coefficient (Fig. 3.3D). Clearly, the diffusion constant is progressively reduced when more jubaea copy numbers are added, with no measurable diffusion remaining for NS20.

3.2.3. TYPES OF NS-JUBAEA INTERACTIONS WITH THE DEPOLYMERIZING MICROTUBULES

Next, we set out to categorize the types of interactions that take place between surface-attached NS constructs (NS6, NS10, NS15, NS20) and depolymerizing MTs. Using TIRF microscopy, we monitored depolymerizing MTs as they encountered NS-jubaea complexes immobilized on a coverslip surface. This approach enabled us to observe and analyze the dynamic events occurring during and after MT-NS encounters, where we also quantified the number of times that no interaction took place. A “no interaction” scenario occurs when an MT approaches an NS but continues to depolymerize without any observable effect on the NS or the MT. In contrast, an interaction is defined by one of several distinct events, which we systematically classified to understand how the NS-jubaea complex modulates MT behavior. These interaction events are as follows (see Fig. 3.4):

1. **Rescue**: The MT undergoes a rescue at the interaction site, transitioning from depolymerization to growth, without an observable effect on the NS. Sometimes the transition from shrinking to growth did not happen immediately but after a pause period. We called such events with visibly longer pause periods **stall** events.

2. **Retention**: A depolymerizing MT pauses temporarily upon encountering an NS before continuing to shrink, without an observable effect on the NS.

3. **NS Extension**: The NS-jubaea complex attaches to the shrinking MT, extends as it follows the shrinking MT, and returns to its original conformation after detachment from the MT.

4. **Extension Rescue**: Similar to NS extension, but the MT is rescued after NS is extended.

5. **Tip Tracking**: The NS detaches from the surface upon MT contact and tracks the shrinking MT tip as it moves.

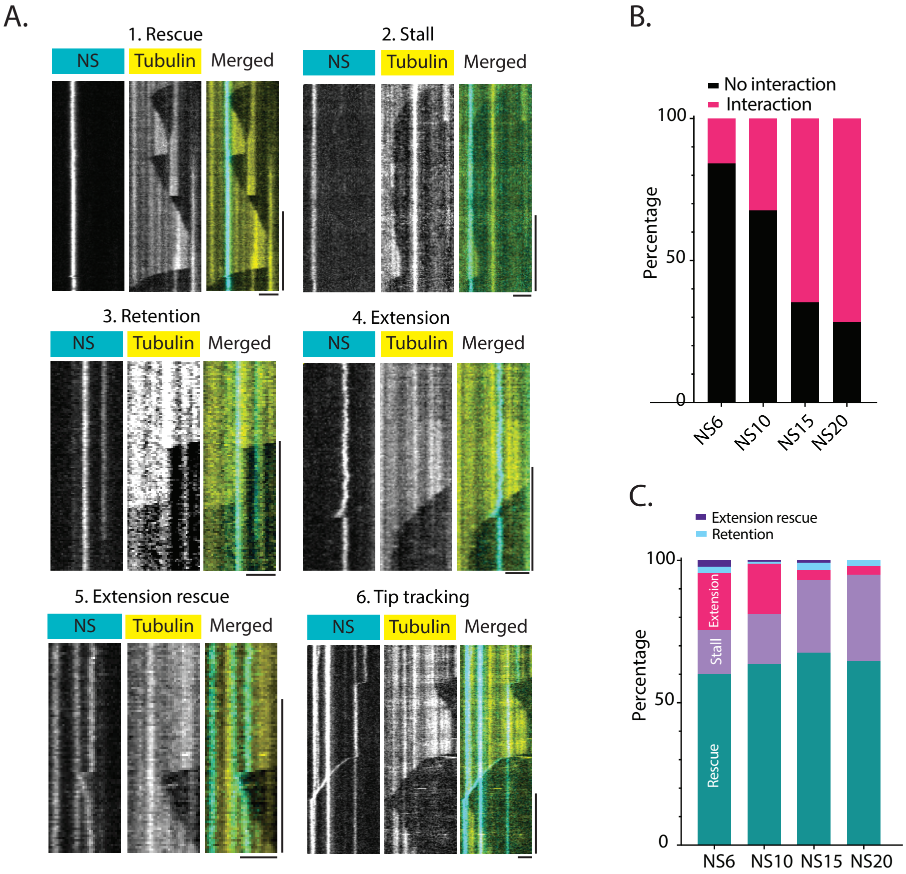

Figure 3.4: *NS-jubaea complex interactions with MT. (A) Categorization of types of interactions between a shrinking MT and an NS. The definition of each event is described in the text and here an example kymograph of each event is provided. Scale bar; spatial: 5 µm, temporal: 1 min. (B) The graph compares the share of presence (magenta) or absence of an interaction (black) every time a depolymerizing MT encounters NS-jubaea complex. Total number of events for NS6, NS10, NS15 and NS20 respectiviely: 379, 1824, 181, 432 (C) The interacting share of events from panel (B) were dissected into their constituent events. Each bar shows what is the percentage of each of the interacting events in (A) among all possible interactions for each NS version, when NS is not detached from the surface.*

Fig. 3.4B illustrates how the number of jubaea handles on the NS influences the occurrence of MT-NS interactions. The data reveal that the interaction probability increases sharply with handle number, rising from 16% for NS6-jubaea (6 handles) to 72% for NS20-jubaea (20 handles). This suggests that higher jubaea copy numbers enhance the NS's ability to engage MTs, likely due to increased binding avidity.

Fig. 3.4C further dissects these interactions into the different types of events, presenting the percentage occurring of each type. Here we only considered events when a shrinking MT passes by a non-detaching NS, thereby the tip tracking events are excluded (). Rescue and stall events without detectable NS extension dominated across constructs, reflecting a stabilizing effects of jubaea oligomers on MT dynamics. For all constructs we also observed NS extension events, with the proportion of these events decreasing with increasing number of jubaea handles: from 20% for NS6 to just 3% for NS20.These results suggest that jubaea oligomerization leads to MT stabilization when NS constructs are immobilized, with higher copy numbers favoring MT rescue and stall over dynamic NS extension.

3.2.4. EFFECT OF JUBAEA COPY NUMBER ON DEPOLYMERIZATION RATE OF MICROTUBULES

As discussed above, NS-MT interactions sometimes lead to detachment of the NS from the surface, allowing us to also quantify the effect of mobile NS constructs on MT dynamics.When Ndc80 is oligomerized it can tip track shrinking microtubules. It has been demonstrated that tip-tracking Ndc80 oligomers can slow down the shrinkage rate of MTs [12, 18]. We tracked the end of the depolymerizing MTs with a custom-made ImageJ macro (see methods and materials). We compared the speed of MT shortening with and without an end-tracking oligomer present, using MTs from the same recording.

In both cases, the shrinkage rate was not always constant. A logistic function was fitted to the position-time coordinates of the tip of the MT to account for rate variability. We calculated the point derivative of the curve to determine the shrinkage rate at any given time/length and then calculated the average shrinkage rate within a certain period (Fig. 3.5A). A logistic function fits the overall trend, reducing sensitivity to random fluctuations or noise in the data and captures the continuous and smooth transition between different shrinking phases, such as slowing down as the MT end approaches the seed. Furthermore, it is less sensitive to the missing datapoints compared to piecewise linear fitting and does not require manual tuning of parameters such as segment length.

We find that binding of a NS to a shrinking MT impacts its depolymerization differently depending on the copy number of jubaea present in the oligomer (Fig. 3.5B). Quantification of the depolymerization rate revealed a trend where higher number of jubaea copy numbers caused more reduction in the rate (Fig. 3.5B). Quantification of the depolymerization rate of MTs with tip tracking NS-jubaea complex revealed a trend where higher number of jubaea copy numbers caused more reduction in the rate (Fig. 3.5C, shaded area), with NS20-jubaea having the strongest impact. The shrinkage rate of the bare MTs in the same samples were quantified as control samples and are shown on the right side of the Fig. 3.5C. No trend is observed in these control data.

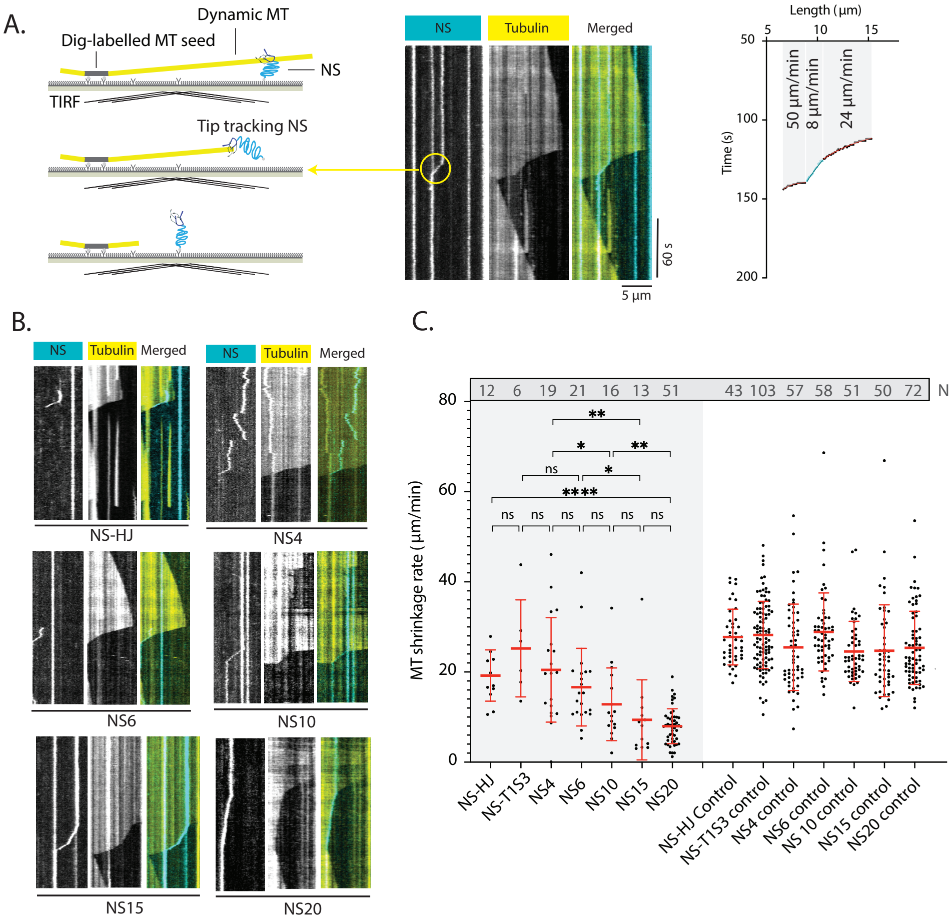

Figure 3.5: *Effect of multimerized jubaea on the depolymerization rate of MTs (A) Schematics of the experimental setup. Binding of a multimerized jubaea alters the depolymerization rate of MTs. An example kymograph is provided. The end of depolymerizing MT was tracked in the presence of a tip tracking NS-jubaea complex or in its absence. A logistic function was fit to the tracked position-time datapoints of MT edge in kymographs and its derivative was used to calculate the shrinkage rate of the MT at any given time. (B) Example kymographs showing shrinkage rate reducing effect of each of NS-jubaea complexes. (C) The shrinkage rate of MT when an NS-jubaea complex is tip tracking (shaded area). The shrinkage rate of MTs in the same field of view with no bound NS-jubaea complex is on the right side of the graph (control samples). Horizontal lines show mean values, error bars are S.D and statistical significance was determined using unpaired two-tailed t test (P-values; NS-T1S3 vs. NS6: 0.0514, NS-HJ vs. NS20: 0.0001, NS6 vs. NS20: 0.0001, NS4 vs. NS15: 0.0067).*

3.2.5. Force-Capturing Abilities of jubaea Oligomers

We next used the extension events to assess the force-capturing abilities of jubaea oligomers. In an extension event, jubaea oligomers dynamically track the shrinking

MT while stretching the NS, a process observable through the fluorescent signal emitted by the NS under TIRF. The extension is followed by detachment from the MT (extension events) or, in rare cases, the regrowth of the MT (extension rescue events). The schematic of the experimental setup is shown in Fig. 3.6A. Previously, we applied this technique to assess the force-capturing capacity of the NS-T1S3-full-length-Ndc80 complex. Those experiments demonstrated that higher copy numbers of full-length Ndc80 (up to nine copies) detached from the MT at greater forces compared to the trimerized Ndc80 stabilized by the T1S3 trimerizer [19]. In these experiments rescues were never observed. Leveraging this established method, we investigated whether jubaea oligomers, when combined with the T1S3 trimerizer, also exhibit force-capturing abilities. Our results confirm that oligomerized jubaea indeed possesses such capabilities (Fig. 3.6).

In this study we performed similar experiments with our other NS constructs , namely NS-HJ, NS4, NS6, NS10, NS15, NS20. Although the exact copy number of bound jubaea to each of these constructs can vary, the upper limit in each case is fixed. We incubated the NS constructs with excess jubaea and washed away the extra unbound jubaea in the flow chamber before conducting the MT dynamic assay experiments (see 3.4). Jubaea molecules oligomerized at the end point of the NS construct would sometimes follow a shrinking MT. Time lapse images in Fig. 3.6B show such an extension event. Here we see colocalization of Atto568-labled jubaea (yellow) with Atto488-labeled NS, indicating the binding of jubaea dimers to the NS. This event is easily identifiable in the kymograph of Fig. 3.6B, where we see a displacement of the jubaea signal at t = 440.1 s. The corresponding NS signal at this timepoint also confirms this extension event. After collection of kyomographs of extension events, they were used to estimate the magnitude of the captured forces by various NS constructs. Although using the jubaea fluorescent signal provides more accurate estimation of extension length and therefore generated forces, we had to rely on the NS signal for force quantification due to poor labeling of jubaea. We measured the forces captured by the NS-jubaea complexes by measuring the displacement observed in the NS signal, using gaussian fitting (see Fig. 3.6C) and compared them to those of the previously studied NS-T1S3-Ndc80 system. The NS-T1S3-jubaea complex captured slightly higher forces, averaging 0.72 (pN), compared to 0.48 pN for NS-T1S3-Ndc80, though this difference lacked statistical significance. We measured similar forces for NS-HJ-jubaea, NS4-jubaea, and NS6-jubaea. However, for the NS10-jubaea complex we measured an average of 2.15 pN, a statistically significant increase. Interestingly, for NS15 and NS20 the forces were again lower. For a subset of constructs we also performed experiments in the presence of additional free jubaea. Across the tested NS-jubaea complexes, forces were consistently higher when free jubaea (50 nM) was added to the imaging buffer (Fig. 3.6D), hinting that unbound jubaea may bolster the complex's stability or microtubule affinity.

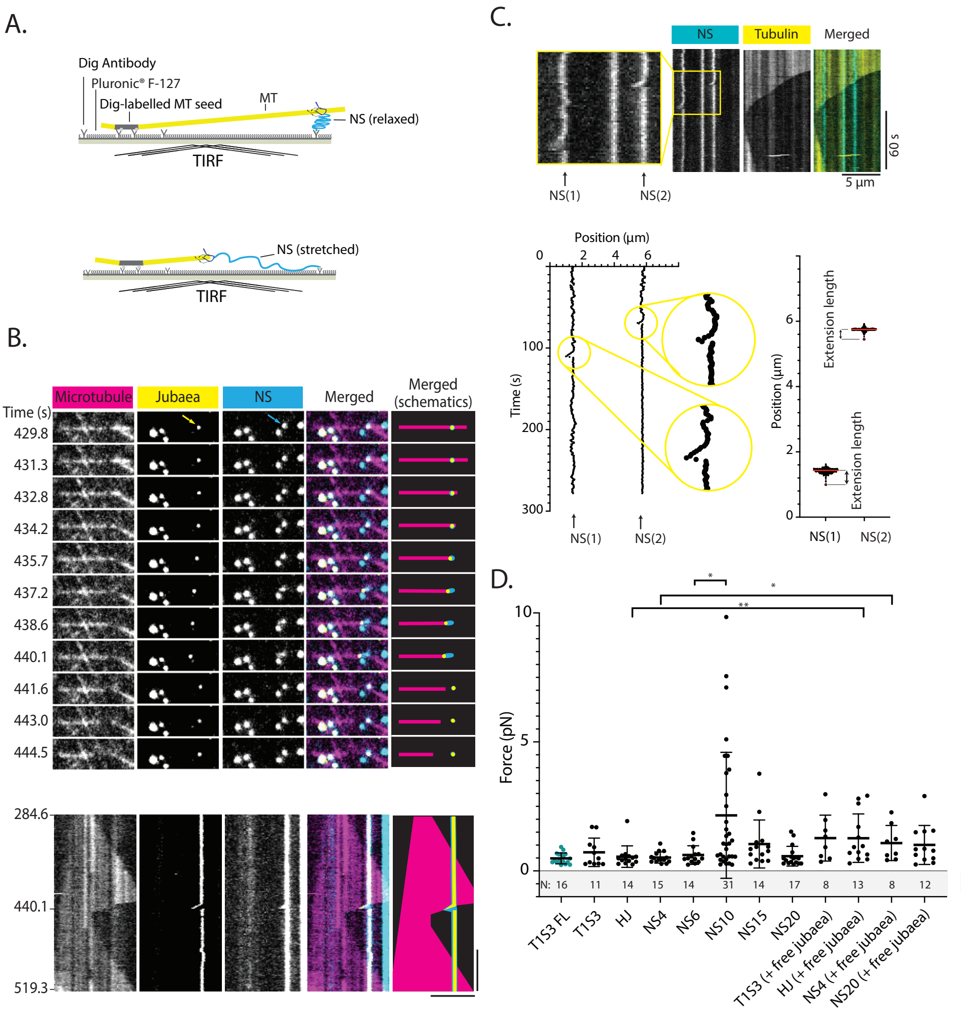

Figure 3.6: *Capturing the force of depolymerizing MTs by NS-jubaea complexes (A) Schematics of experimental setup of force measurement. (B) Time lapsed images of a shrinking MT (magenta) encountering an NS (cyan) with DNA labeled jubaea hybridized to its terminal (yellow). The jubaea oligomer follows the shrinking end of the MT and extends the NS. The extension reaches to its maxium at t = 440.1 s. The kymograph of this event is provided below the time-lapsed images. Scale bars: Temporal 60 s, spatial 5 µm. (C) A kymograph of an NS extension event, visualized in the NS channel. A Gaussian function was fitted to the fluorescent signal of the NS in the kymograph to obtain the position vs. time data points. An example of NS position tracking is provided for the two NSs in the example kymograph. The extension length was defined as the maximum displacement of the NS from its median position as a result of its interaction with a depolymerizing MT. (Continued to the next page ...)*

(Figure 3.6 continued) (D) Quantification of the forces captured by different NS-jubaea complexes, in the absence or in some cases presence of free jubaea in solution. The cyan datapoints are the forces captured by T1S3 construct with the full length Ndc80 (Chapter 2). Horizontal lines show mean values, error bars are S.D and statistical significance was determined using a two-tailed Mann–Whitney test. (P-values; NS-T1S3 FL vs. NS-T1S3: NS10 vs. NS15: 0.2836, NS6 vs. NS15: 0.1597, NS-T1S3 vs. NS-T1S3 (+ free T1S3): 0.1087, NS4 vs. NS4 (+free jubaea): 0.0223, NS-HJ vs. NS-HJ (+ free jubaea): 0.0056, NS20 vs. NS20 (+ free jubaea): 0.0570, NS6 vs. NS10: 0.0202)

3.3. DISCUSSION

In this Chapter we investigated the dynamic properties of different NS constructs with controlled numbers of jubaea handles when interacting with dynamic MTs. We studied their diffusion constants along the MT lattice, the effect of free end-tracking constructs on the shrinking rate of depolymerizing MTs, the ability of surface-attached NS constructs to capture forces generated by shrinking MTs and the effect on MT stalls and rescues in the presence of force. The overall trend seems to be that higher copy numbers of jubaea molecules in the construct lead to slower diffusion (as expected for multivalent interactions) and a progressive reduction in MT depolymerization rates. Furthermore, the probability of a surface-attached NS construct to engage with a shrinking MT increases with copy number. Upon engagement stall and/or rescue events without detectable generation of force are often observed for the NS6-NS20 constructs. When force-generating events are observed the forces appear to be highest at a copy number of about 10. Both for lower and higher copy numbers the observed forces are lower. Before further discussing the possible meaning of these observations, we compare our results to previously published results with full length Ndc80.

The diffusion coefficient of NS connected jubaea trimers ($D = 5.7 \times 10^{-3}$) turned out to be an order of magnitude higher than that of Ndc80 trimer ($D = 4.3 \times 10^{-4}$)). Instead, it was comparable to the diffusion coefficient of loopless Ndc80 trimers ($D = 3.6 \times 10^{-3}$). Note however that the experiments with Ndc80 were done on taxol-stabilized MT lattices, while the jubaea diffusion coefficient measurements were performed with dynamic MTs [12].]. So, either the affinity of the jubaea trimer for the MT lattice is lower than for the Ndc80 trimer or the binding affinity is higher on taxol-stabilitzed MTs than on dynamic GDP MTs. Further experiments are needed to clarify this difference. It is also possible that the stabilizing effect of the loop is not as efficient for jubaea as it is for Ndc80. It will therefore also be interesting to repeat these experiments with loopless jubaea.

For the other constructs with 3 or 4 jubaea handles (NS-HJ and NS4), the diffusion constant was similar or maybe even slightly higher than for NS-T1S3 (the differences were not statistically significant). Possibly the larger distance between the jubaea molecules plays a role here, which could diminish any stabilizing effect of loop-containing jubaea molecules on each other. For constructs NS6 to NS20, which share comparable geometric configurations, a clear inverse relationship was observed between the number of jubaea handles and the diffusion coefficient of

NS-jubaea complexes on the MT lattice.

While Ndc80 trimers were previously demonstrated to have a substantial impact on microtubule depolymerization rates, reducing them by approximately 50%, jubaea trimers exhibited a comparatively modest effect, decreasing depolymerization rates by only 10%. This mild effect on depolymerization rates correlates with a relatively high diffusion coefficient (compared to Ndc80). Intriguingly, jubaea demonstrated a clear copy number-dependent effect on microtubule dynamics: NS-jubaea constructs with an increased number of binding sites produced progressively stronger attenuation of depolymerization rates. This effect was strongest in NS20-jubaea, which reduced microtubule depolymerization rates from 25.4 μm/min to 8.0 μm/min, representing a 70% reduction (correlating with a similar strong reduction of the diffusion coefficient). Previously no clear copy number-dependent relationship was observed among Ndc80 dimers, trimers, and tetramers, but in this case higher copy numbers were not explored. Interestingly, when comparing Ndc80 and jubaea results, it seems that a similar diffusion constant corresponds to a similar reduction of growth: compare for example the numbers for Ndc80 trimers and NS15 jubaea constructs. The relation between diffusion coefficient and reduction of depolymerization rate maybe explained by considering that depolymerization is hindered by slowly diffusing constructs that are bound to the end of the MT [22] through inhibition of the removal of tubulin dimers.

The jubaea constructs, incorporating both the microtubule-binding domains and loop region of Ndc80, demonstrated force-coupling capabilities comparable to Ndc80 trimers, with no statistically significant differences observed between the two for the NS-T1S3 constructs. The enhanced force generation observed in the presence of soluble jubaea is possibly due to the additional recruitment of free jubaea from solution to the oligomeric complex at the NS tip (potentially facilitated by the loop region).

The frequent observation of stalls and rescues is different from our previous observations using NSs as a force sensor [19]. For the NS6-NS20 constructs we often observed stalls and rescues without a detectable extension of the NS (although occasionally the rescue was preceded by NS extension). This means that in these cases a stabilizing effect on MT shrinkage was established at relatively low forces, leading to sufficient stall time for a rescue to occur. We previously showed that it is rather the duration of stall than the actual force that determines the likelihood of a rescue [10]. Potentially the different spacing of DNA linkers on our NS6-NS10 constructs compared to the trimers and multimers that we studied before could be responsible for this difference. When stabilization happens at relatively low forces, the detachment rate of the complex will be low compared to a situation where a force acts on the NS. Therefore, detachment of the complex may be more likely than sufficiently long stalls and rescues for extension events.

Possibly our most interesting observation is the apparent existence of an optimal copy number of jubaea for the generation of forces. Apparently, there is a trade-off between the ability to faithfully follow shrinking MTs (without immediate stabilization and rescue) and the probability to detach. For low copy numbers, diffusion is fast and depolmerizing MT ends can be easily followed (unless the copy number is too low [18]), but the probability to detach increases steeply with force. Higher copy numbers will be able to maintain the connection to the MT end at higher forces more easily, but when the copy numbers become too high, MT depolymerization is hindered leading to more frequent stalls and rescues before significant forces can be developed.

Note that in our previous optical trap experiments using full-length Ndc80, maximum force generation coincided with approximately 12 Ndc80-microtubule interactions above which no increase in the transmitted force was observed [18]. However, in these previous studies with Ndc80 the force plateaued at elevated copy numbers and did not decrease [18]. This discrepancy may be attributed to the more heterogeneous protein distribution inherent in optical trap bead experiments and the different geometry of a large protein-covered bead surface where multiple (clusters of) Ndc80 molecules may (non-simulteneously) interact with the MT end.

The extent to which jubaea serves as an accurate proxy for Ndc80 behavior requires further experimental validation. A limitation of the present study is the inability to precisely determine the number of jubaea molecules actively engaging with microtubules, with NS constructs providing only upper bounds for the number of binding jubaea. Nevertheless, multiple independent lines of evidence—including diffusion analysis, interaction quantification, effects on shortening velocity and force generation, and bulk assays such as electrophoretic mobility shift analysis—demonstrate consistent patterns that indirectly support the progressive recruitment of increased jubaea copy numbers correlating with elevated jubaea binding sites on NS constructs.

Although further experiments may be required to firmly establish our NS results, it is interesting to speculate about the possible biological implications of our findings. The convergence of two key findings—the existence of an optimal jubaea copy number for maximal force generation and a threshold for microtubule stabilization –suggests intriguing possibilities for cellular regulation. Beyond phosphorylation-dependent regulation, cells may modulate kinetochore-microtubule attachments through dynamic control of Ndc80 copy numbers at the kinetochore. This model suggests that elevated Ndc80 concentrations during metaphase and pre-metaphase stages could ensure robust kinetochore-microtubule attachment maintenance. Following spindle assembly checkpoint satisfaction and progression to anaphase, cells could then optimize Ndc80 copy numbers to maximize force generation, thereby ensuring faithful chromatid separation and pole-ward movement

3.4. MATERIALS AND METHODS

3.4.1. DESIGN AND PURIFICATION OF THE DNA NANOSPRING

The p7560 version of M13mp18 single-stranded DNA, ordered from Eurofins Genomics, was used as a scaffold and the staple sequences of the base part (Staples 1-151) were generated according to the protocol described in [19]. The sequence of the scaffold is given in table S1 and table S2 provides the sequence of the base part of the NS. The NS base synthesis mixture contains 20 nM of the scaffold and 200 nM of each staple, dissolved in TAE (40 mM Tris, 20 mM acetic acid, and 1 mM

EDTA) supplemented with 12 mM $MgCl_2$.

We added a biotinylated oligonucleotide after the 151th staple (the staples 1 to 151 form the body of the NS and is the same for all NS versions) to enable binding of T1S3 construct. Nanosprings with a Holliday junction were made by adding 4 extra staples, 2 of which hybridize to the unfolded section of the scaffold immediately after the last staple of the NS shared body. The NS4 version was made by adding two linking oligos that were both complementary to the NS scaffold and a 500-base-long ssDNA. Four extra Atto-Rho14 labelled oligos that partially hybridize to the ssDNA platform can accommodate a maximum of 4 jubaea molecules.

The additional oligos needed for making each of the HJ, T1S3, NS4, NS6, NS10, NS15, and NS20 constructs are mentioned in table S3. The instructions for folding of the NS in a thermocycler and purification are provided in [19].

To count the number of handles on each NS construct, a fluorescently labeled oligo that is complementary to the handles (DY647-TTTTTACAGGGCTGAATCTGACGGACTACGA) was added to the DNA origami mixture and purified.

3.4.2. PHOTOBLEACHING EXPERIMENTS

The NS construct was diluted 50x in TAE + 12 mM $MgCl_2$ and then 4 μL of this solution was placed directly between a microscope glass slide and coverslip directly, and the edges were sealed by wax. The laser intensity at the objective (Plan Apo 100×1.45 NA TIRF oil-immersion objective, Nikon) was set to ~0.01 mW and images were acquired in ring TIRF mode every 1 s, using an Evolve 512 EMCCD camera. A custom script in ImageJ macro language (Github.com) was used to detect the spots and track their intensity over time. These data were smoothed by applying the Chung-Kennedy filter [18].

For NS constructs with fewer handles (NS-HJ and NS4), the number of bleaching steps was determined directly by using a step finder algorithm [20]. For constructs with a higher number of handles, first, the bleaching trajectory of multiple spots was combined, and a histogram of the intensities was created. The histogram highlights the intensities at which the fluorescent dyes spent more time as peaks. The intensity distance between the peaks in such a histogram can provide an estimate of the bleaching step size. The last level of the bleaching trajectory, where the dye completely bleaches, was regarded as the background intensity and was subtracted from intensity values. The number of handles was then determined by dividing the initial intensity of the spots by the bleaching step size.

3.4.3. GEL ANALYSIS

An excess of DY647-labeled oligo complementary to the jubaea linkers on NS was added to the synthesis mixture (for details, see table S2 in the supplementary information). After applying the NS folding procedure explained earlier, each of NS0, NS-HJ, NS6, NS10, NS15, and NS20 was loaded into a lane of 1% agarose gel (Buffer: TBE + 12 mM $MgCl_2$). The gel was run for 3 hours at 80 V while keeping the electrophoresis device on ice and protecting it from external light. The gel was then imaged using a Typhoon™ biomolecular imager. For the visualization of the NS body, the 488 nm fluorescent channel was used, and for visualization of the jubaea handle complementary oligo, the 642 nm channel was selected with a resolution of 200 μm. The bands corresponding to the NS constructs were identified, and their intensities in both channels were quantified using ImageJ by drawing a line over the bands with a thickness set to 6. A plot of pixel value vs. position was created, and the area under the curve for each lane was determined (Fig. 3.2G).

We used the area under the curve of the NS band in each lane in the 488 nm channel as a measure of the number of NS and used it for calibration of the signal obtained from the 642 nm channel. We chose the 642 nm channel signal from NS20 as a reference point and used the following calculations to determine the number of handles in other lanes:

$$N \times \mathrm{NS20}_{488} = \mathrm{NS20}_{488}^{\mathrm{band}}$$

$$N \times 20 \times S_{\mathrm{DY647}} = \mathrm{NS20}_{642}^{\mathrm{band}}$$

where N is the total number of NS in the band, $\mathrm{NS20}_{488}$ is the intensity of individual NS20 in the 488 nm channel, and $\mathrm{NS20}_{488}^{\mathrm{band}}$ is the intensity of the whole band in the 488 nm channel. S_{DY647} is the fluorescent intensity of a single DY647 dye, and $\mathrm{NS20}_{642}^{\mathrm{band}}$ is the total band intensity of NS20 at the 642 nm channel. The number of handles for other constructs can be determined as follows:

$$\text{Number of handles} = 20 \times \frac{\mathrm{NS}_{642}^{\mathrm{band}}}{\mathrm{NS}_{488}^{\mathrm{band}}} \times \frac{\mathrm{NS20}_{488}^{\mathrm{band}}}{\mathrm{NS20}_{642}^{\mathrm{band}}}$$

where $\mathrm{NS}_{642}^{\mathrm{band}}$ and $\mathrm{NS}_{488}^{\mathrm{band}}$ indicate the band intensity of the NS of interest at 642 nm and 488 nm channels, respectively.

3.4.4. FORCE MEASUREMENT ASSAY

These experiments were conducted as described previously [19], including microscope slide coverslip and slide salinization, surface passivation, NS immobilization, and the dynamic MT assay. The data related to the NS-MT interaction type, diffusing NS, and tip tracking NS were obtained from the same assay. All the experiments were conducted at 28°C.

3.4.5. IMAGING AND IMAGE ANALYSIS

The imaging was conducted with a TIRF microscope (Nikon Ti-E microscope) at a nominal temperature of 28°C, which resulted in an actual 26°C on the objective. The spatial resolution of the acquired images was 0.107 μm/pixel, and the temporal resolution varied between 0.5 s to 2 s depending on the experiment and the number of imaged channels (typically 0.8 s for a two-channel acquisition).

All image stacks were corrected for drift using a custom ImageJ macro (available at Github.com) and GDSC SMLM plugin [23]. A custom ImageJ plugin, called Event analyzer, was developed for the categorization of the interactions between MT and NS. This plugin detects the MTs in the field of view using the Filament sensor program [24] and then creates line ROIs (regions of interest) that mark the position of MTs and create kymographs from these ROIs. This plugin allows the user to monitor generated kymographs one by one and categorize them depending on the definitions. The kymographs and the corresponding ROI were automatically saved by this plugin.

Another ImageJ plugin, Force analyzer, was developed to quantify the forces captured by the NS. This plugin uses Gaussian fitting in a user-set segment length to locate the position of the NS on each line of the kymograph and creates a 1 × 1 pixel square ROI at the center of the fitted Gaussian. Then it calculates the median position of these ROIs and takes that as the resting position of the NS. The furthest extension point is determined automatically by the plugin, but the user can change it manually if a wrong point is selected. The amount of force is calculated according to the following equation [19]:

$$F(x) = 0.182e^{3.3x}$$

where F is the force in pN, and x is the NS extension in μm.

The end of depolymerizing MTs in the kymographs was detected using a custom-written ImageJ macro script, called Edge detector. Edge detector works in 3 modes of edge detection: gradient, maximum, and Gaussian fit. The gradient method was used to detect the edges of MTs in the kymographs. The gradient method takes a certain segment length from the user and scans within a rectangle and in a direction determined by the user where the slope of the segment fitted to pixel position and pixel intensity maximizes and identifies that region as the region of maximum gradient. The center of the segment in this region is regarded as the edge, and a point ROI will be created at that site. For the growing MTs, the X scan direction, and for shrinking MTs, the Y scan direction was selected, and a segment size of 3 was used. The coordinates of the detected edges were saved using this macro and further analyzed using a Python script (available at Github.com). This script fits a logistic function to the edge coordinates and uses the derivative of this function to calculate the depolymerization rate at any MT length and then averages these values to report the mean depolymerization rate in the whole shrinking time. The analysis was done separately for NS-bound and bare shrinking MTs.

Edge detector was used for tracking the diffusing NS on the MT lattice, but in Gaussian fit mode. In this mode, it scans line by line within a rectangle determined by the user and fits a Gaussian function to the pixel intensities and creates a point ROI at the center of the fitted Gaussian. The coordinates were saved as a CSV file and further analyzed by a Julia script [12] to calculate MSD values and diffusion coefficient.

This script splits long trajectories into equal overlapping segments (50 seconds) with an offset of 1 datapoint and calculates the MSD for each and returns the average after aligning them. A general diffusion equation was fit to the MSD-time plots as follows:

$$\mathrm{MSD} = 2Dt$$

where D is the diffusion coefficient and t is time.

3.4.6. Electron microscopy

Atomic force microscopy

We obtained images of NS in dry conditions using an AFM from Bruker (Massachusetts, USA) and Scanassyst-Air probes from Bruker. AFM was operated using peakforce-tapping mode and used Gwyddion for processing images. The agarose purified NS was deposited onto a freshly cleaved mica for 30 s and it was washes 3 times with 20 uL of MiliQ and was dried by blowing nitrogen.

Cryo-ET

For electron tomography of NS in presence of GMPCPP-MTs, a 20 µM tubulin solution was supplemented with 1 mM GMPCPP and purified via centrifugation (300,000 ×g, 4°C, 2 minutes). After incubation at 37°C for 30 minutes, unpolymerized tubulin was removed through ultra-centrifugation (300,000 ×g, 37°C, 5 minutes). The microtubules were stored as pellets and resuspended in MRB80 buffer to adjust the concentration.

Microtubules were then mixed with 1 μL of NS solution and 0.01% NP-40 and 10-nm methylated gold particles (Cytodiagnostics CGM5K-10-50) to generate fiducial markers. The solution was deposited onto QUANTIFOIL R 1.2/1.3 Cu 200 grids, which were subsequently blotted using a Vitrobot (Thermo Fisher Scientific) at 22°C with 100% humidity, a blot force of 15, and a duration of 6 seconds. The grids were vitrified with liquid ethane and stored in liquid nitrogen until imaging.

Tilt series acquisition was performed on a Titan Krios G3 (Thermo Fisher Scientific) operating at 300 kV, utilizing a K3 detector in counting mode along with a Quantum-LS energy filter set to a 30 eV slit width. Images were collected at a magnification of 33,000×(pixel size 0̃.26 nm) with defocus values between -2 and -5 µm and a total electron dose of 120 $e^{-}/\text{Å}^{2}$. Tilt angles ranged from -60° to 60° in 2° increments. Data acquisition was conducted using SerialEM.

The recorded image frames were motion-corrected using MotionCor2 [25]. Image processing, including tilt series alignment, contrast transfer function (CTF) correction, gold bead removal, and weighted back-projection, was performed using the Etomo interface of IMOD (v4.11.12).

The tomogram was denoised using TOPAZ-denoise [26] Segmentation of the nanospring and the microtubule was performed using a 2X binned tomogram with the EMAN2 software package [27] The segmented nanosprings were manually traced and visualized using the Segger tool in ChimeraX [28]

3.4.7. Expression, purification and labeling of Ndc80$^{\text{jubaea}}$ constructs

We received the plasmid for the truncated version of Ndc80, jubaea, from [10]. Jubaea is a heterodimer that is made by removing 34% of the coiled coil region of Ndc80 and fusing Hec1 and Spc25 subunits to each other and Nuf2 and Spc24 to each other. Jubaea still contains the Ndc80 loop region, which has been shown to be essential for Ndc80 clustering and formation of force-resistant kinetochore-MT connections [12]. The GST (Glutathione S-transferase) tag on the N-terminal of the Nuf2 domain was used for purification, and a YbbR tag and spy-tag were added to the C-terminal of the Spc24 domain for fluorescent labeling and further bioconjugation. The GST tag was cleaved later by adding 1 v/v % of HRV 3C protease and incubating for 1 h on ice. The sortase tag on the C-terminal of the Spc25 domain was used for fluorescent or DNA labeling (See methods section and Fig. 3.1C). The jubaea construct was further modified to contain a His-tag after the sortase tag as it has been shown to enhance the efficiency of sortase labeling in the presence of Ni^{2+} [29].

"Jubaea" constructs were expressed and purified essentially according to Huis in 't Veld et al., 2019 [10], with the following modifications: complexes were expressed in *Escherichia coli* ER2566 cells (New England Biolabs, fhuA2 lacZ::T7 gene1 [lon] ompT gal sulA11 R(mcr73::miniTn10–Tet^S)2 [dcm] R(zgb-210::Tn10–Tet^S) endA1 Δ(mcrCmrr)114::IS10) co-transformed with a tRNA supplementing plasmid derived from *Escherichia coli* Rosetta™ 2 cells (MerckMillipore). Cells were harvested by centrifugation (10 min 4000 rpm, Beckman JLA8.1000 rotor), washed in PBS (Merck Sigma P4417), resuspended in lysis buffer (50 mM Hepes, pH 8.0, 500 mM NaCl, 10% w/v glycerol, 0.05 mM TCEP, 1 mM EDTA, cOmplete protease inhibitor cocktail) and lysed using a CF1 cell disruptor (Constant Systems) at 20 kpsi, 4°C. Unbroken cells and aggregates were pelleted in a Beckman Ti45 rotor (30 min, 40,000 rpm, 4°C). The clarified lysate was applied to either ~2 ml of Pierce™ Glutathione Superflow Agarose or ~0.5 ml cOmplete™ His-Tag Purification Resin (Sigma) and incubated for one hour while rotating at 4°C. After extensive washing with lysis buffer, Ndc80 complexes were eluted with lysis buffer supplemented with either 10 mM reduced glutathione, 100 mM imidazole, or homemade 3C protease, and concentrated using a MWCO 10 kDa Vivaspin 20 centrifugal concentrator (Merck Sigma Z614610). Size exclusion chromatography was performed on a Superdex 200 Increase 10/300 column (Cytiva 28990944) pre-equilibrated with lysis buffer diluted 1:1 with milliQ.

We used the Sortase tag (LPVTGG) on the C-terminal of the Hec1-Spc25 subunit to label jubaea with triglycinated DNA (GGG-oligo, jubaea handle) and the YbbR tag (GDSLSWLLRLLN) on the C-terminal of the Nuf2-Spc24 subunit to label it with a fluorophore. The items in table 3 were mixed in the mentioned ratios and incubated at 12 or 15°C overnight. Size exclusion was performed post-reaction as explained above, and DNA-labeled jubaea was purified. The percentage of DNA labeling varied between 10 and 20%. DNA-labeled jubaea was then concentrated using a 10 kDa Vivaspin filter, and finally, the GST tag of Nuf2 was cut by adding HRV 3C protease and incubating on ice for 1 hour.

Table 3.1: *Amino acid sequence of jubaea subunits*

Nuf2-Spc24	MSPILGYWKIKGLVQPTRLLLEYLEEKYEEHLYERDEGDKWRNKKFELGLEFPNLPYYIDGDVKLTQSMAIIRYIADKHNMLGGCPKERAEISMLEGAVLDIRYGVSRIAYSKDFETLKVDFLSKLPEMLKMFEDRLCHKTYLNGDHVTHPDFMLYDALDVVLYMDPMCLDAFPKLVCFKKRIEAIPQIDKYLKSSKYIAWPLQGWQATFGGGDHPPKLEVLFQGPMETLSFPRYNVAEIVIHIRNKILTGADGKNLTKNDLYPNPKPEVLHMIYMRALQIVYGIRLEHFYMMPVNSEVMYPHLMEGFLPFSNLVTHLDSFLPICRVNDFETADILCPKAKRTSRFLSGIINFIHFREACRETYMEFLWQYKSSADKMQQLNAAHQEALMKLERLDSVPVEEQEEFKQLSDGIQELQQSLNQDFHQKTIVLQEGNSQKKSNISEKTKRLNELKLSVVSLKEIQESLKTKIVDSPEKLKNYKEKMKDTVQKLKNARQEVVEKYEIYGDSVDCLPSCQLEVQLYQKKIQDLSDNREKLASILKESLNLEDQIESDESELKKLKTEENSFKRLMIVKKEKtEKEVAQSLLNAKEQVHQGGVELQQLEAGLQEAGEEDTRLKASLLQLTRELEELKEIEADLERQEKEVDEDTTVTIPSAVYVAQLYHQVSKIEWDYECEPGMVKGIHHGPSVAQPIHLDSTQLSRKFISDYLWSLVDTEWGDSLSWLLRLLNGSGRGVPHIVMVDAYKRYK
Hec1-Spc25	MKRSSVSSGGAGRLSMQELRSQDVNKQGLYTPQTKEKPTFGKLSINKPTSERKVSLFGKRTSGHGSRNSQLGIFSSSEKIKDPRPLNDKAFIQQCIRQLCEFLTENGYAHNVSMKSLQAPSVKDFLKIFTFLYGFLCPSYELPDTKFEEEVPRIFKDLGYPFALSKSSMYTVGAPHTWPHIVAALVWLIDCIKIHTAMKESSPLFDDGQPWGEETEDGIMHNKLFLDYTIKCYESFMSGADSFDEMNAELQSKLKDLFNVDAFKLESLEAKNRALNEQIARLEQEREKEPNRLESLRKLKASLQGDVQKYQAYMSNLESHSAILDQKLNGLNEEIARVELECETIKQENTRLQNIIDNQKYSVADIERINHERNELQQTINKLTKDLEAEQQKLWNEELKYARGKEAIETQLAEYHKLARKLKLIPKGAENSKGYDFEIKFNPEAGANCLVKYRAQVYVPLKELLNETEEEINKALNKKMGLEDTLEQLNAMITESKRSVRTLKEERMVEMFLEYQNQISRQNKLIQEKKDNLLKLIAEVKGKKQELEVLTANIQDLKEEYSRKKETISTANKANAERLKRLQKSADLYKDRLGLEIRKIYGEKLQFIFTNIDPKNPESPFMFSLHLNEARDYEVSDSAPHLEGLAEFQENVRKTNNFSAFLANVRKAFTATVYNLPVTGGHHHHHH

PREPARATION OF FLUORESCENTLY LABELED CoA

5 μL of 10 mM Atto647N-maleimide was added to 45 μL DMSO and added to 50 μL of 0.91 mM Co-enzyme A (CoA) dissolved in 100 mM sodium phosphate pH 7.0 and incubated for 15 min at room temperature. Then 0.2 μL of 0.5 M TCEP was added to the mixture and incubated 60 min at room temperature. Finally, the reaction was quenched by adding 0.33 μL of 1 M DTT.

We used the same protocol described in [18] for the purification of T1S3 constructs, except in this study jubaea was used instead of Ndc80.

Table 3.2: *List of the plasmids used in this study*

Plasmid	CasI	CasII	Reference / nickname
pGEX 2-rbs Ndc80^{jubaea}	GST-3C-NUF2$^{(1\text{-}351)}$-SPC24$^{(59\text{-}197)}$-Spy	NDC80$^{(1\text{-}506)}$-SPC25$^{(54\text{-}224)}$	(Huis in 't Veld et al., 2019)
pED74	GST-3C-NUF2$^{(1\text{-}351)}$-SPC24$^{(59\text{-}197)}$-Spy	NDC80$^{(1\text{-}506)}$-SPC25$^{(54\text{-}224)}$-SrtA	"Jubaea-SrtA"
pED89	GST-3C-NUF2$^{(1\text{-}351)}$-SPC24$^{(59\text{-}197)}$-YbbR-Spy	NDC80$^{(1\text{-}506)}$-SPC25$^{(54\text{-}224)}$-SrtA	"Jubaea-double tag"
pED138	GST-3C-NUF2$^{(1\text{-}351)}$-SPC24$^{(59\text{-}197)}$-YbbR-Spy	NDC80$^{(1\text{-}506)}$-SPC25$^{(54\text{-}224)}$-SrtA-His6	"Jubaea-double tag -His"

Table 3.3: *The reaction mixes for labeling jubaea with DNA and fluorophores*

Components	MW (kDa)	Stock Conc. (μM)	Volume (μL)	Amount (pmol)	Final Conc. (μM)	Ratio
Jubaea	164	10	200	2000	8.5	1
Sortase A	18	165	2.4	400	1.7	0.2
GGG-oligo	10	1000	10	10000	42	5
Sfp phospho-pantetheinyl transferase	26	74	4	300	1.3	0.15
CoA-Atto568	1.5	500	20	10000	42	5

ACKNOWLEDGMENTS

We thank Vladimir Volkov for his valuable discussions, suggestions, and constructive advice, as well as for providing feedback on the text and overall structure, redesigning figures, and offering suggestions for experiments. We are grateful to Pim J. Huis in 't Veld for kindly providing us with the Jubaea plasmid. We also thank Mitsuhiro Iwaki for his helpful communication and for answering our questions regarding the nanospring.

SUPPLEMENTARY INFORMATION

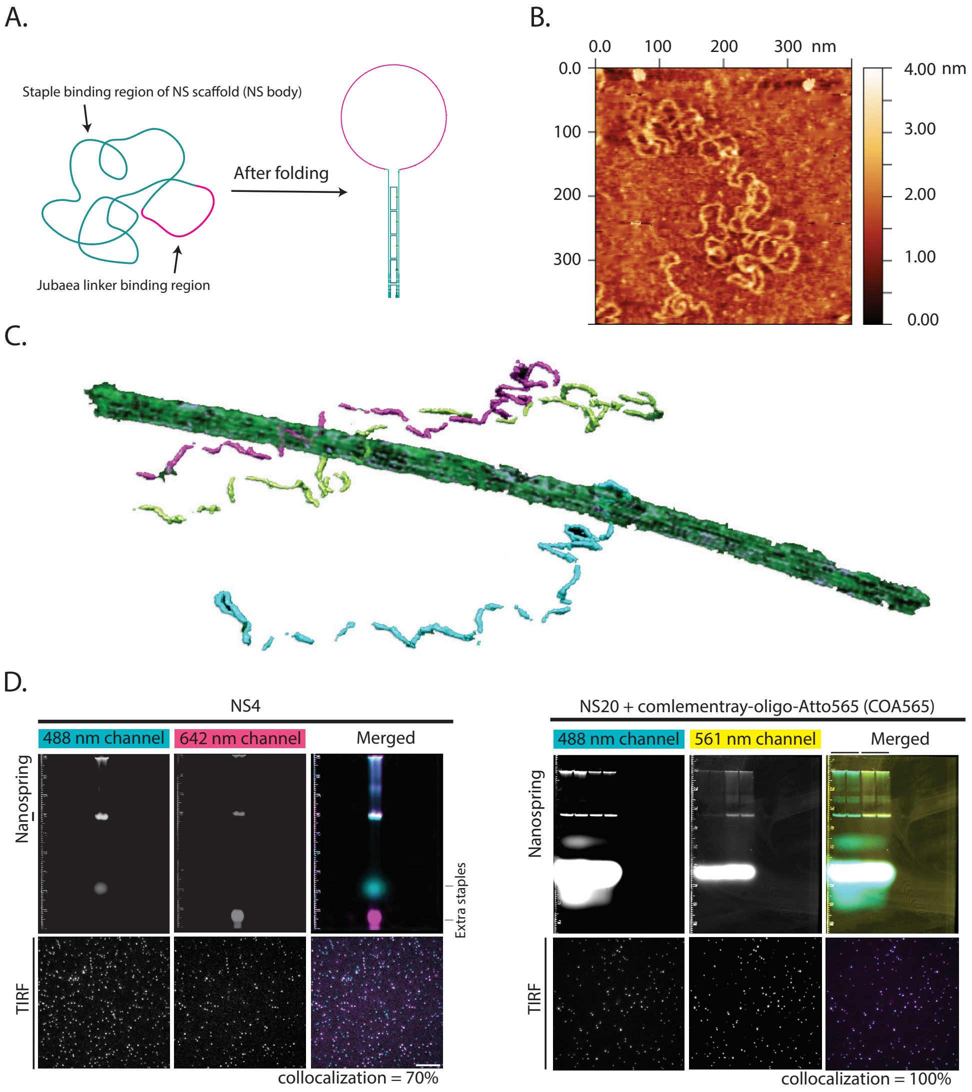

Figure S3.1: *(A) From 7560b of the M13mp18 ssDNA 7000 bases were used as a scaffold for folding NS and the rest were used as a platform to hybridize jubaea linker oligos. (B) AFM image of a an NS. (C) Cryo-ET images of NS (cyan, light green and magenta) next to an MT (dark green). (D) Top row: agarose gel electrophoresis performed on NS4. The signal at 488 nm channel originates from NS body and the signal at 642 nm comes from the jubaea linker. The colocalization of the two signals illustrates that they are connected to each other. Lower row: TIRF images of NS taken at 488nm and 642 nm channels. The merged image shows their colocalization of the fluorescent signal. (E) Agarose gel electrophoresis of NS20 (488 nm channel), with (lanes 3 and 4) and without (lanes 1 and 2) fluorescently labeled oligo complementary to jubaea linkers (561 nm channel). The lower row shows TIRF images showing NS body (488 nm channel) and the bound complementary oligonucleotide. With this method, all of the observed NS on the surface were colocalized with the signal coming from jubaea linker complementary handle.*

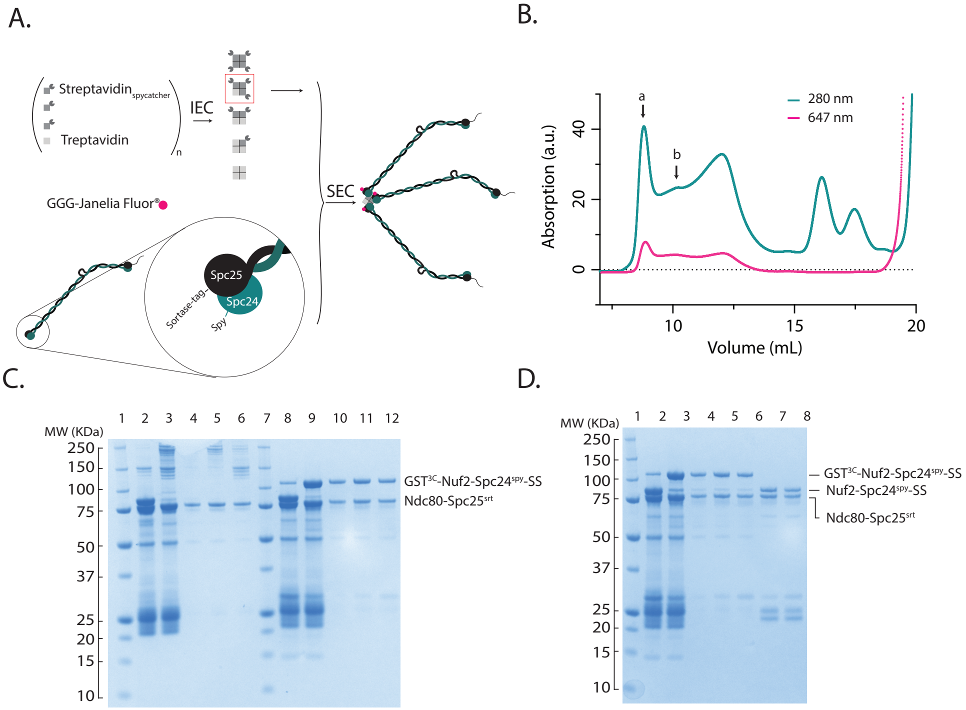

Figure S3.2: *Synthesis and purification of T1[S-jubaea]3 . (A) Schematic representation of the T1[S-jubaea]3 assembly reaction. The subunits of streptavidin were modified to contain a spyCathcer (S) and were mixed into a wildetype subunit (T) with 3:1 ratio. T1S3 was purified by ion exchange chromatography. T1S3 was reacted with spy-tagged jubaea and the resulting T1[S-jubaea]3 construct was purified using size exclusion chromatography (SEC). (B) Chromatogram showing absorbance at 280 nm and 642 nm for eluted fractions of T1[S-jubaea]3 assembly reaction mixture. Pick a indicates the fraction containing T1[S-jubaea]3 construct. (C) Polyacrylamide gel electrophoresis of T1[S-jubaea]3 at different stages of modification. Lane 1 & 7: MW marker, lane 2: pre-reaction assembly, lane 3: post-reaction assembly, lane 4: void peak of SEC, lane 5: peak a of SEC, lane 6: peak b of SEC, lanes 8, 9, 10, 11, 12: same as 2, 3, 4, 5, 6 but after boiling the sample with SDS. (D) Polyacrylamide gel electrophoresis of T1[S-jubaea]3 at different stages of modification. Lanes 1-6: same as lanes 7-12 in the gel on panel C. Lane 7: peak a of SEC after 3C protease treatment (GST removal), lane 8: peak b of SEC after 3C protease treatment. All samples were boiled with SDS before loading them into the gel.*

The DNA sequence of M13mp18 (7560b):

GAAAAACCACCCTGGCGCCCAATACGCAAACCGCCTCTCCCCGCGCGTTGGCCGATTCATTAATGCAGCTGGCACGACAGGTTTCCCGACTGGAAAGCGGGCAGTGAGCGCAA
CGCAATTAATGTGAGTTAGCTCACTCATTAGGCACCCCAGGCTTTACACTTTATGCTTCCGGCTCGTATGTTGTGTGGAATTGTGAGCGGATAACAATTTCACACAGGAAACAGCTAT
GACCATGATTACGAATTCGAGCTCGGTACCCGGGGATCCTCCGTCTTTATCGAGGTAACAAGCACCACGTAGCTTAAGCCCTGTTTACTCATTACACCAACCAGGAGGTCAGAGTTCG
GAGAAATGATTTATGTGAAATGCGTCAGCCGATTCAAGGCCCCTATATTCGTGCCCACCGACGAGTTGCTTACAGATGGCAGGGCCGCACTGTCGGTATCATAGAGTCACTCCAGGG
CGAGCGTAAATAGATTAGAAGCGGGGTTATTTTGGCGGGACATTGTCATAAGGTTGACAATTCAGCACTAAGGACACTTAAGTCGTGCGCATGAATTCACAACCACTTAGAAGAACAT
CCACCCTGGCTTCTCCTGAGAAAGCTTGGCACTGGCCGTCGTTTTACAACGTCGTGACTGGGAAAACCCTGGCGTTACCCAACTTAATCGCCTTGCAGCACATCCCCCTTTCGCCAG
CTGGCGTAATAGCGAAGAGGCCCGCACCGATCGCCCTTCCCAACAGTTGCGCAGCCTGAATGGCGAATGGCGCTTTGCCTGGTTTCCGGCACCAGAAGCGGTGCCGGAAAGCTGGC
TGGAGTGCGATCTTCCTGAGGCCGATACTGTCGTCGTCCCCTCAAACTGGCAGATGCACGGTTACGATGCGCCCATCTACACCAACGTGACCTATCCCATTACGGTCAATCCGCCGT
TTGTTCCCACGGAGAATCCGACGGGTTGTTACTCGCTCACATTTAATGTTGATGAAAGCTGGCTACAGGAAGGCCAGACGCGAATTATTTTTGATGGCGTTCCTATTGGTTAAAAAAT
GAGCTGATTTAACAAAAATTTAATGCGAATTTTAACAAAATATTAACGTTTACAATTTAAATATTTGCTTATACAATCTTCCTGTTTTTGGGGCTTTTCTGATTATCAACCGGGGTACATA
TGATTGACATGCTAGTTTTACGATTACCGTTCATCGATTCTCTTGTTTGCTCCAGACTCTCAGGCAATGACCTGATAGCCTTTGTAGATCTCTCAAAAATAGCTACCCTCTCCGGCATT
AATTTATCAGCTAGAACGGTTGAATATCATATTGATGGTGATTTGACTGTCTCCGGCCTTTCTCACCCTTTTGAATCTTTACCTACACATTACTCAGGCATTGCATTTAAAATATATGAG
GGTTCTAAAAATTTTTATCCTTGCGTTGAAATAAAGGCTTCTCCCGCAAAAGTATTACAGGGTCATAATGTTTTTGGTACAACCGATTTAGCTTTATGCTCTGAGGCTTTATTGCTTAAT
TTTGCTAATTCTTTGCCTTGCCTGTATGATTTATTGGATGTTAATGCTACTACTATTAGTAGAATTGATGCCACCTTTTCAGCTCGCGCCCCAAATGAAAATATAGCTAAACAGGTTATT
GACCATTTGCGAAATGTATCTAATGGTCAAACTAAATCTACTCGTTCGCAGAATTGGGAATCAACTGTTATATGGAATGAAACTTCCAGACACCGTACTTTAGTTGCATATTTAAAACAT
GTTGAGCTACAGCATTATATTCAGCAATTAAGCTCTAAGCCATCCGCAAAAATGACCTCTTATCAAAAGGAGCAATTAAAGGTACTCTCTAATCCTGACCTGTTGGAGTTTGCTTCCGG
TCTGGTTCGCTTTGAAGCTCGAATTAAAACGCGATATTTGAAGTCTTTCGGGCTTCCTCTTAATCTTTTTGATGCAATCCGCTTTGCTTCTGACTATAATAGTCAGGGTAAAGACCTGA
TTTTTGATTTATGGTCATTCTCGTTTTCTGAACTGTTTAAAGCATTTGAGGGGGATTCAATGAATATTTATGACGATTCCGCAGTATTGGACGCTATCCAGTCTAAACATTTTACTATTA
CCCCCTCTGGCAAAACTTCTTTTGCAAAAGCCTCTCGCTATTTTGGTTTTTATCGTCGTCTGGTAAACGAGGGTTATGATAGTGTTGCTCTTACTATGCCTCGTAATTCCTTTTGGCGT
TATGTATCTGCATTAGTTGAATGTGGTATTCCTAAATCTCAACTGATGAATCTTTCTACCTGTAATAATGTTGTTCCGTTAGTTCGTTTTATTAACGTAGATTTTTCTTCCCAACGTCCT
GACTGGTATAATGAGCCAGTTCTTAAAATCGCATAAGGTAATTCACAATGATTAAAGTTGAAATTAAACCATCTCAAGCCCAATTTACTACTCGTTCTGGTGTTTCTCGTCAGGGCAAG
CCTTATTCACTGAATGAGCAGCTTTGTTACGTTGATTTGGGTAATGAATATCCGGTTCTTGTCAAGATTACTCTTGATGAAGGTCAGCCAGCCTATGCGCCTGGTCTGTACACCGTTC
ATCTGTCCTCTTTCAAAGTTGGTCAGTTCGGTTCCCTTATGATTGACCGTCTGCGCCTCGTTCCGGCTAAGTAACATGGAGCAGGTCGCGGATTTCGACACAATTTATCAGGCGATGA
TACAAATCTCCGTTGTACTTTGTTTCGCGCTTGGTATAATCGCTGGGGGTCAAAGATGAGTGTTTTAGTGTATTCTTTTGCCTCTTTCGTTTTAGGTTGGTGCCTTCGTAGTGGCATTA
CGTATTTTACCCGTTTAATGGAAACTTCCTCATGAAAAAGTCTTTAGTCCTCAAAGCCTCTGTAGCCGTTGCTACCCTCGTTCCGATGCTGTCTTTCGCTGCTGAGGGTGACGATCCC
GCAAAAGCGGCCTTTAACTCCCTGCAAGCCTCAGCGACCGAATATATCGGTTATGCGTGGGCGATGGTTGTTGTCATTGTCGGCGCAACTATCGGTATCAAGCTGTTTAAGAAATTCA
CCTCGAAAGCAAGCTGATAAACCGATACAATTAAAGGCTCCTTTTGGAGCCTTTTTTTTGGAGATTTTCAACGTGAAAAAATTATTATTCGCAATTCCTTTAGTTGTTCCTTTCTATTCT
CACTCCGCTGAAACTGTTGAAAGTTGTTTAGCAAAATCCCATACAGAAAATTCATTTACTAACGTCTGGAAAGACGACAAAACTTTAGATCGTTACGCTAACTATGAGGGCTGTCTGTG
GAATGCTACAGGCGTTGTAGTTTGTACTGGTGACGAAACTCAGTGTTACGGTACATGGGTTCCTATTGGGCTTGCTATCCCTGAAAATGAGGGTGGTGGCTCTGAGGGTGGCGGTTC
TGAGGGTGGCGGTTCTGAGGGTGGCGGTACTAAACCTCCTGAGTACGGTGATACACCTATTCCGGGCTATACTTATATCAACCCTCTCGACGGCACTTATCCGCCTGGTACTGAGCA
AAACCCCGCTAATCCTAATCCTTCTCTTGAGGAGTCTCAGCCTCTTAATACTTTCATGTTTCAGAATAATAGGTTCCGAAATAGGCAGGGGGCATTAACTGTTTATACGGGCACTGTTA
CTCAAGGCACTGACCCCGTTAAAACTTATTACCAGTACACTCCTGTATCATCAAAAGCCATGTATGACGCTTACTGGAACGGTAAATTCAGAGACTGCGCTTTCCATTCTGGCTTTAAT
GAGGATTTATTTGTTTGTGAATATCAAGGCCAATCGTCTGACCTGCCTCAACCTCCTGTCAATGCTGGCGGCGGCTCTGGTGGTGGTTCTGGTGGCGGCTCTGAGGGTGGTGGCTC
TGAGGGTGGCGGTTCTGAGGGTGGCGGCTCTGAGGGAGGCGGTTCCGGTGGTGGCTCTGGTTCCGGTGATTTTGATTATGAAAAGATGGCAAACGCTAATAAGGGGGCTATGACCG
AAAATGCCGATGAAAACGCGCTACAGTCTGACGCTAAAGGCAAACTTGATTCTGTCGCTACTGATTACGGTGCTGCTATCGATGGTTTCATTGGTGACGTTTCCGGCCTTGCTAATGG
TAATGGTGCTACTGGTGATTTTGCTGGCTCTAATTCCCAAATGGCTCAAGTCGGTGACGGTGATAATTCACCTTTAATGAATAATTTCCGTCAATATTTACCTTCCCTCCCTCAATCGG
TTGAATGTCGCCCTTTTGTCTTTGGCGCTGGTAAACCATATGAATTTTCTATTGATTGTGACAAAATAAACTTATTCCGTGGTGTCTTTGCGTTTCTTTTATATGTTGCCACCTTTATGT
ATGTATTTTCTACGTTTGCTAACATACTGCGTAATAAGGAGTCTTAATCATGCCAGTTCTTTTGGGTATTCCGTTATTATTGCGTTTCCTCGGTTTCCTTCTGGTAACTTTGTTCGGCTA
TCTGCTTACTTTTCTTAAAAAGGGCTTCGGTAAGATAGCTATTGCTATTTCATTGTTTCTTGCTCTTATTATTGGGCTTAACTCAATTCTTGTGGGTTATCTCTCTGATATTAGCGCTCA
ATTACCCTCTGACTTTGTTCAGGGTGTTCAGTTAATTCTCCCGTCTAATGCGCTTCCCTGTTTTTATGTTATTCTCTCTGTAAAGGCTGCTATTTTCATTTTTGACGTTAAACAAAAAAT
CGTTTCTTATTTGGATTGGGATAAATAATATGGCTGTTTATTTTGTAACTGGCAAATTAGGCTCTGGAAAGACGCTCGTTAGCGTTGGTAAGATTCAGGATAAAATTGTAGCTGGGTGC
AAAATAGCAACTAATCTTGATTTAAGGCTTCAAAACCTCCCGCAAGTCGGGAGGTTCGCTAAAACGCCTCGCGTTCTTAGAATACCGGATAAGCCTTCTATATCTGATTTGCTTGCTAT
TGGGCGCGGTAATGATTCCTACGATGAAAATAAAAACGGCTTGCTTGTTCTCGATGAGTGCGGTACTTGGTTTAATACCCGTTCTTGGAATGATAAGGAAAGACAGCCGATTATTGAT
TGGTTTCTACATGCTCGTAAATTAGGATGGGATATTATTTTTCTTGTTCAGGACTTATCTATTGTTGATAAACAGGCGCGTTCTGCATTAGCTGAACATGTTGTTTATTGTCGTCGTCT
GGACAGAATTACTTTACCTTTTGTCGGTACTTTATATTCTCTTATTACTGGCTCGAAAATGCCTCTGCCTAAATTACATGTTGGCGTTGTTAAATATGGCGATTCTCAATTAAGCCCTAC
TGTTGAGCGTTGGCTTTATACTGGTAAGAATTTGTATAACGCATATGATACTAAACAGGCTTTTTCTAGTAATTATGATTCCGGTGTTTATTCTTATTTAACGCCTTATTTATCACACGG
TCGGTATTTCAAACCATTAAATTTAGGTCAGAAGATGAAATTAACTAAAATATATTTGAAAAAGTTTTCTCGCGTTCTTTGTCTTGCGATTGGATTTGCATCAGCATTTACATATAGTTAT
ATAACCCAACCTAAGCCGGAGGTTAAAAAGGTAGTCTCTCAGACCTATGATTTTGATAAATTCACTATTGACTCTTCTCAGCGTCTTAATCTAAGCTATCGCTATGTTTTCAAGGATTCT
AAGGGAAAATTAATTAATAGCGACGATTTACAGAAGCAAGGTTATTCACTCACATATATTGATTTATGTACTGTTTCCATTAAAAAAGGTAATTCAAATGAAATTGTTAAATGTAATTAAT
TTTGTTTTCTTGATGTTTGTTTCATCATCTTCTTTTGCTCAGGTAATTGAAATGAATAATTCGCCTCTGCGCGATTTTGTAACTTGGTATTCAAAGCAATCAGGCGAATCCGTTATTGTT
TCTCCCGATGTAAAAGGTACTGTTACTGTATATTCATCTGACGTTAAACCTGAAAATCTACGCAATTTCTTTATTTCTGTTTTACGTGCAAATAATTTTGATATGGTAGGTTCTAACCCT
TCCATTATTCAGAAGTATAATCCAAACAATCAGGATTATATTGATGAATTGCCATCATCTGATAATCAGGAATATGATGATAATTCCGCTCCTTCTGGTGGTTTCTTTGTTCCGCAAAAT
GATAATGTTACTCAAACTTTTAAAATTAATAACGTTCGGGCAAAGGATTTAATACGAGTTGTCGAATTGTTTGTAAAGTCTAATACTTCTAAATCCTCAAATGTATTATCTATTGACGGC
TCTAATCTATTAGTTGTTAGTGCTCCTAAAGATATTTTAGATAACCTTCCTCAATTCCTTTCAACTGTTGATTTGCCAACTGACCAGATATTGATTGAGGGTTTGATATTTGAGGTTCAG
CAAGGTGATGCTTTAGATTTTTCATTTGCTGCTGGCTCTCAGCGTGGCACTGTTGCAGGCGGTGTTAATACTGACCGCCTCACCTCTGTTTTATCTTCTGCTGGTGGTTCGTTCGGTA
TTTTTAATGGCGATGTTTTAGGGCTATCAGTTCGCGCATTAAAGACTAATAGCCATTCAAAAATATTGTCTGTGCCACGTATTCTTACGCTTTCAGGTCAGAAGGGTTCTATCTCTGTT
GGCCAGAATGTCCCTTTTATTACTGGTCGTGTGACTGGTGAATCTGCCAATGTAAATAATCCATTTCAGACGATTGAGCGTCAAAATGTAGGTATTTCCATGAGCGTTTTTCCTGTTGC
AATGGCTGGCGGTAATATTGTTCTGGATATTACCAGCAAGGCCGATAGTTTGAGTTCTTCTACTCAGGCAAGTGATGTTATTACTAATCAAAGAAGTATTGCTACAACGGTTAATTTGC
GTGATGGACAGACTCTTTTACTCGGTGGCCTCACTGATTATAAAAACACTTCTCAGGATTCTGGCGTACCGTTCCTGTCTAAAATCCCTTTAATCGGCCTCCTGTTTAGCTCCCGCTCT
GATTCTAACGAGGAAAGCACGTTATACGTGCTCGTCAAAGCAACCATAGTACGCGCCCTGTAGCGGCGCATTAAGCGCGGCGGGTGTGGTGGTTACGCGCAGCGTGACCGCTACAC
TTGCCAGCGCCCTAGCGCCCGCTCCTTTCGCTTTCTTCCCTTCCTTTCTCGCCACGTTCGCCGGCTTTCCCCGTCAAGCTCTAAATCGGGGGCTCCCTTTAGGGTTCCGATTTAGTG
CTTTACGGCACCTCGACCCCAAAAAACTTGATTTGGGTGATGGTTCACGTAGTGGGCCATCGCCCTGATAGACGGTTTTTCGCCCTTTGACGTTGGAGTCCACGTTCTTTAATAGTGG
ACTCTTGTTCCAAACTGGAACAACACTCAACCCTATCTCGGGCTATTCTTTTGATTTATAAGGGATTTTGCCGATTTCGGAACCACCATCAAACAGGATTTTCGCCTGCTGGGGCAAAC
CAGCGTGGACCGCTTGCTGCAACTCTCTCAGGGCCAGGCGGTGAAGGGCAATCAGCTGTTGCCCGTCTCACTGGTGAAAA

Table S3.1: *The sequence of staples in the base part of the NS. The staples colored in cyan show the Atto488 labeled staples.*

Staple position	Sequence
1	CTTAATGCGCCGCTACAGGGCGCGTACTACGTATTGGGCGCCAGGGTGGTTTTTC (Dig-labelled)
2	AATAATTTTTGTAAATGAATTTTCTGTATGGGATTTTGAATTGCGAAT
3	ATCTCCAAAAGTTTTGTCGTCTTTCCAGACGTTATCACGTTGAAA
4	AAAGGAGCCTCCCTCATAGTTAGCGTAACGATCTAAAAAAAGGCTCCA
5	GGTTTATCAGACGCCTGTAGCATTCCACAGACAGTTAATTGTATC
6	GGTGAATTTCTGAGTTTCGTCACCAGTACAAACTACACTTGCTTTCGA
7	GATACCGATAATAGGAACCCATGTACCGTAACACTTAAACAGCTT
8	AATGACAACACCCTCATTTTCAGGGATAGCAAGCCCAGTTGCGCCGAC
9	CGCATAACCGGAACCGCCACCCTCAGAGCCACCAACCATCGCCCA
10	CGCTGAGGCTCCGCCACCCTCAGAACCGCCACCCTCAATATATTCGGT
11	AAAGGCCGCTTCACCGTACTCAGGAGGTTTAGTATGCAGGGAGTT
12	GTCACCCTCAATATAAGTATAGCCCGGAATAGGTGTATTTGCGGGATC
13	CAGCATCGGAGGATAAGTGCCGTCGAGAGGGTTGGCAGCGAAAGA
14	AACGGCTACATTAGCGGGGTTTTGCTCAGTACCAGGCACGAGGGTAGC
15	GACTAAAGACGACTCCTCAAGAGAAGGATTAGGAGAGGCTTTGAG
16	GAAGTTTCCATGAAACATGAAAGTATTAAGAGGCTGATTTTTCATGAG
17	AAATACGTAATGCCTATTTCGGAACCTATTATTCTTAAACGGGTA
18	AGGCACCAACGTGCCCGTATAAACAGTTAATGCCCCCTGCCACTACGA
19	GAGGCAAAAGACGGGGTCAGTGCCTTGAGTAACACTAAAACGAAA
20	ACACTCATCTACAGGAGTGTACTGGTAATAAGTTTTAAATACACTAAA
21	CGATTATACCGCGTCATACATGGCTTTTGATGATTTGACCCCCAG
22	AAAGTACAACCAGTCTCTGAATTTACCGTTCCAGTAAAAGCGCGAAAC
23	TCATCGCCTGTCATTAAAGCCAGAATGGAAAGCGGGAGATTTGTA
24	CGAAATCCGCCCTTGATATTCACAAACAAATAAATCCATAAATTGTGT
25	TGTTACTTAGGGTTGAGGCAGGTCAGACGATTGGGACCTGCTCCA
26	CGCAGACGGTCCAGAGCCGCCGCCAGCATTGACAGGACCGGAACGAGG
27	GAACCGAACTTCAGAGCCGCCACCAGAACCACCACAATCATAAGG
28	AAAGAGGACAGAACCGCCACCCTCAGAGCCACCACCCGACCAACTTTG
29	TACAGACCAGCCTCCCTCAGAGCCGCCACCCTCAGATGAACGGTG
30	GGCTGACCTTCCGGAACCAGAGCCACCACCGGAACCGGCGCATAGGCT
31	ATCTTGACAAGCCATCTTTTCATAATCAAAATCACATCAAGAGTA
32	TCATTACCCATCGGTCATAGCCCCCTTATTAGCGTTTGAACCGGATAT
33	CAAAGCTGCTTGTAGCGCGTTTTCATCGGCATTTAATCAACGTAA
34	TAAGGCTTGCGAATCAAGTTTGCCTTTAGCGTCAGACCATTCAGTGAA
35	ACACCAGAACGCAGCACCGTAATCAGTAGCGACACCTGACGAGAA
36	TGGGCTTGAGGAAACGTCACCAATGAAACCATCGATAGAGTAGTAAAT
37	TCAACTTTAAGCACCATTACCATTAGCAAGGCCGATGGTTTAATT
38	TACCTTATGCGAATTAGAGCCAGCAAAATCACCAGTATCATTGTGAAT
39	CTGGCTCATTCCGTCACCGACTTGAGCCATTTGGGATTTTAAGAA
40	GACGTTGGGAAAATTATTCATTAAAGGTGAATTATCAATACCAGTCAG
41	CGTTAATAAAGGGAGGGAAGGTAAATATTGACGGAGAAAAATCTA
42	GAACAACATTACAAAAGGGCGACATTCAACCGATTGAACGAACTAACG
43	AAAGATTCATTCATATGGTTTACCAGCGCCAAAGATTACAGGTAG
44	TAGGAATACCTTTATTTTGTCACAATCAATAGAAAATCAGTTGAGATT
45	ATGCAGATACAACGCAAAGACACCACGGAATAAGACATTCAACTA
46	AGGAATTACGTACATAAAGGTGGCAACATATAAAAGAATAACGCCAAA
47	GAGCAACACTATGTTAGCAAACGTAGAAAATACAAGGCATAGTAA
48	CGTTTACCAGCATGATTAAGACTCCTTATTACGCAGTATCATAACCCT
49	AACCAAAATATAACGGAATACCCAAAAGAACTGGACGACGATAAA
50	TTGCAAAAGACAGAAGGAAACCGAGGAAACGCAATAAGCGAGAGGCTT
51	AGGGGGTAATAAGCAGATAGCCGAACAAAGTTACAGTTTTGCCAG

Continued on next page

Table S3.1 – continued from previous page

Staple position	**Sequence**
52	TAGACTGGATCTTACCGAAGCCCTTTTTAAGAAAAGTAGTAAAATGTT
53	CTGCGGAATCAAACAATGAAATAGCAATAGCTATAGCGTCCAATA
54	TCATTGAATCTGAGTTAAGCCCAATAATAAGAGCAAGGTCATAAATAT
55	CTTTAAACAGATCAGAGAGATAACCCACAAGAATCCCCTCAAATG
56	AGAATGACCAAAAGTCAGAGGGTAATTGAGCGCTAATTTCAGAAAACG
57	TCAGGTCTTTGAGAATTAACTGAACACCCTGAACTAAATCAAAAA
58	TATAGTCAGAATAAAAACAGGGAAGCGCATTAGACGGACCCTGACTAT
59	TTGCATCAAAAGCAGCCTTTACAGAGAGAATAACAGCAAAGCGGA
60	GAAGCCCGAATTTTTGTTTAACGTCAAAAATGAAAATAAGATTAAGAG
61	ATCGCGTTTTATCCCAATCCAAATAAGAAACGATAGACTTCAAAT
62	CAAAGCGAACGTTACAAAATAAACAGCCATATTATTTAATTCGAGCTT
63	CAAACTCCAAGTCTTTCCAGAGCCTAATTTGCCACAGACCGGAAG
64	TAGAGAGTACTCCTGAATCTTACCAACGCTAACGAGCCAGGTCAGGAT
65	CCTTTTGATAATTTTGCACCCAGCTACAATTTTACTTTAATTGCT
66	TTGCGGATGGTGAAGCCTTAAATCAAGATTAGTTGCTAGAGGTCATTT
67	ATTGCTGAATAACCTCCCGACTTGCGGGAGGTTTCTTAGAGCTTA
68	GCTCAACATGATTCTAAGAACGCGAGGCGTTTTAGCGATAATGCTGTA
69	CAACTAAAGTTCAGATATAGAAGGCTTATCCGGTTTTTAAATATG
70	AAGTTTCATTTCATTACCGCGCCCAATAGCAAGCAAAACGGTGTCTGG
71	TTGATTCCCACCGTTTTTATTTTCATCGTAGGAACCATATAACAG
72	GAGTAGATTTGTACCGCACTCATCGAGAACAAGCAAGATTCTGCGAAC
73	TAGATACATTTTCCAAGAACGGGTATTAAACCAAAGTTTGACCAT
74	CAATAACCTGTCAATAATCGGCTGTCTTTCCTTATCATCGCAAATGGT
75	TTTCATTTGGAATTTACGAGCATGTAGAAACCAATTTAGCTATAT
76	AAAAGGTGGCTGAACAAGAAAAATAATATCCCATCCTGGCGCGAGCTG
77	TAATAGTAGTTGTTTATCAACAATAGATAAGTCCATCAATTCTAC
78	CCAATAAATCACATGTTCAGCTAATGCAGAACGCGCCAGCATTAACAT
79	GCAAAGAATTCTGTCCAGACGACGACAATAAACAATACAGGCAAG
80	GCAATAAAGCAAAGTACCGACAAAAGGTAAAGTAATTAGCAAAATTAA
81	AAGCTAAATCTTCGAGCCAGTAATAAGAGAATATCTCAGAGCATA
82	AAACATTATGCCAACATGTAATTTAGGCAGAGGCATTGGTTGTACCAA
83	CTTTTGCGGGTGAGAATCGCCATATTTAACAACGACCCTGTAATA
84	TTTCAACGCAAGCCAACGCTCAACAGTAGGGCTTAATAGAAGCCTTTA
85	TTTTAGAACCTTATACAAATTCTTACCAGTATAAAGGATAAAAAT
86	TAAATGCAATGAAAAAGCCTGTTTAGTATCATATGCGCTCATATATTT
87	GTGTAGGTAATAAACACCGGAATCATAATTACTAGCCTGAGTAAT
88	GGTGAGAAAGTGTGATAAATAAGGCGTTAAATAAGAAAGATTCAAAAG
89	TCAAATCACCTTTAATGGTTTGAAATACCGACCGGCCGGAGACAG
90	ATTCAACCGTTTAGTTAATTTCATCTTCTGACCTAAAATCAATATGAT
91	AATTAATGCCCGAGAAAACTTTTTCAAATATATTTCTAGCTGATA
92	CTATTTTTGAGCAAATCCAATCGCAAGACAAAGAACGGGAGAGGGTAG
93	AGGCTATCAGATATAACTATATGTAAATGCTGATGAGATCTACAA
94	AGAGTCTGGATTTTTAACCTCCGGCTTAGGTTGGGTTGTCATTGCCTG
95	AATCGATGAAAAATCATAGGTCTGAGAGACTACCGCAAACAAGAG
96	AAACTAGCATTGAGAAGAGTCAATAGTGAATTTATCACGGTAATCGTA
97	GTACCCCGGTTAGCGATAGCTTAGATTAAGACGCGTCAATCATAT
98	AAAGCCCCAAAATTTTCCCTTAGAATCCTTGAAAACATGATAATCAGA
99	TTGTATAAGCTTCTGTAAATCGTCGCTATTAATTAAACAGGAAGA
100	TTGTAAACGTTCAATATATGTGAGTGAATAACCTTGCAAATATTTAAA
101	TAAAATTCGCTTTTTAATGGAAACAGTACATAAATAATATTTTGT
102	GTTAAATCAGCATTTAACAATTTCATTTGAATTACCTATTAAATTTTT
103	ACCAATAGGAACATCAAGAAAACAAAATTAATTACTCATTTTTTA
104	AATAATTCGCCCTGAGCAAAAGAAGATGATGAAACAAACGCCATCAAA
105	CTGTAGCCAGGAGGCGAATTATTCATTTCAATTAGTCTGGCCTTC

Continued on next page

Table S3.1 – continued from previous page

Staple position	Sequence
106	ATTAAATGTGTTGAATACCAAGTTACAAAATCGCGCACTTTCATCAAC
107	ACCCGTCGGACAATAACGGATTCGCCTGATTGCTAGCGAGTAACA
108	AACAAACGGCTAACAGTACCTTTTACATCGGGAGAAATTCTCCGTGGG
109	AATGGGATAGGTTTAACGTCAGATGAATATACAGGGATTGACCGT
110	GTAGATGGGCAAATAAAGAAATTGCGTAGATTTTCAGGTCACGTTGGT
111	GTGCATCTGCCAAAATTATTTGCACGTAAAACAGGCATCGTAACC
112	GACGACGACATAATGGAAGGGTTAGAACCTACCATATCAGTTTGAGGG
113	AGGAAGATCGGATTGTTTGGATTATACTTCTGAAGTATCGGCCTC
114	GCTTTCCGGCATGATGGCAATTCATCAATATAATCCTCACTCCAGCCA
115	TGCCGGAAACTATCATCATATTCCTGATTATCAGACCGCTTCTGG
116	CCATTCGCCACAAAGAAACCACCAGAAGGAGCGGAATCAGGCAAAGCG
117	CAACTGTTGGGAGTAACATTATCATTTTGCGGAATTCAGGCTGCG
118	GGTGCGGGCCCCCGAACGTTATTAATTTTAAAAGTTTGAAGGGCGATC
119	ACGCCAGCTGCGACAACTCGTATTAAATCCTTTGTCTTCGCTATT
120	ATGTGCTGCATAGAAGTATTAGACTTTACAAACAATTGCGAAAGGGGG
121	TTGGGTAACGCAATAGATAATACATTTGAGGATTAGGCGATTAAG
122	CCAGTCACGACACTAACAACTAATAGATTAGAGCCGTCCAGGGTTTTC
123	GACGGCCAGTGGTTATCTAAAATATCTTTAGGAGCGTTGTAAAAC
124	TCAGGAGAAGAATCAACAGTTGAAAGGAATTGAGGAAGCCAAGCTTTC
125	GTTCTTCTAACAATCAATATCTGGTCAGTTGGCACCAGGGTGGAT
126	TTCATGCGCACTTGCTGAACCTCAAATATCAAACCCTGTGGTTGTGAA
127	TCCTTAGTGCCAAATGAAAAATCTAAAGCATCACCGACTTAAGTG
128	CCTTATGACACAACAGTGCCACGCTGAGAGCCAGCAGTGAATTGTCAA
129	AAATAACCCCGGCGGTCAGTATTAACACCGCCTGATGTCCCGCCA
130	ATTTACGCTCCACCAGCAGAAGATAAAACAGAGGTGAGCTTCTAATCT
131	ACTCTATGATCGCCATTAAAAATACCGAACGAACGCCCTGGAGTG
132	GGCCCTGCCAATGCGCGAACTGATAGCCCTAAAACATACCGACAGTGC
133	CTCGTCGGTGTTTTTGAATGGCTATTAGTCTTTATCTGTAAGCAA
134	AGGGGCCTTGGCGTAAGAATACGTGGCACAGACAATAGGCACGAATAT
135	GCATTTCACAAGATAGAACCCTTCTGACCTGAAAAATCGGCTGAC
136	TCCGAACTCTTAATAAAAGGGACATTCTGGCCAACAGTAAATCATTTC
137	TGGTGTAATGCAGATTCACCAGTCACACGACCAGGACCTCCTGGT
138	CTTAAGCTACTCGTCTGAAATGGATTATTTACATTGGAGTAAACAGGG
139	TACCTCGATAAAATACCTACATTTTGACGCTCAAGTGGTGCTTGT
140	TCCCCGGGTACCATTGCAACAGGAAAAACGCTCATGGAAGACGGAGGA
141	TTCGTAATCATATCCAGAACAATATTACCGCCAGCCGAGCTCGAA
142	GTTTCCTGTGAACTCAAACTATCGGCCTTGCTGGTAATGGTCATAGCT
143	TCCGCTCACATAACATCACTTGCCTGAGTAGAAGTGAAATTGTTA
144	CATACGAGCCTTGTAGCAATACTTCTTTGATTAGTAAATTCCACACAA
145	GTGTAAAGCCTCTGTCCATCACGCAAATTAACCGGGAAGCATAAA
146	ATGAGTGAGCAATCAGTGAGGCCACCGAGTAAAAGAGTGGGGTGCCTA
147	AATTGCGTTGCAGAATCCTGAGAAGTGTTTTTATTAACTCACATT
148	CGCTTTCCAGAAGGGATTTTAGACAGGAACGGTACGCCGCTCACTGCC
149	GTCGTGCCAGGGGAGCTAAACAGGAGGCCGATTATCGGGAAACCT
150	AATCGGCCAAACGTGCTTTCCTCGTTAGAATCAGAGCCTGCATTAATG
151	AGGCGGTTTGTGGTTGCTTTGACGAGCACGTATACGCGCGGGGAG

Table S3.2: *Extra oligos needed to make each NS versions*

Construct	Additional needed oligonucleotides
Holiday junction (HJ)	GCTAAACAACTTTCAACAGTTTCAGCTCTCCGGCCTCAAACTACTTTACCGATCGTAGT CCGTCAGATTCAGCCCTGT

Continued on next page

Table S3.2 – continued from previous page

Construct	**Additional needed oligonucleotides**
	TCGGTAAAGTAGTTTGAGGCCGGAGACCGAATGGAGTCTGTTCTCGACGCTTTCGTA GTCCGTCAGATTCAGCCCTGT AAGCGTCGAGAACAGACTCCATTCGGACAATTACGAACCAACTTAGGACCAGTCGTA GTCCGTCAGATTCAGCCCTGT CTGGTCCTAAGTTGGTTCGTAATTGTGTGAGAATAGAAAGGAACAACTAAAG
T1S3	GTGAGAATAGAAAGGAACAACTAAAGGCTAAACAACTTTCAACAGTTTCAGCGGA (5’ end of this oligo is biotinylated)
NS4	500 b ssDNA megamer: ACGGCCTGAAGGTATGGGACAGCGGTGGCTACGGATCCCCTGAAGCTAATGACTATGTGCGGTTGTGAGACCATTGCAGCCACCAGAGTGGTGCGTACTGCATCAGTTCTGAGTTGCAAGGGGTTAATTCTGTGTCTAGAGGATCAGTAAAGCGCAGCAGATAGGGTCGACGGCGATAGTCGGAATGATGGCGCTGTCCTCAACCAGTTGAGGAAGAAATCCATGGCCTAGAGGCTCTAGTCATTGCTGGACTCGCCTGACAACTCTGTCAGGAAAGCCACGAGTACAATACAACTCGCGTCCGCTGCGTCACCGAACAACATCAGGGACAAACGTGAACTACTTTTCTGCCGCACTTCGGTACCGGTACATTCAGTGAAGTCAAACATGGCGGATGCAAATCCAATCGCGATTGTTGTGACAGCATTTATTCTGCCGTTTTCGATGGCCAGTAAGTGAATGCAAGCGTAGACGCCATAGCACACTTCTTCTTGTAACG NS-megamer linker 1: GCTAAACAACTTTCAACAGTTTCAGCGGATTTGCGGACGCGAGTTGTATTGTACTCGTGGCT NS-megamer linker 2: CGTTTGTCCCTGATGTTGTTCGGTGACGCATTTGTGAGAATAGAAAGGAACAACTAAAG Jubaea Linker1: Atto-Rho14-TTTTGCGCCATCATTCCGACTATCGCCGTCG TCGTAGTCCGTCAGATTCAGCCCTGT Jubaea Linker 2: Atto-Rho14-TTTTAGCAATGACTAGAGCCTCTAGGCCATG TCGTAGTCCGTCAGATTCAGCCCTGT Jubaea Linker 3: Atto-Rho14-TTTTATGTTTGACTTCACTGAATGTACCGGT TCGTAGTCCGTCAGATTCAGCCCTGT Jubaea Linker 4: Atto-Rho14-TTTTGAAAACGGCAGAATAAATGCTGTCACA TCGTAGTCCGTCAGATTCAGCCCTGT
NS 6	1. CACCCGCCGCGCTTAATGCGCCGCTTTTCGTAGTCCGTCAGATTCAGCCCTGT 2. GCGGTCACGCTGCGCGTAACCACCTTTTCGTAGTCCGTCAGATTCAGCCCTGT 3. GGGCGCTAGGGCGCTGGCAAGTGTTTTTCGTAGTCCGTCAGATTCAGCCCTGT 4. AGGAAGGGAAGAAAGCGAAAGGAGTTTTCGTAGTCCGTCAGATTCAGCCCTGT 5. GGAAAGCCGGCGAACGTGGCGAGATTTTCGTAGTCCGTCAGATTCAGCCCTGT 6. GAGCCCCCGATTTAGAGCTTGACGTTTTCGTAGTCCGTCAGATTCAGCCCTGT
NS10	Oligos of NS6 + the following oligos: 7. AAGCACTAAATCGGAACCCTAAAGTTTTCGTAGTCCGTCAGATTCAGCCCTGT 8. AGTTTTTTGGGGTCGAGGTGCCGTTTTTCGTAGTCCGTCAGATTCAGCCCTGT 9. ACTACGTGAACCATCACCCAAATCTTTTCGTAGTCCGTCAGATTCAGCCCTGT 10. AAACCGTCTATCAGGGCGATGGCCTTTTCGTAGTCCGTCAGATTCAGCCCTGT
NS15	Oligos of NS10 + the following oligos: 11. GTGGACTCCAACGTCAAAGGGCGATTTTCGTAGTCCGTCAGATTCAGCCCTGT 12. GAACAAGAGTCCACTATTAAAGAATTTTCGTAGTCCGTCAGATTCAGCCCTGT 13. TAGGGTTGAGTGTTGTTCCAGTTTTTTTCGTAGTCCGTCAGATTCAGCCCTGT 14. TATAAATCAAAAGAATAGCCCGAGTTTTCGTAGTCCGTCAGATTCAGCCCTGT 15. TGGTTCCGAAATCGGCAAAATCCCTTTTCGTAGTCCGTCAGATTCAGCCCTGT
NS20	Oligos of NS15 + the following oligos: 16. AGCAGGCGAAAATCCTGTTTGATGTTTTCGTAGTCCGTCAGATTCAGCCCTGT 17. CAAGCGGTCCACGCTGGTTTGCCCTTTTCGTAGTCCGTCAGATTCAGCCCTGT 18. CCGCCTGGCCCTGAGAGAGTTGCATTTTCGTAGTCCGTCAGATTCAGCCCTGT 19. ACGGGCAACAGCTGATTGCCCTTCTTTTCGTAGTCCGTCAGATTCAGCCCTGT 20. GGTGGTTTTTCTTTTCACCAGTGATTTTCGTAGTCCGTCAGATTCAGCCCTGT

SCRIPTS

Below is the list of the scripts used for the analyzes:
skymo: a plugin for making kymorgraph with custom features
NS force analyzer: A custom-made plugin to calculate NS forces based on its extension
Event analyzer: A custom-made plugin to quantify event types in NS-MT interactions
MT end tracker: A macro to detect MT ends in kymorgraphs (a general tool to detect any edges).
Drift correction: To correct drifts in TIRF stacks

See all scripts at https://github.com/aNick256

REFERENCES

[1] A. V. Zaytsev and E. L. Grishchuk. “Basic mechanism for biorientation of mitotic chromosomes is provided by the kinetochore geometry and indiscriminate turnover of kinetochore microtubules”. In: *Molecular Biology of the Cell* 26.22 (Nov. 5, 2015). Publisher: American Society for Cell Biology (mboc), pp. 3985–3998. ISSN: 1059-1524. DOI: 10.1091/mbc.E15-06-0384. URL: https://www.molbiolcell.org/doi/10.1091/mbc.E15-06-0384 (visited on 01/16/2025).

[2] S. Oliferenko. “Understanding eukaryotic chromosome segregation from a comparative biology perspective”. In: *Journal of cell science* 131.14 (2018), jcs203653.

[3] A. Musacchio. “The Molecular Biology of Spindle Assembly Checkpoint Signaling Dynamics”. In: *Current Biology* 25.20 (Oct. 19, 2015), R1002–R1018. ISSN: 0960-9822. DOI: 10.1016/j.cub.2015.08.051. URL: https://www.sciencedirect.com/science/article/pii/S0960982215010453 (visited on 01/16/2025).

[4] G. Manic, F. Corradi, A. Sistigu, S. Siteni, and I. Vitale. “Molecular regulation of the spindle assembly checkpoint by kinases and phosphatases”. In: *International review of cell and molecular biology* 328 (2017), pp. 105–161.

[5] R. T. Wimbish, K. F. DeLuca, J. E. Mick, J. Himes, I. Jiménez-Sánchez, A. A. Jeyaprakash, and J. G. DeLuca. “The Hec1/Ndc80 tail domain is required for force generation at kinetochores, but is dispensable for kinetochore–microtubule attachment formation and Ska complex recruitment”. In: *Molecular Biology of the Cell* 31.14 (July 2020). Publisher: American Society for Cell Biology (mboc), pp. 1453–1473. ISSN: 1059-1524. DOI: 10.1091/mbc.E20-05-0286. URL: https://www.molbiolcell.org/doi/10.1091/mbc.E20-05-0286 (visited on 01/15/2025).

[6] G. M. Alushin, G. C. Lander, E. H. Kellogg, R. Zhang, D. Baker, and E. Nogales. “High-Resolution Microtubule Structures Reveal the Structural Transitions in $\alpha\beta$-Tubulin upon GTP Hydrolysis”. In: *Cell* 157.5 (May 22, 2014), pp. 1117–1129. ISSN: 0092-8674. DOI: 10.1016/j.cell.2014.03.053. URL: https://www.sciencedirect.com/science/article/pii/S0092867414004838 (visited on 01/28/2025).

[7] G. M. Alushin, V. H. Ramey, S. Pasqualato, D. A. Ball, N. Grigorieff, A. Musacchio, and E. Nogales. “The Ndc80 kinetochore complex forms oligomeric arrays along microtubules”. In: *Nature* 467.7317 (Oct. 2010). Publisher: Nature Publishing Group, pp. 805–810. ISSN: 1476-4687. DOI: 10.1038/

nature09423. URL: https://www.nature.com/articles/nature09423 (visited on 01/16/2025).

[8] C. Ciferri, J. De Luca, S. Monzani, K. J. Ferrari, D. Ristic, C. Wyman, H. Stark, J. Kilmartin, E. D. Salmon, and A. Musacchio. "Architecture of the Human Ndc80-Hec1 Complex, a Critical Constituent of the Outer Kinetochore*". In: *Journal of Biological Chemistry* 280.32 (Aug. 12, 2005), pp. 29088–29095. ISSN: 0021-9258. DOI: 10.1074/jbc.M504070200. URL: https://www.sciencedirect.com/science/article/pii/S0021925820564715 (visited on 01/16/2025).

[9] R. R. Wei, J. Al-Bassam, and S. C. Harrison. "The Ndc80/HEC1 complex is a contact point for kinetochore-microtubule attachment". In: *Nature Structural & Molecular Biology* 14.1 (Jan. 2007). Publisher: Nature Publishing Group, pp. 54–59. ISSN: 1545-9985. DOI: 10.1038/nsmb1186. URL: https://www.nature.com/articles/nsmb1186 (visited on 01/15/2025).

[10] P. J. Huis in 't Veld, V. A. Volkov, I. D. Stender, A. Musacchio, and M. Dogterom. "Molecular determinants of the Ska-Ndc80 interaction and their influence on microtubule tracking and force-coupling". In: *eLife* 8 (Dec. 5, 2019). Ed. by A. D. McAinsh and V. Malhotra. Publisher: eLife Sciences Publications, Ltd, e49539. ISSN: 2050-084X. DOI: 10.7554/eLife.49539. URL: https://doi.org/10.7554/eLife.49539 (visited on 10/09/2024).

[11] G. M. Alushin, V. Musinipally, D. Matson, J. Tooley, P. T. Stukenberg, and E. Nogales. "Multimodal microtubule binding by the Ndc80 kinetochore complex". In: *Nature Structural & Molecular Biology* 19.11 (Nov. 2012). Publisher: Nature Publishing Group, pp. 1161–1167. ISSN: 1545-9985. DOI: 10.1038/nsmb.2411. URL: https://www.nature.com/articles/nsmb.2411 (visited on 01/15/2025).

[12] S. Polley, H. Müschenborn, M. Terbeck, A. De Antoni, I. R. Vetter, M. Dogterom, A. Musacchio, V. A. Volkov, and P. J. Huis in 't Veld. "Stable kinetochore-microtubule attachment requires loop-dependent Ndc80-Ndc80 binding". In: *The EMBO Journal* 42.13 (July 3, 2023). Publisher: John Wiley & Sons, Ltd, e112504. ISSN: 0261-4189. DOI: 10.15252/embj.2022112504. URL: https://www.embopress.org/doi/full/10.15252/embj.2022112504 (visited on 10/09/2024).

[13] A. F. Powers, A. D. Franck, D. R. Gestaut, J. Cooper, B. Gracyzk, R. R. Wei, L. Wordeman, T. N. Davis, and C. L. Asbury. "The Ndc80 Kinetochore Complex Forms Load-Bearing Attachments to Dynamic Microtubule Tips via Biased Diffusion". In: *Cell* 136.5 (Mar. 6, 2009), pp. 865–875. ISSN: 0092-8674. DOI: 10.1016/j.cell.2008.12.045. URL: https://www.sciencedirect.com/science/article/pii/S0092867409000233 (visited on 01/15/2025).

[14] J. C. Schmidt, H. Arthanari, A. Boeszoermenyi, N. M. Dashkevich, E. M. Wilson-Kubalek, N. Monnier, M. Markus, M. Oberer, R. A. Milligan, M. Bathe, G. Wagner, E. L. Grishchuk, and I. M. Cheeseman. “The Kinetochore-Bound Ska1 Complex Tracks Depolymerizing Microtubules and Binds to Curved Protofilaments”. In: *Developmental Cell* 23.5 (Nov. 13, 2012), pp. 968–980. ISSN: 1534-5807. DOI: `10.1016/j.devcel.2012.09.012`. URL: `https://www.sciencedirect.com/science/article/pii/S1534580712004236` (visited on 01/15/2025).

[15] J. R. McIntosh, E. L. Grishchuk, M. K. Morphew, A. K. Efremov, K. Zhudenkov, V. A. Volkov, I. M. Cheeseman, A. Desai, D. N. Mastronarde, and F. I. Ataullakhanov. “Fibrils Connect Microtubule Tips with Kinetochores: A Mechanism to Couple Tubulin Dynamics to Chromosome Motion”. In: *Cell* 135.2 (Oct. 17, 2008), pp. 322–333. ISSN: 0092-8674. DOI: `10.1016/j.cell.2008.08.038`. URL: `https://www.sciencedirect.com/science/article/pii/S0092867408011197` (visited on 01/15/2025).

[16] R. Kiewisz, G. Fabig, W. Conway, D. Baum, D. Needleman, and T. Müller-Reichert. “Three-dimensional structure of kinetochore-fibers in human mitotic spindles”. In: *eLife* 11 (July 27, 2022). Ed. by A. L. Marston, A. Akhmanova, and J. R. McIntosh. Publisher: eLife Sciences Publications, Ltd, e75459. ISSN: 2050-084X. DOI: `10.7554/eLife.75459`. URL: `https://doi.org/10.7554/eLife.75459` (visited on 01/15/2025).

[17] A. Suzuki, B. L. Badger, and E. D. Salmon. “A quantitative description of Ndc80 complex linkage to human kinetochores”. In: *Nature Communications* 6.1 (Sept. 8, 2015). Publisher: Nature Publishing Group, p. 8161. ISSN: 2041-1723. DOI: `10.1038/ncomms9161`. URL: `https://www.nature.com/articles/ncomms9161` (visited on 01/15/2025).

[18] V. A. Volkov, P. J. Huis in ’t Veld, M. Dogterom, and A. Musacchio. “Multivalency of NDC80 in the outer kinetochore is essential to track shortening microtubules and generate forces”. In: *eLife* 7 (Apr. 9, 2018). Ed. by J. K. Tyler. Publisher: eLife Sciences Publications, Ltd, e36764. ISSN: 2050-084X. DOI: `10.7554/eLife.36764`. URL: `https://doi.org/10.7554/eLife.36764` (visited on 10/10/2024).

[19] **A. Nick Maleki**, P. J. Huis in ’t Veld, A. Akhmanova, M. Dogterom, and V. A. Volkov. “Estimation of microtubule-generated forces using a DNA origami nanospring”. In: *Journal of Cell Science* 136.5 (Mar. 2, 2022), jcs260154. ISSN: 0021-9533. DOI: `10.1242/jcs.260154`. URL: `https://doi.org/10.1242/jcs.260154` (visited on 10/09/2024).

[20] J. Hummert, K. Yserentant, T. Fink, J. Euchner, and D.-P. Herten. *Photobleaching step analysis for robust determination of protein complex stoichiometries*. Pages: 2020.08.26.268086 Section: New Results. Aug. 26, 2020. DOI: `10.1101/2020.08.26.268086`. URL: `https://www.biorxiv.org/content/10.1101/2020.08.26.268086v1` (visited on 10/10/2024).

[21] E. L. Grishchuk, I. S. Spiridonov, V. A. Volkov, A. Efremov, S. Westermann, D. Drubin, G. Barnes, F. I. Ataullakhanov, and J. R. McIntosh. “Different assemblies of the DAM1 complex follow shortening microtubules by distinct mechanisms”. In: *Proceedings of the National Academy of Sciences* 105.19 (May 13, 2008). Publisher: Proceedings of the National Academy of Sciences, pp. 6918–6923. DOI: 10.1073/pnas.0801811105. URL: https://www.pnas.org/doi/full/10.1073/pnas.0801811105 (visited on 11/28/2024).

[22] E. L. Grishchuk, J. R. McIntosh, M. I. Molodtsov, and F. I. Ataullakhanov. “4.7 Force Generation by Dynamic Microtubule Polymers”. In: *Comprehensive Biophysics*. Ed. by E. H. Egelman. Amsterdam: Elsevier, Jan. 1, 2012, pp. 93–117. ISBN: 978-0-08-095718-0. DOI: 10.1016/B978-0-12-374920-8.00409-4. URL: https://www.sciencedirect.com/science/article/pii/B9780123749208004094 (visited on 02/04/2025).

[23] T. J. Etheridge, A. M. Carr, and A. D. Herbert. “GDSC SMLM: Single-molecule localisation microscopy software for ImageJ”. In: *Wellcome Open Research* 7 (Sept. 29, 2022), p. 241. ISSN: 2398-502X. DOI: 10.12688/wellcomeopenres.18327.1. URL: https://wellcomeopenresearch.org/articles/7-241/v1 (visited on 10/16/2024).

[24] L. Hauke, A. Primeßnig, B. Eltzner, J. Radwitz, S. F. Huckemann, and F. Rehfeldt. “FilamentSensor 2.0: An open-source modular toolbox for 2D/3D cytoskeletal filament tracking”. In: *PLOS ONE* 18.2 (Feb. 6, 2023). Publisher: Public Library of Science, e0279336. ISSN: 1932-6203. DOI: 10.1371/journal.pone.0279336. URL: https://journals.plos.org/plosone/article?id=10.1371/journal.pone.0279336 (visited on 10/16/2024).

[25] S. Q. Zheng, E. Palovcak, J.-P. Armache, K. A. Verba, Y. Cheng, and D. A. Agard. “MotionCor2: anisotropic correction of beam-induced motion for improved cryo-electron microscopy”. In: *Nature methods* 14.4 (2017), pp. 331–332.

[26] T. Bepler, K. Kelley, A. J. Noble, and B. Berger. “Topaz-Denoise: general deep denoising models for cryoEM and cryoET”. In: *Nature communications* 11.1 (2020), p. 5208.

[27] M. Chen, W. Dai, S. Y. Sun, D. Jonasch, C. Y. He, M. F. Schmid, W. Chiu, and S. J. Ludtke. “Convolutional neural networks for automated annotation of cellular cryo-electron tomograms”. In: *Nature methods* 14.10 (2017), pp. 983–985.

[28] T. D. Goddard, C. C. Huang, E. C. Meng, E. F. Pettersen, G. S. Couch, J. H. Morris, and T. E. Ferrin. “UCSF ChimeraX: Meeting modern challenges in visualization and analysis”. In: *Protein science* 27.1 (2018), pp. 14–25.

[29] R. David Row, T. J. Roark, M. C. Philip, L. L. Perkins, and J. M. Antos. “Enhancing the efficiency of sortase-mediated ligations through nickel-peptide complex formation”. In: *Chemical Communications (Cambridge,*

England) 51.63 (Aug. 14, 2015), pp. 12548–12551. ISSN: 1364-548X. DOI: `10.1039/c5cc04657b`.

4

ON CONTROLLING MICROTUBULE NUCLEATION SITES

Ali NICK MALEKI, Tessel HUIBREGTSEN, Marileen DOGTEROM

Order is not pressure which is imposed [...] from without, but an equilibrium which is set up from within

José Ortega y Gasset

...many of the greatest things man has achieved are not the result of consciously directed thought... but of a process in which the individual plays a part which he can never fully understand

Friedrich Hayek

The eukaryotic mitotic spindle apparatus is essential for chromosomal segregation during cell division, relying on microtubule organizing centers (MTOCs) and kinetochores to orchestrate microtubule dynamics and chromosome attachment. Centrosomes, the primary MTOCs in animal cells, facilitate microtubule nucleation through mechanisms like template-based nucleation, involving the γ-tubulin ring complex (γ-TuRC), and condensation-based nucleation, where tubulin subunits coalesce into protein condensates. However, studying these processes in vivo is challenging due to the complexity of cellular environments. To address this, in vitro reconstitution systems have been developed, offering controlled conditions to

---

This chapter includes the results from bachelor end project of Tessel Huibregtsen *investigate microtubule nucleation and organization. This chapter explores methods for creating artificial microtubule asters, focusing on spatial control of microtubule nucleation using minimal components. Techniques such as gold micropatterning for 2D and MT seed-coated beads for controlling growth sites of MTs in 3D was employed, using DNA origami as platforms.*

4.1. INTRODUCTION

The eukaryotic mitotic spindle apparatus functions as the primary mechanism for chromosomal segregation during cell division [1]. This bipolar structure is organized by microtubule organizing centers (MTOCs) positioned at opposing poles, which serve as nucleation sites for microtubule arrays [2]. These microtubules extend their plus ends toward the spindle equator, where they engage with chromosomes through specialized protein complexes known as kinetochores [3]. Kinetochore is a macromolecular multi-subunit complex that is made of overall hundreds of proteins [4]. Initial kinetochore-microtubule interactions occur through lateral associations, followed by motor protein-mediated transport of kinetochores along the microtubule lattice until they reach the microtubule plus ends, where they establish stable end-on attachments [5].

In animal cells, centrosomes are the primary MTOCs [6], a membrane-less organelle which is also composed of tens of different kinds of proteins [7]. During interphase, two centrosomes nucleate microtubules that grow outward radially (called microtubule asters) and assists in maintaining spindle shape in mitosis [8]. Two distinct mechanisms have been proposed for centrosome-mediated microtubule nucleation: template-based and condensation-based nucleation [9]. In the template-based model, the centrosome serves as a platform for the γ-tubulin ring complex (γ-TuRC), which is the primary microtubule nucleation complex [10]. The γ-TuRC is a macromolecular assembly composed of multiple proteins, including 13 γ-tubulin subunits, which correspond to the 13 protofilaments of microtubules. γ-tubulin has the capacity to bind α-tubulin, thereby functioning as a nucleation seed for microtubule polymerization and growth [11].

In the context of condensation-mediated nucleation, it is hypothesized that microtubule polymerizers, or tubulin subunits themselves, are recruited from the cytoplasm to the centrosomes, where they coalesce to form a protein condensate [12]. The localized elevated concentration of microtubule-associated proteins (MAPs), which promote microtubule polymerization, or the high concentration of tubulin alone, facilitates the nucleation of microtubules from these droplet-like protein condensates [13] . The nucleating capacity of centrosomes is dependent on the specific stage of the cell cycle and is proposed to be regulated through phosphorylating proteins [14]. The cellular environment is inherently complex, with a vast number of proteins involved in the formation and function of centrosomes and kinetochores. This presents significant challenges in understanding the mechanisms underlying chromosome segregation. To address these challenges, an in vitro reconstituted system, where the number and types of proteins are precisely controlled and limited, can provide valuable insights into these processes.

Reconstituting MT asters can be achieved by purifying centrosomes for use in in vitro assays. However, this approach presents significant technical challenges, such as the difficulty in obtaining high concentrations of centrosomes and the lack of straightforward methods to accurately determine their concentration. For two-dimensional (2D) reconstitutions on surfaces, these issues are somewhat mitigated, as centrosomes tend to adhere to glass surfaces. When the objective is to study the interaction between two asters in close proximity (e.g., in the presence of microtubule-associated proteins, MAPs), it is feasible to locate asters that are adhered to the surface sufficiently close to one another. However, encapsulating two centrosomes within a vesicle for 3D studies becomes considerably more challenging when the initial centrosome concentration is low. Additionally, centrosomes comprise numerous components which can introduce unknown variables into the in vitro assay system.

In our experimental experience, centrosomes also exhibit a propensity to adhere to DNA and proteins such as actin, further complicating their handling and manipulation in reconstitution studies where multiple components are combined.

Although purified centrosomes can be valuable for certain assays, the aforementioned challenges have motivated us to explore the creation of artificial microtubule (MT) asters, where the nucleating agents and their concentrations can be controlled more precisely. In this chapter, we focus on the reconstitution of artificial microtubule organizing centers (MTOCs) using a minimal set of components. This approach allows for greater experimental control and reproducibility, enabling detailed investigation of the mechanisms of microtubule nucleation and organization.

As previously mentioned, microtubule (MT) assembly involves two key processes: nucleation and subsequent elongation. It is well-established that the sponteneous MT nucleation rate is dependent on the concentration of GTP-bound tubulin, following a power-law relationship [15]. Specifically, the nucleation rate exhibits a high-order dependence on tubulin concentration, with the nucleation exponent typically ranging between 6 and 12. This relationship underscores the critical role of tubulin concentration in the regulation of the kinetics of MT assembly [8]. This number is interpreted as the minimum number of tubulin dimers needed to oligomerize to form the starting point for the growth of MT [16]. This initial step of microtubule (MT) nucleation represents the rate-limiting factor in MT growth and cannot occur below a specific tubulin concentration, known as the critical tubulin concentration [17]. Once microtubule nuclei (or seeds) are formed, the subsequent elongation of MTs exhibits a linear dependence on tubulin concentration [18]. Due to the energy barrier associated with the initial formation of MTs, new microtubules cannot assemble below the critical tubulin concentration; however, pre-existing microtubules can continue to elongate under these conditions [19]. Consequently, this results in a scenario where MT growth is restricted to locations where MT seeds are already present, ensuring that microtubules do not form indiscriminately in other regions. This spatial control is critical for regulating MT dynamics in cellular contexts.

A strategy for spatially controlling microtubule (MT) growth involves the use of MT seeds that are selectively bound to predefined locations. This approach has been successfully employed to grow MTs from microbeads, where stabilized MT seeds are attached to the bead surface, enabling the formation of artificial MT asters [20]. Other studies have implemented a similar strategy in two-dimensional (2D) systems by patterning surfaces to specifically bind linker molecules at desired sites [21–23]. Stabilized MT seeds, functionalized with a tag, are introduced into a flow chamber and allowed to bind to the patterned linkers. Unbound seeds are subsequently washed away, leaving only the immobilized seeds as nucleation sites. At tubulin concentrations below the critical concentration, MT growth is exclusively observed from the patterned regions, ensuring precise spatial control over MT assembly. This method provides a powerful tool for studying MT dynamics and organization in a controlled in vitro environment. Another approach to achieving spatial control over microtubule (MT) nucleation involves coating beads with proteins that facilitate and accelerate MT nucleation. This can be accomplished by directly coating the beads with MT nucleation factors, such as XMAP215, or by using proteins that recruit these nucleation factors to the bead surface [24]. For example, Tsai and colleagues successfully demonstrated MT growth from beads coated with Aurora A, a kinase known to play a role in MT nucleation. Furthermore, they extended this approach to reconstitute spindle-like structures using these protein-coated beads, highlighting the potential of this method to mimic and study complex MT-based assemblies in vitro. This strategy provides a versatile platform for investigating the mechanisms of MT nucleation and organization in a controlled and reproducible manner [25].

The process of microtubule (MT) nucleation from Aurora A (AurA)-coated beads proceeds as follows [25]: beads are first coated with an AurA antibody, which enables the recruitment of AurA from Xenopus egg extract. For successful MT nucleation, the presence of several key components in the extract is essential. These include RanGTP, tubulin nucleation factors such as TPX2 and γ-tubulin ring complex (γ-TuRC) (depletion of either TPX2 or γ-tubulin significantly reduces MT nucleation), and motor proteins Eg5 (inhibition of Eg5 prevents approximately 60% of AurA-coated beads from nucleating MTs) and dynein (which is more critical for proper MT organization than nucleation). In this system, RanGTP activates AurA through TPX2, leading to the recruitment of MT nucleation factors, including γ-tubulin and TPX2. Once RanGTP triggers this recruitment, the nucleating factors remain stably associated with the beads, as demonstrated by the retention of nucleating ability even after washing. This stable association ensures sustained MT nucleation activity, providing a robust platform for studying MT dynamics and spindle assembly in vitro.

This method remains complex, as it requires the presence of multiple proteins and relies on the use of egg extracts to conduct the experiments. The inherent complexity of the system makes it difficult to interpret the results and study the specific roles of individual proteins. Additionally, modulating nucleation activity in this context is challenging. While this approach (AurA coated beads) does not enable microtubule (MT) nucleation from purified tubulin alone (needs pre-treatment in Xenopus egg extract), directly coating beads with XMAP215, a potent MT nucleation factor, has been shown to facilitate MT nucleation from the beads.[26]. This simplified approach offers a more controlled and interpretable system for studying MT nucleation and dynamics, reducing the reliance on complex protein mixtures and extracts.

If the goal is to spatially control microtubule (MT) nucleation, the cleanest approach is to use stable, pre-made MTs as nucleation seeds. By controlling where these seeds can bind, one can dictate the sites from which new MTs will grow. In this chapter we study various methods of immobilizing MT nucleation templates (MT seeds) and methods for spatial positioning control of these nucleators. This is performed both in 3D using microbeads and in 2D using patterned surfaces.

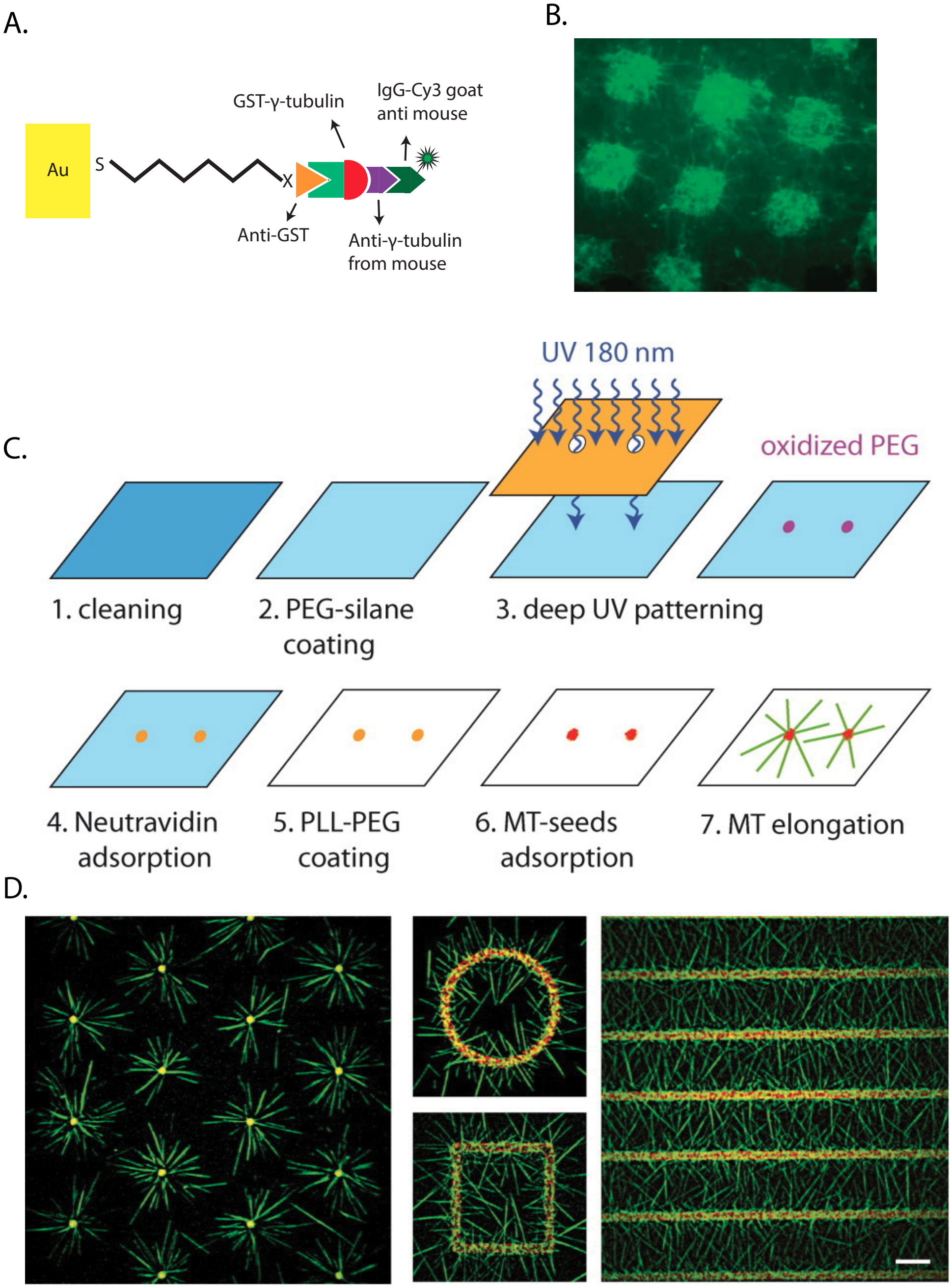

Figure 4.1: *Yang et al used gold patterned surfaces to immobilize γ-tubulin on the surface to nucleate MTs. (A) schematic representation of the immobilization strategy. The zigzag line shows alkanethiols with carboxylic acid functionality that form a self-assembled monolayer on gold. The carboxylic acid terminal could be used to conjugate anti-GST antibodies to it. γ-tubulin and anti-γ-tubulin antibody was added subsequently. A secondary fluorescently labeled antibody was used against anti-γ-tubulin antibody for visualization. (continued ...)*

Figure 4.1 continued ...
(B) Differential growth of MTs from gold-coated areas in the presence of taxol. (C) Schematic representation of the process of making controlled MT nucleation sites used in Portran et al. 2013 [23] (D) Example fluorescent images showing exclusive nucleation of MTs from patterned sites. The images in panel A and B are adopted from [27]. The images in panel C and D are from Portran et al. 2013 [23].

4.2. CONTROLLING MICROTUBULE NUCLEATION ON SURFACE

4.2.1. USING GOLD PATTERNS

Gold micropatterning represents a well-established and highly compatible approach within standard microfabrication protocols, with extensive documentation and widespread implementation in cleanroom facilities. Notably, this methodology has been successfully demonstrated by Yang et al. for γ-tubulin immobilization, achieving differential microtubule nucleation from specifically patterned gold domains (Fig. 4.1A-B) [27] .

Portran and colleagues developed an alternative micropatterning methodology for site-specific microtubule nucleation [23]. Their approach employed uniform surface passivation with polyethylene glycol (PEG), leveraging its intrinsic antifouling properties to minimize non-specific molecular adsorption. Spatially-controlled protein binding sites were then generated through selective PEG degradation using deep UV photolithography with a patterned photomask. The exposed regions were subsequently functionalized with neutravidin, enabling specific immobilization of biotinylated microtubule seeds (Fig. 4.1C). This protocol achieved precise spatial control over microtubule nucleation through selective surface modification (Fig. 4.1D).

While this deep UV patterning approach demonstrated high efficacy for spatially-controlled microtubule nucleation, the requisite deep UV photolithography equipment was not accessible in our laboratory facilities. Therefore, we developed an alternative strategy utilizing pre-fabricated gold surface patterns (ring, line and dot patterns. See Fig. 4.2), wherein microtubule seed linkers were selectively adsorbed to these metallic regions while surrounding areas were passivated with polyethylene glycol (PEG).

The gold patterns were fabricated on glass coverslips using microfabrication techniques. The process began with cleaning the glass to remove organic contaminants and prepare the surface. A thin layer of photoresist was then applied and patterned using either a maskless lithography system or a photomask with UV exposure. This step defined the regions where gold structures would later be deposited.

Once patterned, the samples were coated with thin layers of chromium and gold through electron-beam evaporation. Chromium served as an adhesion layer to help the gold bind firmly to the glass. After deposition, the unwanted material was removed by dissolving the underlying photoresist in acetone, leaving behind the desired gold patterns firmly attached to the glass.

For generating the photomasks themselves, a similar process was used: glass slides were coated with a thin metal layer (aluminum or chromium), covered with photoresist, and exposed with the desired design. After development, the unwanted metal was etched away, producing clean reusable masks that could transfer patterns onto other samples.

The result of this process was a series of gold micro-patterns on glass coverslips. These patterns provided defined sites for organizing microtubules in controlled geometries, enabling precise experimental studies of their behavior.

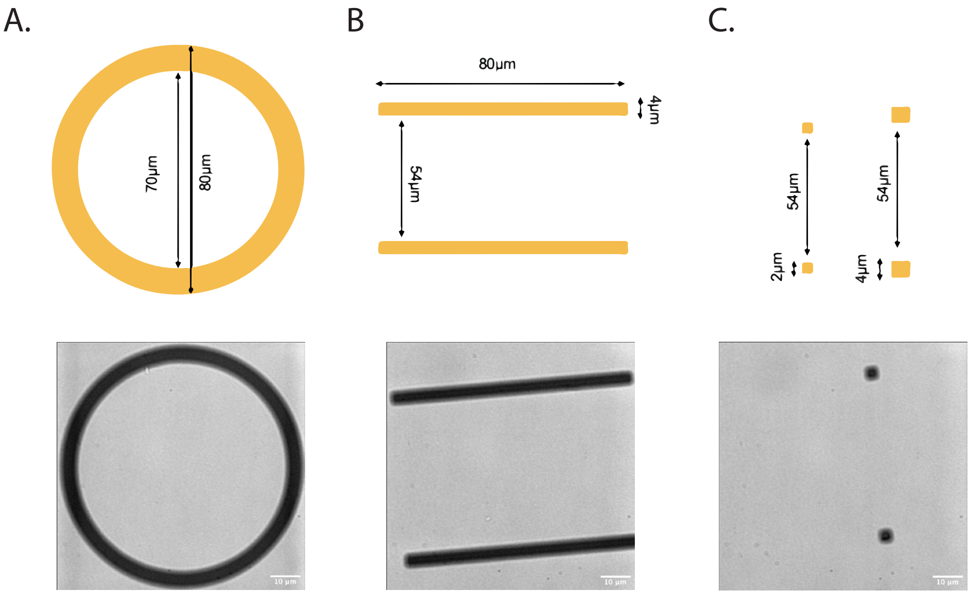

Figure 4.2: *Gold patterns created on cover glass. The top row shows the design of the patterns and the bottom row shows the actual images obtained by wide-field transmission microscopy of the microfabricated cover glasses (A) ring pattern. (B) line pattern. (C) square patterns with 4 and 2 µm sides respectively with a distance of 54 µm. From [28]*

4.2.2. SURFACE PASSIVATION

Surface passivation efficacy of surfaces similar to those surrounding the gold patterns was systematically evaluated to minimize non-specific protein adsorption in non-target regions. We assessed various surface treatment protocols using fluorescently labeled biotinylated kinesin (kinesin-biotin-647) as a reporter protein. The examined surface conditions included untreated glass coverslips, acid-cleaned surfaces, κ-casein-coated surfaces following acid cleaning, silane-PEG functionalized surfaces post acid cleaning, and PLL-PEG coated surfaces following acid cleaning. Non-specific protein adsorption was quantified via fluorescence intensity measurements of bound kinesin-biotin-647.

As demonstrated in Fig. 4.3A, both untreated and acid-cleaned surfaces exhibited comparable levels of non-specific protein adhesion. While κ-casein coating showed a modest reduction in non-specific binding, this effect was minor. In contrast, surfaces functionalized with either silane-PEG or PLL-PEG demonstrated substantial reductions in non-specific protein adsorption, with decreases of 60% and 70%, respectively.

Further optimization of the silane-PEG passivation protocol was achieved through the introduction of an oxygen plasma treatment step between acid cleaning and silane-PEG functionalization. While conventional silane-PEG passivation immediately following acid cleaning resulted in a 55% reduction in non-specific binding, the addition of the intermediate plasma treatment step significantly enhanced passivation efficiency, yielding a 93% reduction in non-specific protein adsorption (Fig. 4.3B).

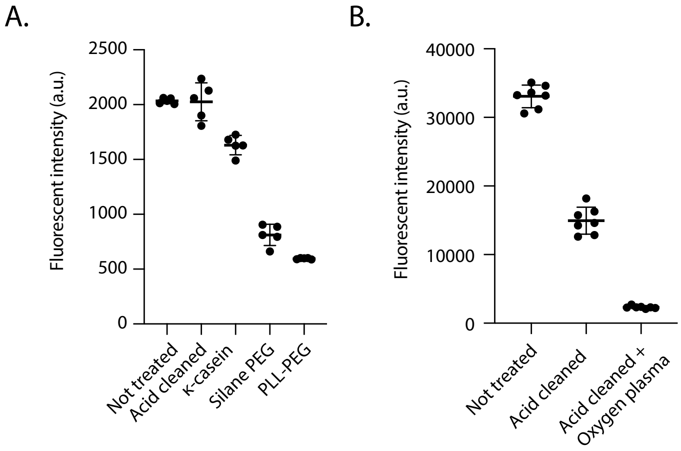

Figure 4.3: *Comparison of different passivation methods in preventing non-specific binding. (A) Tested surfaces include as-purchased coverslips, cleaned with acid piranha, coated with κ-casein after acid cleaning, acid cleaned surface treated with silane PEG and acid-cleaned surface coated with PLL-PEG. (B) Passivation effect of silane-PEGylation on acid cleaned and acid cleaned plus oxygen plasma treated coverslips. No passivating agent was added to the not-treated surface.*

4.2.3. BIOTIN-NEUTRAVIDIN BINDING USED FOR MICROTUBULE SEEDS IMMOBILIZATION ON GOLD

Due to the high-affinity interaction between neutravidin and biotin, this system presents a potential mechanism for robust surface immobilization of biotin- labeled microtubule (MT) seeds. Initial experimental strategies considered direct passivation of glass regions with polyethylene glycol (PEG) or application of antifouling agents to non-patterned areas, followed by non-specific neutravidin adsorption onto gold-coated domains. However, our experimental observations revealed insufficient binding affinity between neutravidin and gold substrates. Presnova and colleagues demonstrated that chemical modification of streptavidin with mercaptosuccinic acid enhances its surface binding affinity for gold substrates [29].

We employed mercaptosuccinic acid modification to enhance neutravidin binding to gold-patterned surfaces. To validate the preservation of biotin-binding functionality in the modified streptavidin, we developed an assay utilizing silica beads functionalized with PLL-PEG-biotin. Following extensive washing procedures, the microspheres were incubated with the mercaptosuccinic acid modified neutravidin (MS-neutravidin) and subsequently exposed to fluorescently labeled, biotinylated kinesin-1. Initial results revealed significant non-specific binding of biotinylated kinesin to the microspheres, even in the absence of neutravidin, necessitating protocol optimization (Fig. 4.5 upper row). The refined methodology incorporated two key modifications: (1) substitution of PLL-PEG-biotin with Amine-PEG-biotin for microsphere functionalization, and (2) introduction of a κ-casein blocking step prior to kinesin addition. These adaptations effectively eliminated non-specific kinesin binding, enabling reliable assessment of neutravidin-biotin interactions. We validated the biotin-binding capability of MS-neutravidin using these PEG-biotin functionalized beads (Fig. 4.4 lower row).

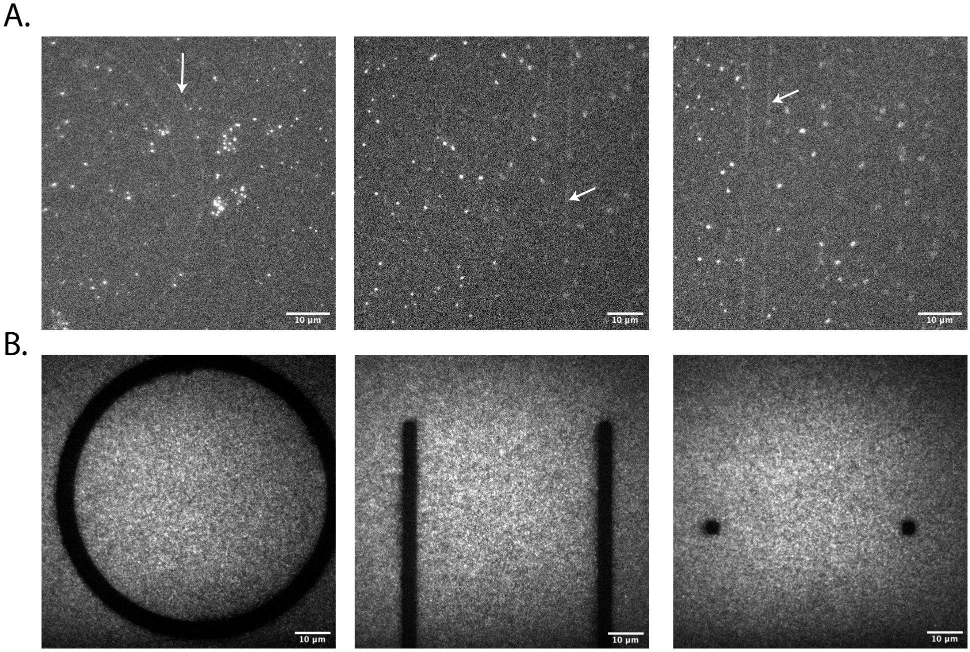

Figure 4.4: *Checking the biotin biding capability of neutravidin and MS-neutravidin with PLL-PEG-biotin (upper row) or Amine-PEG-biotin (lower row) coated beads. (A) PLL-PEG-biotin beads + kinesin-biotin-647 in the absence of neutravidin. The locations of the beads colocalized with the fluorescent signal (red) emitted from kinesins, which was not expected. This could be due to non-specific binding of kinesin-biotin-647 to the beads (negative control) (B) PLL-PEG-biotin beads + neutravidin + kinesin-biotin-647 (positive control) (C) PLL-PEG-biotin beads + MS-neutravidin + kinesin-biotin-647 (D) Amine-PEG-biotin beads + kinesin-biotin-647 (negative control) (E) Amine-PEG-biotin beads + neutravidin + kinesin-biotin-647 (positive control) (F) Amine-PEG-biotin beads + MS-neutravidin + kinesin-biotin-647. The red color shows the fluorescent signal emitted by the bound kinesin-biotin-647 in TIRF mode; The cyan is the image taken from beads in transmission mode. From [28]*

However, this modification did not enhance neutravidin adsorption to gold surfaces in our experimental conditions (Fig. 4.5). We hypothesize that this behavior may be attributed to potential interactions between the gold surface and Pluronic F127, which was employed as a passivation agent. This interference likely stems from our sequential protocol wherein surface passivation with Pluronic F127 precedes the introduction of MS- neutravidin into the flow cell.

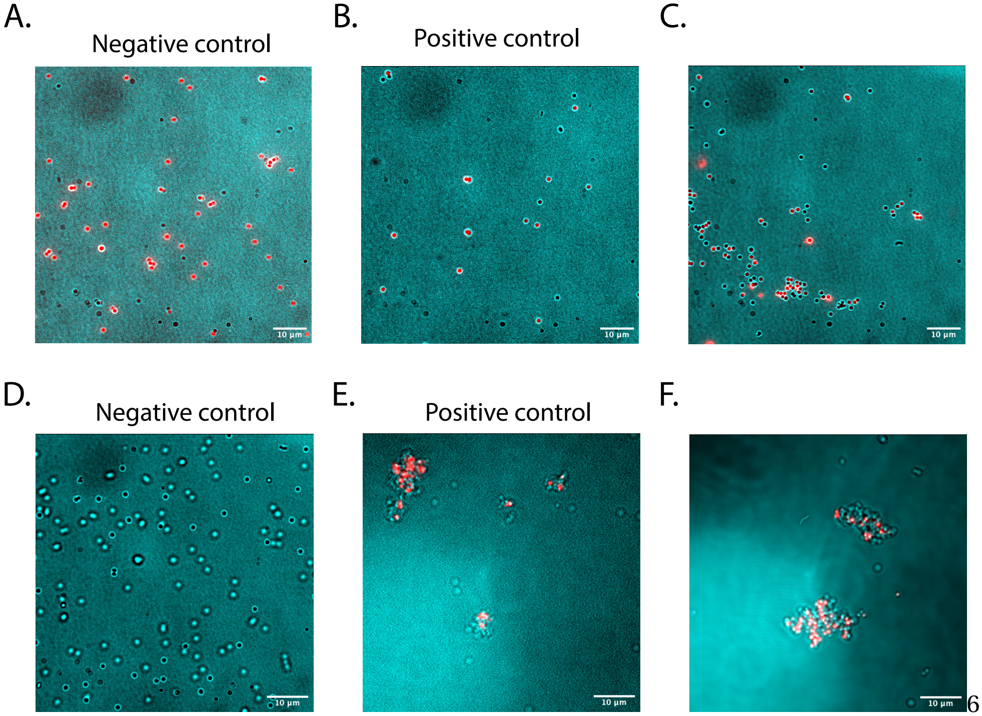

Figure 4.5: *Non-specific binding of fluorescently labeled streptavidin and modified neutravidin to the gold surface. (A) TIRF images show streptavidin did not have strong preferential binding to the gold patterns. (B) MS-neutravidin did not show any binding to the gold patterns. From [28]*

4.2.4. DNA ORIGAMI FOR MICROTUBULE SEEDS IMMOBILIZATION

We next explored an alternative patterning strategy based on the use of DNA origami techniques. DNA origami represents a highly versatile and programmable platform, capable of being precisely engineered to incorporate specific binding sites. This adaptability allows the staple strands, which help fold the DNA origami structure, to be extended and function as molecular handles. Consequently, target proteins conjugated with complementary oligonucleotides can selectively bind to these handles. Additionally, the staple strands can be chemically modified at their $5'$ and $3'$ termini or within their backbone to include functional moieties such as biotin, thiol groups, amine groups, fluorescent dyes, and other molecular tags, further enhancing their utility in diverse applications.

The affinity of thiol (-SH) moieties for gold surfaces is well-established; however, the precise mechanism of this interaction remains a subject of ongoing scientific discourse. The nature of this binding has been variously characterized as physisorption, chemisorption, or covalent bonding, with no consensus yet reached in the literature[30–32].

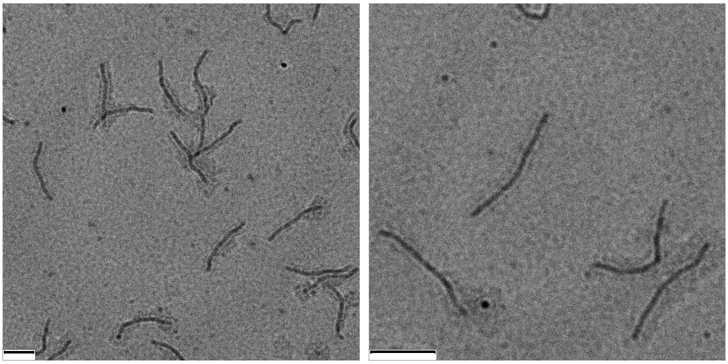

Figure 4.6: *TEM images of 6HB DNA origami purified by agarose gel electrophoresis. Scale bars are 200 nm.*

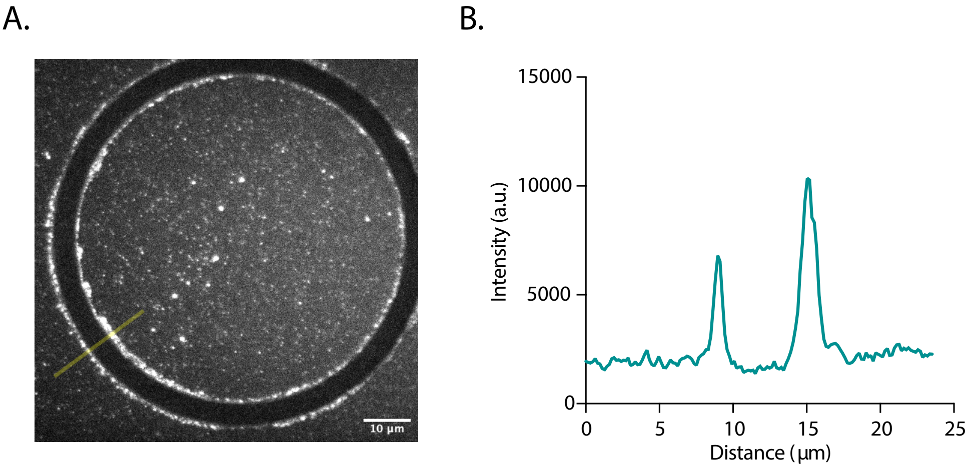

Figure 4.7: *Binding of thiolated DNA origami (6HB) to the gold surface. (A) TIRF image shows an increased fluorescent intensity around the gold patterned areas of the coverslip. (B) Fluorescent intensity profile of the line drawn in panel A. From [28]*

In our study, a 6-helix bundle DNA origami structure (6HB) was utilized (Fig. 4.6), featuring 13 DNA handles distributed across three of its helices [33]. To achieve selective binding of the DNA origami to a gold surface, we leveraged the thiol-gold binding interaction. Specifically, the DNA origami was designed to incorporate three thiolated staples at one end, to enable stable attachment to the gold surface through the formation of gold-thiol bonds. This approach ensures controlled spatial organization of the DNA origami on the surface. The surface was subsequently coated with κ-casein to reduce non-specific binding in downstream experiments.

To visualize the 6-helix bundle (6HB) DNA origami structure using total internal reflection fluorescence (TIRF) microscopy, 1 nM of the fluorescent dye YOYO-1 was added to the imaging buffer, which consisted of MRB80 supplemented with 50 mM glucose and 1x oxygen scavenger cocktail (see Methods and Materials for details). YOYO-1 exhibits increased fluorescence intensity upon intercalation into double-stranded DNA, making it an effective tool for DNA staining. This property allows for clear visualization of the DNA origami structure under TIRF microscopy. Fig. 4.7 shows a clear increase in fluorescent intensity around the gold-coated area, indicating binding of DNA origami to the gold patterns.

4.2.5. MICROTUBULE DYNAMIC ASSAY

To validate the spatial selectivity of microtubule seed attachment to gold-patterned regions, we performed microtubule dynamics assays. Based on our previous findings demonstrating superior differential binding of thiolated DNA origami to gold patterns, we developed a protocol for conjugating complementary (complementary to handles on DNA origami) oligonucleotides to microtubule seeds. This was achieved through a two-step process: first, tubulin was functionalized with azide groups, followed by a click chemistry reaction between DBCO-modified oligonucleotides and the stabilized, polymerized microtubule seeds (see Fig. 4.10). The experimental procedure involved the sequential introduction of DNA origami 6-helix bundles (6HBs) and κ-casein into the flow cell, followed by DNA-functionalized microtubule seeds. Subsequently, microtubule dynamics were initiated by introducing a reaction mixture containing 12.5 μM tubulin. As demonstrated in Fig. 4.8, microtubule growth was predominantly observed near the gold-patterned regions, with minimal nucleation events detected on the glass surface, confirming successful spatial control of microtubule nucleation on the surface.

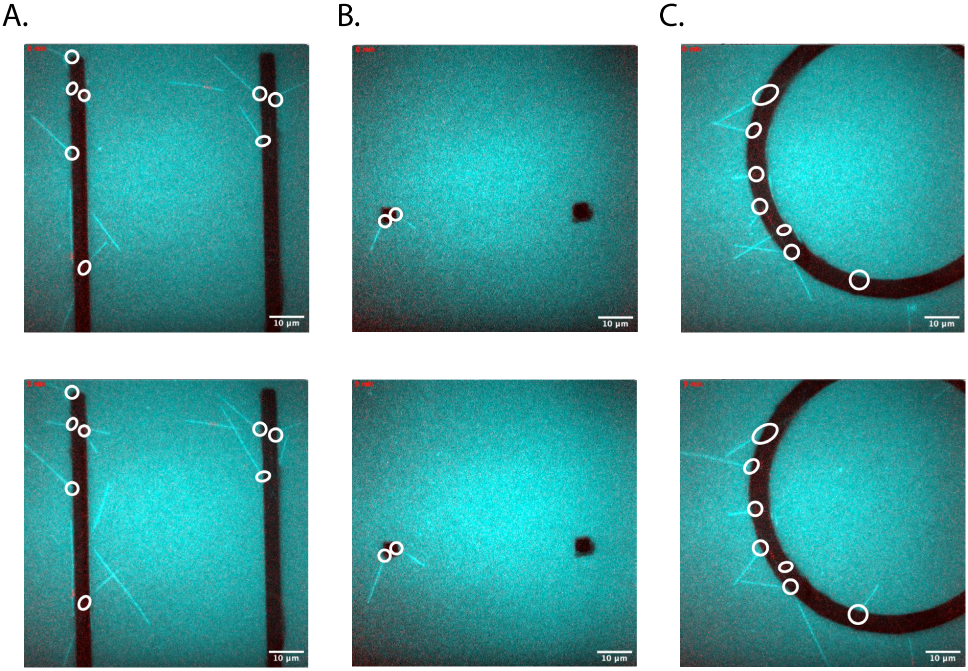

Figure 4.8: *Example TIRF images of MT dynamic assay in the presence of MT seeds immobilized by 6HB DNA origami on gold patterns, showing selectivity of MT growth sites on gold patterns (indicated by circles (A) MTs extending from gold line sites. The lower image shows the same field of view after 4 minutes. (B) MTs extending from gold dot sites. The lower image depicts the same field of view after 9 minutes. (C) MTs extending from circular gold-patterned sites. The lower image captures the same field of view after 9 minutes. From [28]*

Promising results from both DNA origami binding to the gold patterns (Fig. 4.7) and the high specificity of binding of the DNA-labeled seeds to the patterned area (Fig. 4.8) made us conclude that among the methods we investigated, this was the most-promising method to be further explored. Table 4.1 summarizes all the methods that were investigated in this study.

Table 4.1: *Summary of the experimental conditions tested for controlling the growth of MTs on patterned surface (Huibregtsen 2022) [28]*

Passivation Method	**Linker**	**Linker Conc.**	**Linker Wash (μL)**	**Seed Conc.**	**Seed Wash (μL)**	**Tubulin Conc. (μM)**	**Result**
Acid clean + PLL-PEG	Neutravidin	0.5 mg/mL	10	10x diluted	10	16.7	Many floating seeds, not attached to the gold.

Continued on next page

Table 4.1 – continued from previous page

Passivation Method	**Linker**	**Linker Conc.**	**Linker Wash (μL)**	**Seed Conc.**	**Seed Wash (μL)**	**Tubulin Conc. (μM)**	**Result**
Acid clean + 30 min 10 mg/mL silane-PEG + kappa-casein	Neutravidin/ MS neutravidin	0.5 mg/mL	15	10x diluted	15	16.7	Better passivation than Figure 3.11 and some potential attachment.
Acid clean + 30 min 10 mg/mL silane-PEG + kappa-casein	Neutravidin/ MS neutravidin	0.5 mg/mL	50	10x diluted	50	16.7	Same passivation as 3.12/3.13, as well as some attachment.
Acid clean + overnight 10 mg/mL silane pegylation + PLL-PEG	Neutravidin	2.5 mg/mL	50	10x diluted	50	16.7	Due to the long seeds, too crowded to analyze.
Acid clean + overnight 10 mg/mL silane pegylation + PLL-PEG	Neutravidin	2.5 mg/mL	50	10x diluted	50	16.7	Shorter seeds, but barely any passivation.
Acid clean + overnight 10 mg/mL silane pegylation + PLL-PEG	Neutravidin	2.5 mg/mL	200	10x diluted	200	16.7	Too crowded to say anything meaningful.
Acid clean + oxygen plasma + overnight 10 mg/mL silane pegylation + PLL-PEG	Neutravidin	1.7 mg/mL	200	10x diluted	200	12.5	Less crowded than Figure 3.18, but still seeds attached everywhere.
Acid clean + kappa-casein	DNA origami	10x diluted	20	10x diluted	20	16.7	Too crowded to say anything meaningful.
Acid clean + kappa-casein	DNA origami	10x diluted	50	50x diluted	50	12.5	Great passivation and most of the seeds seem to be attached to the gold.
Acid clean + kappa-casein	DNA origami	10x diluted	50	50x diluted	50	16.7	Passivation seems to be less than Figure 3.21, but still a few seeds attached to the gold.

Continued on next page

Table 4.1 – continued from previous page

Passivation Method	**Linker**	**Linker Conc.**	**Linker Wash (μL)**	**Seed Conc.**	**Seed Wash (μL)**	**Tubulin Conc. (μM)**	**Result**
Acid clean + PLL-PEG/kappa-casein	DNA origami	10x diluted	50	10x diluted	50	14.1	Okay passivation, only one microtubule found seemingly attached to the gold.
Acid clean + PLL-PEG/kappa-casein	DNA origami	10x diluted	50	10x diluted	50	16.7	Bad passivation, hard to say whether there are seeds attached to the gold.
Acid clean + oxygen plasma + 1 mg/mL silane-PEG + PLL-PEG/kappa-casein	DNA origami	10x diluted	50	5x diluted	50	16.7	Great passivation, but no seeds found attached to the gold.

4.3. CONTROLLING MICROTUBULE NUCLEATION ON MICROSPHERES (BEADS)

Two distinct approaches were investigated for spatially-controlled microtubule growth on microspheres: direct attachment of biotinylated seeds and DNA origami-mediated immobilization.

In the first approach, carboxylated microspheres were conjugated with PLL-PEG-biotin followed by neutravidin coating to enable biotinylated seed attachment. However, in our hands this method yielded insufficient seed density on the microsphere surface, precluding the formation of observable microtubule asters.

The second strategy employed 6-helix bundle (6HB) DNA origami structures engineered with three biotinylated staples at one terminus for surface attachment to neutravidin-coated microspheres. Microtubule seeds were generated as diblock structures, comprising a DNA-functionalized segment with complementary handles to the 6HB, followed by an unmodified segment polymerized with unlabeled tubulin in the presence of stabilizing agents. This architecture was designed to bias seed orientation, promoting outward-facing microtubule plus ends analogous to centrosomal organization.

Fig. 4.9 illustrates the generation and characterization of diblock microtubule seeds. Panel A provides a schematic representation of the fabrication process, while panel B presents TIRF microscopy validation of the diblock architecture. The differential length of the secondary block enables plus-end identification, exploiting the established enhanced dynamics at microtubule plus ends.

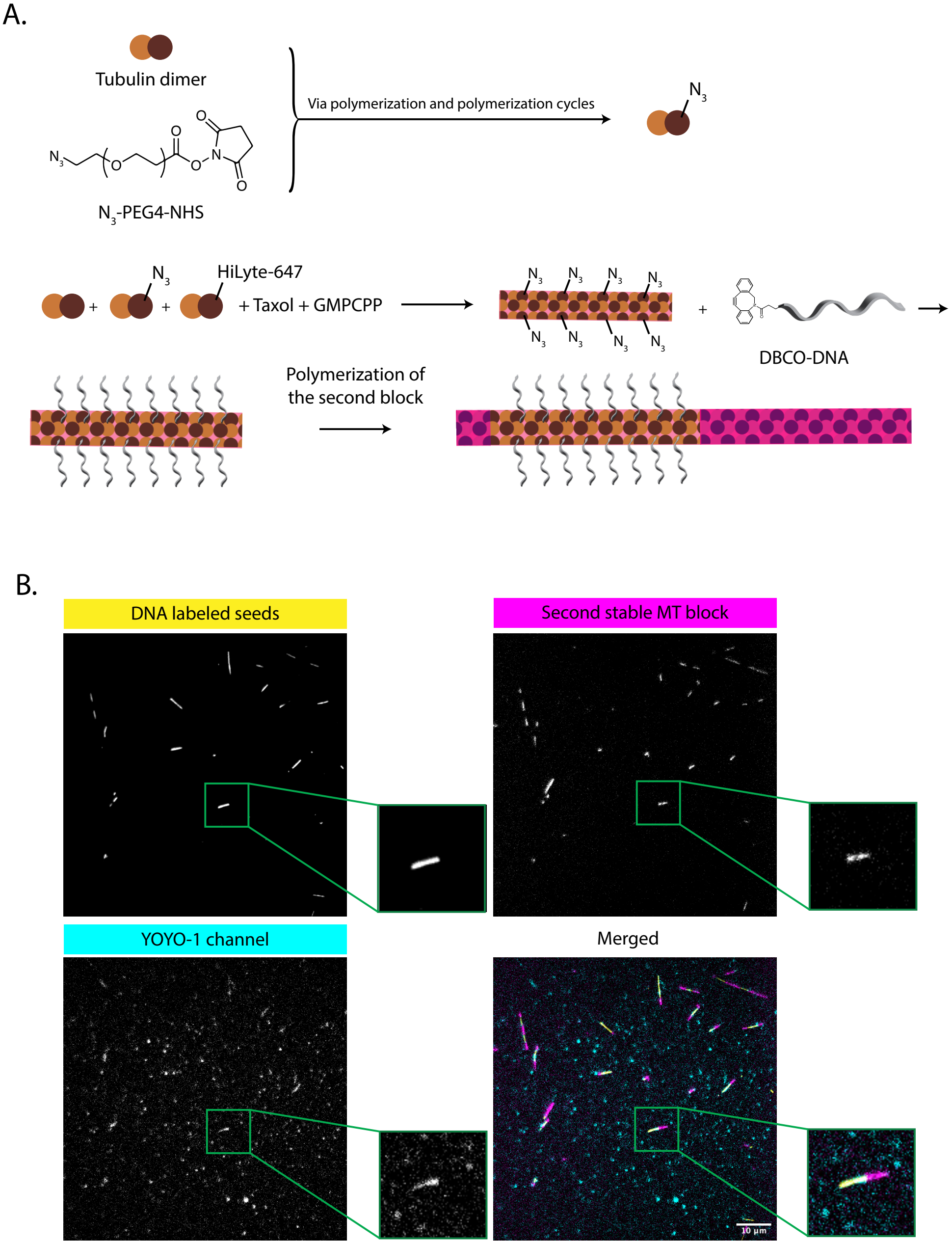

Figure 4.9: *Synthesis and visualization of diblock microtubule seeds. (A) Schematic illustration depicting the fabrication process of making diblock microtubule seeds (Matsuda et al. 2019). The core segment incorporates DNA handles complementary to those present on the 6-helix bundle (6HB) DNA origami structures. (B) Total internal reflection fluorescence (TIRF) microscopy images showing the spatially distinct fluorescent signatures of the DNA labeled core (grown with rhodamine-labeled tubulin, shown inn yellow) and secondary segments (grown with HiLyte642, shown in magenta) and the fluorescent signal from YOYO-1 channel that is visible due to presence of DNA on the core block, with a composite merged image demonstrating the diblock architecture.*

Although YOYO-1 preferentially binds to double-stranded DNA, it demonstrates sufficient affinity for single-stranded DNA conjugated to the core block of the seed to generate detectable fluorescence. Imaging in the 488 nm channel reveals YOYO-1 signal colocalization with core block fluorescence, as evidenced by the spatial correspondence in the yellow channel, cyan channel, and merged images in Fig. 4.9B. Therefore, this colocalization of YOYO-1 fluorescence signal with the core block fluorescence provides direct validation of successful DNA conjugation to the microtubule core segment.

After validation of the formation of diblock MT seeds with their core block being labeled by DNA, they were added to the 6HB coated beads and extra unbound seeds were washed away. The MT dynamic assay mixture was added to the seed-coated beads. Microtubule dynamics were visualized via TIRF microscopy in flow cells containing the functionalized microspheres supplemented with dynamic microtubule assay components (Fig. 4.10A). DNA origami visualization was achieved using YOYO-1 fluorescent dye. As demonstrated in fig. 4.10B, TIRF microscopy reveals the successful formation of artificial asters, characterized by radially-organized dynamic microtubules emanating from a central microsphere. The spatial coincidence of YOYO-1 fluorescence (cyan) and microtubule seed signals (magenta) at microtubule nucleation sites confirms the intended hierarchical assembly of design components. The relatively weak fluorescence intensity of these signals can be attributed to their spatial positioning relative to the TIRF excitation field. The 1 μm diameter of the microsphere places many components outside the optimal imaging plane. Fig. 4.9C presents a representative kymograph analysis, illustrating microtubule dynamic behavior within these artificial asters.

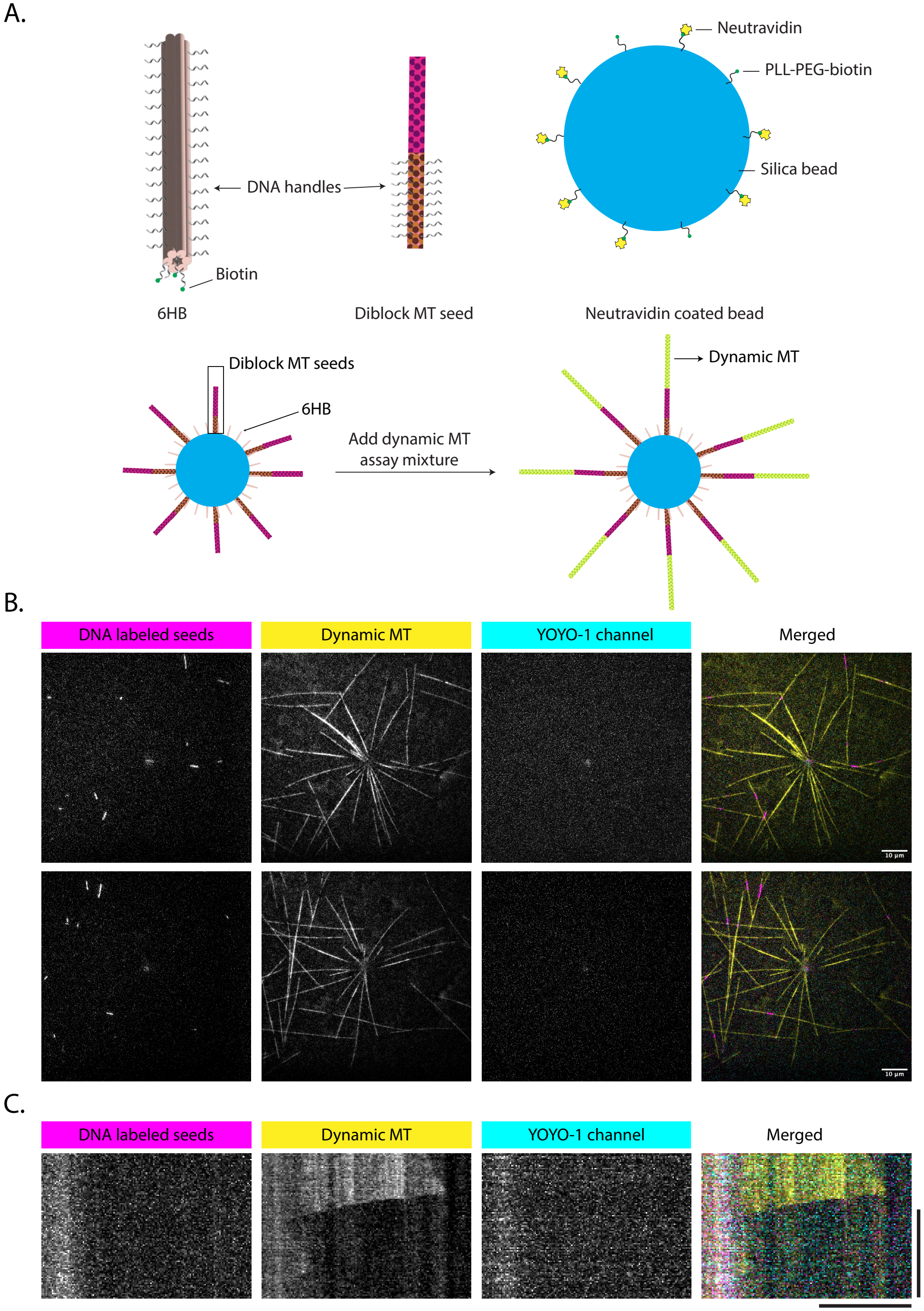

Figure 4.10: *Assembly and characterization of artificial microtubule asters. (Continued ...)*

(Figure 4.10 continued) (A) Schematic representation depicting the hierarchical assembly of microtubule asters using DNA origami structures and DNA-functionalized diblock microtubule seeds. Note: Diagram not drawn to scale. (B) Representative TIRF microscopy images demonstrating artificial aster formation on silica beads. Channels display: DNA-labeled core microtubule seeds (magenta), dynamic microtubules (yellow), and DNA origami structures (cyan). Scale bar: 10 µm. (C) Representative kymograph of a single microtubule emanating from an artificial aster, demonstrating dynamic behavior. Scale bars: spatial, 10 µm; temporal, 1 min.

4.4. CONCLUSION

By systematically testing different strategies—including gold micropatterning, surface passivation, biotin–neutravidin interactions, and DNA origami-based approaches—we identified DNA origami-mediated immobilization as the most promising method for achieving spatially controlled microtubule growth. Furthermore, extending this strategy to three-dimensional systems with functionalized microspheres enabled the successful assembly of artificial microtubule asters.

4.5. MATERIALS AND METHODS

4.5.1. MICROFABRICATION OF GOLD-PATTERNED COVERSLIPS

The location of the microtubules was controlled using various gold patterns. These were created using microfabrication, using a protocol made by Nemo Andrea, which is outlined in the rest of this section.

For the patterning, standard 24x24 mm coverglass pieces (Menzel-Gläser) were used. They were cleaned in a barrel plasma etcher using O_2 gas (200 sccm O2, 600 W, without Faraday cage) for 5-7 minutes. This removes some of the organic contaminants that are present in the glass, but more A thorough cleaning procedure would be preferred if possible. Coating with resist.

After cleaning, a layer of photoresist (positive: MICROPOSIT® S1813 or negative MicroResist technology ma-N 1410) was spin-coated on the coverglass pieces at 3000 rpm and baked at 110 °C for 10 minutes and 100 °C for 2 minutes respectively (step 1 in Fig. 4.11). The photoresist layer was patterned either by a maskless exposure system (Heidelberg Instruments µmla) or through a homemade Cr/Al photomask on a standard UV aligner (EVG® 620) (step 2 in Fig. 4.11).

Exposure through a photomask allowed for higher throughput of the fabrication, which is preferable given that the produced samples are single-use. Photomasks were placed on the spin-coated sample pieces without clamping. Exposure doses for the maskless system were 300mJ (for positive resist). Exposure doses for the UV system were 104 mJ (for positive resist) and 140mJ (for negative resist). The exposed resists were developed after exposure in MF321, a developing solution for the positive resist, for 60 seconds and ma-D33/s, a developing solution for the negative resist, for 70 seconds with continuous agitation of the developer. The developed resist layers were treated in weak oxygen plasma (100 W, 200 sccm O2, with Faraday cage) in a standard barrel etcher to remove any impurities from the patterned surface (step 3 in Fig. 4.11)

EVAPORATION OF CHROMIUM AND GOLD

The samples were then mounted in a custom-made clamping holder for evaporation in a Temescal FC-2000 e-beam evaporation system. The chamber was pumped down to 3.0E-6mbar and 5nm (target value) of Chromium was evaporated onto the samples at 0.5Å/s. After chromium evaporation, 20 nm of gold was evaporated into the sample in the same chamber at a rate of 1Å/s (step 4 in Fig. 4.11). The samples were then submerged in room-temperature acetone (to dissolve the photoresist) and the Cr-Au layer on areas with resist was lifted off with the help of ultrasonication (steps 5 and 6 in Fig. 4.11). The Glass-Cr-Au sections of the pattern have strong adhesion and remain intact during this procedure. Samples were kept in an ultrasonic bath for 10 minutes before being transferred to isopropanol wash steps (3 minutes each). Samples were then left to dry before being transported outside the cleanroom environment.

PHOTOMASK FABRICATION

Photomasks were fabricated starting from the same plasma-cleaned coverglass pieces described above. 100 nm of aluminum or 50nm of chromium was sputtered onto the coverglass pieces, followed by spin-coating and exposure. The written patterns were mirrored versions of the desired final exposure patterns on the gold pieces, as the metal layer must be placed face down onto the sample during exposure. After patterning the resist layer (always using positive resist), the removal of the metal layer was done in different ways for Al and Cr. For Al, the coverglass piece was left in the developer solution (MF321) for extended periods of time (10-12 minutes), as the developer etches aluminum and its native oxide. For Chromium photomasks, the Cr layer was etched in room temperature TechniEtch Cr01chromium etchant for 2 minutes. This produced cleaner patterns than the aluminum at the cost of increased fabrication time.

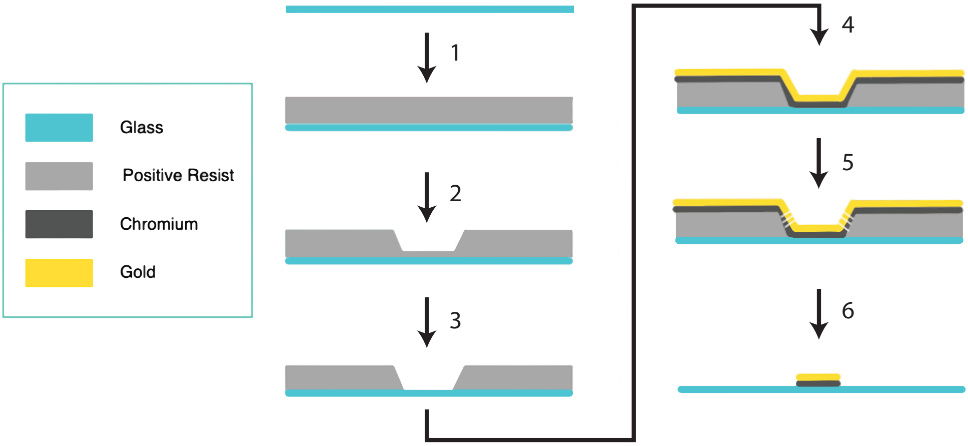

Figure 4.11: *The microfabrication process. (1) Resist is spincoated onto the glass surface. (2) Using either a maskless exposure system or a photomaks, the resist is patterned. (3) The glass is treated with weak oxygen plasma to remove impurities on the surface. (4) Chromium and gold are evaporated onto the glass. (5) While submerged in acetone, the glass is ultrasonication which creates holes in the chromium/gold on the steep parts next to the pattern. (6) The acetone dissolves the resist and therefore takes off the chromium and gold that is not on the patterned part. The result is a coverslip patterned with chromium/gold patterns. From [28]*

4.5.2. GLASS PASSIVATION TECHNIQUES

PIRANHA ACID CLEANING

Piranha acid cleaning was performed to remove metal and organic compounds from the glass. For this procedure, the coverslips are placed in a teflon rack in an appropriate glass beaker. Next, 120ml of sulfuric acid (95-98%) is poured into the beaker. After this, 40ml of hydrogen peroxide (30%) is slowly added. Then, the coverslips are left in this solution for 7 minutes. This solution is a strong oxidizer and removes metal and organic matter in this way. It also hydroxylates (adds OH-groups) glass and leaves it highly hydrophilic. Afterwards, the coverslips are rinsed multiple times in MilliQ (ultrapurified water), to wash away any residue left on the coverslip.

PLL-PEG/κ-CASEIN PASSIVATION

Besides acid cleaning, glass coverslips can be passivated to prevent non-specific binding. Here, poly-l-lysine poly(ethylene glycol) (PLL-PEG) and κ-casein (KS) were used. PLL-PEG is a polymer which consists of a PLL backbone which is positively charged, and a PEG sidechain which is hydrophilic and protein resistant. The positively charged PLL backbones interact with the negatively charged glass and the PEG sidechains create a monolayer of protein-resistant polymer. KS is a subunit of milk casein which is commonly used in microtubule assays to also prevent the binding of tubulin to the glass, but its mechanism is less well understood [34]. For passivation with PLL-PEG and/or κ-casein, concentrations of 0.2mg/ml and 0.5mg/ml, respectively, are used. The passivation with PLL-PEG and/or KS happens right before the experiment it is needed for. Using double-sided tape, a channel of about 4mm wide is created on a microscope slide. The coverslip is put on top and the next 10uL of the PLL-PEG, KS or a mixture of the two is added to the channel. This is incubated for 10min. Next, the experiment for which the passivation was necessary can be started.

PLURONIC F127

Pluronic can also be used as a passivator. Pluronic is a poloxamer manufactured by BSF which consists of a hydrophobic middle part (poly propylene oxide) plus two hydrophilic sides (poly ethylene oxide) [35]. The hydrophobic part sticks to the glass and the hydrophilic parts are oriented upwards and create a non-sticky barrier to the glass. Pluronic 127 was used at 1% concentration and incubated for 10 minutes in a channel, when used.

OXYGEN PLASMA

Another type of procedure used for cleaning and activation of the coverslips is using the oxygen plasma machine (Plasma Prep III Solid state, SPI® Supplies). In this procedure, oxygen radicals created in the oxygen plasma machine react with organic substances on the glass. This reaction creates gaseous products which are removed by the airflow in the machine [36]. For this thesis, oxygen plasma settings of 60 mWatts for 2 minutes were used to clean coverslips using oxygen plasma unless mentioned otherwise.

SILANE-PEG

To passivate the microfabricated coverslips, silane-PEGylation was also tested. Silane-PEG uses the same principle as PLL-PEG, but here an ethoxy silane group binds to a hydroxyl group on the glass instead of the electrostatic interactions of the PLL backbone. Two different pretreatments were tested. The first one is piranha acid cleaning, and the second one is inspired by a paper by Portran et al. [23]. For the first pretreatment, coverslips are piranha acid cleaned, before incubating in mPEG-silane (5K, Biopharma PEG Scientific Inc) in ethanol 96.5 %, on a rocking platform (VWR®) at room temperature for 30 minutes or overnight. Two different concentrations of mPEG-silane were tested, 1 mg/ml and 10mg/ml. The coverslips were sequentially washed in ethanol and ultrapure water, dried using nitrogen, and stored at room temperature away from dust.

For the second pretreatment, the coverslips are first incubated 30 min in acetone, then 15 min in ethanol (96.5 %), next rinsed in ultrapure water before incubating for 2 hours in Hellmanex III (2 % in water, Hellma), and again rinsed in ultrapure water. The coverslips are then dried using filtered airflow, and oxidized in the plasma cleaner for 2 min at 60 mW. After this pretreatment, the coverslips are emerged immediately in a solution of 1 mg/mL mPEG-silane in ethanol 96.5(%) and 0.02% of HCl, and left on the rocking platform at room temperature overnight. Coverslips were then dried and stored in the same way as the first pretreatment.

4.5.3. GLASS PASSIVATION COMPARISONS

To compare the degree of passivation between the various methods, an experiment was done using kinesin labeled with a 647 fluorophore. 10 μL 0.05 mg/mL kinesin-647 was added to a channel on all the coverslips and incubated for 10 minutes.

Next, the channels were washed by 15 μL MRB80 and visualized in the spinning disk TIRF microscope with TIRF642 laser. To compare acid cleaning and silane pegylation versus oxygen plasma and silane pegylation, an experiment with labeled neutravidin (prepared as described in section 4.5.4 was done. Both coverslips were incubated with 0.5 mg/mL labeled neutravidin for 10 minutes and afterwards washed with 150 μL MRB80. Next, the coverslips were imaged using the TIRF488 laser on the spinning disk TIRF microscope.

4.5.4. NEUTRAVIDIN MODIFICATIONS

LABELED NEUTRAVIDIN

To be able to visualize neutravidin with TIRF microscopy, labeled neutravidin was prepared. The neutravidin was labeled with Alexa Fluor 488 TPF Ester. More specifically, 15 µL DMSO was added to 100 µg Alexa Fluor 488. Next, 1 µL of this mixture was added to 100 µL of 5 mg mL^{-1} neutravidin. This is then incubated for five minutes and purified using Zebra™ spin desalting columns (7K MWCO). The column is centrifuged at 1500 RCF for 1 minute to remove the storage solution. Next, the sample is added to the column and is washed three times with MRB80 at 1500 RCF in the centrifuge (Labnet Prism™ R Refrigerated Microcentrifuge) for 1 minute and then once more at 2 minutes at 1500 RCF. The labeled neutravidin is found in the flow through.

NEUTRAVIDIN TREATED WITH MERCAPTOSUCCINIC ACID

Next to regular neutravidin, another approach was tested to increase the affinity of neutravidin for gold. In this approach, neutravidin is treated with mercaptosuccinic acid. This method is adapted from Presnova et al. [29]. The method should allow neutravidin to form covalent bonds with gold as the mercaptosuccinic acid adds sulfur groups to the neutravidin, which can form thiol-gold bonds [37]. First, neutravidin is mixed with mercaptosuccinic acid. For this, 3.4 mg mercaptosuccinic acid is mixed with 200 µL HEPES. Also, 3.1 mg of EDC is added to this mixture, which was then sonicated for 5 minutes to ensure dissolving. Afterwards, 200 µL of 5 mg mL^{-1} neutravidin is added and incubated on ice for one hour. Secondly, 5 µL of 0.01M DTT, to prevent disulfide bonds, and 10 µL of 10mM EDTA are added and mixed in a shaker for 30 minutes at room temperature. Lastly, the treated neutravidin is purified using Zebra™ spin desalting columns (7K MWCO). The column is centrifuged at 1500 RCF for 1 minute to remove the storage solution. 130 µL of the sample is added to the center of the compacted resin bed. This is centrifuged at 1500 RCF for 2 minutes to collect the desalted sample.

TESTING ACTIVITY OF MERCAPTOSUCCINIC TREATED NEUTRAVIDIN

To check whether the mercaptosuccinic treated neutravidin (MS neutravidin) was just as active as regular neutravidin, and thus able to bind to biotin in the same manner, two assays were done. One with silica beads coated with PLL-PEG-Biotin, and one with amine PEG-biotin beads. Silica beads coated with PLL-PEG-biotin were used to bind the MS neutravidin and neutravidin to. First, the beads are washed by taking three samples of 20 µL of beads coated with a 1:3 ratio of PLL-PEG:PLL-PEG-biotin and adding 80 µL MRB80 to each sample. Next, the samples were put in the centrifuge, at a temperature of 25 °C, 17200 RCF for one minute. The supernatant was discarded and 10 µL of 0.5 mg mL^{-1} neutravidin was added to one tube, 10 µL of 0.5 mg mL^{-1} MS neutravidin to another and the last tube was left on ice. The tubes were incubated for 10 minutes on ice. Tubes 1 and 2 were centrifuged again at the same settings and the supernatant was discarded again. Next, 10 µL 10x diluted kinesin-biotin-647 was added to these tubes and incubated on ice for 10 minutes.

These were then washed at the same centrifuge settings with 100 µL MRB80 twice, with supernatant being discarded after both centrifuge steps. The pellets were suspended in 10 µL MRB80. The three mixes (with MS neutravidin, neutravidin and no neutravidin added) were then visualized using the spinning disk TIRF microscope with transmission (for beads) and TIRF647 for visualizing the kinesin-biotin-647.
For the amine PEG-biotin beads, a buffer of 84 µL κ-casein and 756 µL MRB80 was made. Three tubes with 20 µL amine beads and 80 µL buffer were incubated for 10 minutes on ice. Next the tubes were centrifuged at 17200 RCF for 1 minute. Supernatants were discarded and 100 µL buffer was added to both tubes. Tubes were centrifuged at the same settings and supernatants were discarded before adding 10 µL 0.5 $\mathrm{mg\,mL^{-1}}$ neutravidin to one tube, 10 µL 0.5 $\mathrm{mg\,mL^{-1}}$ MS neutravidin to another tube and nothing to the last one. This was incubated on ice for 10 minutes. Next, 90 µL buffer was added to the two tubes with neutravidin and they were again centrifuged at the same setting after which the supernatants were discarded. Next 10 µL of 10x diluted kinesin-biotin-647 was added to all tubes and incubated for 10 minutes. The tubes were then washed with 100 µL buffer twice and the supernatants were discarded before adding 10 µL buffer. These mixes were diluted 10 times to visualize with TIRF using transmission and TIRF647.

NEUTRAVIDIN TO GOLD

In this experiment, labeled neutravidin and labeled MS neutravidin (labeled in the same manner as regular neutravidin) were used to observe its binding to the gold. One experiment consisted of creating a channel of 4 mm wide, flowing in 10 µL 1% Pluronic and incubating that for 10 minutes. This was then washed with 10 µL MRB80 and 2x diluted neutravidin or MS neutravidin was added and incubated for another 10 minutes. This was again washed with 10 µL MRB80 and the next 100x diluted kinesin-biotin-647 was added and incubated for 10 minutes. This was then also washed with 10 µL MRB80, before visualizing the coverslip with TIRF and analyzing the images with ImageJ.

4.5.5. DNA ORIGAMI

Besides immobilizing seeds on the surface of gold by using the binding of neutravidin and biotin, we tested the use of DNA origami to immobilize the seeds using thiol-gold binding and complementary base pairing.

PREPARATION

For the DNA origami approach, 6HB DNA origamis with thiolated ends were prepared. The preparation of these DNA origamis starts with creating two mixes. The first mix consists of the strand and staples for the basic 6HB structure. These are the oligonucleotides 1-174. Their sequences are listed in Table S4.1. The second mix consists of the added oligonucleotides for the thiolated strands, which are oligonucleotides 175-177. These sequences are listed in Table S4.2.
The final concentration of each oligonucleotide in the 6HB basic structure mix is 4 $\mathrm{\mu mol\,L^{-1}}$. For the thiolated strands oligonucleotides, the final concentration is

$33\,\mu\mathrm{mol\,L^{-1}}$ each. Next, the DNA origami mix is made. Table 4.2 lists its constituents.

Table 4.2: *Constituents of DNA origami mix. The volume and final concentration of the substances that make up the DNA origami.*

Reagents	**Volume** (µL)	**Final Concentration**
10x Folding Buffer	10	1x
100 nM ssDNA (M13, p7249)	20	$20\,\mathrm{nmol\,L^{-1}}$
Oligo mix 1-174	5	$200\,\mathrm{nmol\,L^{-1}}$
Oligo mix 175-177	0.55	$200\,\mathrm{nmol\,L^{-1}}$
MilliQ	64.5	-
Total	100	

PCR

This mix is then separated into two PCR tubes of 50 µL. The following PCR protocol is run on them:

1. 90 °C for 00:05:00
2. From 90 °C to 25 °C at a rate of $1\,^{\circ}\mathrm{C\,min^{-1}}$
3. Keep at 12 °C

PURIFICATION

The result of the PCR is purified using Amicon cut-off filters (100kDa, Millipore). The DNA origami was also once, less successfully, purified using gel electrophoresis; more about this can be found in SI A.3. The Amicon cut-off filter is washed with 1x folding buffer at 6000 RCF for 4 minutes in the centrifuge. Next, the 50 µL sample is added together with 400 µL 1x folding buffer and centrifuged for 4 minutes at 6000 RCF. Then, the sample is washed six times with 400 µL folding buffer through the filter, for four minutes at 6000 RCF in the centrifuge every time. This washing is done to get rid of any unbound DNA staples that could still be present in the sample. Loose DNA is smaller than the DNA origami and will therefore flow through the filter, whereas DNA origami will not. Lastly, the filter is inverted into a tube and it is run at 1000 RCF for two minutes in the centrifuge. The DNA origami is found in the tube.

VISUALIZATION DNA ORIGAMI

A 3 microliter sample of purified 6HB solution was deposited onto a freshly glow-discharged grid coated with a continuous carbon layer, as described in Nick Maleki et al. 2022 [38]. The sample was then blotted and quickly rinsed three times. Next, 3 μL of a 2% uranyl acetate solution was applied for 3 minutes. The grids were blotted again using blotting paper and left to air-dry for 20 minutes. Imaging was performed using a JEOL JEM1200 microscope fitted with a TVIPS F416 camera, at a magnification of 41,000×, yielding a pixel size of 0.38 nanometers.

To visualize the DNA origami with fluorescent microscopy, either on a microfabricated coverslip or a regular coverslip, YOYO-1 dye was used. YOYO-1 dye is a high affinity nucleic acid dye and is therefore used to visualize DNA. It fluoresces when bound to DNA. The YOYO-1 concentrations used to visualize DNA origami varied from $1\,\mathrm{nmol\,L^{-1}}$ to $20\,\mathrm{nmol\,L^{-1}}$. The stock concentrations of YOYO-1 dye were $100\,\mathrm{nmol\,L^{-1}}$ or $200\,\mathrm{nmol\,L^{-1}}$ and the dye was diluted with folding buffer before adding the DNA origami. If the visualization was done in a channel and there were washing steps, YOYO-1 dye was added to the washing buffer to make sure the YOYO-1 dye wasn't washed out either.

4.5.6. PREPARATION OF MICROTUBULE SEEDS

BIOTINYLATED SEEDS

For the neutravidin/biotin approach, biotinylated seeds were prepared. In the first few experiments, seeds were used with a biotinylated tubulin percentage of 10%. For this preparation, first a tubulin mix was created using $2\,\mathrm{\mu mol\,L^{-1}}$ biotinylated tubulin (Porcine, Cytoskeleton Inc), $2\,\mathrm{\mu mol\,L^{-1}}$ 488-labeled tubulin (Porcine, Cytoskeleton Inc), $16\,\mathrm{\mu mol\,L^{-1}}$ unlabeled tubulin (Porcine, Cytoskeleton Inc), 1mM GMPCPP and 1X MRB80 for a final volume of $8.3\,\mathrm{\mu L}$. The biotinylated tubulin is to recruit the seeds using neutravidin. The 488-labeled tubulin is added to be able to visualize the seeds in the microscope using a 488 nm laser. GMPCPP is a GTP replacement which hydrolyzes slower and is therefore more stable than GTP. Thus, it stabilizes microtubules against depolymerization, and is more useful for microtubule formation at room temperature.

This mix is incubated on ice for 5 minutes. Next, it is put in an Airfuge (Beckman) for 5 minutes at 30psi in a cold rotor. The supernatant is extracted and added to $0.8\,\mathrm{\mu L}$ 10mM GMPCPP. The tube is covered with aluminum foil to prevent bleaching and the mix is incubated at 37 °C for 30 minutes. This mix is then centrifuged again in the airfuge at the same settings, but with the rotor at room temperature. Now the supernatant is discarded, and the microtubule pellet is resuspended in $5.94\,\mathrm{\mu L}$ MRB80. Assuming 80% recovery, we now have about $20\,\mathrm{\mu mol\,L^{-1}}$ tubulin. This is then incubated on ice for 20 minutes to depolymerize the microtubules. Afterwards, $0.66\,\mathrm{\mu L}$ of 10mM GMPCPP is added and the solution is incubated firstly on ice for another 5 minutes and then at 37 °C for 30 minutes. After another round of centrifuging in the airfuge at RT, the pellet is resuspended in $20\,\mathrm{\mu L}$ of MRB80 with 10% glycerol, flash frozen in liquid nitrogen and stored at −80 °C.

For later experiments, seeds with a biotinylated tubulin percentage of 30% were used so that it would bind more easily to neutravidin. For this preparation, $13\,\mathrm{\mu mol\,L^{-1}}$ biotinylated tubulin, $4\,\mathrm{\mu mol\,L^{-1}}$ 647-labeled tubulin and $25\,\mathrm{\mu mol\,L^{-1}}$ regular tubulin were added together with $0.35\,\mathrm{\mu L}$ MRB80, $16.8\,\mathrm{\mu mol\,L^{-1}}$ taxol and 1 mM GMPCPP to a total volume of $5.95\,\mathrm{\mu L}$. Next they were airfugged for 5 minutes at 30psi and the supernatant was taken and added to $0.5\,\mathrm{\mu L}$ of 10mM of GMPCPP. The seeds were incubated at 37 °C for either 30 minutes (from here on referred to as "long seeds") or for 5 minutes (from here on referred to as "short seeds"), and again airfugged for

5 minutes at 30 psi. Lastly, the pellet is resuspended in 20 µL of MRB80 with 10% glycerol, flash frozen in liquid nitrogen and stored at −80 °C.

DNA LABELED SEEDS

In the DNA origami approach, DNA-labeled seeds are used, with handles complementary to the handles on the DNA origami. For these seeds, 4 µL of 56 µmol L^{-1} azide-tubulin, 0.6 µL 647-labeled tubulin, 2 µL 100 µmol L^{-1} tubulin and 0.74 µL 1mM GMPCPP are added together. This mix is then incubated at 37 °C for 30 minutes. Next, 1 µL of 1mM DBCO-DNA and 20 µmol L^{-1} taxol is added. The DBCO-DNA are the handles complementary to the DNA origami, and the taxol provides stability to the seeds. This is incubated at 37 °C for 6 hours to let the seeds form. Next, the mix is airfrugged for 5 minutes at 30 psi. The supernatant gets discarded and the tube, without touching the pellet, is washed twice with 50 µL MRB80 + 10% glycerol + 20 µmol L^{-1} taxol, to get rid of any loose DNA strands which are not incorporated into the seeds. Lastly, the pellet is resuspended in 20 µL of the same buffer the tube was washed with.

4.5.7. MICROTUBULE ASSAYS

In this thesis, the main experiment done was a microtubule assay. In this assay, the microfabricated coverslips are first passivated. Then a linker is added that is supposed to bind to the gold, after which the seeds are added that will bind to the linker and, lastly, a tubulin mix is added which makes microtubules grow from the seeds.

PREPARING THE COVERSLIP

In these assays, first the coverslip would get passivated in one of the ways described in section 4.5.2 above. Acid cleaning and silane pegylation happens with the entire coverglass, after which a channel of about 4 mm wide is made on a microscope slide using double-sided tape. The coverslip is put on top and if either PLL-PEG or KS is used, this is now added to the channel and incubated upside down in a wet petri dish for 10 minutes. PLL-PEG is added at a concentration of 0.2 mg mL^{-1} and KS is added at a concentration of 0.5 mg mL^{-1}. Next, the linker between the gold and the microtubules is added. This could be the neutravidin, the MS neutravidin or the DNA origami. Neutravidin and MS neutravidin are added at 0.5 mg mL^{-1} for 10 minutes in a wet petri dish. The DNA origami purified by a filter is 10x, 2x or 1x diluted with folding buffer, added to the channel and incubated for 20 minutes in a wet petri dish. Next, the linker is washed out of the channel with 10 µL to 200 µL MRB80 or folding buffer, for neutravidin or DNA origami respectively.

ADDING THE SEEDS

After preparation of the coverslip, the seeds are added. DNA-labeled seeds are first incubated in a 37 °C water bath together with 0.2 µL GMPCPP for 5 to 15 minutes. Next, 1 µL of either biotinylated or DNA-labeled seeds is added to 8 µL of MRB80, 1 μL of 10mM GTP and 0.2 μL of 100 $\mu\mathrm{mol\,L}^{-1}$ tubulin. This is added to the channel and incubated for 20 minutes.

ADDING TUBULIN MIX

While incubating the seeds, the tubulin mix is made (see Table 4.3).

Table 4.3: *Tubulin mix. Stock concentrations, dilutions, final concentrations and volumes added of the substances that make up the tubulin mix.*

Name	**Stock Conc.**	**Dilution**	**Final Conc.**	**Vol.** (μL)
Tubulin	100 $\mu mol\,L^{-1}$	1×	16.7 $\mu mol\,L^{-1}$	2.0
κ-casein	5 $\mathrm{mg\,mL}^{-1}$	1×	0.5 $\mathrm{mg\,mL}^{-1}$	1.2
Methylcellulose	1%	1×	1.1%	1.3
GTP	50 $\mathrm{mmol\,L}^{-1}$	50×	1 $\mathrm{mmol\,L}^{-1}$	1.2
Oxygen scavenger	50x	50×	1x	1.2
Rhodamine-labeled tubulin	12.5 $\mu mol\,L^{-1}$	1×	1.04 $\mu mol\,L^{-1}$	1.0
Glucose	1 $\mathrm{mol\,L}^{-1}$	1×	50 $\mathrm{mmol\,L}^{-1}$	0.64
MRB80 buffer	–	1×	–	3.45
Total volume				12

This mix is added lastly and is responsible for growing the microtubules from the seeds. The methylcellulose in this mix keeps the microtubules crowded to the surface layer. Methylcellulose is a long hydrophobic molecule that lies on top of the microtubules to keep them in one layer so you can visualize them properly using TIRF microscopy [39]. The oxygen scavenger together with glucose is needed to remove oxygen from the solution, as oxygen can destabilize the fluorescent molecules during visualization and therefore make interpretation of the results more difficult [40]. Rhodamine labeled tubulin, is fluorescent tubulin that can be visualized with a 561 nm laser. The regular tubulin concentration was varied between 16.7 $\mu mol\,L^{-1}$ and 12.5 $\mu mol\,L^{-1}$. The MRB80 volume was then varied as well, to keep the total volume at 12 μL.

This mix is airfugged without the GTP and glucose in it, for 5 minutes at 30psi. The supernatant is taken out and added to the GTP and glucose. Next, the seeds are washed out the channel with 50 μL to 200 μL MRB80. Then the tubulin mix is added, the channel is sealed with vaseline and the sample is visualized using a TIRF microscope.

4.5.8. VISUALIZATION USING TIRF MICROSCOPY

For visualization, two Total Internal Reflection Fluorescence (TIRF) microscopes were used. One of them being the inverted Nikon TiE microscope, equipped with:

iLas 2 TIRF/FRAP dual laser illuminator, and an Andor iXon Ultra 888 camera. This microscope will from here on out be referred to as TIRF2. Its 488 nm laser operated at 150 mW, the 561 nm at 150 mW and the 642 nm at 140 mW. The scale of the images acquired with this microscope was 7.76 pixels/microns. The other being an inverted Nikon TiE microscope, equipped with: iLas2 TIRF/FRAP dual laser illuminator, 2X EVOLVE 512 Camera and a Yokogawa CSU-W1-T2 Spinning Disk Confocal Scanning Unit. This microscope will from here on out be referred to as a spinning disk TIRF microscope. The 488 nm laser operated at 150 mW, the 561 nm at 100 mW and the 642 nm at 110 mW. The scale of the images acquired with this microscope was 6.25 pixels/microns.

For this thesis, the 488 nm, 561 nm and 642 nm lasers were used at varying powers (from 0 to 5% for TIRF2 and from 10 to 30% for spinning disk TIRF). A 16-bit (10 MHz EM gain) digitizer and a standard gain of 4x was used. The EM gains ranged from 250-2000 for TIRF2 and from 250-600 for spinning disk TIRF.

SUPPLEMENTARY INFORMATION

Table S4.1: *The oligonucleotide sequences 1-174 used for creating the 6HB DNA origami [33]*

ID	Sequence
6HB 1	GCATCAATTCTACTAA
6HB 2	TAGTAGTAGCTGATTGCCCTT
6HB 3	CACCGCCTGGCCCTGAGAGGAGCCGTCAATA
6HB 4	GAGACGGGCAACAGCATTAACATCCAATAAATGAAAAGGTG
6HB 5	TAGATTAAGTTGCAGCAAGCGGTCAAACACCAGT
6HB 6	GATAATACATTTGAGGATTTAGAAGTCAACTAA
6HB 7	TTTACAATTCATTTGGGGCGCGAGCTCATACAGGC
6HB 8	AAGGCAAAGAATTAGCCAGGGTGGTTTTTCTACGCTG
6HB 9	GTTTGCCCTATCTTTAGGAGCACTAAATTAGAC
6HB 10	AAGCAATAAAGTCAATAACCTGTTTAGCTATATTACAATTCGACAACT
6HB 11	AAATCCTGTTTGCGTATTGGGCGCAAAATT
6HB 12	CGTATTAAATCCTTGGAATTGAGGAAGGTTATCTAAAACAGCAGGCGA
6HB 13k	ACGTTATAGATACATTTCGCAATGGCCTCAGTTTTCAACAACAACAACAA
6HB 14k	AGCATAACGCGCGGGGAGAGGCGGTTTGATGTTTTCAACAACAACAACAA
6HB 15k	GTGGTTCCGAAATCGGCGCAAATCAACAGTTGAAATGCCCGA
6HB 16k	CGGTTGTACCTTAGTTTGACCATTTAATTTTAAAATTTTCAACAACAACAACAA
6HB 17	ATAAATCGCCAGCTGCATTAATGAATCGGCCAAGCTAAAT
6HB 18k	GTTTGAGTAACATTATCCCTCAATCAATATCTGGTCAGTTGAAAATCCCTT
6HB 19	GGAACAATGATTCCCAATTCTGCGAACGAGTAGATAAAAACATTA
6HB 20	TGACCCTGTAATACGTCGGGAAACCTGTCGTAAAAGAATAGCCCG
6HB 21	AGATAGGGTTGGAAACTCAAATATCAAACATTTTGC
6HB 22	GAGAAGCCTTTTCCATATAACAGTAGAAACCACCAGAA
6HB 23	CAGTTTGCGTTGCGCTCACTGCCCGCTTTCCATTTTGCGG
6HB 24	GGAGCGGAATTATCAAAAATCTAAAGCATCACCTTGCTAGTGTTGTTC
6HB 25k	TCCTGATAACTAAAGTACGGTGTCTGGAAGTTTCATATTTCAATTTTCAACAACAACAACAA
6HB 26k	ACGCAAGGATAAAAATTCTAACTCACATTAATTGGAACAAGATTTTCAACAACAACAACAA
6HB 27k	GTCCACTATTAAAGAACGAGAGCCAGCAGCAAATGATCATAT
6HB 28k	CCTCATATATTTGTTTTAAATATGCATCACATGATTTTTCAACAACAACAACAA
6HB 29	ACGTCAAAAGCCTGGGGTGCCTAATGAGTGAGTTTAGAAC
6HB 30k	GGCAATTCATCAATATACACCGCCTGCAACAGTGCCACGCTGTGGACTCCA
6HB 31	TTGTTTGTTGCTGAATATAATGCTGTAGCTCAACATTTAAATGCA
6HB 32	ATGCCTGAGTAATGCGGAAGCATAAAGTGTAAGGGCGAACAACCG
6HB 33	TCTATCAGGGCCTGAGGCGGTCAGTATTAAATCCTGA
6HB 34	AAGATTCAAAGGCTTAGAGCTTAAGATTATACTTCTGA
6HB 35	TACGTGATCACAAATCCACACAACATACGAGCTGTAGGTA
6HB 36	ATAATGGAAGGGTTACACCAGCAGAAGATAAAACAGAGGATGGCCCAC
6HB 37k	ACCATATCTTTTGATAAGAGGTCATTTTGCGGATAGGGTGATTTTCAACAACAACAACAA
6HB 38k	GAAAGGCCGGAGACAGTGTGAAATTGTTATCCGCACCATCATTTTCAACAACAACAACAA
6HB 39k	CCAAATCAAGTTTTTTGTAAAAATACCGAACGAACAGAACCT
6HB 40k	CATCAATATGACCTTTAATTGCTCCAAAATTATTTTTTTCAACAACAACAACAA
6HB 41	GCCGTAAATCATGGTCATAGCTGTTTCCTGTCAAATCAC
6HB 42k	GCACGTAAAACAGAAATCTGATAGCCCTAAAACATCGCCATGGGTCGAGGT
6HB 43	TTGCGTAAAACTCCAACAGGTCAGGATTAGAGAGTATATTCAACC
6HB 44	GTTCTAGCTGATAAACCGAAGCTCGAATTCGTAGCACTAAATCGGA
6HB 45	ACCCTAAAGGGTAGTCTTTAATGCGCGAAAAAGAAA
6HB 46	CGGAGAGGGTACCAGACCGGAAGCGATTTTCAGGTTTA
6HB 47	TTAGAGCGGTCGACTCTAGAGGATCCCCGGGTATTAATGC
6HB 48	ACGTCAGATGAATACAGACAATATTTTTGAATGGCTATAGCCCCCGAT
6HB 49k	ACAGTACTCGCGTTTTAATTCGAAGCTTCAAAGCGAAGCTATTTTTTCAACAACAACAACAA

Continued on next page

Table S4.1 – continued from previous page

ID	Sequence
6HB 50k	TTTGAGAGATCTACAAAAAGCTTGCATGCCTGCATTGACGGGTTTTCAACAACAACAACAA
6HB 51k	GAAAGCCGGCGAACTGGCGTAAGAATACGTGGCATACAGTA
6HB 52k	GGTCATTGCCAAAGACTTCAAATACTTTTACATCGTTTTCAACAACAACAACAA
6HB 53	AAGGGAAACGTTGTAAAACGACGGCCAGTGCCGGCTATCA
6HB 54k	GGAGAAACAATAACGGAAAGATAGAACCCTTCTGACCTGAAAGCGAGAAAGG
6HB 55	GATTGCTTGCATCAAAAAGATTAAGAGGAAGCCCGTGAGAGTCTG
6HB 56	GAGCAAACAAGAGGGATTTTCCCAGTCACGGAAAGCGAAAGGAG
6HB 57	CGGGCGCTAGGGGACATTCTGGCCAACAGTTCGCCT
6HB 58	ACGGTAATCGGAAGCAAAGCGGATTTGAATACCAAGTT
6HB 59	GTGTAGCAAGGCGATTAAGTTGGGTAACGCCAATCGATGA
6HB 60	ACAAAATCGCGCAGCAGTCACACACCAAGTAATAAAGCGCTGGCA
6HB 61k	TTATTCACAGGTCTTTACCCTGACTATTATAGTCATAAAACTTTTTCAACAACAACAACAA
6HB 62k	AGCATGTCAATCATATGAAAGGGGGATGTGCTGCGGTCACGCTTTTCAACAACAACAACAA
6HB 63k	TGCGCGTAACCACCACATTACATTGGCAGATTCACAGGCGAA
6HB 64k	TTGATAATCACATAAATCAAAAATTTTCAATTACCTTTTCAACAACAACAACAA
6HB 65	TTAATGCCTCTTCGCTATTACGCCAGCTGGCGTACCCGG
6HB 66k	TGAGCAAAAGAAGATGAGCTCAATCGTCTGAAATGGATTATCCCGCCGCGC
6HB 67	AACATCATTTAAACAGTTCAGAAAACGAGAATGACGAAAAGCCCC
6HB 68	AAAAACAGGAAGATGGGCGATCGGTGCGGGCGCCGCTACAGGGCG
6HB 69	CGTACTATGGTAAATACCTACATTTTGAACTGAAACA
6HB 70	CAAATATTTATCCCCCTCAAATGCAGAAAACAAAATTA
6HB 71	AGCACGTATTCAGGCTGCGCAACTGTTGGGAATGTATAAG
6HB 72	ATTACATTTAACAATTGCAACAGGAAAAACGCTCATGGTGCTTTGACG
6HB 73k	TGAATTATGCGGAATCGTCATAAATATTCATTGAAATTGTATTTTCAACAACAACAACAA
6HB 74k	AACGTTAATATTTTGTTGCAACAGCGCCATTCGCCATAACGTGTTTTCAACAACAACAACAA
6HB 75k	CTTTCCTCGTTAGAATCCAATATTACCGCCAGCCATTTCATT
6HB 76k	CATTAAATTTATAGCGTCCAATACCCATTTTTAATTTTTCAACAACAACAACAA
6HB 77	CTAAACACACCGCTTCTGGTGCCGGAAACCAGAAAATTCG
6HB 78k	GGAAACAGTACATAAATCGGCCTTGCTGGTAATATCCAGAAAGAGCGGGAG
6HB 79	TGTGAGTGGGGGTAATAGTAAAATGTTTAGACTGGTTGTTAAATC
6HB 80	AGCTCATTTTTTAATCCAGCCAGCTTTCCGGGGAGGCCGATTAAA
6HB 81	GGGATTTTAGATAGAAGAACTCAAACTATCAATATA
6HB 82	AACGCCATCAGAAGTTTTGCCAGAGAATAACCTTGCTT
6HB 83	ACGCCAGAGTATCGGCCTCAGGAAGATCGCACCCAATAGG
6HB 84	CTGTAAATCGTCGCTAGTAATAACATCACTTGCCTGAGCAGGAACGGT
6HB 85k	TAATTTTACCAAAATAGCGAGAGGCTTTTGCAAAAAAAATAATTTTCAACAACAACAACAA
6HB 86k	TTCGCGTCTGGCCTTCCTTTGAGGGGACGACGACAATCCTGATTTTCAACAACAACAACAA
6HB 87k	GAAGTGTTTTTATAATCTAGCAATACTTCTTTGATTATTAAT
6HB 88-2k	GCTTTCATCAAGACGACGATAAAACCCTTAGAATTTTCAACAACAACAACAA
6HB 89	CCGAGTACGCATCGTAACCGTGCATCTGCCAGTTGTAGCCA
6HB 90-2	TCCTTGAAACAAATTAACCGTTGAGTGAGGCCA
6HB 91-2	CTTAGATTAAGAAGCAACACTATCATAACCCTCGTTTACCACATTAAATG
6HB 92	TGAGCGAGTAACAAACGTTGGTGTAGATGGGAAAGAGTCTACCAGAAG
6HB 93-2	GAAACCGAGGAGCCGAAACAAGTTGTCCATCACGACATAGCGATAG
6HB 94-2	TAGTAAGCGCTGAGAAGAGTCAATAGTGAATTTATAAGCCCTTTT
6HB 95-2	TGGGATAGGTCCCCGTCGGATTCTCCGTGCGAGGCA
6HB 96-2	TAAGAAAAGTAAGCGGAACGCAAATAATAACGGAATACCCA
6HB 97	ATAGGTCTGCAGATACATAACGCCAAAAGGAATTAGGAACAAACACCAGTAC
6HB 98-2	AAACTACACACTGAGTTTCGTCGGCGGATTGACCGTAA
6HB 99-2	AAAGAACTGGCATGAGCAATAGCTATCTTACCGCAAAATC
6HB 100	TAGCATTCCACCACATTCAACTAATGAGAGACTACCTT
6HB 101	TTATTACGCCCAATAGGAACCCATGTACCGTAAACGCCTG
6HB 102	TTTAACCTCCGGCTATAAGAGCAAGAAACAATGAAATATTAAAGACTCC
6HB 103k	GGTTATAAAGATTCATCAGTTGAGATTTAGGAATACAGACAGTTTTCAACAACAACAACAA

Continued on next page

Table S4.1 – continued from previous page

ID	Sequence
6HB 104k	CCCTCATAGTTAGCGTAATTTTCAGGGATAGCAAGCAGTATGTTTTCAACAACAACAACAA
6HB 105k	TTAGCAAACGTAGAAAAATTGAGTTAAGCCCAATATAGGTTG
6HB 106k	AAGTTTTGTCTTATTACAGGTAGATAACTATATGTATTTTCAACAACAACAACAA
6HB 107	AAGGTGGCGCCACCCTCAGAGCCACCACCCTCACGATCTA
6HB 108k	AAATGCTGATGCAAATCATATCAGAGAGATAACCCACAAGATACATACATA
6HB 109	AAGACAAGTTAATAAAACGAACTAACGGAACAACAGTCTTTCCAG
6HB 110	ACGTTAGTAAATGAACCGCCACCCATCAGAACCAACATATAAAAGA
6HB 111	AACGCAAAGACGAGGTAATTGAGCGCTACAATCGC
6HB 112	TATGGGATTTGAAGAAAAATCTACAGAACGCGAGAAAA
6HB 113	AAGTTTAGAGGTTTAGTACCGCCACCCTCAGAATTTTCTG
6HB 114	CTTTTTCAAATATAAACTGAACACCCTGAACAAAGTCAACCACGGAAT
6HB 115k	TAATTTCTGGCTCATTATACCAGTCAGGACGTTGGTGCTAAATTTTCAACAACAACAACAA
6HB 116k	CAACTTTCAACAGTTTCTGTATCACCGTACTCAGTTTTGTCATTTTCAACAACAACAACAA
6HB 117k	CAATCAATAGAAAATTCGCATTAGACGGGAGAATTTTTTAGT
6HB 118k	GAGAATAGAAGCGATTTTAAGAACATCTTCTGACCTTTTCAACAACAACAACAA
6HB 119	CCAGCGCTGATATAAGTATAGCCCGGAATAGGAGCGGAGT
6HB 120k	TAAATTTAATGGTTTGAAAGAATACATAAAAACAGGGAAGCATATGGTTTA
6HB 121	ACCGTGTCAACTTTAATCATTGTGAATTACCTTATAGGAACAACT
6HB 122	AAAGGAATTGCGAAAGTGCCGTCGAGAGGTCAAAGACAAAAGGG
6HB 123	CGACATTCAACATAGCAGCCTTACAGAGAATACCG
6HB 124	TTTTCACGTTAGATGGTTTAATTTGATAAATAAGGCGT
6HB 125	AGGGAAGGGTTTTGCTCAGTACCAGGCGGATATAATAATT
6HB 126	TAAATAAGAATAAATTTTGTTTAACGTCAAAAATGAAACGATTGAGGG
6HB 127k	ATCATAACACCAGAACGAGTAGTAAATTGGGCTTGGAAAATCTTTTCAACAACAACAACAA
6HB 128k	TCCAAAAAAAAGGCTCCAGGATTAGGATTAGCGGGTAAATATTTTTCAACAACAACAACAA
6HB 129k	TGACGGAAATTATTCATTCCAAATAAGAAACGATTCACCGGA
6HB 130k	CCTTTAATTGGCCCTGACGAGAAATTACTAGAAAATTTTCAACAACAACAACAA
6HB 131	TTATCACTAAGAGGCTGAGACTCCTCAAAGAGAAAAGGAG
6HB 132k	AGCCTGTTTAGTATCATAAACAGCCATATTATTTATCCCAAATAAAGGTGAA
6HB 133	ATACAAAAAAGCTGCTCATTCAGTGAATAAGGCTTTATCGGTTTA
6HB 134	TCAGCTTGCTTTCGCTGAAACATGAAAGTATCGTCACCGACTTGA
6HB 135	GCCATTTGGGAATTTGCCAGTTACAAAATATGCGTT
6HB 136	TTCTTAAACACAAATCAACGTAACATTCTTACCAGTATA
6HB 137	GCAAAATCCTGCCTATTTCGGAACCTATTATTAGGTGAAT
6HB 138	AAGCCAACGCTCAATAACGAGCGTCTTTCCAGAGCCTAATTAGAGCCA
6HB 139k	GCTTAATTCTTGACAAGAACCGGATATTCATTACCGCTTGATTTTTCAACAACAACAACAA
6HB 140k	ACCGATAGTTGCGCCGAATAAACAGTTAATGCCCCACCAGTATTTTCAACAACAACAACAA
6HB 141k	GCACCATTACCATTAGCCCTGAATCTTACCAACGCCAGTAGG
6HB 142k	ACAACCATCGTTCATCAAGAGTAAATGAGAATCGCCTTTTCAACAACAACAACAA
6HB 143	ACGTCACCAGTGCCATGAGTAACAGTGCCCGTCAATGACA
6HB 144k	ATATTTAACAACGCCAATTTTGCACCCAGCTACAATTTTATAAGGCCGGAA
6HB 145	TTTAGGCACAGACCAGGCGCATAGGCTGGCTGACCCCCACGCATA
6HB 146	ACCGATATATTGGGATAAGTTTTAACGGGGTCAATGAAACCATCG
6HB 147	ATAGCAGCACCATCAAGATTAGTTGCTACATGTAA
6HB 148	GCTTGCAGGGCAGATGAACGGTGTAGAGGCAATTTTCGA
6HB 149	GCGACAGTTGATGATACAGGAGTGTACTGGTAACGCTGAG
6HB 150	GCCAGTAATAAGAGCTTGCGGGAGGTTATGAAGCCATAGTAAATAGTA
6HB 151k	AGTACCGAACCGAAGTGACCAACTTTGAAAGAGGAAGTTAAATTTTCAACAACAACAACAA
6HB 152k	GGCCGCTTTTGCGGGATAGCGTCATACATGGCTTAATCAAGTTTTTCAACAACAACAACAA
6HB 153k	TTGCCTTTAGCGTCAGATTTTAGCGAACCTCCCGAAATATAA
6HB 154k	TCAGCAGCGAGTCAATCATAAGGGACAAAAGGTAATTTTCAACAACAACAACAA
6HB 155	TTTTCATAGTCTCTGAATTTACCGTTCCAGTACGTCACCC
6HB 156k	AGTAATTCTGTCCAGACCCGGTATTCTAAGAACGCGAGCGCTGTAGCGCG
6HB 157	ATAAACAGTTACTTAGCCGGAAACGAGGCGCAGACGAAGACAGCAT

Continued on next page

Table S4.1 – continued from previous page

ID	**Sequence**
6HB 158	CGGAACGAGGGTAGGCCAGAATGGAAAGCGCCGGCATTTTCGGTC
6HB 159	ATAGCCCCCTTCAGATATAGAAGGCTTATGACGACA
6HB 160	ACAGAGGCTTGCGACCTGCTCCATACATGTTCAGCTAA
6HB 161	GCCATCTCACAAACAAATAAATCCTCATTAAACAACGGCT
6HB 162	TGCAGAACGCGCCTTACCGCGCCCAATAGCAAGCAATATTTAGCGTTT
6HB 163k	AACAATACATCGCCTGATAAATTGTGTCGAAATCCTGAGGACATTTTCAACAACAACAACAA
6HB 164k	TAAAGACTTTTTCATGACGATTGGCCTTGATATTTTTCATAATTTTCAACAACAACAACAA
6HB 165k	TCAAAATCACCGGAACCTTTCATCGTAGGAATCATGTTTATC
6HB 166k	CCATTAAACGACGGAGATTTGTATGATAAGTCCTGTTTTCAACAACAACAACAA
6HB 167	CCGGAACTGACAGGAGGTTGAGGCAGGTCAGAGGAAAGTTT
6HB 168k	AACAAGACAAGCCGTTTTTATAGAGCCACCA
6HB 169	TCCTAATTTAGATTATACCAAGCGCGAAACAAAGTACAGGTAAAATAC
6HB 170	GTAATGCCACTACGAGAGCCGCCGCCAGCATCGCCTCC
6HB 171	CTCAGAGCGCACTCATCGAGAACAAGAAAATAATATCCCA
6HB 172	AACCTAAAACCTTTGACCCCCAGCCGAGCATGT
6HB 173	AGAACCGACCAGAACCACCACCAAGGCACC
6HB 174	AGAAACCAAAGAACGGGTATTAAACCAAAGTACCGCCACCCTC
6HB 175	TACACTAAAACACTCATGAAAGAGGCAACAGAA
6HB 176	CACCCTCAGAGCCGCCCCCACCCTCAGAGCCAC
6HB 177	TTTCCTTATCATTCCATCAATAATCGGCTGTC

Table S4.2: *The thiolated oligonucleotide sequences 175-177 used for creating the DNA origami. The thiols are added to the* $5'$ *end.*

ID	Sequence	Modification
6HB 175	ATCTAC ACTAAAA CACTCAT GAAAGAG GCAAAAG AA	Thiol C6
6HB 176	ATCGATCCACCCT CAGAGCC GCC CCA ACCCTCAG AGCCAC	Thiol C6
6HB 177	TTTCCT TATCATT CCA TCA ATAATCG GCTGTC	Thiol C6

REFERENCES

[1] S. L. Kline-Smith and C. E. Walczak. “Mitotic Spindle Assembly and Chromosome Segregation: Refocusing on Microtubule Dynamics”. In: *Molecular Cell* 15.3 (2004), pp. 317–327. ISSN: 1097-2765. DOI: https://doi.org/10.1016/j.molcel.2004.07.012. URL: https://www.sciencedirect.com/science/article/pii/S1097276504004186.

[2] S. Gadde and R. Heald. “Mechanisms and Molecules of the Mitotic Spindle”. In: *Current Biology* 14.18 (2004), R797–R805. ISSN: 0960-9822. DOI: https://doi.org/10.1016/j.cub.2004.09.021. URL: https://www.sciencedirect.com/science/article/pii/S0960982204006979.

[3] B. Akiyoshi and K. Gull. “Evolutionary cell biology of chromosome segregation: insights from trypanosomes”. In: *Open Biology* 3.5 (May 2013). Publisher: Royal Society, p. 130023. DOI: 10.1098/rsob.130023. URL: https://royalsocietypublishing-org.tudelft.idm.oclc.org/doi/full/10.1098/rsob.130023 (visited on 12/20/2024).

[4] M. Hara and T. Fukagawa. “Kinetochore assembly and disassembly during mitotic entry and exit”. In: *Current Opinion in Cell Biology*. Cell Nucleus 52 (June 1, 2018), pp. 73–81. ISSN: 0955-0674. DOI: 10.1016/j.ceb.2018.02.005. URL: https://www.sciencedirect.com/science/article/pii/S0955067417301515 (visited on 12/20/2024).

[5] R. L. Shrestha and V. M. Draviam. “Lateral to End-on Conversion of Chromosome-Microtubule Attachment Requires Kinesins CENP-E and MCAK”. In: *Current Biology* 23.16 (Aug. 19, 2013), pp. 1514–1526. ISSN: 0960-9822. DOI: 10.1016/j.cub.2013.06.040. URL: https://www.ncbi.nlm.nih.gov/pmc/articles/PMC3748344/ (visited on 12/20/2024).

[6] S. L. Jaspersen. “Anatomy of the fungal microtubule organizing center, the spindle pole body”. In: *Current opinion in structural biology* 66 (Feb. 2021), pp. 22–31. ISSN: 0959-440X. DOI: 10.1016/j.sbi.2020.09.008. URL: https://www.ncbi.nlm.nih.gov/pmc/articles/PMC7965227/ (visited on 12/20/2024).

[7] P. T. Conduit, A. Wainman, and J. W. Raff. “Centrosome function and assembly in animal cells”. In: *Nature Reviews. Molecular Cell Biology* 16.10 (Oct. 2015), pp. 611–624. ISSN: 1471-0080. DOI: 10.1038/nrm4062.

[8] D. Job, O. Valiron, and B. Oakley. “Microtubule nucleation”. In: *Current Opinion in Cell Biology* 15.1 (Feb. 1, 2003), pp. 111–117. ISSN: 0955-0674. DOI: 10.1016/S0955-0674(02)00003-0. URL: https://www.sciencedirect.com/science/article/pii/S0955067402000030 (visited on 12/20/2024).

[9] S. Petry and R. D. Vale. "Microtubule nucleation at the centrosome and beyond". In: *Nature cell biology* 17.9 (2015), pp. 1089–1093.

[10] J. M. Kollman, A. Merdes, L. Mourey, and D. A. Agard. "Microtubule nucleation by γ-tubulin complexes". In: *Nature reviews Molecular cell biology* 12.11 (2011), pp. 709–721.

[11] M. Moritz and D. A. Agard. "γ-Tubulin complexes and microtubule nucleation". In: *Current Opinion in Structural Biology* 11.2 (Apr. 1, 2001), pp. 174–181. ISSN: 0959-440X. DOI: `10.1016/S0959-440X(00)00187-1`. URL: `https://www.sciencedirect.com/science/article/pii/S0959440X00001871` (visited on 12/20/2024).

[12] M. R. King and S. Petry. "Phase separation of TPX2 enhances and spatially coordinates microtubule nucleation". In: *Nature Communications* 11 (2019). DOI: `10.1038/s41467-019-14087-0`. URL: `https://consensus.app/papers/phase-separation-of-tpx2-enhances-and-spatially-king-petry/6c6470c48b895212aab369ca2ba83010/` (visited on 01/22/2025).

[13] M. J. Rale, R. S. Kadzik, and S. Petry. "Phase Transitioning the Centrosome into a Microtubule Nucleator". In: *Biochemistry* 57.1 (Jan. 9, 2018), pp. 30–37. ISSN: 0006-2960. DOI: `10.1021/acs.biochem.7b01064`. URL: `https://www.ncbi.nlm.nih.gov/pmc/articles/PMC6193265/` (visited on 12/20/2024).

[14] V. Centonze and G. Borisy. "Nucleation of microtubules from mitotic centrosomes is modulated by a phosphorylated epitope." In: *Journal of cell science* (Mar. 1, 1990). URL: `https://www.semanticscholar.org/paper/Nucleation-of-microtubules-from-mitotic-centrosomes-Centonze-Borisy/279b420a245d02e5001b5fab4640aec3dc17f26c?utm_source=consensus` (visited on 01/22/2025).

[15] D. Kuchnir Fygenson, H. Flyvbjerg, K. Sneppen, A. Libchaber, and S. Leibler. "Spontaneous nucleation of microtubules". In: *Physical Review E* 51.5 (May 1, 1995). Publisher: American Physical Society, pp. 5058–5063. DOI: `10.1103/PhysRevE.51.5058`. URL: `https://link.aps.org/doi/10.1103/PhysRevE.51.5058` (visited on 01/22/2025).

[16] W. A. Voter and H. P. Erickson. "The kinetics of microtubule assembly. Evidence for a two-stage nucleation mechanism". In: *The Journal of Biological Chemistry* 259.16 (Aug. 25, 1984), pp. 10430–10438. ISSN: 0021-9258.

[17] K. A. Johnson and G. G. Borisy. "Kinetic analysis of microtubule self-assembly *in vitro*". In: *Journal of Molecular Biology* 117.1 (Nov. 25, 1977), pp. 1–31. ISSN: 0022-2836. DOI: `10.1016/0022-2836(77)90020-1`. URL: `https://www.sciencedirect.com/science/article/pii/0022283677900201` (visited on 02/05/2025).

[18] R. A. Walker, E. T. O'Brien, N. K. Pryer, M. F. Soboeiro, W. A. Voter, H. P. Erickson, and E. D. Salmon. "Dynamic instability of individual microtubules analyzed by video light microscopy: rate constants and transition frequencies." In: *The Journal of cell biology* 107.4 (Oct. 1, 1988), pp. 1437–1448. ISSN: 0021-9525, 1540-8140. DOI: 10.1083/jcb.107.4.1437. URL: https://rupress.org/jcb/article/107/4/1437/58973/Dynamic-instability-of-individual-microtubules (visited on 01/28/2025).

[19] J. Howard and A. A. Hyman. "Growth, fluctuation and switching at microtubule plus ends". In: *Nature Reviews Molecular Cell Biology* 10.8 (2009), pp. 569–574.

[20] T. E. Holy, M. Dogterom, B. Yurke, and S. Leibler. "Assembly and positioning of microtubule asters in microfabricated chambers". In: *Proceedings of the National Academy of Sciences* 94.12 (June 10, 1997). Publisher: Proceedings of the National Academy of Sciences, pp. 6228–6231. DOI: 10.1073/pnas.94.12.6228. URL: https://www-pnas-org.tudelft.idm.oclc.org/doi/10.1073/pnas.94.12.6228 (visited on 12/20/2024).

[21] W. Shang, J. S. Dordick, R. E. Palazzo, and R. W. Siegel. "Direct patterning of centrosome arrays as templates for the assembly of microtubules". In: *Biotechnology and bioengineering* 94.5 (2006), pp. 1012–1016.

[22] D. C. Turner, C. Chang, K. Fang, S. L. Brandow, and D. B. Murphy. "Selective adhesion of functional microtubules to patterned silane surfaces". In: *Biophysical Journal* 69.6 (1995), pp. 2782–2789.

[23] D. Portran, J. Gaillard, M. Vantard, and M. Thery. "Quantification of MAP and molecular motor activities on geometrically controlled microtubule networks". In: *Cytoskeleton* 70.1 (2013). _eprint: https://onlinelibrary.wiley.com/doi/pdf/10.1002/cm.21081, pp. 12–23. ISSN: 1949-3592. DOI: 10.1002/cm.21081. URL: https://onlinelibrary.wiley.com/doi/abs/10.1002/cm.21081 (visited on 12/23/2024).

[24] B. R. King, M. Moritz, H. Kim, D. A. Agard, C. L. Asbury, and T. N. Davis. "XMAP215 and γ-tubulin additively promote microtubule nucleation in purified solutions". In: *Molecular Biology of the Cell* 31.20 (2020), pp. 2187–2194.

[25] M.-Y. Tsai and Y. Zheng. "Aurora A Kinase-Coated Beads Function as Microtubule-Organizing Centers and Enhance RanGTP-Induced Spindle Assembly". In: *Current Biology* 15.23 (Dec. 6, 2005), pp. 2156–2163. ISSN: 0960-9822. DOI: 10.1016/j.cub.2005.10.054. URL: https://www.sciencedirect.com/science/article/pii/S0960982205013072 (visited on 12/20/2024).

[26] A. Thawani, R. S. Kadzik, and S. Petry. "XMAP215 is a microtubule nucleation factor that functions synergistically with the γ-tubulin ring complex". In: *Nature Cell Biology* 20.5 (May 2018). Publisher: Nature Publishing Group, pp. 575–585. ISSN: 1476-4679. DOI: 10.1038/s41556-018-0091-6. URL: https://www.nature.com/articles/s41556-018-0091-6 (visited on 01/22/2025).

[27] Y. Yang, P. A. Deymier, L. Wang, R. Guzman, J. B. Hoying, H. J. McLaughlin, S. D. Smith, and I. N. Jongewaard. "Nucleation and Growth of Microtubules from γ-Tubulin-Functionalized Gold Surfaces". In: *Biotechnology Progress* 22.1 (2006). _eprint: https://aiche.onlinelibrary.wiley.com/doi/pdf/10.1021/bp050150j, pp. 303–312. ISSN: 1520-6033. DOI: 10.1021/bp050150j. URL: https://onlinelibrary.wiley.com/doi/abs/10.1021/bp050150j (visited on 12/23/2024).

[28] T. Huibregtsen. "Microtubule nucleation control". PhD thesis. Bionanoscience Department, Delft: TU Delft, 2022. 52 pp.

[29] G. V. Presnova, M. Y. Rubtsova, D. E. Presnov, V. G. Grigorenko, I. V. Yaminsky, and A. M. Egorov. "Streptavidin conjugates with gold nanoparticles for visualization of single DNA interactions on the silicon surface". In: *Biochemistry (Moscow) Supplement Series B: Biomedical Chemistry* 8.2 (Apr. 1, 2014), pp. 164–167. ISSN: 1990-7516. DOI: 10.1134/S1990750814020103. URL: https://doi.org/10.1134/S1990750814020103 (visited on 12/23/2024).

[30] G. Pacchioni. "A not-so-strong bond". In: *Nature Reviews Materials* 4.4 (Apr. 2019). Publisher: Nature Publishing Group, pp. 226–226. ISSN: 2058-8437. DOI: 10.1038/s41578-019-0094-3. URL: https://www.nature.com/articles/s41578-019-0094-3 (visited on 01/06/2025).

[31] N. Ukah and H. A. Wegner. "Ullmann Coupling Reactions on Gold Nanoparticles". In: *ChemistryEurope* 2.5 (2024). _eprint: https://onlinelibrary.wiley.com/doi/pdf/10.1002/ceur.202400024, e202400024. ISSN: 2751-4765. DOI: 10.1002/ceur.202400024. URL: https://onlinelibrary.wiley.com/doi/abs/10.1002/ceur.202400024 (visited on 01/06/2025).

[32] M. W. Brett, C. K. Gordon, J. Hardy, and N. J. L. K. Davis. "The Rise and Future of Discrete Organic–Inorganic Hybrid Nanomaterials". In: *ACS Physical Chemistry Au* 2.5 (Sept. 28, 2022). Publisher: American Chemical Society, pp. 364–387. DOI: 10.1021/acsphyschemau.2c00018. URL: https://doi.org/10.1021/acsphyschemau.2c00018 (visited on 01/06/2025).

[33] K. Matsuda, A. M. R. Kabir, N. Akamatsu, A. Saito, S. Ishikawa, T. Matsuyama, O. Ditzer, M. S. Islam, Y. Ohya, K. Sada, A. Konagaya, A. Kuzuya, and A. Kakugo. "Artificial Smooth Muscle Model Composed of Hierarchically Ordered Microtubule Asters Mediated by DNA Origami Nanostructures". In: *Nano Letters* 19.6 (June 12, 2019). Publisher: American Chemical Society, pp. 3933–3938. ISSN: 1530-6984. DOI: 10.1021/acs.nanolett.9b01201. URL: https://doi.org/10.1021/acs.nanolett.9b01201 (visited on 01/06/2025).

[34] A. Maloney, L. J. Herskowitz, and S. J. Koch. "Effects of surface passivation on gliding motility assays". In: *PloS One* 6.6 (2011), e19522. ISSN: 1932-6203. DOI: 10.1371/journal.pone.0019522.

[35] J.-C. Wang, W. Liu, Q. Tu, C. Ma, L. Zhao, Y. Wang, J. Ouyang, L. Pang, and J. Wang. “High throughput and multiplex localization of proteins and cells for in situ micropatterning using pneumatic microfluidics”. In: *Analyst* 140.3 (Jan. 20, 2015). Publisher: The Royal Society of Chemistry, pp. 827–836. ISSN: 1364-5528. DOI: `10.1039/C4AN01972E`. URL: `https://pubs.rsc.org/en/content/articlelanding/2015/an/c4an01972e` (visited on 02/24/2025).

[36] K. Raiber, A. Terfort, C. Benndorf, N. Krings, and H.-H. Strehblow. “Removal of self-assembled monolayers of alkanethiolates on gold by plasma cleaning”. In: *Surface Science* 595.1 (Dec. 5, 2005), pp. 56–63. ISSN: 0039-6028. DOI: `10.1016/j.susc.2005.07.038`. URL: `https://www.sciencedirect.com/science/article/pii/S0039602805008927` (visited on 02/24/2025).

[37] C. D. Bain, E. B. Troughton, Y. T. Tao, J. Evall, G. M. Whitesides, and R. G. Nuzzo. “Formation of monolayer films by the spontaneous assembly of organic thiols from solution onto gold”. In: *Journal of the American Chemical Society* 111.1 (Jan. 1989), pp. 321–335. ISSN: 0002-7863, 1520-5126. DOI: `10.1021/ja00183a049`. URL: `https://pubs.acs.org/doi/abs/10.1021/ja00183a049` (visited on 02/24/2025).

[38] **A. Nick Maleki**, P. J. Huis in ’t Veld, A. Akhmanova, M. Dogterom, and V. A. Volkov. “Estimation of microtubule-generated forces using a DNA origami nanospring”. In: *Journal of Cell Science* 136.5 (Mar. 2, 2022), jcs260154. ISSN: 0021-9533. DOI: `10.1242/jcs.260154`. URL: `https://doi.org/10.1242/jcs.260154` (visited on 10/09/2024).

[39] L. Farhadi, C. Fermino Do Rosario, E. P. Debold, A. Baskaran, and J. L. Ross. “Active Self-Organization of Actin-Microtubule Composite Self-Propelled Rods”. In: *Frontiers in Physics* 6 (2018). ISSN: 2296-424X. DOI: `10.3389/fphy.2018.00075`. URL: `https://www.frontiersin.org/journals/physics/articles/10.3389/fphy.2018.00075`.

[40] C. E. Aitken, R. A. Marshall, and J. D. Puglisi. “An oxygen scavenging system for improvement of dye stability in single-molecule fluorescence experiments”. In: *Biophysical Journal* 94.5 (Mar. 1, 2008), pp. 1826–1835. ISSN: 1542-0086. DOI: `10.1529/biophysj.107.117689`.

5

TOWARDS BI-ORIENTATION

Freedom is the foundation of science; and science is the key to progress

M. A. Foroughi

Man, in his arrogance, thinks himself a great work, worthy of the interposition of a deity

Charles Darwin

Accurate chromosome segregation during cell division depends on sister chromatid bi-orientation, which is acquired by means of kinetochore-microtubule stable attachments and dynamic microtubules. This chapter traces the experimental and historical milestones of mechanism discovery of bi-orientation, from early micromanipulation experiments to in vitro reconstitution of tension-sensitive kinetochore-microtubule interactions. Emphasis is placed on primary protein complexes Dam1, Ska, and Ndc80 which ensure attachment stability and mechanical and biochemical signaling. In an attempt to design a minimal model system, an origami nanospring-based synthetic platform is introduced to model chromosome bi-orientation and segregation. Using engineered dimers of nanosprings joined by photocleavable connectors, kinesin-directed transport, and Ndc80-driven microtubule binding, the system models the key features of chromosome motion and tension-dependent stability. This reductionist approach provides a useful technique for dissecting the biophysical principles behind chromosome segregation.

5.1. INTRODUCTION

The establishment of proper chromosome segregation requires microtubule-kinetochore biorientation, wherein microtubules establish stable attachments to sister chromatid kinetochores. The way to the understanding of how chromosomes ensure proper segregation during cell division has been paved through the efforts of decades of pioneering work, starting with the first micromanipulation experiments. In a seminal paper, Nicklas and Koch demonstrated that stress on chromosomes in insect spermatocytes was adequate to stabilize their attachment to microtubules from opposite spindle poles [1]. This was the first clear evidence that mechanical tension plays a critical role in promoting proper kinetochore-microtubule attachments, a central tenet for ensuring faithful chromosome segregation.

Reconstitution of these stable attachments in vitro was the puzzle that began in earnest in the mid-1980s. Mitchison and Kirschner showed that kinetochores can capture microtubules in vitro, an ATP-regulated process, the beginning of biochemical approaches to untangle kinetochore function [2]. Around the same time, yeast and other model organism studies set controversy ablaze over whether correct chromosome orientation arises spontaneously through kinetochore geometry—i.e., back-to-back sister kinetochore arrangement—or whether corrective cellular processes correct orientation errors. The experiments showed faulty attachments, or mal-orientations, which are normal early in mitosis but are later corrected, pointing towards the existence of active tension-dependent error correction mechanisms[3–5].

One important milestone in uncovering the source of tension came with the discovery of the cohesin complex. Yanagida demonstrated that cohesin keeps sister chromatids attached by a physical bond and resists microtubule pulling forces until anaphase [6]. The bond allows tension to be generated across bi-oriented kinetochores, providing a mechanical signal for proper attachment.

In yeast, the discovery of the Dam1 complex added another crucial piece to the puzzle. Westermann et al. showed that Dam1 complex could self-assemble into ring structures around microtubules [7]. The rings were capable of binding kinetochores to dynamic microtubule ends, facilitating tracking of depolymerization events by chromosomes—a crucial necessity for stable attachments under tension. This concept was later taken a step further in 2009 by Kiermaier et al., when they artificially directed the Dam1 complex to a centromere-less plasmid in yeast [8]. The artificial system formed an functional kinetochore that could bind to microtubules, bi-orient, and segregate mini-chromosomes without native DNA-binding factors. Similarly, Lacefield et al. used a specific component of the Dam1 complex, Ask1, to assemble a synthetic kinetochore on a centromere-less plasmid [9]. These studies successfully proved that the Dam1 complex by itself can be utilized to trigger bi-orientation and segregation in yeast.

Further elucidation of Dam1 complex function was offered in 2010 where it was shown Dam1 is required for the Ndc80 complex to track dynamic plus microtubule ends [10]. This cooperation ensures stable kinetochore-microtubule attachments during both polymerization and depolymerization, necessary for precise chromosome alignment. Later the same year, Akiyoshi et al. made a major breakthrough in isolating native yeast kinetochores and reconstituting their in vitro microtubule interactions [11]. They demonstrated that mechanical tension alone is sufficient to stabilize such attachments directly—firm evidence of a mechanosensitive mechanism of bi-orientation.

MMore recently, vertebrate systems were investigated. In 2012, Jeyaprakash et al. reported the initial complete structural characterization of the human Ska complex and discovered it to be dimeric in nature with microtubule-binding activity [12]. The Ska complex is structurally similar to the yeast Dam1 complex and is responsible for kinetochore-microtubule stabilizing function in vertebrates. Abad et al. enhanced this by showing that the Ska complex interacts with straight and curved microtubule structures at multiple contact points through which it remains attached even through dynamic remodeling [13]. More recently in 2014, Akiyoshi and Biggins provided a comprehensive protocol for purifying kinetochores and assaying their interaction with microtubules. While methodological in nature, this paper was invaluable for later reconstitution studies, which improved our understanding of the molecular underpinnings of bi-orientation [14]. Chakraborty used a reconstitution system in 2018 to investigate how kinetochores transition from lateral to end-on attachments to microtubules, an essential maturation step towards stable bi-orientation [15]. The transition ensures correct alignment and preparation of the chromosomes for segregation.

Further mechanistic detail was revealed in 2019, when Zhang et al. demonstrated that Cdk1-induced phosphorylation of the Ska complex facilitates its association with the Ndc80 complex to form a stable macro-complex at the kinetochore [16]. This phosphorylation-regulated process is important for generating stable kinetochore-microtubule attachments under mitosis' dynamic conditions. Meanwhile there has been efforts to reconstitute kinetochore motility. For example Trvi et al. proved that the kinesin-8 motor protein Kip3 in yeast plays a critical role in promoting end-on attachments between kinetochores and microtubules [17]. The motor-mediated process facilitates chromosome congression and also secures accurate connections to facilitate bi-orientation.

Most recently, Asai et al. built artificial kinetochore by coating beads with NDC80-NUF2 [18]. Astonishingly, beads that were placed at the spindle equator established stable bipolar attachments, with the same properties as native kinetochores. In this work, they demonstrated that NDC80-NUF2 alone is sufficient to induce a biorientation-like state in mammalian cells, highlighting the conserved and universal function of these subunits.

Over the decades, research has routinely evolved from descriptive in vivo accounts to sophisticated reconstitution systems. We now understand that a combination of tension, phosphorylation, motor activity, and multiprotein complexes such as Dam1, Ska, and Ndc80 is needed to stabilize kinetochore-microtubule attachments. While basic principles such as tension-based stabilization are conserved, the precise mechanisms vary between organisms, and there remains controversy regarding relative importance of geometric, biochemical, and mechanical cues in ensuring faithful chromosome segregation.

5.2. TOWARDS A MINIMAL SYSTEM FOR CHROMOSOME BI-ORIENTATION AND SEGREGATION

The spindle assembly checkpoint constitutes a highly regulated cellular mechanism that ensures appropriate chromosome-microtubule spindle connections. Subsequently, chromatid separation is achieved through microtubule depolymerization-generated forces, which facilitate movement toward the spindle poles [19]. This machinery exhibits substantial complexity, involving in excess of hundreds of proteins both in kinetochore assembly and in centrosomal microtubule nucleation centers [20, 21]. Implementation of a reconstituted minimal system presents an opportunity to elucidate the fundamental mechanisms and identify essential components of this process. The methodological developments described in this Chapter enable progression toward this objective. Ndc80 represents a critical kinetochore component that facilitates the harnessing of microtubule depolymerization forces [22]. We implemented nanosprings as a platform enabling controlled Ndc80 immobilization [23]. Additionally, plus-end-directed kinesin motor proteins facilitate complex transportation to microtubule plus ends. This experimental approach recapitulates end-on conversion, a process typically mediated by CENP-E and Ndc80, wherein lateral microtubule attachments transition to end-on configurations necessary for the capture of depolymerization forces. Fig. 5.1A illustrates a modified nanospring design incorporating five extended internal staples that function as recruitment sites for kinesin-1 molecules conjugated with complementary DNA handles. The nanospring termini maintain their previously described configuration: one terminus carries digoxigenin while the other presents biotin. The biotin-modified terminus is engineered to bind streptavidin-mediated Ndc80 trimers (T_1[S-Ndc80]3, as detailed in chapters 2 and 3. In our in vitro artificial environment, we have the flexibility to employ simplified mechanisms for initiating chromatid segregation, in contrast to the complex processes utilized by cells. One viable approach is the implementation of optogenetic control, which allows for light-induced activation of the segregation process. This method is particularly compatible with our DNA origami platform, as it permits the incorporation of photocleavable oligonucleotides that can be selectively cleaved upon exposure to UV light.

To emulate biorientation and subsequent segregation, we devised a design comprising two nanosprings interconnected via a photocleavable linker, each labeled with distinct fluorophores, Atto488 and Cy5, respectively (Fig. 5.1A). Fig. 5.1B illustrates two methodologies employed to generate the nanospring (NS) dimer. The left panel depicts the initial approach, wherein an oligonucleotide is partially complementary to both the $5'$ terminus of the NS-Atto488 scaffold and the $3'$ terminus of the NS-Cy5 scaffold. This was utilized in conjunction with a photocleavable oligonucleotide partially complementary to the $3'$ end of NS-Atto488 and the $5'$ end of NS-Cy5. However, this design proved problematic due to the identical sequences of the two nanosprings, resulting in potential self-folding of the photocleavable linkers on the same scaffold instead of creating inter-nanospring connections.

To address this issue, we developed an improved design, as illustrated in the right panel. This refined approach incorporates an atypical photocleavable oligonucleotide featuring either two 3′ termini or two 5′ termini at its extremities, effectively mitigating the self-folding issue and enabling successful NS dimer formation.

To synthesize the double 3′ photocleavable linker, we employed a strategic approach utilizing two distinct oligonucleotides. The first oligonucleotide, comprising 33 bases complementary to the 3′ direction of the nanospring (NS) scaffold, was designed with dibenzocyclooctyne (DBCO) functionality at both termini and a photocleavable moiety inserted immediately preceding the DBCO group. A second oligonucleotide, identical in sequence but featuring an azide functionality exclusively at its 5′ terminus, was also synthesized (Fig.5.1C).

The conjugation of these oligonucleotides was achieved via copper-free click chemistry, with the reaction proceeding overnight. Subsequent purification was performed using 10% polyacrylamide Tris/Borate/EDTA (TBE) gel electrophoresis (Fig. 5.1D). Gel imaging clearly demonstrated the formation of a larger oligonucleotide product, approximately 66 bases in length, confirming the successful conjugation of the two initial oligonucleotides.

A similar methodology was employed for the synthesis of the double 5′ end oligonucleotide, with the primary distinction being the placement of functional groups at the 3′ termini of the oligonucleotides and the use of sequences complementary to the 5′ end of the NS scaffold (Fig. 5.1C).

Agarose gel electrophoresis was utilized to analyze the NS constructs (Fig. 5.1E). Lanes 1 and 2 were loaded with NS in combination with the photocleavable linkers, while lanes 4 and 5 contained NS alone. In lanes 4 and 5, NS bands were observed at their expected positions (magenta arrowhead). However, in lanes 1 and 2, the samples appeared to be retained within the loading wells of the gel, likely due to the formation of NS dimers with dimensions exceeding the pore size of the gel. This observation was corroborated by transmission electron microscopy (TEM) imaging of the NS dimers, where length measurements of the observed structures corresponded to the theoretical contour length of an NS dimer (Fig. 5.1F).

photo-responsiveness of the nanospring (NS) dimers was evaluated using neutravidin-coated beads as platforms These dimers were engineered with biotin functionality on only one NS, anticipating initial colocalization of signals from NS-Atto488 and NS-Cy5, followed by selective signal loss from the non-biotinylated NS upon UV or near-UV irradiation. Fig. 5.1G demonstrates this phenomenon, which persists when the order of attachment and biotinylated side is reversed (compare upper and lower images). Colocalization of signals and subsequent loss of the non-biotinylated NS signal upon near-UV exposure was further corroborated using individual dimers immobilized via biotin antibodies (data not presented).

To exclude the possibility of accidental signal colocalization, we also anchored the biotinylated component of the dimer to a supported lipid bilayer (SLB) and monitored the spatiotemporal correspondence between the two NS. Fig. 5.1H illustrates the space-time trajectory of a representative NS dimer, revealing coordinated movement until 405 nm laser illumination, after which independent motion of each NS was observed.

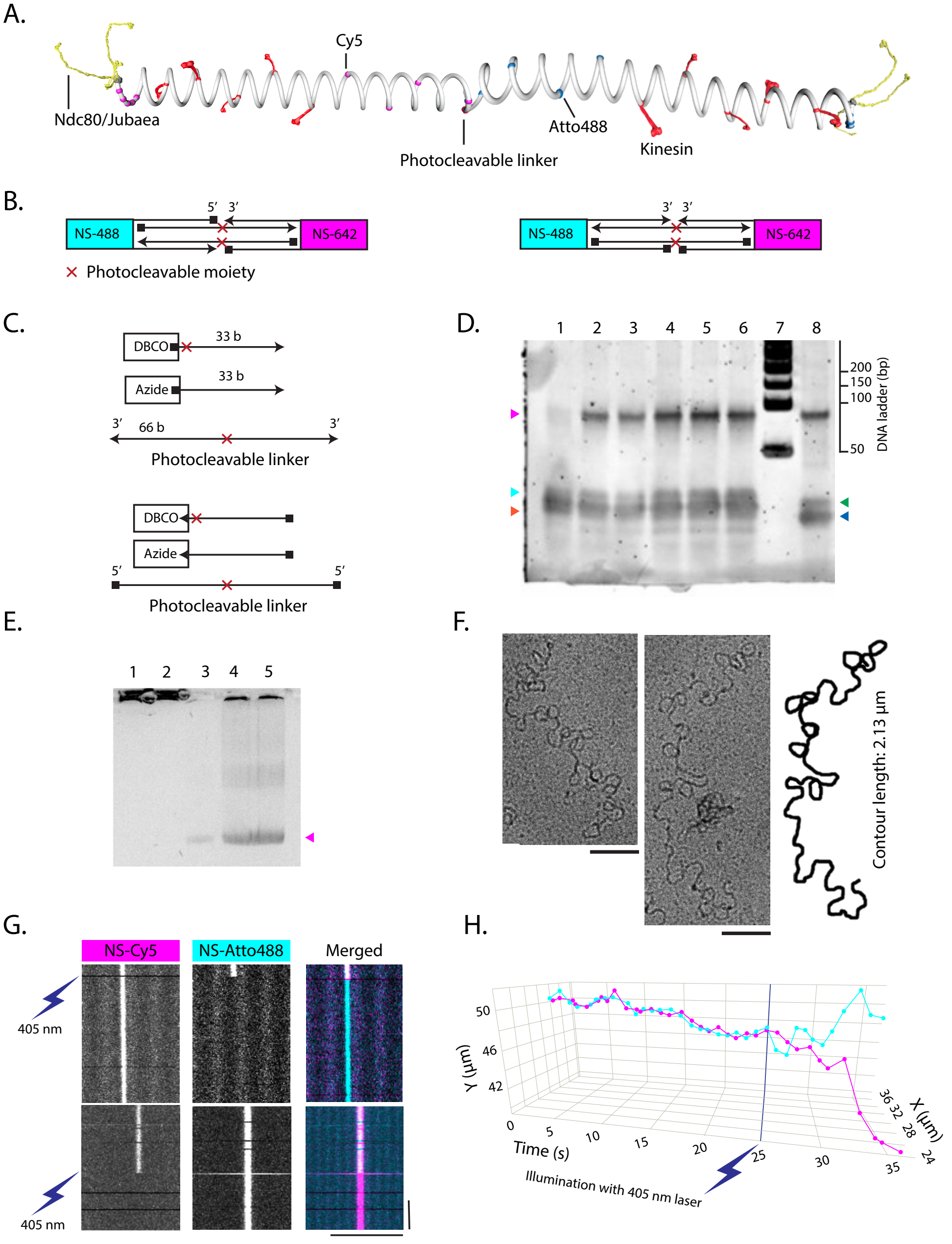

Figure 5.1: *Engineering of NS Dimers. (A) Schematic illustration of an NS dimer constructed by tethering two NS structures via photocleavable linkers. Each NS is functionalized with attachment sites capable of accommodating up to five kinesin motors. The biotin termini of the NS structures were utilized to conjugate T_1 [S-Ndc80]$_3$ trimers. (continued ...)*

Figure 5.1 continued
Fluorescent labeling was achieved by tagging one NS with Atto488 and the other with Cy5. (B) Conceptual designs for NS dimer assembly. The initial design (left) was abandoned due to issues with self-folding. Subsequent experiments employed the alternative design (right), which utilized double $3'$ *and double* $5'$ *oligonucleotides. (C) Diagrams depicting the synthesis of double* $3'$ *and double* $5'$ *photocleavable oligonucleotides. (D) Analysis on a 10% polyacrylamide TBE gel. Lane 1 contains pre-synthesized double* $3'$ *end photocleavable linker (PL) exposed to UV prior to loading. Lanes 2-4 contain reaction mixtures of DBCO-NPOM-DNA and azide-DNA incubated overnight. The magenta triangle indicates the position of the double* $3'$ *end PL, while cyan and orange triangles mark unreacted oligonucleotides. Lane 7: DNA marker. Lane 8: double* $5'$ *end reaction mixture, with green and blue triangles indicating unreacted oligonucleotides. (E) Electrophoresis on a 1% agarose gel in TBE buffer supplemented with 12 mM* $MgCl_2$*. All lanes contain purified NS, with photocleavable linkers added to lanes 1 and 2. The NS band is clearly visible in lanes 4 and 5 (magenta triangle) but absent in lanes 1 and 2, likely due to dimerization and formation of larger structures that impede migration through the gel matrix. The band in lane 3 resulted from leakage from the adjacent lane. (F) Transmission electron microscopy (TEM) images of NS dimers. The contour length of a representative dimer was measured and compared to the theoretical value. Scale bars: 100 nm. (G) Kymographs depicting fluorescent signals from bead-bound NS dimers. The top row shows an example where NS-Cy5 is biotinylated and attached to the bead via neutravidin, while NS-Atto488 is linked solely to NS-Cy5 via the photocleavable linker. Upon cleavage of the linker using 405 nm laser light, the NS-Atto488 signal is lost. The lower row illustrates the reverse configuration, where NS-Atto488 is biotinylated and NS-Cy5 is linked via the photocleavable linker. Scale bars: spatial, 10* μm*; temporal, 1 min. (H) Space-time trajectory of an NS dimer, with magenta representing NS-Cy5 and cyan representing NS-Atto488. The colocalization of their signals in space and time provides additional evidence for dimer formation. At* $t = 25$ *s, illumination with 405 nm laser light cleaves the dimer, resulting in the loss of colocalization.*

We next tested the functionality of kinesin molecules in our system. In a system where two MTs with opposing polarity face each other, kinesins attached to the nanospring (NS) can facilitate DNA congression. Fig. 5.2A demonstrates a motility gel shift assay in which the addition of DNA-labeled kinesin to the NS results in an upward shift of the NS band (cyan triangle to magenta triangle), indicating successful binding of kinesins to the NS. Fig. 5.2B shows that the motility speed of the NS-kinesin complex on dynamic MT tracks is comparable to the gliding speed of MTs on kinesin-immobilized surfaces, confirming that kinesins remain active when bound to the NS. This is further illustrated in Fig. 5.2D and Fig. 5.2E, where kymographs show an NS-kinesin complex or an NS-dimer-kinesin complex moving along an MT. Surprisingly, the NS-kinesin complex was even able to follow shrinking MTs after it was brought to the plus end by the action of motors, a property that was not reported before for kinesin-1 and arises likely due to multimerization of kinesin by the NS.

When two anti-parallel MTs overlap and cross each other, the NS dimer is expected to be confined to back-and-forth movement within the overlap region, as kinesins are + end-directed motors (Fig. 5.2C, middle panel). To create this configuration, we used centrosomes and antiparallel MTs emanating from them in the presence of Ase1, which is known to stabilize antiparallel overlaps [24].

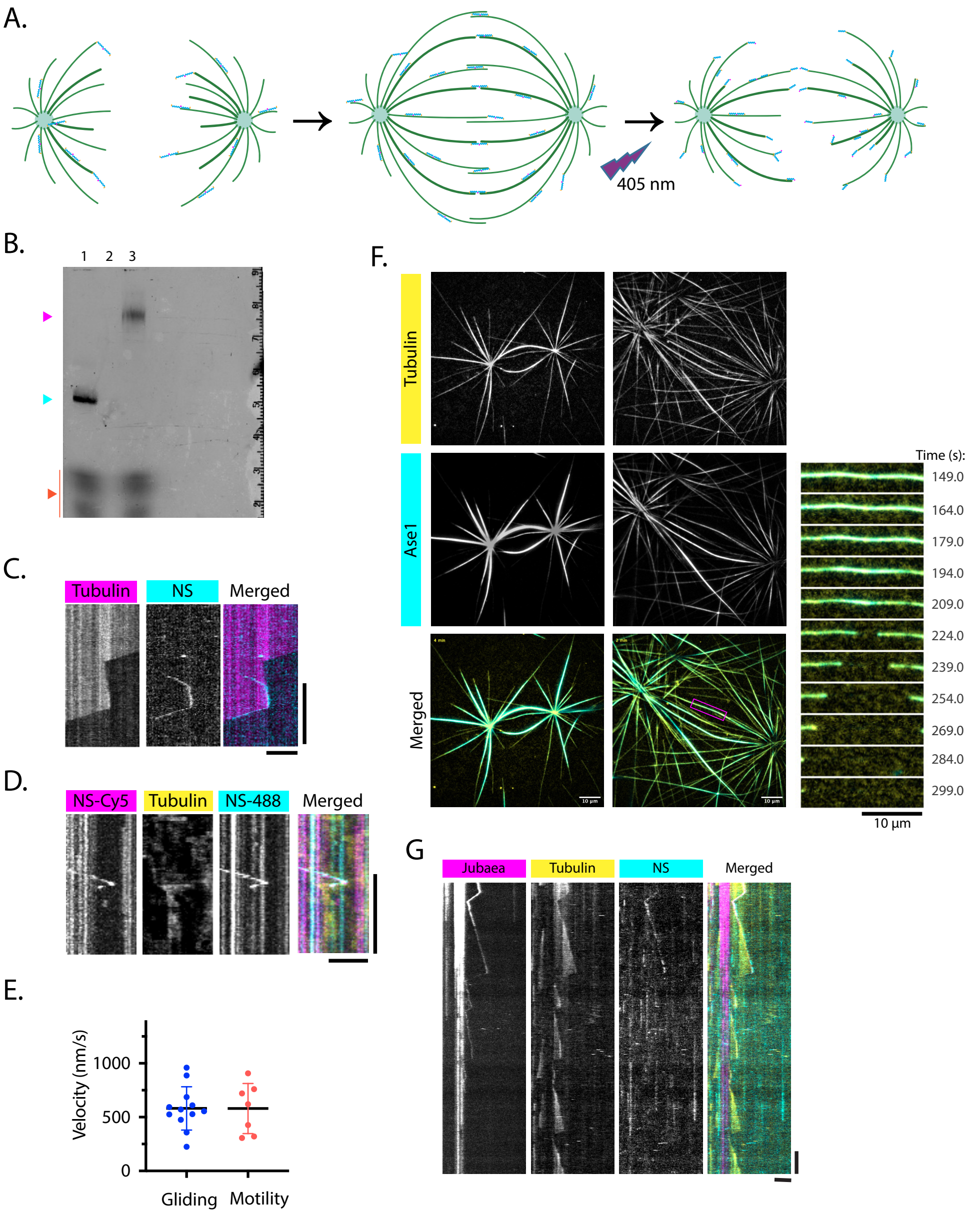

Figure 5.2: *Elements for Reconstitution of a DNA Congression and Segregation System. (A) Schematic representation of the design strategy employed in this study: NS dimers are connected via photocleavable linkers (see also Fig. 5.1A). Kinesins bound to the NS can transport the dimer toward the MT plus end, where Ndc80 multimers can attach to shrinking MTs. If this connection remains stable, DNA segregation can be initiated by cleaving the NS dimer using 405 nm laser light. The NS dimers are shown in cyan. (Continued ...)*

(Figure 5.2 continued) (B) Kinesin motors were utilized to drive plus-end-directed movement of NS monomer, mimicking DNA congression. The image depicts a 1% agarose gel in TBE buffer supplemented with 12 mM $MgCl_2$ and 0.05% LDS. Lane 1: NS alone (cyan arrowhead), Lane 2: blank, Lane 3: NS combined with kinesin (magenta arrowhead). The lanes at the bottom of the gel are dissociated fluorescently labeled staples (red arrowhead)(C) Kymograph illustrating an example of MT plus-end-directed motility and subsequent MT end-tracking of an NS-kinesin complex. Scale bars: spatial, 5 µm; temporal, 1 min. (E) An example kymograph showing kinesin-mediated motility and subsequent MT end-tracking of an NS dimer. Scale bars: spatial, 5 µm; temporal, 1 min. (E) The motility speed of NS-kinesin complexes on MTs was compared to the gliding speed of MTs on a surface, which move due to non-specifically bound kinesin motors to the surface. Error bars: standard deviation. (F) TIRF image displaying two centrosomes positioned adjacent to each other. In this case, multiple MTs from each centrosome are interconnected with counterpart MTs from the other centrosome via Ase1, forming antiparallel bundles. The time-lapsed image on the right illustrates an example of this interaction. At t = 209 s, two antiparallel shrinking MTs loose contact and start moving apart. An NS dimer capable of stable attachment to each MT at this position (not yet present in this experiment) could provide a system mimicking chromosome biorientation. (G) Example kymograph obtained from TIRF imaging of an NS-kinesin-Jubaea construct in a dynamic MT assay. Soluble T_1 [S-Jubaea]$_3$ and kinesin-DNA were present in the solution at 10 nM concentration. Analysis of the Jubaea and NS signals in the kymograph indicates that the NS-kinesin-Jubaea complex forms a stable structure capable of remaining attached to the MT tip through multiple cycles of polymerization and depolymerization. Scale bars: spatial, 5 µm; temporal, 1 min.

As MTs begin to depolymerize, the overlapping region shrinks (time-lapse images in Fig. 5.2F), which we expect would bring the NS dimer to the ends of the MTs. The Jubaea multimers can attach to depolymerizing MT ends on both sides, and if the connection is sufficiently stable to withstand depolymerization forces, a bioriented NS dimer should be able to form.

However, this configuration requires robust connections between Jubaea multimers and (stalled) shrinking MT ends on both sides. While a Jubaea trimer was found incapable of forming such connections (see Chapter 3), it was still tested in these preliminary experiments. Note that in these assays, the exact number of jubaea complexes and kinesins associated with the NS remains unknown, as they were present in solution at a concentration of 10 nM. Fig. 5.2G provides a representative kymograph showing an NS-kinesin-Jubaea complex interacting with a dynamic MT. The complex binds to the growing MT end and tracks it until a catastrophe occurs; it then remains attached to the shrinking end until rescue occurs, after which it resumes tracking the growing end. In the future it will be interesting to study the behavior of this complex on anti-parallel bundles of (shrinking) MTs and potentially replace the trimer with larger copy numbers of jubaea (see Chapter 3).

5.3. CONCLUSION

In this chapter the first elements were presented to establish a minimal system based on NS dimers that captures the ability of an artificial chromosome pair to congress to the midplane of bi-oriented spindle, establish bi-oriented end-on load-barring connections to MT ends, and subsequently segregate DNA to the spindle poles. In Chapter 6 we discuss current limitations and possible follow-ups of these experiments.

5.4. MATERIALS AND METHODS

5.4.1. IMAGING AND MICROSCOPY

See Materials and Methods at chapter 2.

5.4.2. ESTABLISHMENT OF SUPPORTED LIPID BILAYER

CLEANING COVERSLIPS

Glass coverslips were cleaned using a two-step process: Coverslips were placed in a Teflon holder and sonicated in 2% (v/v) Hellmanex solution in MilliQ water at 60 °C for 15 min in a bath sonicator. After thorough rinsing with MilliQ water, coverslips were dried either by heating at approximately 80 °C for 10 min or by nitrogen gas blow-drying.

For acid piranha treatment, all safety precautions were strictly followed (chemical-resistant gloves, goggles, apron, fume hood lined with aluminum foil, and appropriate signage). Acid piranha solution was prepared by carefully mixing 75 mL concentrated sulfuric acid with 25 mL 30% hydrogen peroxide. Dry coverslips were immersed in this solution for 7 min, rinsed extensively with MilliQ water, and sonicated for 5 min in MilliQ water. Coverslips were then stored in fresh MilliQ water until use. The piranha solution was allowed to cool before safe disposal in acid waste. The solution remained stable for at least two weeks.

CLEANING OBJECTIVE SLIDES

Objective slides were sonicated in 2% (v/v) Hellmanex solution for 15 min, rinsed thoroughly with MilliQ water, sonicated for an additional 5 min in MilliQ, rinsed again, and stored in MilliQ water until use.

PREPARATION OF SMALL UNILAMELLAR VESICLES (SUVS)

All glassware and syringes were cleaned with methanol and chloroform prior to use. Lipid mixtures were prepared by combining stock solutions (in chloroform) in a glass vial:

- 20 µL DOPC (25 mg/mL)
- 20 µL DOPS (12.5 mg/mL)
- 15 µL biotin-PE (1.0 mg/mL)
- 2 µL TRITC (0.1 mg/mL, optional)

Chloroform was evaporated by gentle nitrogen gas flow, followed by 2 hours of vacuum desiccation. Lipids were rehydrated in 2 mL of H-Buffer150 (150 mM NaCl, 10 mM HEPES, pH 7.4) by bath sonication for 30 min. SUVs were formed by probe sonication for 60 min using 10 sec on/off pulses at 25% amplitude. Samples were centrifuged at maximum speed for 10 min, and the supernatant containing SUVs was stored at 4 °C. (Alternatively, SUVs were prepared by extrusion through a 30 nm pore-size filter.)

SUPPORTED LIPID BILAYER (SLB) FORMATION

A flow cell was prepared and washed with H-Buffer150. Then, 20 µL of SUV solution was flowed in and incubated for 5 min to allow bilayer formation. Excess SUVs were washed away with buffer.

5.4.3. PURIFICATION OF SYMMETRIC PHOTOCLEAVABLE LINKERS

DBCO–NPOM–DNA and azide–DNA oligonucleotides (biomers.net) were mixed in a 1:1 molar ratio and incubated overnight at room temperature to allow click conjugation. Reaction products were resolved on a 10% polyacrylamide gel prepared in 1× TBE buffer. Electrophoresis was performed at 200 V for 30 min. The gel was stained with SYBR Gold (Thermo Fisher Scientific), and bands corresponding to the desired double $3'$ or $5'$ end products were excised. Gel slices were fragmented into small pieces using a custom-made gel breaker and incubated with 500 μL of 300 mM NaCl overnight at 840 rpm on a rotary shaker to allow diffusion of the oligonucleotides. DNA was recovered from the gel slurry using Freeze and Squeeze spin columns (Bio-Rad). The buffer was exchanged to MiliQ using Zeba spin desalting columns (Thermo Fisher Scientific). Oligonucleotide concentrations were determined using a NanoDrop spectrophotometer in single-stranded DNA mode.

5.4.4. PREPARATION OF NANOSPRING DIMERS

NS-Atto488 NS-Cy5 mixture was prepared as described in chapter 2, where in the former case Atto488 labeled oligonucleotides were used and in the later Cy5 labeled oligonucleotides. In addition, 400 nM of the symmetric photocleavable linkers was present in the NS-Atto488 DNA origami mix. Both DNA origami mixtures were purified separately with the same method described in chapter 2.

The biotinylated terminal staple can be added to either of the DNA origami mixtures, depending on which NS is preffered to be proximal (always anchored) and which one to be the distal (dissociable after photocleavage). The two purified NS versions were mixed in 1:1 ratio to and incubated overnight to make the NS dimers.

5.4.5. NANOSPRING PHOTOCLEAVAGE EXPERIMENTS

IMMOBILE NS DIMERS

The flow chamber was assembled using silanized glass slides and coverslips, as described in 2. Biotin anitbody (10%) was incubated in the flow chamber for 5 min and washed with 30 μL of NS buffer. The rest of surface was passivated using Pluranic F127 and κ-casein, as described in chapter 2. The NS dimers dilluted 100x in the NS buffer and were added to flow chamber for 10 min. The excess unbound

NS was washed away with 30 μL of NS buffer. The FRAP areas were define where NS dimers were observed. The area was illuminated with 405 nm laser with maximum intensity for 100 ms, while image aqcuisition being continued in the 488 nm and 642 nm fluorescent channels with 0.8 s frame interval.

NS DIMERS ON SLBS

Neutravidin (0.5 mg/ml) was incubated in the SLB coated flow chambers for 5 min and then washed away using 30 μL of NS buffer. The NS dimers diluted 100x in the NS buffer and added to the chamber for 10 min. Extra unbound NS was washed away with 30 μL of NS buffer. FRAP areas were set on the slowly Diffusing NS spots. The area was illuminated with 405 nm laser with maximum intensity for 100 ms, while image aqcuisition being continued in the 488 nm and 642 nm fluorescent channels with 0.8 s frame interval.

5.4.6. CENTROSOME ISOLATION

Centrosomes were purified from KE37 cells using a sucrose-gradient–based protocol adapted from Bornens & Moudjjou and Gegendeau et al. [25, 26].

In this protocol all solutions filtered through a 0.22 µm filter, except sucrose solutions, which were filtered through a 0.4 µm filter using a 10 mL syringe with Luer-lock. All procedures after cell treatment were performed at 4°C unless otherwise stated.

The following reagents and stock solutions were prepared: protease inhibitor cocktail (Sigma Aldrich, P8340-5ML), PMSF (87 mg in 5 mL ethanol; 100 mM stock), NP40 (0.5% final; Tergitol), 1 M $MgCl_2$ (95.3 g/L, filter-sterilized, stored at 4°C), 1 M 2-β-mercaptoethanol (prepared fresh, diluted 14.3-fold from pure liquid), 10% Triton X-100 (v/v), 1 M HEPES pH 7.4, DNAse I (1 mg/mL), 1 M PIPES pH 7.2, TBS 10× (1× = 20 mM Tris-HCl pH 7.4, 150 mM NaCl), cytochalasin B (10 mg/mL in DMSO), and nocodazole (10 mg/mL in DMSO, MW 301 g/mol).

Buffers were prepared as follows. TBS 1×: 200 mL TBS 10× in 1.8 L ddH_2O (final volume 2 L). TBS 1/10×: 15 mL TBS 10× in ddH_2O to 1.5 L. TBS 1/10× + 8% sucrose: 120 g sucrose dissolved in TBS 1/10× to 1.5 kg final weight. Lysis buffer (per 500 mL): 1 mM HEPES, 0.5% NP40, 0.5 mM $MgCl_2$, 0.1% β-mercaptoethanol, protease inhibitor cocktail, 1 mM PMSF in ddH_2O. Gradient buffer (per 50 mL): 10 mM PIPES, 0.1% Triton X-100, 0.1% β-mercaptoethanol in ddH_2O. Sucrose solutions (w/w in gradient buffer): 70% (3.5 g sucrose to 5 g final), 60% (12 g sucrose to 20 g final), 50% (1.5 g sucrose to 3 g final), and 40% (1.2 g sucrose to 3 g final).

KE37 cells were cultured to 2–4 L at $1–1.5 \times 10^6$ cells/mL. For large volumes, cells were grown in autoclaved spinning flasks with constant stirring. One hour prior to harvesting, nocodazole was added to 200 nM (1:5000 dilution from 10 mg/mL stock; 200 µL per L culture) and cytochalasin B to 1 µg/mL (1:5000 dilution from 10 mg/mL stock; 200 µL per L culture). Cultures were incubated at 37°C with stirring. Cells were harvested by centrifugation at 800 $\times g$ for 5 min (rotor F8-6×1000y). Pellets were washed once in ice-cold TBS 1× (half the initial culture volume) and once in TBS 1/10× + 8% sucrose (one-quarter of initial volume), with centrifugation at

800 ×*g* for 5 min between washes. Final resuspension was in 10 mL TBS 1/10× + 8% sucrose per liter of initial culture volume (~ 1–1.5 × 10^8 cells/mL).

Cells were diluted to 1 × 10^7 cells/mL in lysis buffer, mixed gently, and incubated on ice for 5–10 min. Lysates were centrifuged at 2000 ×*g* for 10 min (rotor F14-6×250y) to remove nuclei and chromatin. Supernatants were filtered through nylon mesh, supplemented with 10 mM HEPES and 1 µg/mL DNAse I, and incubated for 30–60 min. For the first concentration step, lysates were underlaid with 12.5 mL of 60% sucrose solution and centrifuged at 10,400 ×*g* for 30 min. The supernatant was removed, leaving approximately 25 mL above the cushion. The interface was resuspended and briefly vortexed.

For the second concentration step, centrosome suspensions were layered onto pre-formed sucrose gradients (3 mL each of 70%, 50%, and 40% sucrose) in Beckman ultra-clear thinwall tubes and centrifuged at 130,000 ×*g* (27,600 rpm, SW rotor) for 75 min with maximum acceleration and no brake. Fractions (500 µL) were collected from the bottom using a 0.8 mm needle, flash-frozen in liquid nitrogen, and stored in liquid nitrogen.

5.4.7. 2D SPINDLE RECONSTITUTION WITH ASE1

The centrosome-containing fraction was diluted fivefold in MRB80 and incubated in an acid-cleaned flow channel (coverslip and slide prepared as previously described) for 5 min. The channel was washed with 30 µL MRB80, followed by incubation with PLL-PEG for 5 min, and washed again with 30 µL MRB80. Subsequently, κ-casein was added for 5 min and removed by washing with 30 µL MRB80. The microtubule polymerization mix was then introduced added with 80 nM Ase1 (obtained from Roth et al. [27]), and total internal reflection fluorescence (TIRF) microscopy was performed at 30°C. The microtubule mix contained 20 µM tubulin (1% rhodamine-labeled), 0.5 mg/mL κ-casein, 0.1% methylcellulose, 1 mM GTP, 50 mM glucose, an oxygen scavenging system (20 mM DTT, 1 mg/mL catalase, 2 mg/mL glucose oxidase).

5.4.8. NS-KINESIN-JUBAEA COMPLEX FORMATION

The tubulin mix was prepared as described above. Silanizing both slides and coverslips improves control over non-specific protein adsorption to glass but makes the introduction of aqueous solutions into a pre-assembled hydrophobic flow chamber challenging. To overcome this, anti-DIG IgG (Roche, 11333089001) diluted in MRB80 to a final concentration of 0.2 µM was applied in 0.5–1 µL drops between strips of double-sided tape (10–15 µL total) and covered with a silanized coverslip, followed by a 5 min incubation. The chamber was then washed with 30 µL MRB80, followed by 30 µL of 1% Pluronic F-127 in MRB80, and incubated for an additional 20–60 min. Subsequently, 10 µL of nanosprings diluted in MRB80 were added. These nanosprings were prepared without the DIG-labeled staple.

For kinesin-binding nanosprings, five of the fourteen Atto488-labeled staples were replaced with staples of identical sequence but extended at one end to hybridize with a DNA handle conjugated to kinesin. The biotinylated staple at the opposite terminus of the nanospring was designed to bind the T_1[S-jubaea]$_3$ complex. This nanospring preparation was incorporated into the microtubule dynamics assay mix at final concentrations of 10 nM T_1[S-jubaea]$_3$, 50 nM kinesin, and 100 pM nanosprings.

REFERENCES

[1] R. B. Nicklas and C. A. Koch. "CHROMOSOME MICROMANIPULATION". In: *The Journal of Cell Biology* 43.1 (Oct. 1, 1969), pp. 40–50. ISSN: 1540-8140, 0021-9525. DOI: 10.1083/jcb.43.1.40. URL: https://rupress.org/jcb/article/43/1/40/1644/CHROMOSOME-MICROMANIPULATION-III-Spindle-Fiber (visited on 08/05/2025).

[2] K. Kirchner and E. Mandelkow. "Tubulin domains responsible for assembly of dimers and protofilaments." In: *The EMBO Journal* 4.9 (Sept. 1985). Num Pages: 2402 Publisher: John Wiley & Sons, Ltd, pp. 2397–2402. ISSN: 0261-4189. DOI: 10.1002/j.1460-2075.1985.tb03945.x. URL: https://www.embopress.org/doi/abs/10.1002/j.1460-2075.1985.tb03945.x (visited on 01/31/2025).

[3] J. G. Ault and C. L. Rieder. "Chromosome mal-orientation and reorientation during mitosis". In: *Cell Motility* 22.3 (Jan. 1992), pp. 155–159. ISSN: 0886-1544. DOI: 10.1002/cm.970220302. URL: https://onlinelibrary.wiley.com/doi/10.1002/cm.970220302 (visited on 08/05/2025).

[4] R. B. Nicklas. "How Cells Get the Right Chromosomes". In: *Science* 275.5300 (Jan. 31, 1997), pp. 632–637. ISSN: 0036-8075, 1095-9203. DOI: 10.1126/science.275.5300.632. URL: https://www.science.org/doi/10.1126/science.275.5300.632 (visited on 08/05/2025).

[5] R. B. Nicklas and S. C. Ward. "Elements of error correction in mitosis: microtubule capture, release, and tension." In: *The Journal of cell biology* 126.5 (Sept. 1, 1994), pp. 1241–1253. ISSN: 0021-9525, 1540-8140. DOI: 10.1083/jcb.126.5.1241. URL: https://rupress.org/jcb/article/126/5/1241/56303/Elements-of-error-correction-in-mitosis (visited on 08/05/2025).

[6] M. Yanagida. "Cell cycle mechanisms of sister chromatid separation; Roles of Cut1/separin and Cut2/securin". In: *Genes to Cells* 5.1 (Jan. 2000), pp. 1–8. ISSN: 1356-9597, 1365-2443. DOI: 10.1046/j.1365-2443.2000.00306.x. URL: https://onlinelibrary.wiley.com/doi/10.1046/j.1365-2443.2000.00306.x (visited on 08/05/2025).

[7] S. Westermann, A. Avila-Sakar, H.-W. Wang, H. Niederstrasser, J. Wong, D. G. Drubin, E. Nogales, and G. Barnes. "Formation of a Dynamic Kinetochore-Microtubule Interface through Assembly of the Dam1 Ring Complex". In: *Molecular Cell* 17.2 (Jan. 2005), pp. 277–290. ISSN: 10972765. DOI: 10.1016/j.molcel.2004.12.019. URL: https://linkinghub.elsevier.com/retrieve/pii/S1097276505010014 (visited on 08/05/2025).

[8] E. Kiermaier, S. Woehrer, Y. Peng, K. Mechtler, and S. Westermann. “A Dam1-based artificial kinetochore is sufficient to promote chromosome segregation in budding yeast”. In: *Nature Cell Biology* 11.9 (Sept. 2009), pp. 1109–1115. ISSN: 1465-7392, 1476-4679. DOI: `10.1038/ncb1924`. URL: `https://www.nature.com/articles/ncb1924` (visited on 08/05/2025).

[9] S. Lacefield, D. T. C. Lau, and A. W. Murray. “Recruiting a microtubule-binding complex to DNA directs chromosome segregation in budding yeast”. In: *Nature Cell Biology* 11.9 (Sept. 2009), pp. 1116–1120. ISSN: 1465-7392, 1476-4679. DOI: `10.1038/ncb1925`. URL: `https://www.nature.com/articles/ncb1925` (visited on 08/05/2025).

[10] F. Lampert, P. Hornung, and S. Westermann. “The Dam1 complex confers microtubule plus end–tracking activity to the Ndc80 kinetochore complex”. In: *Journal of Cell Biology* 189.4 (May 17, 2010), pp. 641–649. ISSN: 1540-8140, 0021-9525. DOI: `10.1083/jcb.200912021`. URL: `https://rupress.org/jcb/article/189/4/641/35836/The-Dam1-complex-confers-microtubule-plus-end` (visited on 08/05/2025).

[11] B. Akiyoshi, K. K. Sarangapani, A. F. Powers, C. R. Nelson, S. L. Reichow, H. Arellano-Santoyo, T. Gonen, J. A. Ranish, C. L. Asbury, and S. Biggins. “Tension directly stabilizes reconstituted kinetochore-microtubule attachments”. In: *Nature* 468.7323 (Nov. 2010). Publisher: Nature Publishing Group, pp. 576–579. ISSN: 1476-4687. DOI: `10.1038/nature09594`. URL: `https://www.nature.com/articles/nature09594` (visited on 02/17/2025).

[12] A. A. Jeyaprakash, A. Santamaria, U. Jayachandran, Y. W. Chan, C. Benda, E. A. Nigg, and E. Conti. “Structural and Functional Organization of the Ska Complex, a Key Component of the Kinetochore-Microtubule Interface”. In: *Molecular Cell* 46.3 (May 2012), pp. 274–286. ISSN: 10972765. DOI: `10.1016/j.molcel.2012.03.005`. URL: `https://linkinghub.elsevier.com/retrieve/pii/S1097276512002122` (visited on 08/05/2025).

[13] M. A. Abad, B. Medina, A. Santamaria, J. Zou, C. Plasberg-Hill, A. Madhumalar, U. Jayachandran, P. M. Redli, J. Rappsilber, E. A. Nigg, and A. A. Jeyaprakash. “Structural basis for microtubule recognition by the human kinetochore Ska complex”. In: *Nature Communications* 5.1 (Jan. 13, 2014), p. 2964. ISSN: 2041-1723. DOI: `10.1038/ncomms3964`. URL: `https://www.nature.com/articles/ncomms3964` (visited on 08/05/2025).

[14] J. W. Driver, A. F. Powers, K. K. Sarangapani, S. Biggins, and C. L. Asbury. “Measuring Kinetochore–Microtubule Interaction In Vitro”. In: *Methods in Enzymology*. Vol. 540. Elsevier, 2014, pp. 321–337. ISBN: 978-0-12-397924-7. DOI: `10.1016/B978-0-12-397924-7.00018-2`. URL: `https://linkinghub.elsevier.com/retrieve/pii/B9780123979247000182` (visited on 08/05/2025).

[15] M. Chakraborty, E. V. Tarasovetc, and E. L. Grishchuk. “In vitro reconstitution of lateral to end-on conversion of kinetochore–microtubule attachments”. In: *Methods in Cell Biology*. Vol. 144. Elsevier, 2018, pp. 307–327. ISBN: 978-0-12-814144-1. DOI: 10.1016/bs.mcb.2018.03.018. URL: https://linkinghub.elsevier.com/retrieve/pii/S0091679X18300189 (visited on 08/05/2025).

[16] Q. Zhang, L. Hu, Y. Chen, W. Tian, and H. Liu. *In vitro Reconstitution Unveils the Phospho-regulated Ska-Ndc80 Macro-complex*. June 23, 2019. DOI: 10.1101/680314. URL: http://biorxiv.org/lookup/doi/10.1101/680314 (visited on 08/05/2025).

[17] J. R. Torvi, J. Wong, D. Serwas, A. Moayed, D. G. Drubin, and G. Barnes. “Reconstitution of kinetochore motility and microtubule dynamics reveals a role for a kinesin-8 in establishing end-on attachments”. In: *eLife* 11 (July 5, 2022), e78450. ISSN: 2050-084X. DOI: 10.7554/eLife.78450. URL: https://elifesciences.org/articles/78450 (visited on 08/05/2025).

[18] K. Asai, Y. Zhou, O. Takenouchi, and T. S. Kitajima. “Artificial kinetochore beads establish a biorientation-like state in the spindle”. In: *Science* 385.6715 (Sept. 20, 2024), pp. 1366–1375. ISSN: 0036-8075, 1095-9203. DOI: 10.1126/science.adn5428. URL: https://www.science.org/doi/10.1126/science.adn5428 (visited on 08/05/2025).

[19] A. R. Bunning and M. L. Gupta Jr. “The importance of microtubule-dependent tension in accurate chromosome segregation”. In: *Frontiers in Cell and Developmental Biology* 11 (Jan. 23, 2023), p. 1096333. ISSN: 2296-634X. DOI: 10.3389/fcell.2023.1096333. URL: https://www.frontiersin.org/articles/10.3389/fcell.2023.1096333/full (visited on 01/22/2025).

[20] S. L. Kline-Smith, S. Sandall, and A. Desai. “Kinetochore–spindle microtubule interactions during mitosis”. In: *Current Opinion in Cell Biology* 17.1 (Feb. 1, 2005), pp. 35–46. ISSN: 0955-0674. DOI: 10.1016/j.ceb.2004.12.009. URL: https://www.sciencedirect.com/science/article/pii/S0955067404001772 (visited on 01/22/2025).

[21] J. S. Andersen, C. J. Wilkinson, T. Mayor, P. Mortensen, E. A. Nigg, and M. Mann. “Proteomic characterization of the human centrosome by protein correlation profiling”. In: *Nature* 426.6966 (Dec. 2003). Publisher: Nature Publishing Group, pp. 570–574. ISSN: 1476-4687. DOI: 10.1038/nature02166. URL: https://www.nature.com/articles/nature02166 (visited on 01/22/2025).

[22] A. Suzuki, B. L. Badger, J. Haase, T. Ohashi, H. P. Erickson, E. D. Salmon, and K. Bloom. “How the kinetochore couples microtubule force and centromere stretch to move chromosomes”. In: *Nature Cell Biology* 18.4 (Apr. 2016). Publisher: Nature Publishing Group, pp. 382–392. ISSN: 1476-4679. DOI: 10.1038/ncb3323. URL: https://www.nature.com/articles/ncb3323 (visited on 01/22/2025).

[23] **A. Nick Maleki**, P. J. Huis in 't Veld, A. Akhmanova, M. Dogterom, and V. A. Volkov. "Estimation of microtubule-generated forces using a DNA origami nanospring". In: *Journal of Cell Science* 136.5 (Mar. 2, 2022), jcs260154. ISSN: 0021-9533. DOI: `10.1242/jcs.260154`. URL: `https://doi.org/10.1242/jcs.260154` (visited on 10/09/2024).

[24] J. Krattenmacher, M. Lera-Ramirez, A. Beber, S. Herynek, L. Grycova, X. Liu, P. Neuzil, F. Nedelec, S. Diez, M. Braun, and Z. Lansky. "Ase1 selectively increases the lifetime of antiparallel microtubule overlaps". In: *Current Biology* 34.17 (Sept. 9, 2024), 4071–4080.e6. ISSN: 0960-9822. DOI: `10.1016/j.cub.2024.07.055`. URL: `https://www.sciencedirect.com/science/article/pii/S0960982224009941` (visited on 01/14/2025).

[25] D. Gogendeau, P. Guichard, and A.-M. Tassin. "Purification of centrosomes from mammalian cell lines". In: *Methods in Cell Biology*. Vol. 129. Elsevier, 2015, pp. 171–189. ISBN: 978-0-12-802449-2. DOI: `10.1016/bs.mcb.2015.03.004`. URL: `https://linkinghub.elsevier.com/retrieve/pii/S0091679X1500076X` (visited on 08/13/2025).

[26] M. Bornens and M. Moudjou. "Chapter 2 Studying the Composition and Function of Centrosomes in Vertebrates". In: *Methods in Cell Biology*. Vol. 61. Elsevier, 1998, pp. 13–34. ISBN: 978-0-12-544163-6. DOI: `10.1016/S0091-679X(08)61973-1`. URL: `https://linkinghub.elsevier.com/retrieve/pii/S0091679X08619731` (visited on 08/13/2025).

[27] S. Roth, I. C. Gârlea, M. Vleugel, B. M. Mulder, and M. Dogterom. *Reconstitution of basic mitotic spindles in cell-like confinement*. Sept. 16, 2019. DOI: `10.1101/770602`. URL: `http://biorxiv.org/lookup/doi/10.1101/770602` (visited on 07/31/2025).

6

CONCLUSION AND OUTLOOK

Every decision is a bet on the future, and all bets have trade-offs

Annie Duke

All models are wrong, but some are useful.

George Box

In this study, we have presented steps to reconstitute a minimal mitotic spindle system using a reductionist approach involving DNA origami techniques to dissect the fundamental mechanisms underlying DNA congression and segregation. By constructing kinetochore mimics via DNA origami nanosprings (NS), controlling microtubule (MT) nucleation sites, and incorporating photocleavable oligonucleotide linkers, we have been able to mimic key aspects of spindle architecture and dynamics. In this chapter summarize the conclusions and discuss possible follow-ups of our experiments.

The work presented in this thesis set out to shed light on one of the central challenges in cell biology: understanding the mechanistic basis of spindle-mediated chromosome congression and segregation Because of its complexity and the involvement of hundreds of proteins, this process is notoriously difficult to dissect in vivo. To overcome this, we pursued a modular, bottom-up reconstitution strategy, aiming to rebuild essential aspects of spindle function using a minimal set of well-defined components.

The guiding principle of this thesis was to divide spindle-mediated DNA segregation into four functional modules: (1) establishing stable, load-bearing connections between shrinking microtubule plus ends and DNA cargos, (2) controlling microtubule nucleation and aster organization, (3) mimicking DNA congression using motor-driven transport, and (4) reconstituting chromosome bi-orientation and segregation through controlled, symmetric microtubule attachments. Each experimental chapter focused on one or more of these modules, gradually building toward an integrated reconstitution of spindle-like behavior.

Chapters 2 and 3 addressed Module 1 by developing and applying nanoscale tools to probe the mechanics of kinetochore–microtubule attachments. Using DNA origami nanosprings, we quantified forces generated by dynamic microtubules and systematically varied the copy number of Ndc80-like complexes to identify conditions for stable and processive load-bearing interactions. Chapter 4 turned to Module 2, implementing microfabrication and DNA nanotechnology to spatially control microtubule nucleation, ultimately enabling the assembly of artificial asters. Chapter 5 extended this framework towards Modules 2–4, presenting experimental steps for constructing a minimal spindle-like system in which opposing microtubules could establish bi-oriented attachments to a DNA cargo via a photocleavable linker, allowing light-controlled segregation. Together, these efforts constitute a stepwise reductionist reconstitution of key spindle functions.

This concluding chapter synthesizes the main findings across the different modules and evaluates how they contribute to our overarching goal: identifying the minimal requirements for spindle-mediated chromosome segregation. We begin by reflecting on the technical advances and mechanistic insights gained from each approach, before considering the limitations inherent to reductionist systems and the challenges of translating these findings to the in vivo context. Finally, we outline future directions for integrating additional regulatory layers and advancing toward a fully reconstituted, three-dimensional spindle apparatus.

6.1. DNA ORIGAMI NANOSPRINGS AS FORCE SENSORS

Our deployment of DNA origami nanosprings as force sensors provides quantitative insights into the forces generated by dynamic MT ends connected to kinetochore-like molecular complexes. The nanospring's non-linear force–extension relationship is particularly sensitive in the sub-piconewton range, allowing for multiplexed force measurements within a single microscopic field. This method does have limitations, including lower temporal resolution (1–100 Hz) relative to optical trapping and potential instability at forces exceeding ~10 pN.

Although the DNA origami nanospring provides valuable force measurements in the sub-piconewton regime, its performance at higher forces and temporal resolution could be thus improved. Future work could focus on chemical crosslinking or ligation strategies to enhance nanospring stability, as well as integrating complementary high-speed imaging techniques.

6.2. JUBAEA COPY NUMBER EFFECTS ON KINETOCHORE-MICROTUBULE INTERACTIONS

In chapter 3 We used the truncated variant of Ndc80 called Ndc80$^{\mathrm{jubaea}}$ (jubaea), which can be expressed in bacteria and retains the loop domain critical for stable attachments [1], to investigate how copy number influences kinetochore-microtubule coupling. To control stoichiometry, we incorporated defined numbers of jubaea complexes (3–20) into DNA origami nanosprings (NS), generating oligomers of increasing valency.

We observed that jubaea oligomers end-tracked microtubules and coupled to dynamics in a copy number–dependent manner. As valency increased, the likelihood of successful MT interactions rose, diffusion along the lattice decreased, and outcomes shifted from detachment toward stabilization. High-valency constructs (NS15 and NS20) strongly promoted rescue events and suppressed depolymerization, with NS20 reducing shrinkage rates by up to 70%. Diffusion assays confirmed a progressive loss of mobility with increasing valency, and NS15–NS20 became essentially immobile on the lattice.

Using nanosprings, we found that jubaea oligomers captured and withstood maximum forces near 10 pN. Interestingly, force efficiency peaked at intermediate valency: NS10 captured the highest amount of force, whereas for higher copy numbers the maximum captured force was lower, likely due to impaired mobility and stabilization of MT shrinkage at MT tips. Supplementing reactions with soluble jubaea further enhanced force capture, suggesting that inter-protein interactions can stabilize attachments. Taken together, our experiments show that increasing Ndc80 copy number tunes the balance between mobility, stability of MT attachment and dynamics, and force generation. Low copy numbers allow diffusion but weak attachment, while high copy numbers stabilize tips and suppress dynamics at the cost of efficient transmission of MT depolymerization forces. The most efficient force coupling emerged at intermediate valency, indicating an optimal stoichiometry. Our results suggest that kinetochores may regulate Ndc80 occupancy to achieve robust yet dynamic attachments, ensuring reliable chromosome segregation.

6.3. MICROTUBULE NUCLEATION

This study (chapter 4) developed a method for controlling microtubule (MT) nucleation sites on surfaces with precise spatial positioning. Pre-fabricated gold surface patterns (rings, lines, and dots) on coverslips were used to serve as selective binding sites for MT seed linkers, while surrounding areas were passivated to prevent non-specific binding. Surface passivation was systematically optimized through rigorous testing of various protocols, with significant success achieved using silane-PEG functionalization. While conventional silane-PEG treatment following acid cleaning reduced non-specific binding by 55%, the introduction of an intermediate oxygen plasma treatment step dramatically enhanced passivation efficiency, yielding a remarkable 93% reduction in non-specific protein adsorption compared to untreated surfaces. This optimized dual-treatment approach—acid cleaning followed by oxygen plasma treatment and then silane-PEG application—created a highly effective contrast between the gold-patterned regions designated for MT seed attachment and the surrounding passivated glass areas. The spatial control achieved through this method and via the use of thiolated DNA origami platforms and MT seeds labeled by complementary handles to the DNA origami, enabled MT growth to be precisely directed from specific predetermined locations on the surface, creating a reliable platform for studying MT dynamics and organization in controlled in vitro environments. This approach overcame the need for specialized deep UV photolithography equipment required by previously established techniques, providing an accessible alternative for laboratories studying MT nucleation dynamics.

By immobilizing microtubule nucleation sites on beads, we successfully reconstituted artificial asters with radial growth. This approach offers a controlled system for examining MT organization. Compared to cellular contexts, where MTs emerge from centrosomes in a highly orchestrated manner, our system provides a more simplified yet tractable model.

6.4. BI-ORIENTATION

We touched on possible synthetic approaches on reconstituting chromosome bi-orientation in Chapter 5. We developed and applied a set of techniques to reconstitute key elements of chromosome biorientation and segregation in vitro. We engineered a symmetric photocleavable linker, designed to connect two identical nanospring binders in a load-bearing, symmetric configuration that could be cleaved on demand by external light stimulus. This allowed us to create responsive nanospring dimers that could be separated in a controlled manner using light. To mimic DNA congression and the transition from lateral to end-on microtubule attachments, we coupled nanosprings to kinesin motors, which actively transported the constructs toward microtubule plus ends and enabled end-on conversion. To recreate stable, load-bearing attachments at dynamic microtubule ends, we employed Jubaea multimers in combination with Ndc80 complexes, which provided resistance against depolymerization forces. We further implemented structural mimics of spindle architecture by using surface-attached centrosomes to nucleate facing asters, thereby generating geometries in which bi-orientation could occur. Note that the artificial asters described in Chapter 4 where not (yet) used in these experiments. To stabilize antiparallel overlaps and increase the probability of bioriented connections by our symmetric nanospring constructs, we introduced Ase1, which crosslinked antiparallel microtubules. Through this combination of synthetic linkers, motor-driven transport, load-bearing attachments, and controlled spindle-like geometries, we took significant steps towards establishing an artificial system that recapitulates central mechanistic steps of chromosome congression, biorientation, and segregation. tral mechanistic steps of chromosome congression, biorientation, and segregation.

6.5. Limitations and Considerations

While this thesis demonstrates that key features of spindle-mediated segregation can be reconstituted in a modular manner, several technical and conceptual limitations must be acknowledged. These reflect both the intrinsic constraints of the reductionist approach and the practical challenges associated with reconstituting such a complex process from minimal components.

1. Force measurements with DNA origami nanosprings: The DNA origami nanospring proved to be a versatile tool for quantifying forces at microtubule plus ends; however, its applicability is restricted to a limited force window (~0.2–10 pN). Above this range, nanospring stability and accuracy diminish. In addition, the temporal resolution of the system (on the order of seconds for two-channel acquisition) is significantly lower than that of optical trapping, limiting our ability to resolve very fast events. Furthermore, in Chapter 3, fluorescent nanospring signal was used for force quantification. Because this signal is spatially more diffuse, it systematically underestimates forces, which needs to be considered when interpreting the measurements.

2. Oligomerization and copy-number control: In our DNA-origami–based oligomerization system, the nanospring provided a defined maximum binding capacity for Jubaea molecules. In practice, however, the actual number of bound proteins could be lower than the theoretical maximum, meaning that the true stoichiometry could be variable from construct to construct. This introduces uncertainty when interpreting copy-number–dependent effects. In addition, diffusion analyses may be subject to observer bias: fast-diffusing nanosprings are visually more conspicuous and thus more likely to be noticed and selected for analysis, potentially skewing the distribution of measured diffusivities.

3. Controlling microtubule nucleation sites: The micropatterning and DNA-origami–based bead platforms used in Chapter 4 enabled control over microtubule nucleation, but both approaches are labor intensive. More importantly, in the bead-based approach, while individual nucleation sites could be positioned, the relative spacing between asters was not directly controlled; instead, experiments relied on identifying chance encounters where asters happened to form at suitable distances from one another. This limits the throughput and reproducibility of bi-astral assays.

4. Reconstitution of bi-orientation: The full bi-orientation assay presented in Chapter 5 remains technically challenging. Achieving two microtubules that directly oppose one another is rare, and it is not yet clear how nanospring-bound complexes behave when encountering crosslinked antiparallel overlaps.

Furthermore, our current assays were performed in the presence of soluble kinesin and Jubaea proteins in solution, rather than being restricted to the nanospring scaffold. This creates a less defined interaction landscape, and although we demonstrated persistent end-binding and processive complexes, the maximum force these assemblies can withstand remains unknown.

5. General considerations: Beyond these specific challenges, several broader limitations should be highlighted. First, our assays employed highly defined connection geometries and constrained protein copy numbers, which inevitably differ from the dynamic and spatially heterogeneous cellular environment. This reduction in complexity, while powerful for mechanistic dissection, limits direct extrapolation to in vivo conditions. Second, there is a potential survival bias in the quantification of NS involved events. Also, low probability events might occur purely by accident rather than as a result of tested conditions. Third, comparisons between Jubaea constructs and Ndc80 trimers must be made with caution, since differences in lattice conditions (e.g., taxol-stabilized versus dynamic microtubules) can significantly alter observed behaviors. Finally, the in vivo relevance of Jubaea as a proxy for Ndc80 remains unresolved. Although our findings are suggestive, only direct cellular validation will establish whether the mechanisms observed here are faithfully reproduced in physiological settings.

Taken together, these limitations illustrate both the strengths and boundaries of the reductionist framework. While it enables the controlled study of fundamental principles, it also demands cautious interpretation when mapping these results back onto the native spindle.

6.6. OUTLOOK AND FUTURE DIRECTIONS

The insights gained from this study open several avenues for future exploration:

1. Refinement of Force-Sensing Tools: While the DNA origami nanospring provides valuable force measurements in the sub-piconewton regime, its performance at higher forces and its temporal resolution could be improved. Future work could focus on enhancement strategies for nanospring stability and resolution.

2. Stoichiometry and Regulation: A critical next step will be the precise quantification of the number of kinetochore mimetic proteins engaged with MTs under dynamic conditions. Furthermore, exploring how post-translational modifications influence binding affinity and force generation could provide deeper insight into in vivo regulatory mechanisms.

3. Integration of Additional Spindle Components: To better recapitulate the cellular environment, incorporating regulatory proteins—such as spindle assembly checkpoint components, microtubule-associated proteins, and additional motors—will eventually be important for studying the interplay between these factors and the core kinetochore–MT interface.

4. Three-Dimensional Spindle Architecture: Expanding the system to mimic the three-dimensional architecture of the mitotic spindle will help bridge the gap between reductionist models and cellular complexity. Advanced imaging modalities and microfabricated environments could simulate the spatial constraints of the cell.

6.7. CONCLUSION

Our work demonstrates that reconstituting the mitotic spindle with minimal components provides a powerful platform to elucidate the mechanistic basis of DNA congression and segregation. The experimental results reveal that an optimal number of kinetochore mimetic proteins is required for both robust MT stabilization and effective force coupling—a finding that may reflect a general regulatory strategy employed by cells. The integration of DNA origami nanosprings, photocleavable oligonucleotides, and kinesin-driven dynamics not only mimics key aspects of spindle function but also introduces novel methods for the spatiotemporal control of molecular interactions. By reconstituting key features of the mitotic spindle with minimal components, we have provided new insights into kinetochore-microtubule attachment and force generation, and provided new avenues for studying the complex dynamics of bi-oriented chromosome-mimics in minimal spindles. Our results highlight the role of multivalency in microtubule binding and demonstrate how motor activity can complement Ndc80-like end-on attachment to facilitate DNA congression. While our approach offers a powerful means to dissect spindle mechanics and dynamics, further work is needed to fully integrate these findings into the broader landscape of mitotic regulation. This study underscores the value of reductionist strategies in uncovering fundamental principles of spindle function while emphasizing the need for continued integration with in vivo systems to achieve a comprehensive understanding of mitotic chromosome segregation.

REFERENCES

[1] S. Polley, H. Müschenborn, M. Terbeck, A. De Antoni, I. R. Vetter, M. Dogterom, A. Musacchio, V. A. Volkov, and P. J. Huis in ’t Veld. “Stable kinetochore-microtubule attachment requires loop-dependent Ndc80-Ndc80 binding”. In: *The EMBO Journal* 42.13 (July 3, 2023). Publisher: John Wiley & Sons, Ltd, e112504. ISSN: 0261-4189. DOI: `10.15252/embj.2022112504`. URL: `https://www.embopress.org/doi/full/10.15252/embj.2022112504` (visited on 10/09/2024).

Curriculum Vitæ

Ali Nick Maleki

01-05-1994	Born in Komijan, Iran.

Education

2012–2016	BSc in Solid-State Physics Iran University of Science & Technology
2016–2018	MSc in Solid-State Physics Sharif University of Technology
2018–2020	MSc in Nanoscience and Nanotechnology - Nanobiophysics Katholic University of Leuven & Technical University of Dresden
2020–2024	PhD in Biophysics Technical University of Delft

LIST OF PUBLICATIONS

1. **A. Nick Maleki**, P. J. Huis in 't Veld, A. Akhmanova, M. Dogterom, and V. A. Volkov. "Estimation of microtubule-generated forces using a DNA origami nanospring". In: *Journal of Cell Science* 136.5 (Mar. 2, 2022), jcs260154. ISSN: 0021-9533. DOI: `10.1242/jcs.260154`. URL: `https://doi.org/10.1242/jcs.260154` (visited on 10/09/2024)
2. **A. Nick Maleki**, E. van der Sluis, and M. Dogterom. "Regulation of stability and force coupling at the microtubule-kinetochore interface via Ndc80 copy number". In: *Under preparation* (2025)

ACKNOWLEDGEMENTS

Life's journey can feel like walking with a headlamp in the dark. Our vision extends only so far, illuminating the immediate path but leaving the distant stretches unseen. Similarly, our grasp of the past has a limited resolution; what's close feels vivid, but the further we travel, the harder it becomes to intuitively grasp the distance covered. Our perception of time's passage shifts, making even four years seem to vanish in the blink of an eye. Yet, this trajectory is punctuated by significant landmarks that add richness to our narrative. For me, the people I've encountered along the way are the most vital of these landmarks, imbuing my experience with vibrancy.

If we imagine that each person carries their own headlamp, casting light on their individual path and surroundings, then together we illuminate a broader landscape, making the 'travel' through time a shared and easier experience. This moment is an opportunity for me to celebrate and deeply appreciate this interconnected reality. I want to express my sincere gratitude to those who have walked alongside me during my PhD journey, a period that indeed feels like it passed in an instant.

First and foremost, I want to thank my supervisor, Marileen. Your compassion for the lab members and your ability to shield us from unnecessary stress were invaluable. Thank you also for your open and nurturing mindset, which fostered an environment where creativity, even in its nascent or seemingly 'stupid' forms, could flourish. Eli, your remarkable tolerance and patience made me feel comfortable approaching you at any time. Your vast reservoir of knowledge and experience has been an incredible asset to our group, and I'm so grateful for your presence. Ontzettend bedankt dat je met mij Nederlands probeert te spreken, ik vond het heel nuttig. While-doing-experiment conversations in the lab about politics were fun too. Esengul, thank you for your assistance with experiments and for creating such a friendly and welcoming atmosphere that truly made the lab feel like home. Ashmiani, your infectious energy brightened the lab, and we deeply appreciate the precious proteins you provided. Roland, thank you for ensuring our essential microscopes were always functioning smoothly. Ilja, Jan, Wiel, Theo, Anke, Allard, Cecilia, and Frank, your frequent help in the lab was indispensable, and I thank you all.

I extend my gratitude to all the PhD students and postdocs in the MDo lab who contributed to my journey. Illina, thank you for introducing me to the fascinating world of microtubule dynamics – the mighty and powerful MT dynamic assay. Yash I admired your approach to conducting research with such composure, and I appreciate the insightful ideas and practical tips you shared for tackling lab challenges. Either you don't have any stress or you don't show it, I assume the former and try to copy you. Nemo, your ability to achieve the seemingly impossible is remarkable, though I still maintain that Minecraft's greatness remains unproven! What is put in the treasure boxes are not always treasures. Ask Reza and he can explain this well to you. Thank you for championing open science and meticulous documentation, ensuring our work remains understandable even after our departure. Prince Reza, thank you for illuminating the tricks of navigating both lab life and life beyond. Let the spirit of the young, live long in the old guy. Tomohiro, you were instrumental in my entry into the motor protein domain, and I'm grateful for your guidance on using Fiji macros for automation. I feel incredibly fortunate that my early PhD days coincided with your presence here; your extensive knowledge was a significant benefit. Thank you for hosting me in your Tokyo lab – the Takoyaki and onsens are unforgettable memories. Hanjin, Hiroshi and Lennart, thanks a lot for helping me create and reconstruct beautiful Cryo-EM images of MT and the nanospring. Thank you Beatriz, the podcast master, for your kindness and willingness to help others. Your reactions to cute goslings and ducklings tempt us to show or mention them so that we see more of those reactions. Sinda, the lab dweller, you adopted the Dutch protestant hard working ethics very seriously, not knowing it has changed and it is almost a crime to work after 17:00 here. But this doesn't stop me admiring you. Thank you Vincent, your open and non-judgmental attitude created a safe and intellectually stimulating space for conversation. A genZ who managed to escape the genZ doom. Congrats! I see some elements of Iranian-ness in you, I'm not sure if this is a compliment or the opposite, I leave the interpretation to you, but the final result was that it made it easy for me to connect. You and Beatriz honored me to be my paranymph, much appreciated. Vladimir, thank you for your constructive critiques that consistently improved our work and for generously sharing your expertise. I criticized criticism in the preface, but that was for personal life, in the professional life it is a razor that cuts embellishments and help carving out something real. Alejandro, thank you for guiding me in the intricacies of AFM. Lisa, Joris, Prashali and Brigit you are newer in the BN, but already have proven to be very nice colleagues. Curious to see how your projects take shape and evolve in the coming years

Last but certainly not least, I want to thank my cherished friends here in Delft: Masoud, Arash, Khatereh, Siamak, Atusa, Artemis, Sirus, Reza, Mohammad, Anna, Annija, Darya, Mathijs and Mehdi. And to my dear friends overseas: Milad, Mehdi, Ali, Mohammad, Mohsen, Arman, Meysam and Abed. Your presence is like precious jewelry, adding brilliance to life. Finally, my deepest gratitude goes to my family: Ghodrat, Khadijeh, Reza, Hossein, Parisa, and Zohreh, for their unwavering support and for accompanying me through every stage of my life.

You have made my path brighter, my heartfelt blessings and good wishes to you all.

Sincerely,
Ali Nick Maleki
Delft, October 2025